From structural distortions to physical properties in orthorhombic rare-earth perovskites

Rui Miguel Abreu Vilarinho da Silva
Doutoramento em Física
Departamento de Física e Astronomia
2019

Orientador
Joaquim Agostinho Gomes Moreira, Professor Auxiliar, Faculdade de Ciências da Universidade do Porto

Coorientador
Abílio de Jesus Monteiro Almeida, Professor Associado, Faculdade de Ciências da Universidade do Porto

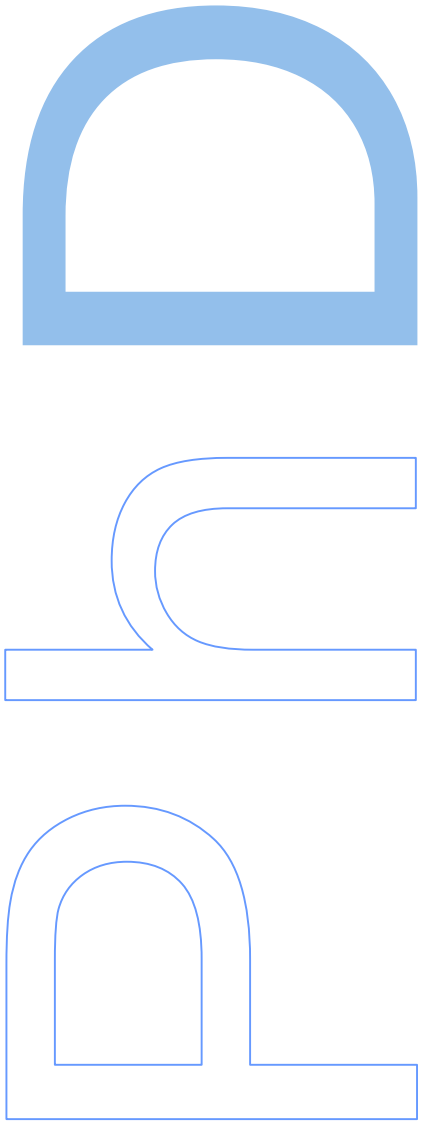

Aos meus pais e <.

Agradeço a todos os amigos e colegas do IFIMUP que me ajudaram.

The samples used in this thesis were synthesized by the groups of P. Tavares at UTAD and M. Mihalik at IEP-SAS.

Most of the experimental work of this thesis used the techniques and staff of the IFIMUP facilities at FCUP.

The majority of the citations of this thesis were obtained through Sci-Hub.

A special thanks to them and to all who also collaborated with me.

Funded by PD/BI/106014/2015 and PD/BD/114456/2016.

Resumo

Nesta tese, apresentamos um estudo sistemático da estrutura, dinâmica de rede e propriedades físicas de manganites ($R\mathrm{MnO_3}$) e ferrites ($R\mathrm{FeO_3}$) de terras raras com simetria ortorrômbica, em função da substituição química e de parâmetros externos. O principal objectivo desta tese é investigar uma possível relação entre as distorções estruturais e as propriedades físicas desta notável classe de compostos pertencentes às perovskites do tipo $\mathrm{GdFeO_3}$. As distorções que desencadeiam a redução de simetria do grupo espacial $Pm\bar{3}m$ cúbico para o $Pnma$ são as inclinações dos octeadros BO_6. Focamos a nossa atenção nas principais distorções que caracterizam a estrutura cristalina destes compostos: as inclinações dos octeadros e o efeito de Jahn-Teller. É bem conhecido que ambas estas distorções são ingredientes chave das complexas interacções eléctronicas e magnéticas nestes compostos e, consequentemente, das suas propriedades polares e magnetoelétricas.

Apresentamos um estudo detalhado da dinâmica de rede das $R\mathrm{FeO_3}$ (R = Sm até Dy) e $\mathrm{TbMn_{1-x}Fe_xO_3}$ por espectroscopia Raman, em condições de ambiente. Propomos uma identificação detalhada dos modos activos Raman. Evidenciamos que, pelo menos para as $R\mathrm{FeO_3}$, existem dois racionais diferentes entre os modos de rotação em fase e anti-fase com os respectivos ângulos de inclinação, enquanto um racional único foi considerado em outras perovskites ortorrômbicas. Além disso, discutimos o papel fundamental desempenhado pelas distorções internas dos octaedros na definição destes racionais, como foi encontrado no $\mathrm{TbMn_{1-x}Fe_xO_3}$.

A transição de fase paramagnética para a antiferromagnética das $R\mathrm{FeO_3}$ (R = Nd até Tb) não é revelada por nenhuma anomalia na dependência na temperatura das vibrações da rede, indicando que não envolve distorções estruturais. Além disso, para o $\mathrm{NdFeO_3}$ e $\mathrm{TbFeO_3}$, verificamos um claro acoplamento spin-fonão, próximo às transições de reorientação de spin com origem na interação magnética Fe-R.

Seguimos a dependência na pressão da distorção de Jahn-Teller nas $R\mathrm{MnO_3}$ (R = Gd e Dy), bem como, as inclinações dos octeadros e os comprimentos médios da ligação Fe-O nas $R\mathrm{FeO_3}$ (R = Nd até Dy), e o seu papel na transição de fase induzida por pressão existente nestes compostos. Descobrimos que a distorção de Jahn-Teller é fortemente reduzida a pressões bastante baixas (P = 6 GPa), prevalecendo até 30 GPa. Em relação à inclinação dos octeedros das $R\mathrm{FeO_3}$, os resultados experimentais evidenciam a diminuição/aumento à medida que a pressão aumenta, para catiões de terras-raras maiores/menores. O $\mathrm{EuFeO_3}$ está no limite, apresentando ângulos de inclinação quase independentes da pressão. Para os compostos onde as inclinações aumentam com a pressão, os octaedros de FeO_6 são comprimidos a taxas menores do que aqueles que exibem uma dependência na pressão das inclinações oposta, o que está correlacionado com o valor da pressão crítica.

Provamos, a partir dos estudos apresentados nesta tese, que mecanismos microscópicos adicionais devem ser incorporados na discussão dos dados experimentais. Do ponto de vista estrutural, embora as distorções de $R\mathrm{MnO_3}$ and $R\mathrm{FeO_3}$ apresentem uma dependências no raio iónico da terras raras e na pressão semelhantes, nomeadamente uma semelhante transição de fase metal-isolador induzida por pressão, o diagrama de fases magnético das $R\mathrm{FeO_3}$ não pode ser simplesmente descrito pelo ângulo de inclinação, onde também as interações de spins R-Fe devem ser consideradas. Além disso, no sistema $\mathrm{TbMn_{1-x}Fe_xO_3}$, temos evidências experimentais para o desaparecimento da distorção de Jahn-Teller para a concentrações de Fe acima de 50%, mas o diagrama de fases que propomos para este sistema não reflecte esta mudança. De facto, existem mudanças significativas em relação à sequência de fases magnética, e propriedades polares e magnetoelétricas acopladas, mesmo quando o ângulo de inclinação dos octaedros e a distorção de Jahn-Teller são mantidos constantes, como na região do $\mathrm{TbMn_{1-x}Fe_xO_3}$ com $x < 0.05$. Observamos um aumento da sensibilidade da polarização elétrica a um campo magnético aplicado, e a sua eventual supressão, devido ao favorecimento de um alinhamento oblíquo pela introdução do Fe, que altera as interacções dos eléctrões-e_g, desbalanceando os integrais de troca ferro- e antiferromagnéticos.

Palavras-Chave: sistema de electrões fortemente correlacionado, perovesquites de manganites e ferrites de terras-raras, distorções estruturais, magnetoelectricidade, distorção de Jahn-Teller

Abstract

In this thesis, we present a systematic study of the structure, lattice dynamics, and physical properties of rare-earth orthomanganites (RMnO$_3$) and orthoferrites (RFeO$_3$) as a function of chemical substitution and external parameters. The main objective of this thesis is to search for a possible relationship between structural distortions and physical properties behavior of this outstanding class of compounds that belong to the GdFeO$_3$-type perovskites. The primary distortions triggering the symmetry lowering from the cubic $Pm\bar{3}m$ to the $Pnma$ space group are assigned to the octahedral tiltings. We focus our attention on the main distortions characterizing the crystalline structure of these compounds: the BO_6octahedral tiltings and the Jahn-Teller effect. It is well known that both distortions are the key ingredient underlying the complex electronic and magnetic interaction in these compounds and, consequently, the polar and magnetoelectric properties.

A detailed Raman scattering study of the lattice dynamics of RFeO$_3$ (R = Sm to Dy) and TbMn$_{1-x}$Fe$_x$O$_3$ at room conditions, is presented. Here, we propose a detailed assignment of the Raman-active modes. We evidenced that, at least for the RFeO$_3$, two different rationales exist between the in-phase and anti-phase rotation modes with the respective tilt angles, while a unique rational has been considered in other orthorhombic perovskites. Moreover, we also discuss the key role played by the internal octahedra distortions defining these rationales, as it was found in TbMn$_{1-x}$Fe$_x$O$_3$.

The paramagnetic to antiferromagnetic phase transition in RFeO$_3$ (R = Nd to Tb) is not revealed by any anomalous temperature dependence of the lattice vibrations, pointing that it does not involve structural distortions. Moreover, for NdFeO$_3$ and TbFeO$_3$, clear spin-phonon coupling, close to the spin-reorientation transitions, arising from the magnetic interplay between the Fe- and R-sublattices were ascertained.

We followed the pressure dependence of the Jahn-Teller distortion in RMnO$_3$ (R = Gd and Dy), as well as, the octahedral tilts and mean Fe-O bond lengths in RFeO$_3$ (R = Nd to Dy) and their role on the pressure-induced phase transition displayed by all of these compounds. We have found that the Jahn-Teller distortion is strongly reduced at rather low pressures (P = 6 GPa), prevailing up to 30 GPa. Regarding the anti- and in-phase octahedral tilting in RFeO$_3$, the experimental results evidences for the decrease/increase as pressure increases, for larger/smaller rare-earth cations. EuFeO$_3$ stands at the borderline, with nearly pressure-independent tilt angles. For the compounds where the tilts increase with pressure, the FeO$_6$ octahedra are compressed at lower rates than for those ones exhibiting opposite pressure tilt dependence, which correlates with the critical pressure value.

We have proved from the studies presented in this thesis that further microscopic mechanisms have to be incorporated in the discussion of the experimental data. From the structural point of view, though the distortions of RMnO$_3$ and RFeO$_3$ exhibits rather similar rare-earth ionic radius and pressure dependencies, namely a common pressure-induced structural insulating-to-metallic phase transition, the magnetic phase-diagram of the RFeO$_3$ cannot be simply scaled by the tilt angle, where also the R-Fe spins interactions have to be considered. Furthermore, on TbMn$_{1-x}$Fe$_x$O$_3$, we have experimental evidences for the disappearance of the Jahn-Teller distortion for Fe-concentration above 50%, yet the phase diagram that we have proposed for this system does not mirror this change. Indeed, there exist significant changes concerning the magnetic phase sequence, and coupled polar and magnetoelectric properties, even when the octahedral tilt angle and the Jahn-Teller distortion are kept constant, as in the case of TbMn$_{1-x}$Fe$_x$O$_3$ with $x < 0.05$. We observe an increase of the electric polarization sensitivity to an applied magnetic field, and its eventual suppression, due to the promotion of a spin-canted alignment by the Fe-substitution, which alters the interactions of the e_g-electrons, unbalancing the ferro- and antiferromagnetic exchanges.

Keywords: strongly correlated electron systems; rare-earth orthomanganites and orthoferrites perovskites; structural distortions; magnetoelectricity, Jahn-Teller distortion

Contents

List of Figures

List of Tables

List of Publications

During the development of this thesis I had 7 stays with accepted proposals for beamtime at international infrastructures (European Synchrotron Radiation Facility, Isis Neutron and Muon Source and Paul Scherrer Institut) and 6 stays with collaborations at international laboratories (Micro and Nanotechnology Innovation Centre, Centre de Recherche Public Gabriel Lippmann and Institut Néel). I have also attended to 5 international schools on subjects related to this thesis.

The developed work has resulted in 1 award of "Best Student Talk" at the VIII IFIMUP-IN Workshop, 2 invited oral presentations, 14 regular oral presentations and 10 poster contributions mainly in international conferences, as well as 1 conference proceeding:

1. M. Mihalik jr., M. Mihalik, M. Fitta, M. Vavra, M. Zentková, R. Vilarinho, D. A. Mota, M. Webber, G. Mael, J. Kreisel, P. Tavares, J. Agostinho Moreira, A. Almeida, "Magnetic, dielectric and dynamical properties of TbMn1-xFexO3 ceramics". Journal of Physics: Conference proceedings (2014). DOI: 10.1088/1742-6596/592/1/012119

The vast majority of the work presented in this thesis has been, or will soon be, published as regular papers in peer-reviewed international papers, achieving already 40 citations. Their list is the following:

1. R. Vilarinho, D. J. Passos, E. C. Queirós, P. B. Tavares, A. Almeida, M. C. Weber, M. Guennou, J. Kreisel, and J. Agostinho Moreira, "Suppression of cooperative Jahn-Teller distortion and its effect on Raman octahedra rotation modes of TbMn1-xFexO3", Physical Review B 97, 1441110 (2018). DOI: 10.1103/PhysRevB.97.144110

2. R. Vilarinho, E. C. Queirós, D. J. Passos, D. A. Mota, P. B. Tavares, M. Mihalik jr., M. Zentkova, M. Mihalik, A. Almeida and J. Agostinho Moreira, "On the ferroelectric and magnetoelectric mechanisms in low Fe3+ doped TbMnO3", Journal of Magnetism and Magnetic Materials 437, 167 (2017). DOI: 10.1016/j.jmmm.2017.04.085

3. M. Mihalik jr., M. Mihalik, J. Jaglicic, R. Vilarinho, J. Agostinho Moreira, E. Queirós, P. B. Tavares, A. Almeida and M. Zentková, "Magnetic phase diagram of the TbMn1-xFexO3 solid solution system", Physica B: Condensed Matter 506, 163-167 (2017). DOI: 10.1016/j.physb.2016.11.015

4. M. Weber, M. Guennou, H. J. Zhao, J. Íñiguez, R. Vilarinho, A. Almeida, J. Agostinho Moreira and J. Kreisel, "Raman spectroscopy of rare-earth orthoferrites RFeO3 (R = La, Sm, Eu, Gd, Tb, Dy)", Physical Review B 94, 214103 (2016). DOI: 10.1103/PhysRevB.94.214103

5. R. Vilarinho, M. Guennou, M. Weber, P. Bouvier, I. Peral, A. Almeida and J. Agostinho Moreira, "Pressure evolution of elementary distortions and phase transition in RFeO3 perovskites", accepted in Physical Review B.

6. R. Vilarinho, B. Mota, C. Dias, M. Guennou, M. Weber, P. Bouvier, A. Almeida, J. Kreisel and J. Agostinho Moreira, "Anomalous Spin-Phonon Coupling of RFeO3", to be submitted.

7. R. Vilarinho, R. M. Costa, V. Cuartero, T. Irifune, V. Monteseguro, A. M. Pereira, A. Almeida and J. Agostinho Moreira, "Weakened Jahn-Teller distortion persistence on RMnO3 under high-pressure", in preparation.

Part I

Introduction

Chapter 1

Fundamentals

The demand for new materials with higher performance and versatility has been focused on those exhibiting coupling between elementary excitations [1, 2]. The transition metal oxides, with perovskite structure, have been largely studied because these materials exhibit strong coupling between orbital, electronic, spin and lattice degrees of freedom [1, 3]. This is because the transition metal s-electrons are transferred to the oxygen ions, and the remaining strongly correlated d-electrons determine their physical properties such as electrical transport, magnetism, optical response, thermal conductivity and superconductivity [4]. These electron correlations constrain the number of electrons at a given lattice site, and induce a local entanglement of the charge, spin and orbital degrees of freedom, giving rise to a variety of phenomena, for example, Mott insulators, various charge, spin and orbital orderings, metal to insulator transitions, multiferroicity and superconductivity [4]. The interplay among the electronic degrees of freedom produces various forms of symmetry-breaking patterns, leading to novel emergent phenomena that appear only through the collective behavior of electrons and cannot be expected from individual electrons [4]. In recent years, there has been a burst of activity to manipulate these phenomena, as well as to create new ones [4].

In this scope, an interesting class are the multiferroics, that present co-existence of more than one primary ferroic order in a single phase material [1]. The coexistence of several order parameters brings about novel physical phenomena and offers possibilities for new device functions. These ferroic orders can correspond to ferromagnetism, ferroelectricity, ferroelasticity and ferrotoroidicity [2]. Though the term multiferroic was first used for materials that exhibit ferroelectricity and ferromagnetism, as shown in the diagram of Figure 1.1(a), it has been extended to those displaying both ferroelectricity and antiferromagnetism [5].

The existence of a cross-coupling between the magnetic, electric and elastic orders is of great interest (see Figure 1.1(b)). Piezoelectricity is already widely used at the industrial scale for high-sensitivity sensors (transforming small mechanic displacements into electric voltage) or actuators (transforming applied voltages into small mechanic displacements). Magnetoelasticity is very rare and scarcely studied. Here, we will focus on the magnetoelectric coupling, as magnetism and ferroelectricity are essential to many forms of current technology, and the quest for multiferroic materials where these two phenomena are intimately coupled, is of great technological and fundamental importance. For instance, they can be exploited in novel types of memory elements. As ferroelectric polarization and magnetization are used to encode binary information in FeRAMs (ferroelectric random access memories) and MRAMs (magnetic random access memories), respectively, the coexistence of magnetization and polarization in a multiferroic material allow the realization of four-state logic in a single device [3]. More complex schemes have even been proposed in order to store up to eight logic states [3]. The exciting new development is the discovery that even a weak magnetoelectric interaction can lead to spectacular cross-coupling effects when it induces electric polarization in a magnetically ordered state [6]. Such ferroelectricity, showing an unprecedented sensitivity to applied magnetic fields, occurs in frustrated magnets

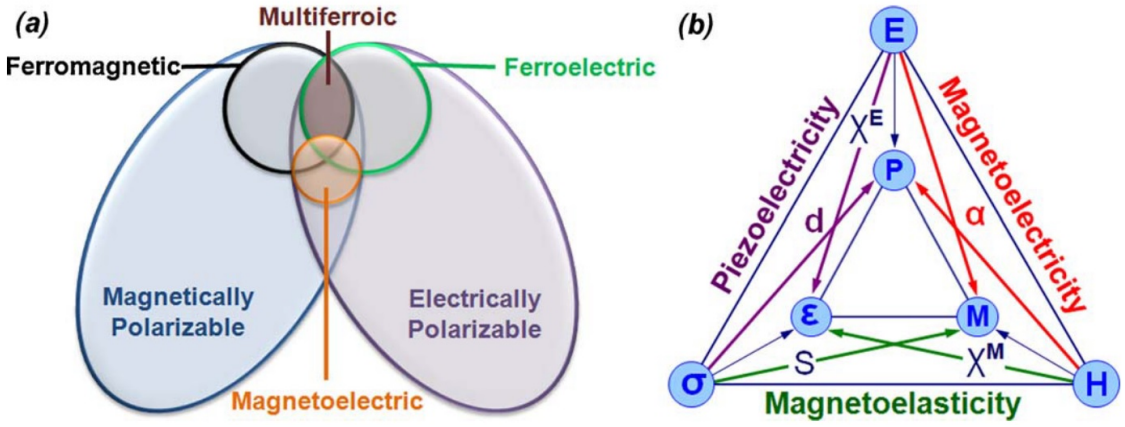

Figure 1.1: (a) Relationship between multiferroic and magnetoelectric material and (b) schematic illustrating different types of coupling present in materials. Adapted from [1] and [7].

with competing interactions between spins and complex magnetic structures [6]. This coupling enables the control of the ferroelectric polarization by a magnetic field and, conversely, the manipulation of magnetization by an electric field [3].

However, multiferroic and magnetoelectric materials are rare, as ferroelectricity and magnetism tend to be mutually exclusive and interact weakly with each other when they coexist [8]. This is because the transition metal d-electrons, which are essential for magnetism, reduce the tendency for off-center ferroelectric distortion. Consequently, an additional electronic or structural driving force must be present for ferromagnetism and ferroelectricity to be both present. One scenario for multiferroicity is when ferroelectric materials contain magnetic ions that are capable to magnetically order at lower temperatures, such as $BiFeO_3$, $BiMnO_3$ and $YMnO_3$ [9, 10]. At higher temperatures (T_C), they present only polar properties, but below a certain temperature a spin order, typically antiferromagnetic, is established (T_N), turning the material into a multiferroic (i.e. $T_C \gg T_N$). In $YMnO_3$, ferroelectricity emerges as a double potential well is created by the fivefold oxygen coordination. In $BiMnO_3$ and $BiFeO_3$, the asymmetry is created by the Bi-O hybridization [11]. Yet, in these kind of materials, as two distinct mechanisms are at the origin of each ordering, the magnetic transition is only slightly sensed by the polar properties, mirroring a weak magnetoelectric coupling. This happens because the order parameter associated with the electric polarization is already saturated when the magnetic order parameter emerges. For example, the $BiFeO_3$ and $YMnO_3$, though presenting rather larger electric polarizations of 100 and 6 $\mu C.cm^{-2}$, their T_C is of 1100 and 913 K, while T_N is of 640 and 70 K, respectively [9, 10]. Thus, they are not the most suitable for magnetoelectric applications. In these cases, a solution to increase the magnetoelectric coupling is by bringing T_C and T_N closer together.

Another scenario is observed when the ferroelectricity emerges from a complex modulated spin structure that breaks the spatial inversion symmetry. This is the case of $TbMnO_3$ and $DyMnO_3$, demonstrated to be highly promising for magnetoelectric applications [12, 13]. The ferroelectricity is of improper nature (i.e. a second-order parameter), assuming values of 0.05 $\mu C.cm^{-2}$ [14]. Still, as the electric polarization is intrinsically connected with the spin structure, the coupling between the magnetic and polar properties is much stronger, which makes these materials much more interesting. It is at this point crucial to highlight that their spin structure has been proved to be highly dependent on the elementary structural distortions, which is mediated by a driving force based on the subtle balance between competitive ferro- and antiferromagnetic super-exchanges. In this regard, these materials have been at the focus of intense research, because of their remarkable structurally distortion controlled phase transitions sequences, accompanied by changes on the

magnetic, transport and ferroelectric properties. It is on these kind of materials, presenting strong couplings between different degrees of freedom, that this work will focus.

This thesis is then aimed at unraveling the role of the elementary distortions and exploring the variety of the physical properties in different rare earth oxides series. To accomplish these main goals, we have selected the rare-earth orthomanganites ($R\mathrm{MnO_3}$) and orthoferrites ($R\mathrm{FeO_3}$) series and their solid solution $R\mathrm{Mn_{1-x}Fe_xO_3}$ (R = Tb), for two main reasons. On one hand, the fact that all the compounds have the same $Pnma$ symmetry, due to the similarity of the Mn^{3+} and Fe^{3+} ions. In this regard, the dependence of the structural distortions on the rare-earth ion and external parameters will enable to reach a much deeper insight of their importance in driving the behavior of these materials. On the second hand, the possibility of changing their magnetic structure through substitution of Mn^{3+} and Fe^{3+} will enable a detailed investigation of their magnetic, polar and magnetoelectric properties, tracing the corresponding phase diagrams.

The results are divided into two large parts. In the first, we aim at describing how the structural distortions of these materials evolve with the compositions, hydrostatic pressure and temperature. In the second, we study their physical properties, namely the magnetic orderings and the coupled polar properties that arise via the magnetoelectric effect, at the largest possible extent of temperature and magnetic field.

1.1 Structural Distortions of Orthorhombic Perovskites

Most of the known multiferroics present a crystallographic structure that originates from the ideal cubic perovskite of symmetry $Pm\bar{3}m$, shown in Figure 1.2(a). It is one of the most known structure for solid materials, and its general formula is given by ABX_3. Typically, the A-cation is a rare-earth (La to Lu) or a post-transition metal (Pb or Bi), the B-cation is a transition metal and the X anion is nitrogen, oxygen or fluorine. The simple ideal perovskite structure consist in corner shared BX_6 octahedra, where the B cation occupies the octahedra centers and the A cations the dodecahedra centers. The BX_6 octahedra then form chains along the cubic axis, and the A-cation occupying the dodecahedron cavity created by them. However, for the cubic symmetry to be preserved, the ionic diameter of the A-cation must match the cavity between the BX_6 octahedra chains. This matching can be geometrically calculated by the relation between the ionic radii (12th coordination for the A- and 6th for the B-cation) given by the Goldschmidt tolerance factor, expressed as [15]:

$$t = \frac{r_A + r_X}{\sqrt{2}\,(r_B + r_X)}\,. \tag{1.1}$$

Actually, the situation of $t = 1$ of the ideal perovskites structure is rarely observed, being the most notable case the $SrTiO_3$. Yet, in most perovskite-like structures this is not the case. If X is oxygen and A is a rare-earth, its ionic radius is typically smaller than the formed cavity ($t < 1$). To compensate this and improve cationic coordination, there is a short-period cooperative rotation of the BO_6 octahedra. This lowers the cubic symmetry, often to a tetragonal (e.g. $SrTiO_3$ below 105 K), hexagonal (e.g. $YMnO_3$ and $HoMnO_3$) or orthorhombic symmetry (e.g. TbMnO3 and $DyMnO_3$). This thesis will focus solely on the orthorhombic $Pnma$ symmetry, found on the rare-earth orthomanganites ($R\mathrm{MnO_3}$) and orthoferrites ($R\mathrm{FeO_3}$) and their solid solution, which will be hereafter designated simply as rare-earth manganites and ferrites, respectively. Their structure is shown in Figure 1.2(b). Yet, before further advancing, it is worth to understand how this orthorhombic $Pnma$ structure is obtained from the ideal cubic $Pm\bar{3}m$ structure.

The symmetry-lowering distortions to the $Pnma$ structure consist in in-phase and anti-phase tilts of the BO_6 octahedra, causing a fourfold increase of the primitive unit cell ($Z = 4$) [17–19]. The in-phase tilt occurs around the $[010]_{\mathrm{pc}}$ and the anti-phase tilt around the $[101]_{\mathrm{pc}}$ pseudocubic axes, with respect to the ideal $Pm\bar{3}m$ perovskite structure [17]. The pseudocubic axes are an approximation as if the cubic symmetry was

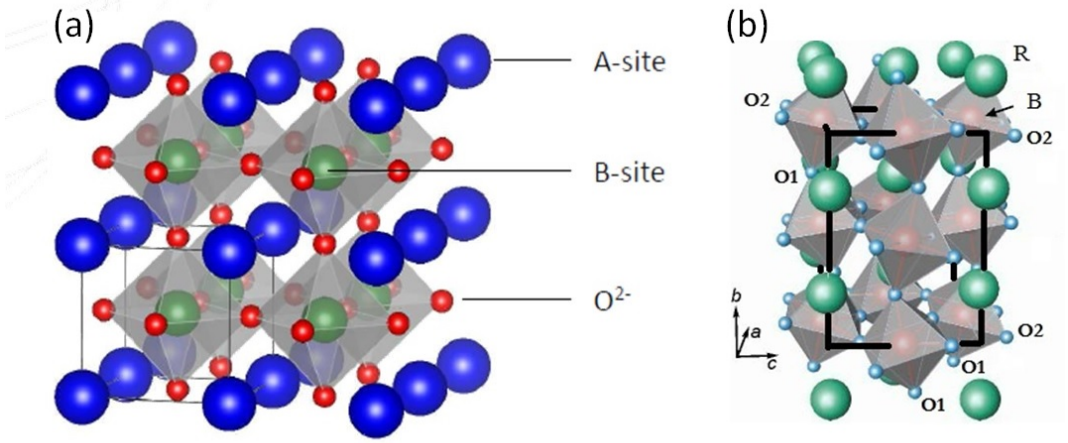

Figure 1.2: (a) Structure of an ideal cubic perovskite with $Pm\bar{3}m$ symmetry and general formula ABX_3. (b) Distorted perovskite structure with $Pnma$ symmetry resulting from the octahedra rotation due to the small A-cation size. Adapted from [16].

maintained, and are widely used to compare the distortions of the symmetry lowering to the ideal cubic metric. For the case of the orthorhombic $Pnma$ structure they are given by [17]:

$$a_{pc} = \frac{a}{\sqrt{2}},\ b_{pc} = \frac{b}{2},\ c_{pc} = \frac{c}{\sqrt{2}}\ , \tag{1.2}$$

where the $V_{pc} = \frac{V}{4}$, with Z = 1.

The tilt system of this kind of materials is usually described using the Glazer's notation [17]. In this notation, the $a^0a^0a^0$ designates an untilted system [17]. When tilts are present around a given axis, a + is introduced on the index of that respective axis if the tilt is in-phase, and a − if the tilt is anti-phase. Figure 1.3(a) and (b) show a view along the tilt axis for a single in-phase and anti-phase tilt, respectively. When more than one tilt is present with different values, then different letters are used [17]. In the $Pnma$ perovskites, Megaw has shown that it is sufficient to consider two independent angles θ and ϕ in order to describe the octahedral rotations of the $Pnma$ phase, assuming that the octahedral tilts a_x^- and a_z^- are approximately equal [20]. The angle can be then expressed as $cos(\Phi) = cos(\theta).cos(\phi)$ [21]. Thus, the in-phase tilt about the $[010]_{\text{pc}}$ axis is represented as $a^0b^+a^0$, while the anti-phase tilts about the $[101]_{\text{pc}}$ axis are represented as $a^-b^0a^-$ [17]. Finally, the coexistence of these three tilts in the $Pnma$ structure results in the $a^-b^+a^-$ designation, and the positive and negative rotation of the octahedra in adjacent layers is presented in Figure 1.3(c). It is worth to stress that the coexistence of two anti-phase tilts imposes a deformation of the otherwise regular octahedra. The reason for this is schematically shown in Figures 1.3(d) to (f), and is as follows. Before any rotation (Figure 1.3(d)), the top oxygen of the bottom layer (black circle) and bottom oxygen of the upper layer (white circle), which in fact are the same shared oxygen, are in the same position. When the first anti-phase tilt along the $[100]_{\text{pc}}$ axis ($a^-b^0b^0$) is considered, both these oxygens are displaced equally (Figure 1.3(e)). However, when we apply the second anti-phase tilt along the $[001]_{\text{pc}}$ axis ($a^0a^0c^-$), the upper layer and the bottom layer octahedra displace the same oxygen into opposite directions (Figure 1.3(f)). The obtained octahedra are no longer regular, one of its direction is deformed.

This structural symmetry reduction affects the symmetry constrains on the position of each atom in the structure. These can be described by the respective Wyckoff positions, shown in Tables 1.1 for the $Pm\bar{3}m$ and the $Pnma$ phase of the ABO_3perovskite structure. In the $Pm\bar{3}m$ phase, both the A and B-cations occupy symmetry inversion sites (vertices and center of the cube, respectively), while the oxygens are at the center of

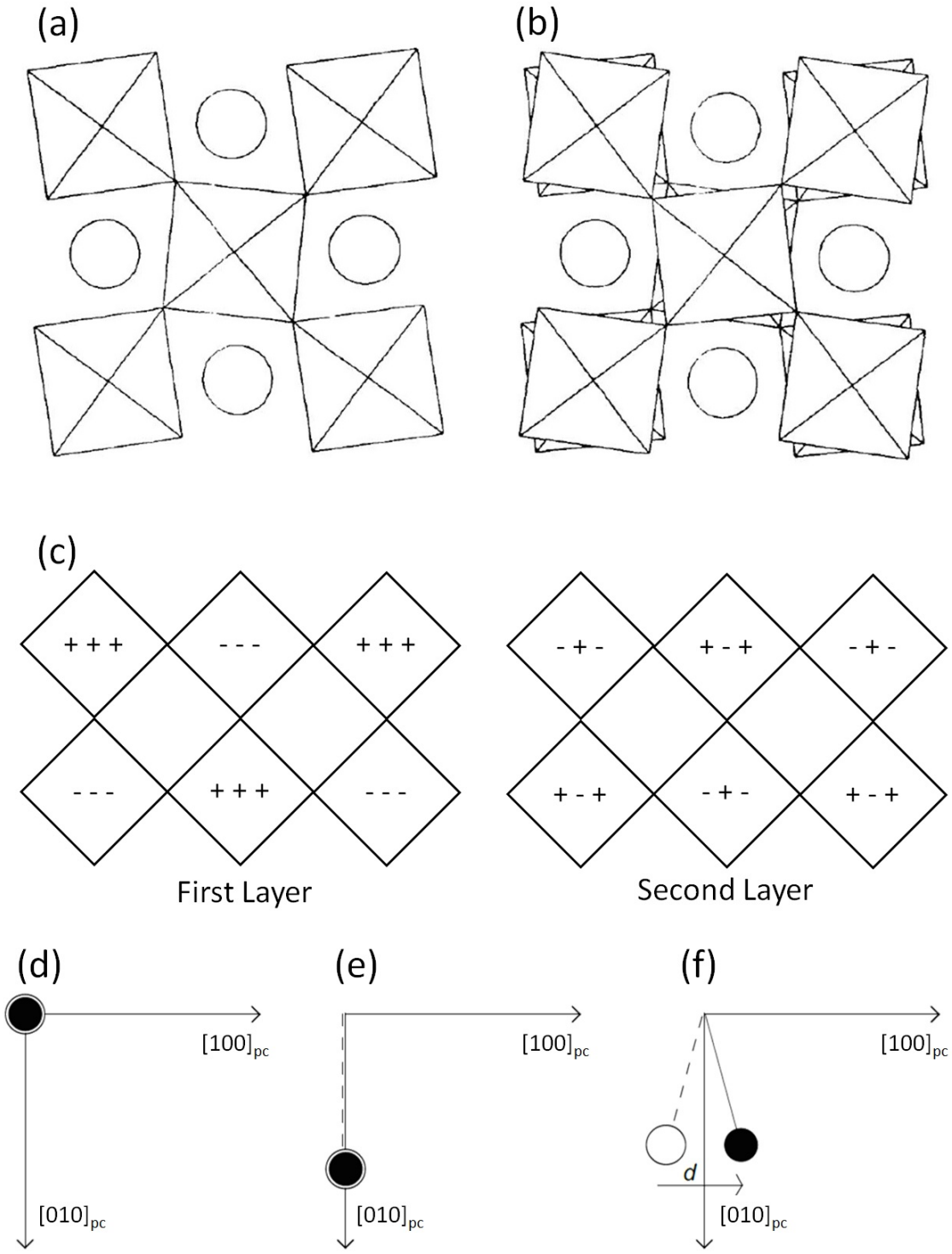

Figure 1.3: View along the $[010]_{pc}$ direction of two adjacent layers of octahedra for (a) the $a^0b^+a^0$ tilt system, (b) the $a^0b^-a^0$ tilt system and (c) the $a^-b^+a^-$ tilt system. + and - represent positive and negative rotations, respectively, of each octahedron along one of its three axes. Projection in the $[100]_{pc}$ plane between two octahedra layers. The white circle stands for the shared bottom anion of the octahedron on the upper layer and the black circle stands for the upper anion in bottom layer. The situation is represented (d) before any rotation, (e) after the first anti-phase tilt about $[100]_{pc}$ axis and (f) after the second anti-phase tilt about the $[001]_{pc}$ axis. After the second anti-phase tilt the octahedra are no longer connected. Adapted from [19].

Atom	Multiplicity	Wyckoff letters	Site symmetry
A	1	a	$m\bar{3}m$
B	1	b	$m\bar{3}m$
O	3	c	4/mm.m

Atom	Multiplicity	Wyckoff letters	Site symmetry
A	4	c	.m.
B	4	b	$\bar{1}$
O1	4	c	.m.
O2	8	d	1

Table 1.1: Wyckoff positions for the $Pm\bar{3}m$ (top) and the $Pnma$ (bottom) phase of the ABO_3perovskite structure.

the cube faces. All the coordinates of each atom are absolutely fixed by symmetry. In the $Pnma$ phase, the B-cation remains at the symmetry inversion site, while the A-cation now occupies a site with a mirror plane symmetry, with two unconstrained coordinates (x and z). The oxygens are now divided into two different sites. The two O1 (the apical oxygens of the octahedron) have the same symmetry as the A-cation, occupying the same xz-plane. The four O2 (the equatorial oxygens of the octahedron) are in what is designated as general positions, without any constrains on their coordinates, meaning that they are left invariant only for the identity operation. It is worth to mention that due these oxygen displacements, the A-cation now forms 8 shorter bonds and 4 longer bonds with the oxygens. Thus, its coordination is reduced from 12 to 8, which must be taken into account when calculating the tolerance factor.

A quantitative way of expressing the structural distortions of a given lower-symmetry phase (the $Pnma$ phase in our case), is by calculating its amplitude by the atomic displacements with respect to the high-symmetry phase (the $Pm\bar{3}m$ phase in our case). The two tilts are the two primary order parameters, with symmetries given by the irreducible representations (irreps) R4+ and M3+, respectively, of the high symmetry cubic space group [22, 23]. This symmetry lowering allows the displacements of the A-cations on the ac-plane that were otherwise forbidden by symmetry constrains. Thus, two anti-polar displacements of the rare-earths appear, with X5+ and R5+ symmetries, which act as secondary order parameters [22]. The A-cation displacement with X5+ symmetry is larger, and couples with the two primary order parameters. This was recently referred to be crucial in further decreasing the energy, making the $Pnma$ symmetry so widely stable in these perovskites [24, 25]. Finally, the BO_6 octahedra slightly deform with M2+ symmetry, due to the strain imposed by the formation of the two tilts [18, 19], also a secondary order parameter [22]. For clarity, Figure 1.4 shows the described atomic movements for each symmetry-adapted distortion mode.

In some special cases, the deformation of the octahedra is greatly increased due to the cooperative Jahn-Teller distortion, with M2+ symmetry [22]. Note that this does not further lower the $Pnma$ phase symmetry [22]. It follows from the Jahn-Teller theorem stating that any nonlinear molecule with a spatially degenerate electronic ground state will undergo a distortion that removing that degeneracy, as the distortion lowers the overall energy. In our case, it occurs when a transition metal cation, with partially filled $3d$ e_g-orbitals, occupies the B-site, such as the Mn^{3+} ion in the $R\mathrm{MnO}_3$. Firstly, the fivefold degeneracy of the Mn^{3+} ion $3d$-orbitals is partially lifted by the crystal field of the cubic array of the $Mn\mathrm{O}_6$ octahedra into three degenerate t_{2g}-orbitals and two degenerate e_g-orbitals. Following the Hund rules, to maximize the total spin, the d^4 electronic configuration of the Mn^{3+} ion gives three electrons in the t_{2g}-orbitals, and one electron in the e_g-orbitals, as seen in Figure 1.5(a). Then, the Jahn-Teller effect lifts these degeneracies, namely on the e_g-orbitals, causing the $d_{(x^2-y^2)}$ to be half-filled and the $d_{(3z^2-r^2)}$ completely empty. Note that this would not happen if just one electron was added (Fe^{3+} ion) or removed (Cr^{3+} ion). This effect yields an additional distortion of the already tilted distorted BO_6 octahedra, with a gain in electronic energy that is larger than

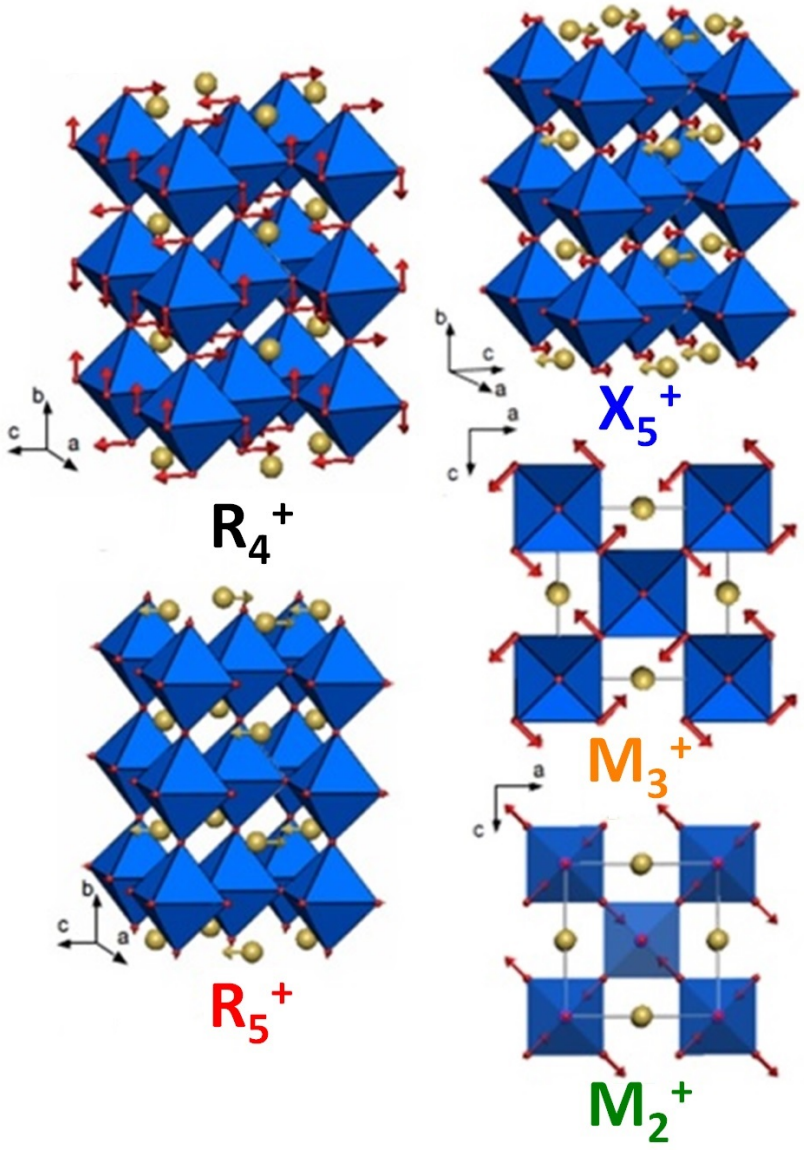

Figure 1.4: Symmetry-adapted distortion modes of the orthorhombic *Pnma* structure with respect to the cubic $Pm\bar{3}m$ perovskite structure, along with their respected symmetries. The atomic movements are described in the text. Adapted from [26].

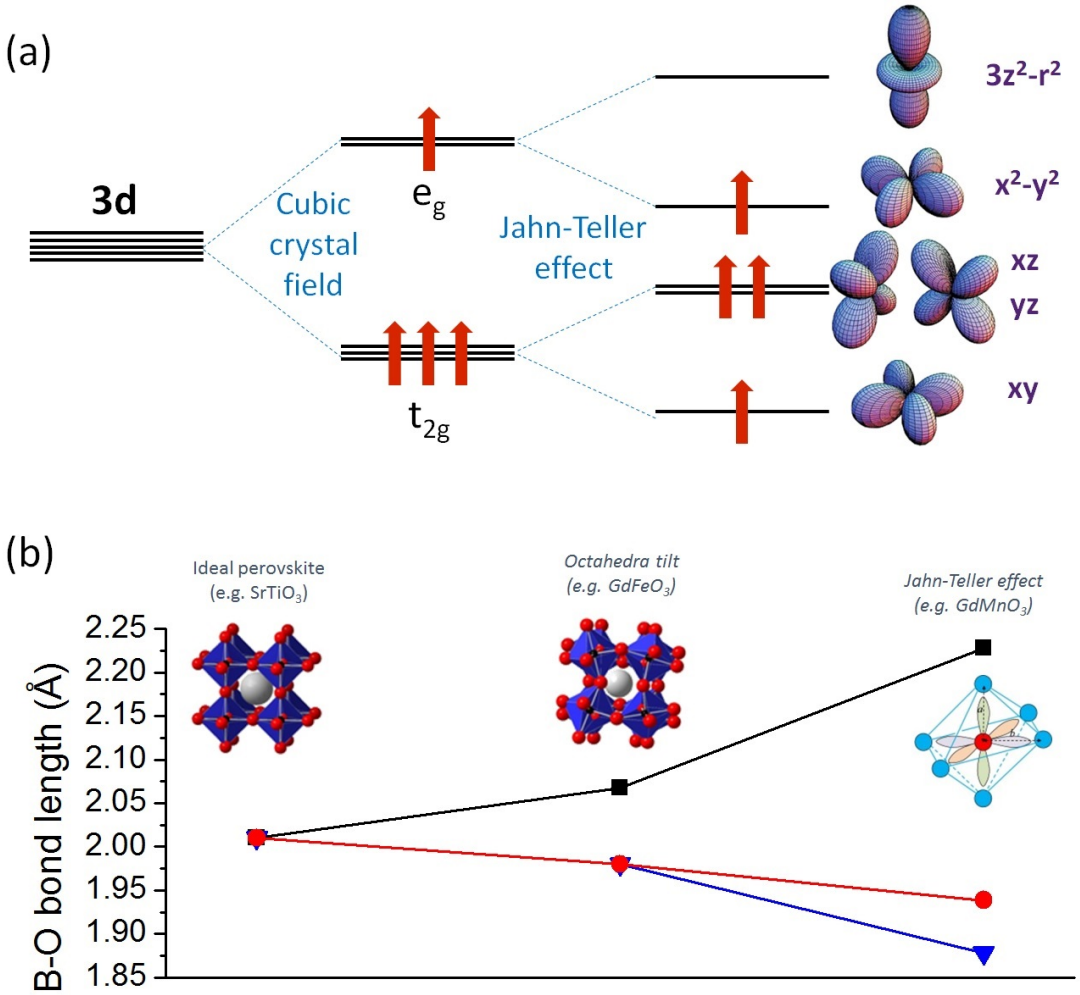

Figure 1.5: (a) The fivefold degeneracy of the d-orbitals is lifted by the cubic crystal field into two e_g-orbitals $[(x^2-y^2), (3z^2-r^2)]$ and three t_{2g}-orbitals $[(xy), (yz), (zx)]$, whose degeneracy is then lifted by the Jahn-Teller effect. (b) Effect of the *Pnma* tilt system and of the Jahn-Teller effect on the B-O bond lengths of the BO_6 octahedra.

the elastic energy paid for the distortions of the octahedron and the lattice [27]. The local distortions from the Jahn-Teller effect present a staggered long range order due to the also staggered orbital ordering on the ac-plane [22, 23, 28]. The Jahn-Teller distortion is then called cooperative [22, 23, 28]. Figure 1.5(b) shows the effect of the tilts and of the Jahn-Teller effect on distorting the BO_6 octahedra, by the distance between the center B-cation and each pair of oxygens along each of three octahedron axes. The tilts cause a slight elongation of one pair of the B-O2 bond lengths, which is further elongated by the Jahn-Teller distortion, while the other pair of B-O2 bond lengths and the pair of B-O1 bond lengths both decrease.

The octahedra tilts are key elements for understanding the elastic, magnetic and electronic properties of the perovskites, and can be tuned by the size of the rare-earth [29]. The tilt angles are given by the angle between neighbors octahedra, which can be expressed as a function of the angle between the neighbors B-O-B atoms [17]:

$$\theta_{tilt} = \frac{180 - (B - \mathrm{O} - B)}{2} . \tag{1.3}$$

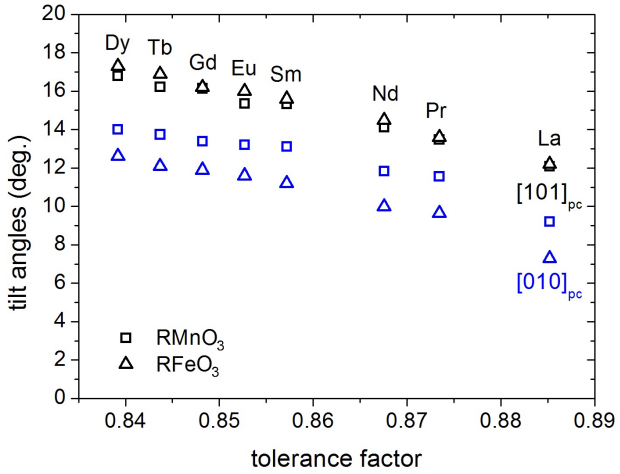

Figure 1.6: Tilt angles about the $[101]_{pc}$(black) and $[010]_{pc}$ (blue) axes as a function of rare-earth ionic radius for RMnO$_3$ (squares) and RFeO$_3$ (triangles). Values taken from [30–32].

The magnitude of the tilt angles around the $[101]_{pc}$ and $[010]_{pc}$ directions increase as the tolerance factor decreases for the RMnO$_3$ and RFeO$_3$, as shown in Figure 1.6. Compounds with smaller rare-earth ions present greater tilt angles, and thus greater tilt distortions. Moreover, the magnitude of the anti-phase tilt angle around the $[101]_{pc}$ direction is always larger than the value of the in-phase tilt angle around the $[010]_{pc}$ direction. Comparing both systems, they have similar values for the tilt angle around the $[101]_{pc}$ direction, while the RMnO$_3$ present slightly larger values for the tilt angle around the $[010]_{pc}$ direction than the RFeO$_3$. Again, this is related with the Jahn-Teller distortion, as the $[010]_{pc}$ tilt angle involves the oxygens on the ac-plane affected by this distortion.

Figure 1.7(a) shows the B-O (i.e. Fe-O and Mn-O) bond lengths along the 3 different axis as a function of the tolerance factor, for the RFeO$_3$ and RMnO$_3$ [33]. It is readily seen that for the RFeO$_3$ (open symbols) the three Fe-O bond lengths take very similar values. Only for the compounds with the smallest rare-earths one of the Fe-O is elongated. This is due to the increase of the strain imposed by the two co-existing tilts that increase as the tolerance factor decreases. In the case of RMnO$_3$, three very distinct Mn-O distances are found, the difference being due to the Jahn-Teller effect. As explained before this effect further distorts the octahedra in a much stronger way than the octahedra tilt. Figure 1.7(b) presents a schematic c-axis view of the these bonds and tilt angles of the RMnO$_3$ structure. The Mn-O medium bond length is always along the b-direction, while the short and long bond lengths are staggered on the ac-plane.

The lattice parameters of the primitive unit cell of the $Pnma$ structures of RMnO$_3$ and RFeO$_3$, as a function of the tolerance factor, are shown in Figure 1.8. As the tolerance factor increases, the b and c lattice parameters also increase. Yet, the a lattice parameter is only slightly dependent on the tolerance factor increases, presenting a maximum between the Gd and Eu rare-earths. Comparing the RMnO$_3$ and RFeO$_3$, there is a substantial difference on the values of the a and b lattice parameters. This is due to the Jahn-Teller distortion, although it is mostly present on the ac-plane.

These aforementioned distortions can be tuned by chemical substitution and various external parameters, such as temperature, stress, hydrostatic pressure. The chemical substitution is an easy way to tune the effective A-cation size, by controlled substitution of the rare-earth cation by another different atom. As we will see, the effect of the effective A-site size on both structural and physical properties of RMnO$_3$ has been extensively studied as it changes the tilt angles in an extensive way. However, the chemical substitution of the B-cation

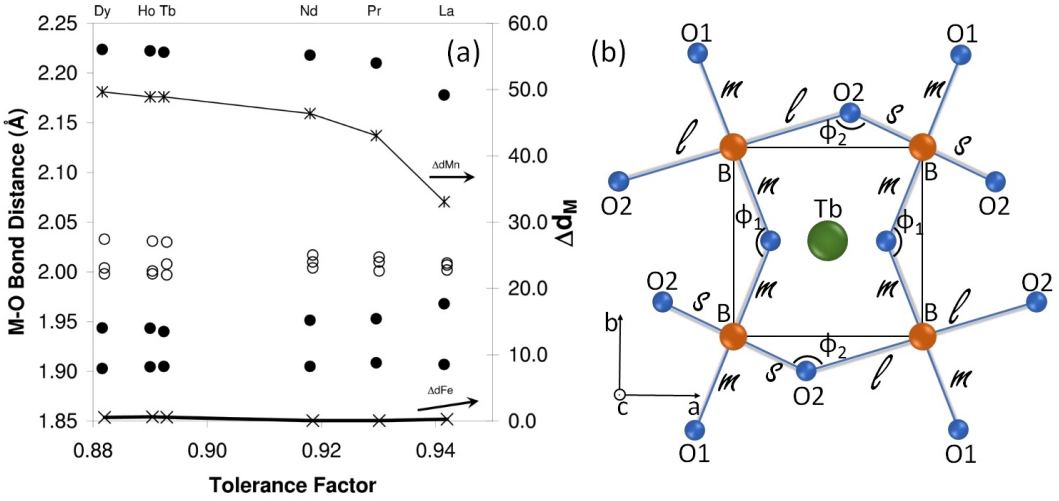

Figure 1.7: (a) B-O distances as a function of the tolerance factor for the RFeO$_3$ (open symbols) and RMnO$_3$ (closed symbols) series. Adapted from [33](b) c-axis view of a RMnO$_3$ structure (R = Tb). s, m and l stand for the short, medium, and long B-O bonds, whereas ϕ_1 and ϕ_2 correspond to the $[101]_{\mathrm{pc}}$ and $[010]_{\mathrm{pc}}$ tilt angles, respectively. Adapted from [26].

is far less studied. In this regard, the RMnO$_3$ and RFeO$_3$ with *Pnma* structure are an interesting option, since they share the *Pnma* symmetry and also because Mn^{3+} and Fe^{3+} have the exact same ionic radius in high-spin configuration. Yet, one is Jahn-Teller active and the other inactive. This fact can be used to tune the Jahn-Teller distortion by the solid solution $R\mathrm{Mn}_{1-x}\mathrm{Fe}_x\mathrm{O}_3$, with x from 0 to 1 for a given fixed R. Lets first address the physical properties of the pure RMnO$_3$ and RFeO$_3$series for the different rare-earths.

1.2 Physical Properties of Orthorhombic RMnO$_3$ and RFeO$_3$

In the rare-earth manganites it is important to note that, since the spins of the rare-earth ions only order at temperatures much lower than the ones considered, the magnetic properties (and the coupled polar or elastic properties) have been ascribed mainly to the spin ordering of the Mn^{3+} ions. Nevertheless, the spin structure found can still be continuously changed by size rare-earth ion. This is due to the alterations of the strength of the structural distortions as the rare-earth ionic radius varies, which will change the magnetic super-exchange integrals between neighboring Mn^{3+} through the intermediate oxygens. This allows a parametrization of the magnetic and polar properties with the tolerance factor. However, this is not always the case on rare-earth ferrites, where the Fe^{3+} spins order at a much higher temperature and interact in a stronger way with the rare-earth spins. This interaction increases the ordering temperature of the rare-earth spins on the RFeO$_3$. Moreover, the rare-earth spins can also play important roles on the magnetic structure of the Fe^{3+}, even before they order. From this, the magnetic and polar properties of the RFeO$_3$ are not simply parameterizable by the tolerance factor, and very distinct properties are found for each different compound. A description of the magnetic and polar properties for the different RFeO$_3$ and RMnO$_3$ will be given.

1.2.1 Physical Properties of Rare-earth Ferrites

As mentioned, the rare-earth ferrites, with R = La to Lu, crystallize in the very common orthorhombic *Pnma* structure [17]. These materials present a wide-range of interesting physical properties, being all ferroelastic and magnetic at room temperature. Before addressing their often complex magnetic orderings it is worth to

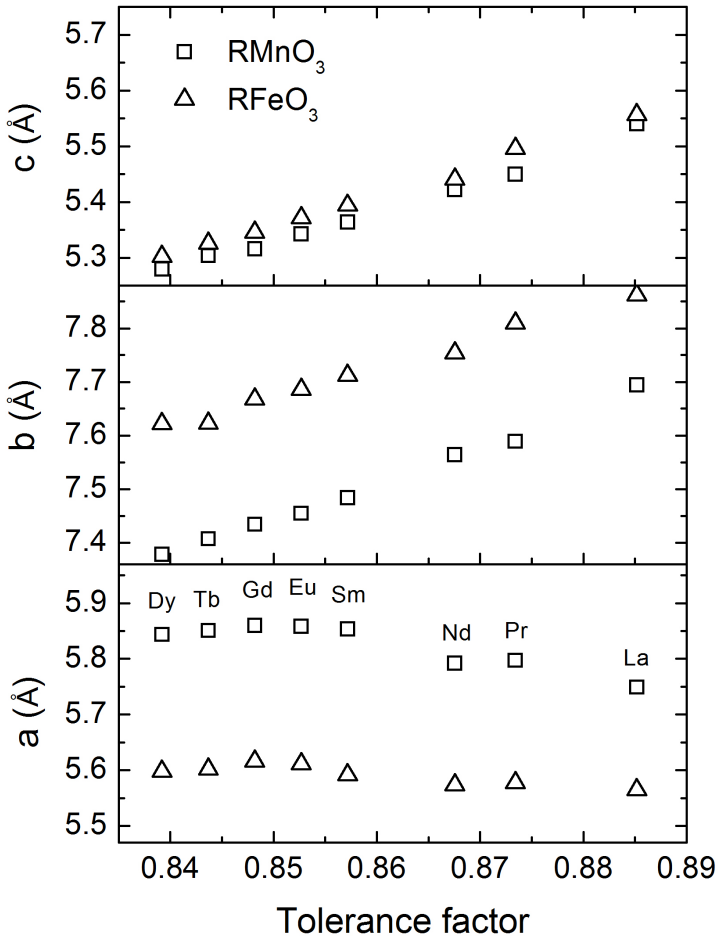

Figure 1.8: Lattice parameters of the *Pnma* structures of $R\mathrm{MnO_3}$ (squares) and $R\mathrm{FeO_3}$ (triangles), as a function of the tolerance factor. Values taken from [30–32].

explain the four possible collinear spin structures for the four B-cations within the primitive unit cell of the *Pnma* structure. We will also introduce here the Bertaut's notation, used in most of the literature on RFeO$_3$ materials. Assuming a cubic array for the B-cations (in fact their actual array on the *Pnma* structure is almost cubic), the four possible collinear magnetic orders are (see Figure 1.9(a) for each scheme):

- Ferromagnetic: all spins pointing along the same direction (F-type);
- Antiferromagnetic arrangement of ferromagnetic layers: spins pointing along the same direction on each layer, with opposite directions between layers (A-type);
- Antiferromagnetic arrangement of ferromagnetic lines: spins pointing along the same direction on each line, with opposite directions between lines (C-type);
- Antiferromagnetic: all neighboring spins point in opposite directions (G-type).

The complex non-collinear magnetic orderings are described using this basis to describe the spins direction along each axis. For example, the Bertaut's notation of a F-type arrangement along the x-axis, a A-type along the y-axis, and a C-type along the z-axis is $F_xA_yC_z$.

The RFeO$_3$, with R = La to Lu, all present an $A_xF_yG_z$ antiferromagnetic ordering of the Fe^{3+} spins below T_N = 625 to 750 K , respectively, denoted by the blue area in the magnetic phase diagram of Figure 1.9(a) [34, 35]. This Fe^{3+} spin structure is represented by the arrows in Figure 1.9(c). At a lower temperature, between 3 to 480 K depending on the rare-earth cation, most RFeO$_3$ (except R = La, Eu, Gd and Lu) exhibit a spin-reorientation into different antiferromagnetic phases, marked on yellow and green in the magnetic phase diagram of Figure 1.9(a) [35–37]. The most common is the $C_xG_yF_z$ structure, shown by the arrows in Figure 1.9(d), stabilized at different temperatures for R = Pr, Nd, Sm, Tb, Ho, Er, Tm and Yb. This phase phase originates from the continuous rotation of the easy axis from z to y. Only CrFeO$_3$ and DyFeO$_3$ present a different low-temperature magnetic structure ($G_xC_yA_z$). Except for the case of R = Gd, these spin-reorientations are seen whenever the rare-earths have non-zero spin. This correlation suggests an interaction between the Fe^{3+} and the R^{3+} spins at temperatures well above the ordering of the latter.

Among the RFeO$_3$, those with R = Nd, Sm and Er present particularly interesting magnetic properties. Below the spin-reorientation of the Fe^{3+} spins, the rare-earth spins align antiparallel to them, originating a spin-switching and even a magnetization reversal, i.e. a magnetic response contrary to the applied magnetic field [38]. The temperature at which there is no magnetic response is designated as compensation temperature, being 7.6, 3.9 and 46 K for NdFeO$_3$, SmFeO$_3$ and ErFeO$_3$, respectively. This effect is shown for NdFeO$_3$, as an example, by its magnetic response with temperature in Figure 1.10(a). The sign of the magnetic response depends on whether a cooling magnetic field is used, being driven by a spin-lattice coupling mediated mechanism [38]. This temperature-induced magnetization reversal effects have been attributed to the ordering of the rare-earth spins in opposite direction to the weak-ferromagnetic component of the Fe^{3+} spins, as described in Figure 1.10(b). This antiparallel alignment of the Fe^{3+} and R^{3+} spins arises from the negative exchange resulting from the competing Fe-Fe, Fe-R and R-R interactions [39].

Recently the interest in these compounds as potential room-temperature multiferroics has been renewed by Lee *et al.* by the report of a reversible large ferroelectric polarization of 90 μC.m^{-2} along the a-axis, at room temperature in SmFeO$_3$ ceramics, stabilizing below T_N = 640 K, as shown in Figure 1.10(a) [40]. However, these findings were readily refuted by Kuo *et al.* that by powder and single-crystal neutron diffraction found a magnetic structure incompatible with ferroelectricity emerging by the Dzyaloshinskii-Moriya effect [37]. Moreover, they found neither a dielectric anomaly associated with a ferroelectric transition on this compound below T_N, nor a hysteresis typical of ferroelectricity on the capacitance-voltage and loss-voltage measurements, which are shown in Figure 1.10(b) at room temperature [37]. In fact the technique of pyrocurrents to measure the polarization used by Lee *et al.* is very prone to misinterpretations, as it measures any charges released at

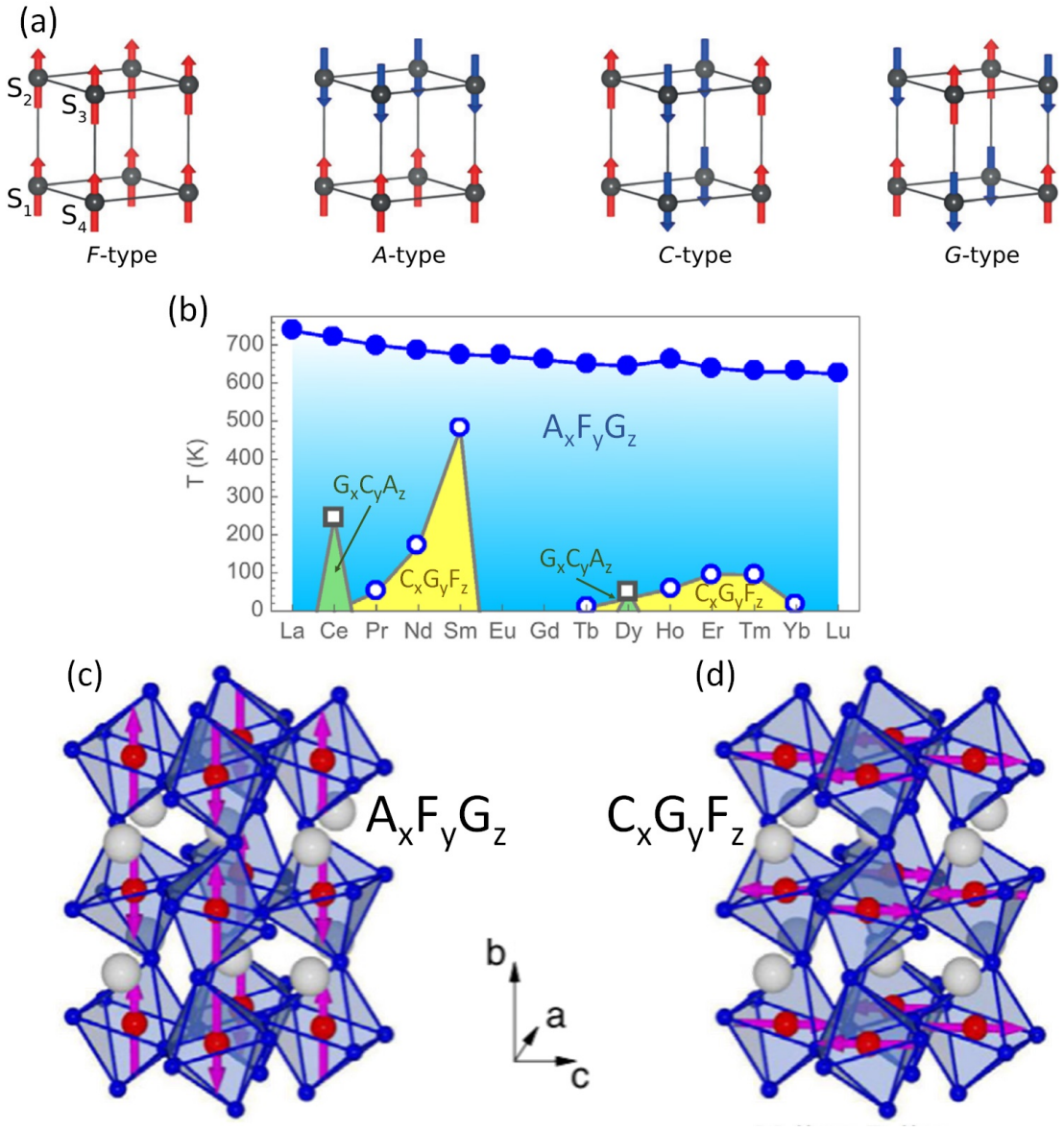

Figure 1.9: (a) The four different types of collinear magnetic orders possible on the *Pnma* perovskite. (b) Magnetic phase diagram of orthorhombic *R*FeO3, with respective magnetic orderings of the Fe^{3+} spins. Closed symbols represent T_N, open symbols represent T_{SR}. Magnetic structure of (c) $A_xF_yG_z$ and (c) $C_xG_yF_z$. Adapted from [35] and [37].

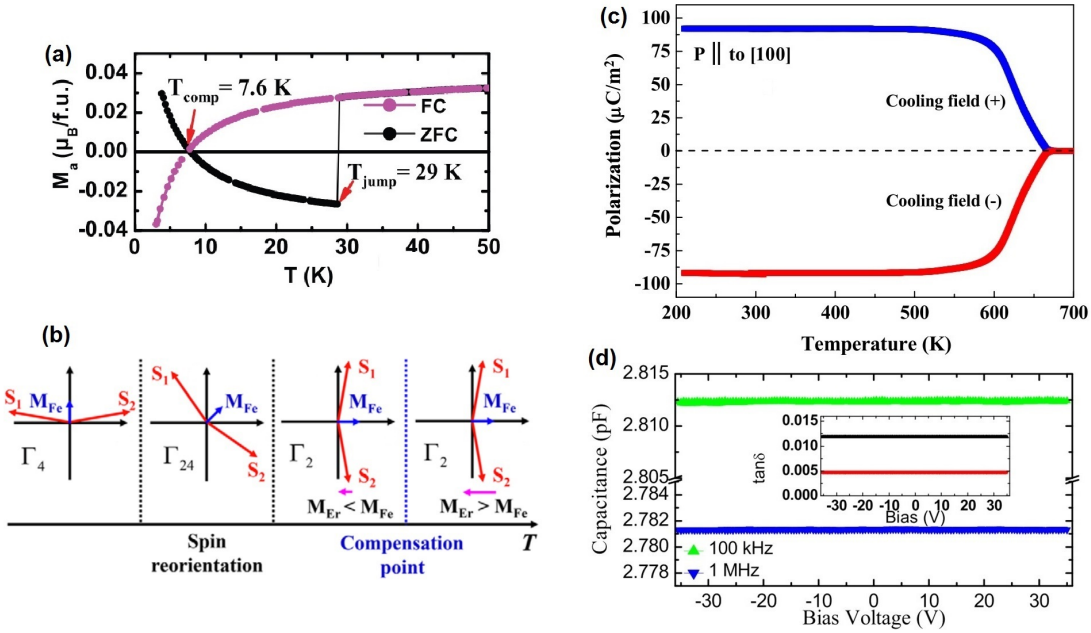

Figure 1.10: (a) Magnetic response of $NdFeO_3$ as a function of temperature in ZFC and FC conditions. (b) Scheme of the magnetization reversal effect. (c) Spontaneous electric polarization along [010] as a function of temperature and (e) room-temperature C-V curve (loss data in inset) of $SmFeO_3$. Adapted from [38], [41], [40] and [37].

the sample contacts, often arising from spurious effects. For this, a low poling electric field should be used and measured under different heating rates to confirm that the profile of the pyrocurrents follow the known physical models. Lee *et al.* do not provide neither of these details [40]. Thus, no convincing evidences have been given for the multiferroicity of $SmFeO_3$, though this material deserved to be further studied in detail.

Excluding the questionable $SmFeO_3$, in the RFeO$_3$, unlike in the RMnO$_3$ that we will address on the following section, the magnetic ordering of the Fe^{3+} spins is not enough to break the space inversion symmetry and induce ferroelectricity. Yet, for the cases of R = Gd or Dy, at very low-temperatures (below 4 K), the antiferromagnetic ordering of the rare-earth spins, combined with that of the Fe^{3+} spins, does break this symmetry, giving rise to interesting multiferroic and magnetoelectric properties [42, 43]. In $GdFeO_3$ a ferroelectric ground-state with an electric polarization of 0.12 μC.cm^{-2} is found below 2.5 K along the b-axis, arising from a cooperative displacement of the rare-earths due to the spin-exchange striction between the Gd and Fe spins [42]. Thus a strong magnetoelectric effect emerges, as Figure 1.11(a) shows, being possible to suppress the ferroelectricity with an applied magnetic field by inducing a reorientation of the Fe^{3+} and Gd^{3+} spins [42]. In $DyFeO_3$, although no ferroelectric ground-state emerges from the Dy^{3+} spins ordering, a ferroelectric polarization of 0.20 μC.cm^{-2}, along the b-axis, can be induced by an applied magnetic field above 24 kOe along the same axis, as seen in Figure 1.11(b) [43]. Moreover, it has one of the strongest linear magnetoelectric tensor component of 0.024 ever observed in single materials, two times larger than $TbPO_4$ [43].

With respect to their lattice dynamics, these are scarcely studied. There is no detailed Raman mode assignment for the RFeO$_3$ family, being the works of Venugopalan *et al.* and Gupta *et al.* addressing the Raman spectra of RFeO$_3$ only we know [44, 45]. Despite the interesting properties discussed above, there is no temperature dependent measurements of their lattice dynamics to study how magnetization reversal and magnetoelectric effect may be coupled to the structure via the spin-phonon coupling. Conversely, the magnonic spectra were studied in temperature by Venugopalan *et al.* and White *et al.* for most RFeO$_3$ [45, 46]. In most

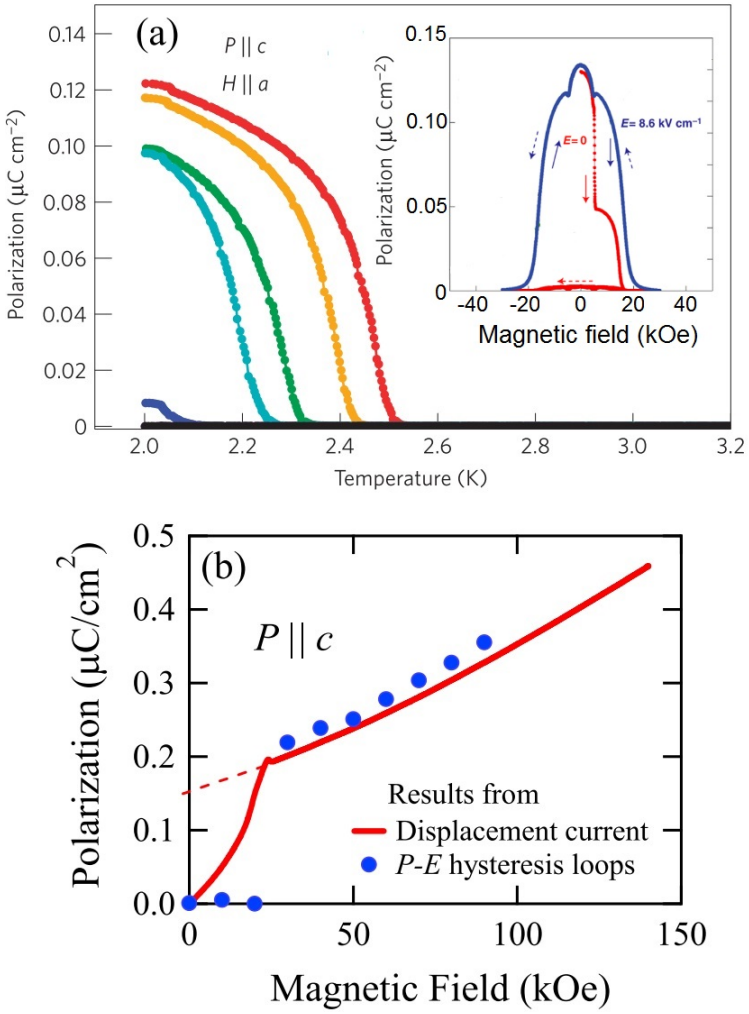

Figure 1.11: (a) Electric polarization of $GdFeO_3$along the b-axis for several values of magnetic field applied along the a-axis. The inset shows the saturation polarization as a function of the applied magnetic field, with and without applied electric field of 8.6 kV/cm. Adapted from [42]. (b) Magnetic field dependence of the polarization along the b-axis for $DyFeO_3$ at T = 3 K, obtained by P-E hysteresis loops (filled circles) and displacement current measurement (solid line). Adapted from [43]

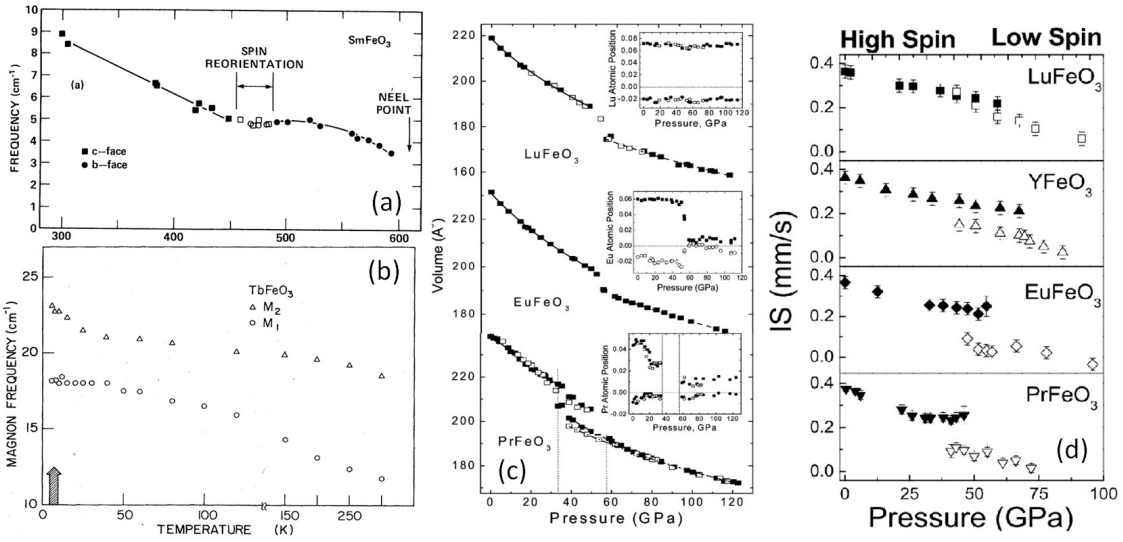

Figure 1.12: Temperature dependence of the magnons frequencies (a) $SmFeO_3$ and (b) $TbFeO_3$. Phase-transition temperatures are marked by arrows. (c) Pressure evolution of the unit cells volumes of $LuFeO_3$, $EuFeO_3$,and $PrFeO_3$. The solid, and dashed lines are theoretical fits using the second-order Birch-Murnaghan equation of state. The insets show the pressure dependence of the atomic coordinates of Lu, Eu and Pr. The circle and square symbols correspond to the X and Y coordinates, respectively. Adapted from [49]. (d) Pressure dependence of the isomer shift for the various RFeO$_3$ from Mössbauer spectroscopy. The open symbols correspond to the low-spin configuration. Adapted from [48]

materials, a simple hardening of the magnons frequency was found with decreasing temperature. However, in $SmFeO_3$ and $TbFeO_3$, anomalies of the frequency of these excitations were found at the spin-reorientation temperatures, as shown in Figures 1.12(a) and (b), respectively. These anomalies deviate from the predictions of theoretical models for the Fe^{3+} spins, confirming the active role of the rare-earth spins in these cases [45, 46].

The high-pressure behavior of some RFeO$_3$ (R = La, Pr, Nd, Eu, Gd and Lu) has already been studied to some extent by x-ray powder diffraction and Mössbauer spectroscopy measurements, at room temperature [47, 48]. From the x-ray diffraction, a structural phase transition of the first-order was found in all the studied compounds, with a volume reduction of between 4 and 6%, as it can be seen in Figure 1.12(c). However, the details of the crystal structures before the phase transition have usually not been reported in the past studies. Namely, it is not known how the structural distortions such as the octahedra tilting evolves with applied pressure and rare-earth ionic radius. Using Mössbauer spectroscopy this phase transition was found to be a consequence of a high-spin to low-spin transition of the Fe^{3+} cation, as shown by the isomer-shift in Figure 1.12(d) [48]. This transition also induces an insulator-to-metal transition [48]. This confirms that the electronic, spin and lattice degrees of freedom are intimately coupled in RFeO$_3$. Thus, the phonons may be important probes of the structural distortions and their interplay with the interesting physical properties found that will be better understood by changing external parameters like chemical substitution, temperature and pressure.

Despite the intensive research already done, a systematic study of the pressure evolution of the elementary structural distortions in orthorhombic perovskites is still missing, as well as, the careful search for crossover events, including the experimental search for the existence of a borderline compound. Thus, there is still much to be explored in these materials, and there is no systematic work done that brings together the whole family of the rare-earth ferrites, which by studying the big-picture could be able to give new insights on the physical properties of these materials, as it was already done in others, such in the rare-earth manganites.

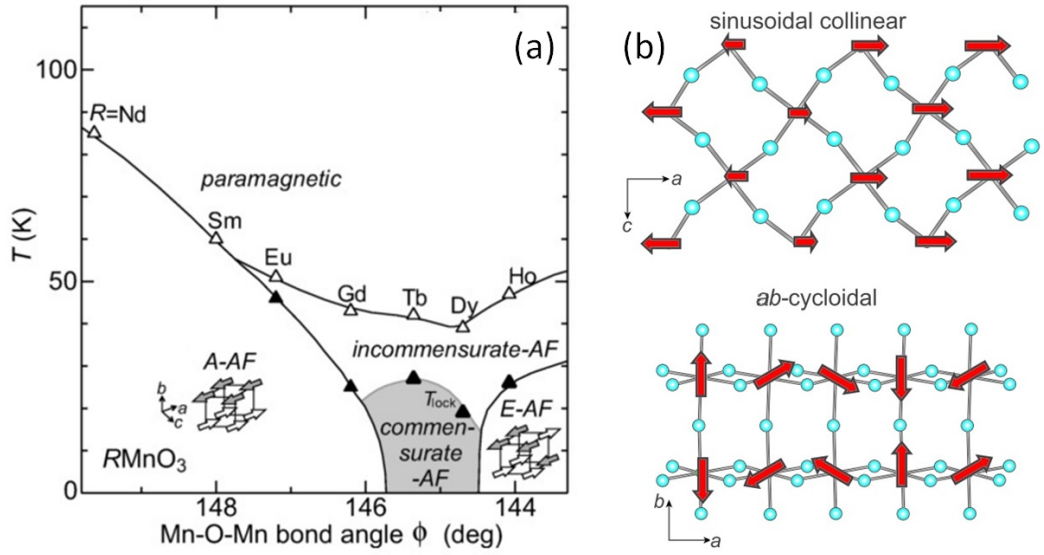

Figure 1.13: (a) Experimental magnetic phase diagram of $R\mathrm{MnO_3}$ as a function of the magnitude of the $[101]_{\mathrm{pc}}$-tilt distortion. Adapted from[50]. (b) Ordering of the collinear-sinusoidal incommensurate (above) and cycloidal commensurate antiferromagnetic (below) spin structures of $R\mathrm{MnO_3}$. Adapted from [51].

1.2.2 Physical Properties of Rare-earth Manganites

In the case of orthorhombic $R\mathrm{MnO_3}$, regarding the magnetic properties, decreasing the ionic radius of the rare-earth changes the balance of the geometrically frustrated antiferro- and ferromagnetic superexchange interactions of Mn^{3+} ions. The spins of the rare-earths are typically neglected, as they only order at temperatures below 10 K [50]. By increasing the tilt angle, the Mn-O-Mn bond angle reduces, and so, the orbital overlap between adjacent Mn^{3+} and O^{2-} ions is altered, which consequently modifies the magnetic superexchange integrals [51]. The balance between competitive ferro- and antiferromagnetic interactions is crucial for the stabilization of spin arrangement. Unlike the $R\mathrm{FeO_3}$, this allows a continuously tailoring of the the magnetic phases in the $R\mathrm{MnO_3}$, to have the desired physical properties [52]. In fact, a magnetic phase diagram of $R\mathrm{MnO_3}$ as a function of the magnitude of the $[101]_{\mathrm{pc}}$-tilt distortion has been obtained experimentally, and it is presented in Figure 1.13 [14].

At very high temperatures, above 1000 K, all the referred compounds present an orbital ordering transition associated with stabilization of the Jahn-Teller distortion. At room temperature, they are all paramagnetic and paraelectric. At low temperatures, for R = Nd to Sm, there is a single phase transition at T_N = 88 and 62 K, respectively, from the paramagnetic state to a canted A-type antiferromagnetic phase [50]. For R = Eu and Gd, two phase transitions are observed. One at T_N, from the paramagnetic to a collinear-sinusoidal incommensurate antiferromagnetic phase on the ac-plane with a propagation vector along the a-axis, and another at lower temperature to a canted A-type antiferromagnetic phase (cf. Figure 1.13(a)). As the A-site ionic radius further decreases, for R = Tb and Dy, beyond the collinear-sinusoidal incommensurate antiferromagnetic phase, at T_{lock}, around 27 K and 20 K, respectively, the spin ordering changes into a cycloidal commensurate antiferromagnetic structure on the ab-plane (see Figure 1.13(b)), and the magnetic modulation vector $(q_m, 0, 0)$ is locked into a fixed value q_m = 0.27 and 0.38, respectively. The structural modulation vector k_l presents a similar behavior and is given by: $k_l = 2q_m$. The magnetic structure allows a spontaneous ferroelectric ordering in the plane of the ab-cycloidal along the b-axis, which can be microscopically explained through different models, via the Dzyaloshinskii-Moriya interaction mechanism [53–55]. These models will be later addressed. The orthorhombic $\mathrm{HoMnO_3}$ exhibits the first phase transition, undergoing a transition into

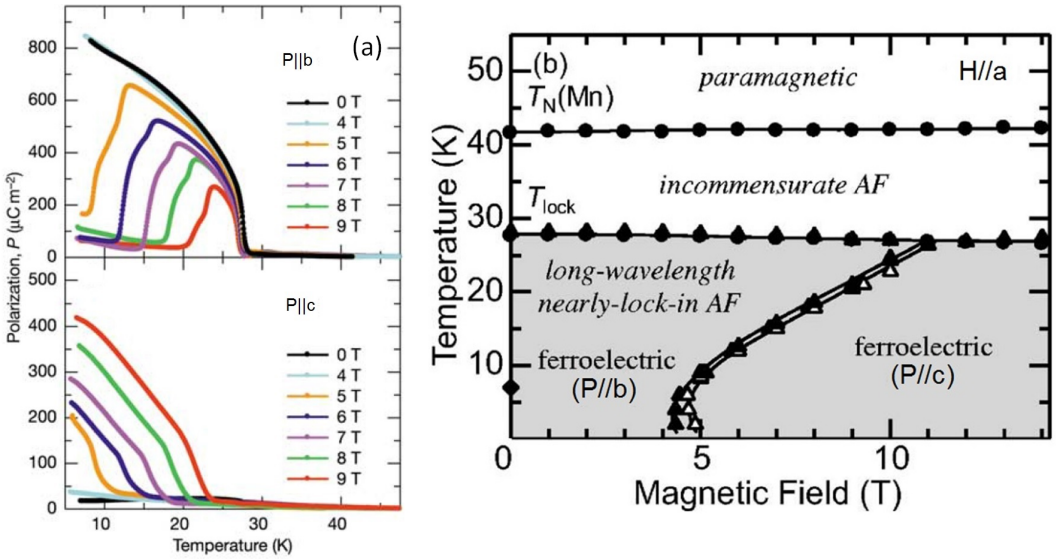

Figure 1.14: (a) Polarization as a function of temperature and applied magnetic field along the a-axis of $TbMnO_3$. A reorientation of the electric polarization is induced from the b- to the c-axis above 5 T. Adapted from [13]. (b) (T, B) magnetic phase diagram of $TbMnO_3$. Magnetic field applied along the a-axis. The gray area represents the ferroelectric phases. Adapted from [52].

a E-type at 48 K , shown in Figure 1.13(a) [50].

Interesting magnetoelectric effects were reported on four of these materials since 2004 (R = Eu, Gd, Tb and Dy). [14, 29, 52]. Goto *et al.* have shown that, for R = Tb and Dy compounds, a spontaneous electric polarization of around 800 μCm^{-2} is observed along the b-axis [14]. Later, Kimura *et al.* have reported very interesting magnetoelectric properties of these materials, as summarized in Figure 1.14(a) for $TbMnO_3$. At the lowest temperatures (below 6 K), an applied magnetic field of 5 T or higher along the a-axis (along the magnetic/structural modulation vector) reorients the polarization from the b- to the c-axis [52]. Accordingly to the Dzyaloshinskii-Moriya model, this means that the cycloidal spin structure flops from the ab- to the ac-plane. Figure 1.14(b) shows the complete (T, B) magnetic phase diagram. The gray area represents the ferroelectric phases, with the corresponding phase boundaries dependent on temperature.

Contrarily, for R = Gd and Eu there is no spontaneous ferroelectric ground-state, though it can be induced by applying a magnetic field of 2 T and 20 T, respectively [52, 56]. Figure 1.15(a) shows the electric polarization along the c-axis of $GdMnO_3$ as a function of applied magnetic field along the a-axis, for different temperatures [52]. Without applied magnetic field, the polarization is always zero. However, when a magnetic field is applied along the a-axis, a electric polarization emerges [52]. From these measurements, a (T, B) magnetic phase diagram was drawn, shown in the Figure 1.15(b) [52]. For magnetic fields between 0.25 and 0.5 T a re-entrant ferroelectric phase is found, which is only stable down to the lowest temperatures above 1 T (note that the gray ferroelectric phase should not touch the vertical axis, as $GdMnO_3$ is not ferroelectric without the applied magnetic field). Until 10 T, the ferroelectricity is always found along the c-axis (i.e. ac-cycloidal spin structure), without the possibility for reorientation.

The use of hydrostatic pressure as an external parameter on the main structural distortions has been extensively studied at room temperature using both Raman scattering and synchrotron x-ray diffraction [16, 57–59]. In all cases, a high-pressure structural phase transition is observed by the disappearance of the Raman signal at a critical pressure that strongly depends on the A-site cation. For the compounds with R = Pr to Dy, x-ray diffraction confirmed the presence of a corresponding structural transition to a non-cubic phase that allows Raman activity. Thus, considering that the loss of the Raman spectrum is a

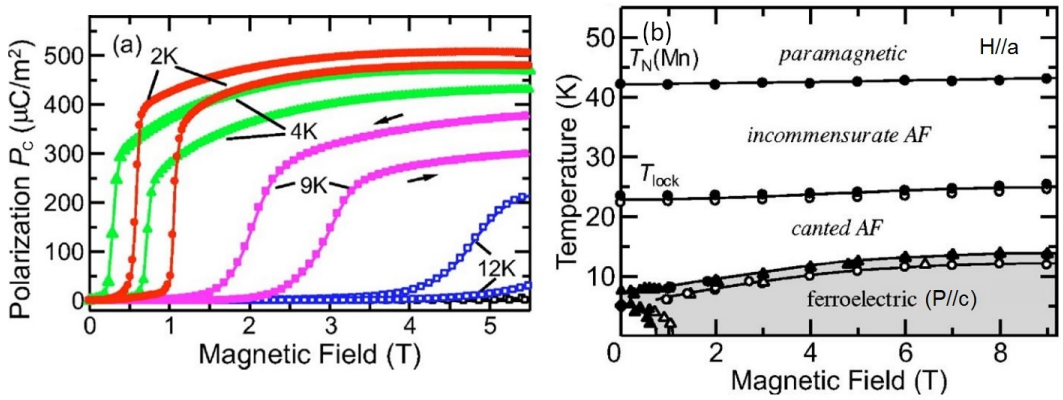

Figure 1.15: (a) Polarization as a function of applied magnetic field for different temperatures for $GdMnO_3$. An electric polarization along the c-axis is induced by the magnetic field applied along the a-axis. (b) (T, B) magnetic phase diagram of $GdMnO_3$. A re-entrant ferroelectric phase is found between 0.25 and 0.5 T. Both adapted from [52].

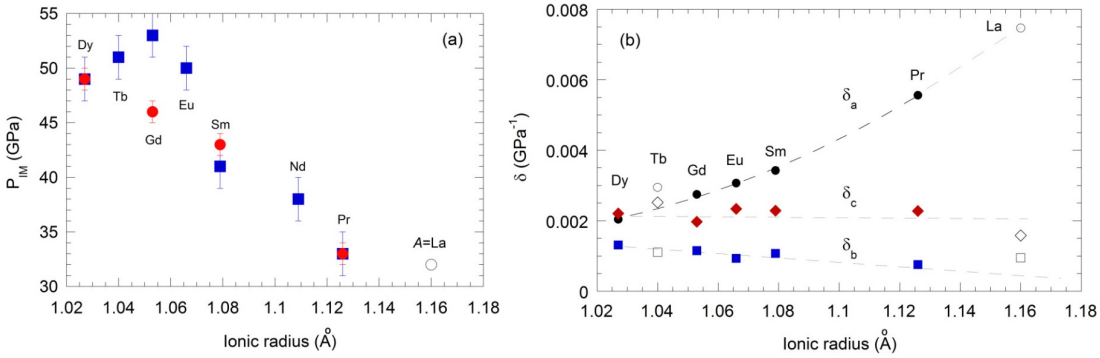

Figure 1.16: (a) Critical pressure P_{IM} obtained by x-ray diffraction (circles) and Raman scattering (squares) and (b) compressibilities of the lattice parameters as a function of the rare-earth ionic radius for the $R\mathrm{MnO_3}$. The point of $LaMnO_3$ was taken from [16]. Adapted from [57].

consequence of free-electron screening, the high-pressure phase must be metallic. So the disappearance of the Raman spectrum can be interpreted as an insulator to metal transition [57]. The critical pressure of the insulator-to-metal phase transition (P_{IM}) is plotted in Figure 1.16(a) for the different rare-earths, where it is observed that as the rare-earth ionic radius decreases, the critical pressure increases. Figure 1.16(b) shows the compressibilities along the crystallographic axes as a function of the ionic radius, to analyze the compression mechanisms. The $R\mathrm{MnO_3}$ series can be separated in two different kinds of distortion behavior. For the smaller ones (Dy and Tb), the compression is nearly isotropic in the ac-plane, with only small evolutions of the tilt angles and cooperative Jahn-Teller distortion [57]. However, as the ionic radius of the rare-earth increases, the pressure-induced reduction of Jahn-Teller distortion becomes more pronounced and increasingly significant as a compression mechanism, while the pressure-induced tilting of octahedra chains becomes conversely less pronounced.

Regarding the evolution of the Jahn-Teller distortion in the $\mathrm{RMnO_3}$ under applied pressure, before the P_{IM}, it still persists an open question resulting from contradictory results obtained for R = La. First, Loa *et al.* reported the disappearance of the Jahn-Teller distortion around P_C = 18 GPa, before the P_{IM} observed at 32 GPa [16]. Their interpretation is based on the results shown in Figures 1.17 (a) and (b). From the Mn-O bond lengths pressure evolution, obtained by x-ray diffraction, they extrapolate the low-pressure linear

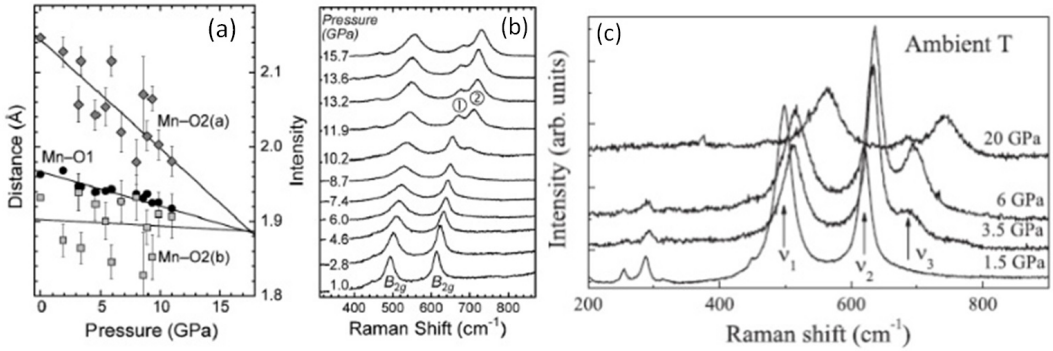

Figure 1.17: (a) Mn-O bond lengths and (b) Raman spectra as a function of pressure for $LaMnO_3$. The disappearance of the Jahn-Teller effect is proposed at $P_C = 18$ GPa. Adapted from [16]. (c) Raman spectra as a function of pressure for $LaMnO_3$. The persistence of the Jahn-Teller effect is proposed up to $P_{IM} = 32$ GPa. Adapted from [59].

behavior until the three distinct bond lengths become the same (i.e. undistorted MnO_6 octahedra) at $P_C = 18$ GPa [16]. This extrapolation was required, because the quality of the spectra worsens as the applied pressure increases, hindering the possibility of following the Mn-O bond lengths above 11 GPa [16]. Nevertheless, it is a speculative approach, as the low-pressure regimes typically saturate before a critical pressure. To complement, they saw a splitting of a Raman band associated with the MnO_6 octahedra stretching mode, interpreting that it is originated on undistorted octahedra (see Figure 1.17(b)) [16]. As pressure increases, there is an intensity transfer between these modes, in such a way that around 16 GPa almost only the mode associated with the undistorted MnO_6 octahedra is seen [16]. Thus, they propose two different phase transitions (P_C and P_{IM}) [16]. Conversely, Baldini *et al.* present a work based on a detailed study of the Raman spectra of $LaMnO_3$ under pressure that shows the Jahn-Teller distortion remains until the P_{IM}, as shown in Figure 1.17(c) [59]. They claim that, although a Raman mode associated with undistorted octahedra appears, the one associated with the distorted octahedra persists [59]. They interpret that the insulator to metal transition happens when a critical ratio of undistorted over distorted octahedra is reached, though the distorted fraction is never null before P_{IM} [59]. No other works report on the Jahn-Teller distortion under pressure for smaller rare-earths in $R\mathrm{MnO}_3$. Clearly, the current studies are still insufficient to ascertain the interplay between the Jahn-Teller and the tilt distortion under high-pressure.

1.3 Theoretical Models

In this section, we will present the theoretical models, developed by different authors, that we consider the most relevant. The main outcomes here described will be used to guide the experimental work presented in this thesis and to interpret and discuss the obtained results.

We will start by the theoretical models concerning the structural properties, namely to explain the phase stability of the tilts that originate the *Pnma* symmetry, and how these are expected to change with applied hydrostatic-pressure. Then, we present the theoretical models that aim to understand the microscopic interactions underlying the rich phase diagrams of rare-earth manganites and reproduce the physical behavior of the systems under study. First, we will address how the magnetic orderings are stabilized, then how the symmetries of these magnetic structures allow the emergence of the ferroelectric phases and finally the model for the microscopic origin of the polarization itself. The physical properties models are mainly focused on the rare-earth manganites, as to the best of our knowledge, similar works on rare-earth ferrites are still missing.

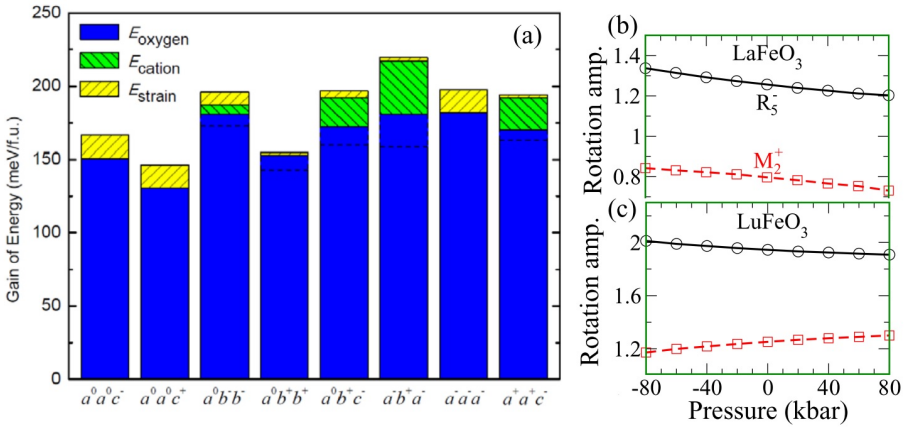

Figure 1.18: (a) The calculated energy gains with respect to the ideal cubic $SrRuO_3$ phase taken as reference, for different tilt systems. Pressure effect on octahedral tilts for (b) $LaFeO_3$ and (c) $LuFeO_3$. Adapted from [24] and [60].

1.3.1 Stability and pressure-evolution of octahedra tilts

The theoretical models in this sub-section are based on calculations using DFT packages, whose detailed description is out of the scope of this thesis.. Hence, we will only address the main outcomes that are more relevant to this thesis.

Miao *et al.* have investigated the energetic gain of different octahedra tilt systems on ABO_3 perovskites, in order to understand why the *Pnma* structure is so widely stabilized on the perovskite materials [24]. Using $SrRuO_3$ as a case study, they have calculated the energetic gains shown in Figure 1.18(a) for the different octahedra tilt systems [24]. The blue area stands for the energetic gain from oxygen movement, the yellow from the strain relaxation and the green from the A-cation movement. As it can be seen, there is a large energetic gain from the appearance of one tilt ($a^0a^0c^-$ and $a^0a^0c^+$ cases), which does not proportionally increase when two or three tilts are stabilized. This increase is not proportional due to a competitive biquadratic coupling between the tilts. It is also seen that the majority of the energy gain comes from the oxygen movements. These movements are the primary-order parameters, identified by the M3+ and R4+ distortions described above. It is also seen that this energy gain from the oxygens is the largest whenever two anti-phase tilts co-exist, independently of the existence of a third tilt ($a^0b^-b^-$, $a^-b^+a^-$ and $a^-a^-a^-$ cases). For the cases where more than one tilt co-exists, the second largest energy gain comes from the A-cation movement. Moreover, this contribution is larger if an in-phase and an anti-phase tilt co-exist. This is due to the fact that, by symmetry constrains, only in those cases a trilinear coupling between the A-cation X5+ distortion and the M3+ and R4+ distortions can be introduced [24]. This trilinear coupling lowers the energy of the ground state, thus increasing the energy gain from the A-cation movement, making the X5+ distortion an important secondary-order parameter. Combining these two rules, the coexistence of two anti-phase tilts and the coexistence of an in-phase and an anti-phase tilt, one necessarily obtains the $a^-b^+a^-$ tilt system of the *Pnma* structure [24]. Later Chen *et al.* presented a work with a similar aim for a much wider range of materials, having reached to the same two rules to explain the stability of the *Pnma* structure [25].

In order to predict and explain the structural behavior of the octahedra tilts under high-pressure, several rules have been developed [25, 60, 61]. Based on the bond-valence concept, Zhao *et al.* have predicted that the AO_{12} dodecahedra are expected to be significantly less compressible than the BO_6 octahedra [61]. Thus, the octahedral tilts should decrease with increasing pressure [61]. Moreover, the decrease of the octahedra tilting with pressure should yield a structural phase transition from the orthorhombic into a higher symmetric

structure [61]. As a matter of fact, these rules are not followed by many of 3:3 perovskites. For instance, new results in rare-earth chromites ($R\mathrm{CrO_3}$), with small R-cations, show that octahedra tilting increase with pressure and some rare-earth ferrites undergo a pressure induced isostructural phase transition [49, 62]. To unravel the mechanisms underlying the distinct pressure dependencies of octahedra tilting, Xiang *et al.* conducted first-principles calculations on representative perovskites and proposed a set of rules governing the tilt evolution with pressure [60]:

1. As the tolerance factor decreases, within the same system, the derivative of the tilt angles with pressure increases;
2. The derivative of the tilt angles with pressure increases from the $A^{3+}B^{3+}\mathrm{O}_3^{2-}$ to $A^{2+}B^{4+}\mathrm{O}_3^{2-}$ and to $A^{1+}B^{5+}\mathrm{O}_3^{2-}$, if the tolerance factor is fixed;
3. When the B-cation has low-lying empty d-states the derivative of the tilt angles with pressure increases, within the same system with tolerance factor fixed;
4. As the BO6 rotation decreases, the derivative of the tilt angles with pressure absolute value increases, within the same system with tolerance factor fixed.

In this framework, they simulated the pressure dependence of both in-phase and anti-phase octahedra tilts of $\mathrm{LaFeO_3}$ and $\mathrm{LuFeO_3}$, as border cases in the rare-earth ferrites series [60]. These predictions are shown in Figures 1.18(b) and (c). For $\mathrm{LaFeO_3}$, they found that both octahedra tilts are suppressed as pressure increases in agreement with Zhao's prevision [60]. However, pressure suppresses the anti-phase but enhances the in-phase tilting in $\mathrm{LuFeO_3}$ [60]. This pressure behavior was interpreted by taking into account the contribution of a trilinear coupling between these two rotations and the anti-polar mode involving the A-cation [60]. Thus, a new rule emerges for the orthorhombic *Pnma* perovskites, which simultaneously exhibit the in-phase and anti-phase octahedra tilts, stating that they are not inevitably both suppressed or enhanced by pressure [60]. Unfortunately, the authors do not present results concerning intermediate rare-earth ferrites in order to check where the crossover between the two aforementioned distinct pressure behaviors occurs.

1.3.2 Microscopic Model for the Magnetic Phase Diagram

Mochizuki and Furukawa presented an approach that purely focus on the magnetic properties of the rare-earth manganites, in an attempt to describe the magnetic phase diagram [51]. They did not develop a model for the magnetoelectric coupling. Instead, they simply took into account the results on the magnetoelectric effect obtained from other models [55]. Their scheme describes the $\mathrm{Mn^{3+}}$ ions spins by a classical S = 2 Heisenberg model in a three-dimensional cubic lattice.

The total Hamiltonian of this model is then written as follows [51]:

$$H = H_{ex} + H_{SIA} + H_{DM} + H_{cub}, \tag{1.4}$$

The first term, H_{ex}, accounts for the superexchange magnetic interactions between neighbors and nearest-neighbors $\mathrm{Mn^{3+}}$ 3d-spins, respectively, as depicted in Figure 1.19. It is expressed as [51]:

$$H_{ex} = -J_{ac} \sum_{<i,j>}^{x,y} S_i \cdot S_j + J_2 \sum_{<i,j>}^{a} S_i \cdot S_j + J_b \sum_{<i,j>}^{b} S_i \cdot S_j \,, \tag{1.5}$$

where the J_{ac} is a ferromagnetic exchange orientated along the Mn-Mn bonds in the x and y axes, while J_2 and J_b are the antiferromagnetic exchanges, orientated along the in-plane diagonal between the Mn-Mn bonds (a-axis) and the Mn-Mn bonds (b-axis), respectively. The antiferro-arrangement of the e_g-orbitals in the ac-plane

and their ferro-arrangement along the b-axis, caused by the Jahn-Teller distortion, defines the ferromagnetic nature of the J_{ac} and the antiferromagnetic nature of the J_b exchanges. The J_2 is a second-neighbor exchange via the oxygen $2p$-orbitals. Although in other orthorhombic perovskites this second-neighbor exchange is usually smaller, in the $R\mathrm{MnO_3}$ it is comparable in strength to the J_{ac} ferromagnetic exchange, as in the latter the ferromagnetic contribution from the e_g-electrons is partially canceled by the antiferromagnetic contribution from the t_{2g}-electrons.

The second term, H_{SIA}, represents the single-ion anisotropies, due to the valence electron of the $\mathrm{Mn^{3+}}$ ion occupying the e_g-orbital, which affects mainly the environment inside the MnO_6 octahedra.

The third term, H_{DM}, accounts for the interactions mediated by the Dzyaloshinskii-Moriya mechanism. This term includes the Dzyaloshinskii-Moriya vector $\left(d^{\alpha}_{i,j}\right)$, which is defined on the Mn(i)-O-Mn(j) bond, along the α direction, where $\alpha = x$, y or z, and obeys the relation $d^{\alpha}_{i,j} = -d^{\alpha}_{j,i}$. When i and j define Mn ions in the ac-plane, the vector is nearly perpendicular to it, as the spin-exchange is controlled by the Mn-O-Mn path. However, if i and j are aligned out of the plane, then the spin exchange between these Mn^{3+} ions is not necessarily perpendicular to the Mn-O-Mn path, since the e_g-orbitals along the b-direction are not occupied. Moreover, experimental results in $\mathrm{LaMnO_3}$ show that the out-of-plane vector is around four times larger than the in-plane one [51].

The last term, H_{cub}, describes the cubic anisotropy that arises from the nearly cubic symmetry of the distorted perovskite structure. The contribution to this term coming from the lattice distortions was neglected, as it is expected to be very small.

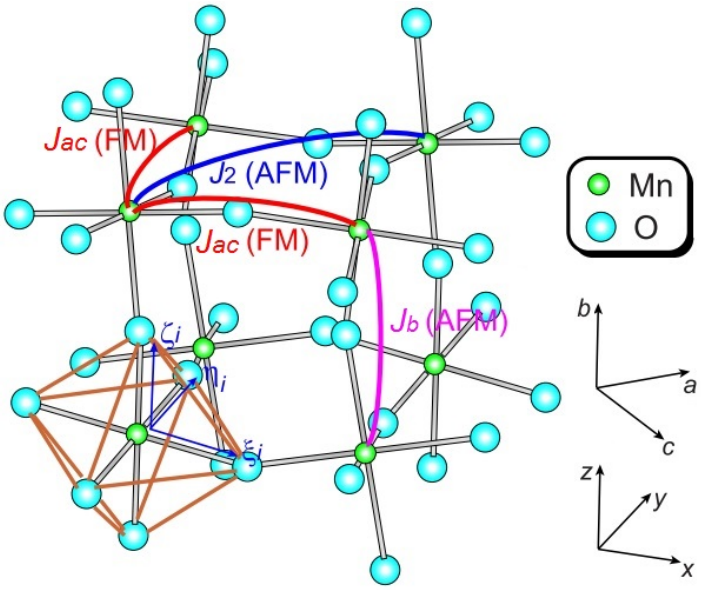

Figure 1.19: Ferro- and antiferromagnetic superexchange interactions of the $\mathrm{Mn^{3+}}$ cations in the $R\mathrm{MnO_3}$ [51].

Besides the minimization of the energy of the Hamiltonian in Equation 1.4, its ground state properties were studied by solving the following Landau-Lifshitz-Gilbert equation with effective local magnetic fields [51]:

$$\frac{dS_i}{dt} = -S_i \times H_i^{eff} + \frac{\alpha_G}{S} S_i \times \frac{dS_i}{dt} \ . \tag{1.6}$$

The J_{ac} and J_b exchanges do not strongly depend on the structural distortions, from $\mathrm{DyMnO_3}$ to $\mathrm{EuMnO_3}$ they vary from 0.76 to 0.85 meV and 1.20 to 1.27 meV, respectively. Thus, their dependency on r_R was neglected and only the r_R-dependence of the antiferromagnetic exchange J_2 was taken into account, which

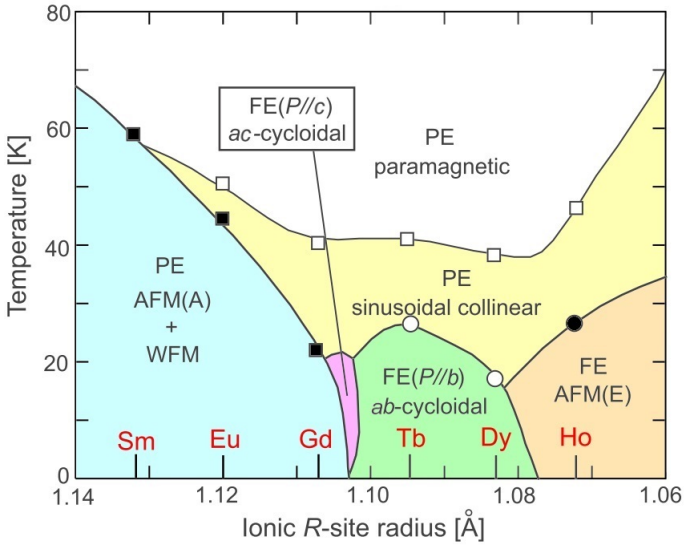

Figure 1.20: Theoretically obtained (T, r_R) magnetic phase diagram for the rare-earth manganites. [51].

from $DyMnO_3$ to $EuMnO_3$ varies from 1.12 to 0.5 meV. The reason for this is that the tilt distortion of the MnO_6 octahedra enhances the hybridization of the $3d$-orbitals from the Mn^{3+} ion with the $2p$-orbitals from the oxygens. The values in the parameters of H_{ex} and H_{SIA} were theoretically calculated whereas those of H_{DM} and H_{cub} were taken from experimental electron-spin resonance measurements [63].

The use of the above method then led to a theoretical (T, r_R) magnetic phase diagram, which is drawn in Figure 1.20. This phase diagram is remarkably similar to the experimental phase diagram as a function of the $[101]_{pc}$-tilt angle shown in Figure 1.13(a). All the experimentally observed magnetic phase transitions reported for each compound are theoretically obtained. Furthermore, the intermediate multiferroic phase between $TbMnO_3$ and $GdMnO_3$ seen by Goto *et al.* on the solid solution $Tb_{1-x}Gd_xMnO_3$ [64], where the spin cycloidal structure is on the *ac*-plane, is also predicted in this theoretical phase diagram. These results provided insight into the experimental phase diagram, namely the important role of the tilt distortion in the definition of the magnetic structure. Their main finding is that the change of the tilt distortion alters the overlap of the electronic orbitals of the neighbor manganese and oxygen ions, which then changes the magnetic superexchange integral J_2, that unbalance the competition with the exchange ones and ultimately determines the stabilized magnetic order.

1.3.3 Phenomenological Model of the Magnetoelectric Coupling

A simple symmetry based phenomenological model was published to derive the relation between modulated magnetic structure and emergence of ferroelectricity, as is the case of $TbMnO_3$ and $DyMnO_3$ [53]. Other similar studies are also available, such as Ref [65], but they are beyond the scope of this section.

The coupling terms between electric polarization ($\vec{P}$) and magnetization ($\vec{M}$) can be derived using symmetry arguments. The invariance upon time reversal yields the lowest-order coupling to be squared in the magnetization, since $\vec{M} \rightarrow -\vec{M}$ under time reversal. The polarization in this case has no restrictions, as it is invariant under time reversal. Still, the coupling must be invariant under spatial inversion as well. Due to the fact that $\vec{P} \rightarrow -\vec{P}$ under this inversion, while the magnetization remains invariant, one would expect the lowest-order coupling to be squared both in M and P: M^2P^2. However, experimentally, the ferroelectricity is often found in magnetic geometrically frustrated materials, with modulated magnetic phases, such as the aforementioned $TbMnO_3$ and $DyMnO_3$ and the ferroelectric Kagomé magnet $Ni_3V_2O_8$ [13, 66]. This means

that the magnetization has a spatial dependence. In this case, the lowest-order coupling that concerns both the time and spatial inversion symmetries is linear in the polarization but contains a factor involving the magnetization gradient. This kind of coupling, linear in the gradient of the order parameter, called Lifshitz invariant, is only allowed in systems where periodic spacial modulations of magnetization occurs [53]. Actually, the magnetic structures that correlate with the electric polarization usually exhibit periodically modulation.

Taking the simplest case of cubic symmetry, the lowest-order coupling term contributing to the emergence of uniform polarization is written as follows [53]:

$$\Phi_{me}\left(\vec{P}, M\right) = \gamma\vec{P}\left[\vec{M}\left(\nabla\cdot\vec{M}\right) - \left(\vec{M}\cdot\nabla\right)\vec{M}\right]. \tag{1.7}$$

Considering that the ferroelectricity is stabilized by the magnetic ordering, the obtained polarization from this coupling is [53]:

$$\vec{P} = \gamma\chi_e\left[\left(\vec{M}\cdot\nabla\right)\vec{M} - \vec{M}\left(\nabla\cdot\vec{M}\right)\right], \tag{1.8}$$

where χ_e is the electric susceptibility in the absence of magnetic order. Let us now consider a spin-density-wave with wave vector $\vec{q}_m$, expressed as [53]:

$$\vec{M} = M_1\vec{e}_x cos\left(q_m x\right) + M_2\vec{e}_y sin\left(q_m x\right) + M_3\vec{e}_z\,, \tag{1.9}$$

where $\vec{e}_x$, $\vec{e}_y$ and $\vec{e}_z$ form an orthogonal basis. Mathematically, either M_1 or M_2 need to be non-zero in order that $\vec{M}$ describes a collinear-sinusoidal wave. In the case that both M_1 and M_2 are non-zero, $\vec{M}$ describes an helix, which can be conical if M_3 is also non-zero. Considering the magnetic order $\vec{M}$ in Equation 1.8 one can calculate the electric polarization that originates from the magnetoelectric coupling. The result for the average polarization is then[53]:

$$\left\langle\vec{P}\right\rangle = \frac{1}{V}\int\vec{P}dV = \gamma\chi_e M_1 M_2\left[\vec{e}_z\times\vec{q}_m\right]. \tag{1.10}$$

The modulation of the magnetic dipole moments for the collinear-sinusoidal wave and the elliptical helix are shown in Figure 1.21, along with the resulting electric polarization. In the case of a collinear-sinusoidal wave, where either M_1 or M_2 are zero (Figure 1.21(a)), there is no net polarization. Thus, for electric polarization to emerge, one needs an elliptical helix as shown in Figure 1.21(b), either conical or not, since $\left\langle\vec{P}\right\rangle$ does not depend of M_3. This result on a cubic lattice can be extended to an orthorhombic one, such as the rare-earth manganites, if the necessary conditions of $\vec{e}_z$ and q_m to be parallel to the crystal axes are met.

From the results presented to above, the phase sequence of $TbMnO_3$ and $DyMnO_3$ can be understood. As presented before, they order magnetically at T_N to a sinusoidal spin-density-wave, which is paraelectric, as it is predicted by this model. It is only at lower temperatures, where the magnetic phase changes to an helix spin-density-wave at T_{lock}, that the polar properties emerge, in good agreement with the above derived results.

1.3.4 Spin-Current Quantum Model

Katsura, Nagaosa and Balatsky developed a complete quantum model to explain the origin of the magnetoelectric effect in non-collinear magnetic systems [55]. Figure 1.22 shows a schematic representation of the Mn-O-Mn bond along with the parameters relevant for the model. If we consider a non-collinear spin order, as it is found in Mn^{3+} spins ordering of the magnetoelectric $TbMnO_3$ and $DyMnO_3$, the direction of the spins of two neighbor Mn^{3+} ions are necessarily not equal. Thus, as the electron hops between them, through an intermediate oxygen atom, it generates a spin-current that carries a spin-polarization given by $\vec{j_s} = \vec{e}_1\times\vec{e}_2$. This spin-polarization is perpendicular to the vector connecting the two neighbor Mn^{3+} ions.

From the symmetry point of view, the spin-current and the electric polarization transform in the same way.

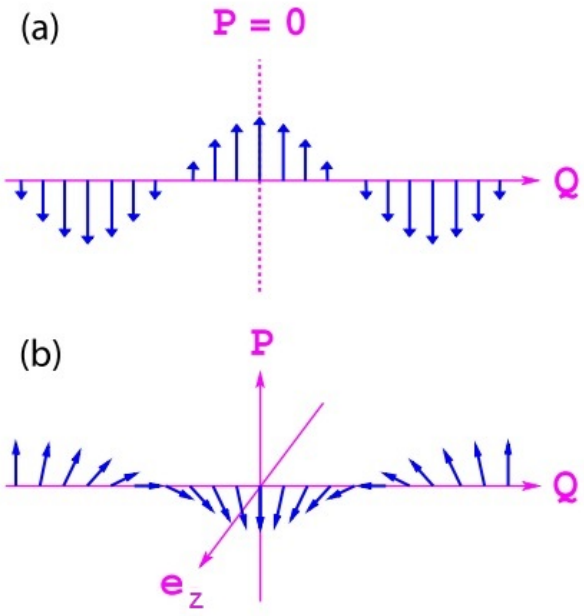

Figure 1.21: (a) Collinear-sinusoidal and (b) elliptical helix arrangements of the magnetic dipoles moments, along with the resulting polarization. Adapted from [53].

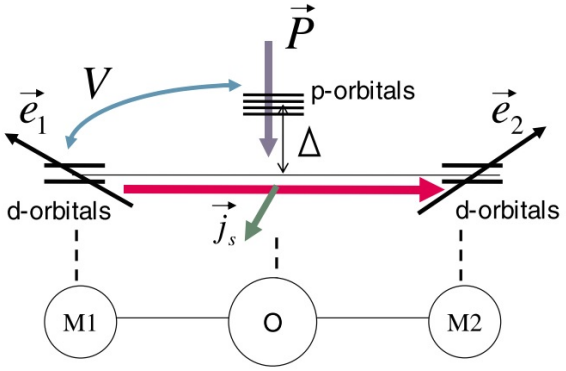

Figure 1.22: Spin-current model for rare-earth manganites. Due to the non-collinear spin directions, a spin-current is generated when an electron hops between neighboring Mn^{3+}, via the oxygen. The generated spin-polarization of the spin-current is shown by $\vec{j_s} = \vec{e}_1 \times \vec{e}_2$. Adapted from [55].

Unlike the charge-current, the spin-current is even in time, as the spin-polarization is reversed along with the direction of the spin-current. Thus, a natural coupling between them is expected. It is not here addressed, but from second-order perturbation theory to the lowest energy levels of the d-orbitals, the originated electric polarization can be derived (see Ref [55]). These lowest energy levels are twofold degenerated, and are obtained by the spin-orbit coupling energy. The local electric polarization ($\overrightarrow{p}$) can then be expressed as [55]:

$$\vec{p} \propto \vec{e}_{ij} \times \vec{j}_s = \vec{e}_{ij} \times (\vec{e}_i \times \vec{e}_j) \ , \tag{1.11}$$

where $\vec{e}_i$ is the magnetic moment of the ith site and $\vec{e}_{ij}$ being the unit vector connecting the sites i and j. The total electric polarization ($\vec{P}$) is thus proportional to the non-collinearity of the Mn^{3+} spins, with its direction being perpendicular to the vector connecting them. As the e_g-orbitals along the b-direction are not occupied, this hopping happens only in the ac-plane. Thus, the resulting polarization from this model will be perpendicular to this plane, along the b-direction, in agreement with the experimental measurements. The value for the total polarization can be obtained by summing over all the existing neighbors.

1.3.5 Mechanism of the Electric Polarization

After understanding the symmetry requirements for the emergence of the ferroelectric properties from the magnetic ordering, we will discuss the model of Sergienko and Dagotto regarding the underlying microscopic mechanism, for the case of $TbMnO_3$ [54]. Unlike the model of Mochizuki and Furukawa, it does not attempt to provide a theoretical explanation for the stabilization of the different magnetic structures. Instead, they start from the known magnetic structure of $TbMnO_3$ and show how it causes the emergence of the ferroelectricity in a more detailed way than the phenomenological model of Mostovoy or the quantum model of Katsura, Nagaosa and Balatsky [53, 55]. It takes into account neutron diffraction results regarding the spin structure, that below T_N, yield a collinear-sinusoidal magnetic ordering, described as [54]:

$$S_n = S_0 cos(n\theta + \alpha) \tag{1.12}$$

where $S_0 = 1.4$, $\theta = 0.28\pi$ for the nth Mn^{3+} ion (the value of α is not given). Furthermore, it was experimentally known that this magnetic phase is paraelectric, and that only below T_{lock}, where the modulation vector is $(q_m, 1, 0)$, a polarization builds up [13]. The ferroelectricity is expected to arise as a consequence of displacements of the oxygens ions from their equilibrium position. In the ideal cubic perovskite, as the 2 neighboring oxygens of the Mn along a given direction are in symmetric positions and the superexchange is invariant under inversion, the considered Hamiltonian must only depend on even powers of the oxygen displacement. Thus, Sergienko and Dagotto describe the magnetic exchange by the following Hamiltonian term [54]:

$$H_{ex} = -\sum_n \left[J_0 + \frac{1}{2} J'_{||} x_n^2 + \frac{1}{2} J'_{\perp} \left(y_n^2 + z_n^2 \right) \right] \left(\vec{S}_n \cdot \vec{S}_{n+1} \right) \ , \tag{1.13}$$

where J_0, $J'_{||}$ and $J'_{\perp}$ are constants, $\vec{r}_n = (x_n, y_n, z_n)$ is the displacement of the oxygen between the nth and the $n+1$th Mn^{3+} cation, and S_n is the spin of the nth Mn^{3+} cation. However, the displacement of the oxygens in the orthorhombically distorted structure is actually given by [54]:

$$r_n = (-1)^n r_0 + \delta r_n \ , \tag{1.14}$$

where r_0 is a constant of the order of 10^{-1}Å and δr_n, of the order of 10^{-3}Å, is the additional displacement caused by the magnetic structure. This additional displacement affects the Hamiltonian by the following magnetoelastic term [54]:

$$\delta H_{ex} = \sum_n (-1)^{n+1} \left[J'_{||} x_0 \delta x_n + J'_{\perp} \left(y_0 \delta y_n + z_0 \delta z_n \right) \right] \left(\vec{S}_n \cdot \vec{S}_{n+1} \right) + H_{el} \ , \tag{1.15}$$

where H_{el} is simply an isotropic elastic energy. Minimizing the magnetoelastic Hamiltonian term with respect to the oxygens displacements, using the mentioned spin structure of $TbMnO_3$, an isotropic modulated displacement is found $(k_l, 0, 0)$, with the correct $k_l = 2q_m$. Although it reproduces the known structural modulation with the correct wave vector, it is not sufficient to explain the emergence of the ferroelectric properties, as the sum over the oxygen positions gives a null net polarization ($\sum_n r_n = 0$). The ferroelectric properties emerge upon the introduction in the Hamiltonian of the Dzyaloshinskii-Moriya anisotropic exchange interaction term [54]:

$$\delta H_{DM} = \sum_n D^x(\delta r_n) \cdot (\vec{S}_n \times \vec{S}_{n+1}) + H_{el} \ . \tag{1.16}$$

Minimization of the corresponding energy results in oxygen displacements only along the z-direction (b-axis of the orthorhombic structure) gives then rise to a ferroelectric polarization along the same direction, which is correct to the experimental measurements. From this, Sergienko and Dagotto were able to confirm the important role played by the Dzyaloshinskii-Moriya interaction mechanism in the origin of the ferroelectric properties of the cycloidal magnetic phase. Moreover, they also confirm that the collinear-sinusoidal magnetic phase is paraelectric, as no displacements are found when introducing it in the Hamiltonian.

1.4 Structural Tailoring of Physical Properties

The possibility of performing a fine tuning of the structural distortions can be achieved through chemical substitution, towards the desired physical properties. Here, we will only consider isovalent substitutions on oxide perovskites, where the valency $A^{3+}B^{3+}O_3^{2-}$ and the $Pnma$ phase are always maintained. This enables a continuous and controlled change of the structural distortions, up to a certain degree of phase stability when the used end-members have different structures (e.g. the hexagonal $YMnO_3$). The obtained structure is considered $Pnma$ under the virtual crystal approximation, where average structure with average lattice parameters, tilts and deformations are considered, instead of the actual local values that differ around the substituted and the substitutional ions. With these conditions, the chemical substitution can be divided into 2 groups: substitution of the A-site cation and substitution of the B-site cation. The first type of chemical substitution allows the tuning of the tilt distortion, while the second is associated with the octahedra distortion. In the past, the effect of changing the tilt distortion was extensively studied by A-site chemical substitution in rare-earth manganites. In the rare-earth ferrites this chemical substitution was not so much studied, which may be due to the fact that the rare-earth sublattice can also couple with iron sublattice, yielding a more intricated behavior of these compounds. Thus, this substitution cannot be reduced to a simple tune of the structure, as the interplay between the R^{3+} and the Fe^{3+} spins is also being changed. The B-site chemical substitution remains much unexplored, though it must be noted that the substituted ion is the one whose spins are magnetically ordered (Mn^{3+} and Fe^{3+} spins in our case). Then, both the structure distortions and the magnetic properties are simultaneously changed.

The discovery of the phase diagram as a function of the tilt angle for the $RMnO_3$, first experimentally [64] and later theoretically [51], paved the way for the chemical substitution studies on these materials. Since it was known that reducing the rare-earth ionic radius increases the tilt distortion, which tends to unbalance the competition between ferro- and antiferromagnetic interactions, its tuning was understood to be of critical importance. Moreover, as the rare-earth spins are not ordered at these temperatures, the change on the number of electrons of the rare-earth cation has no direct consequence aside from changing the tolerance

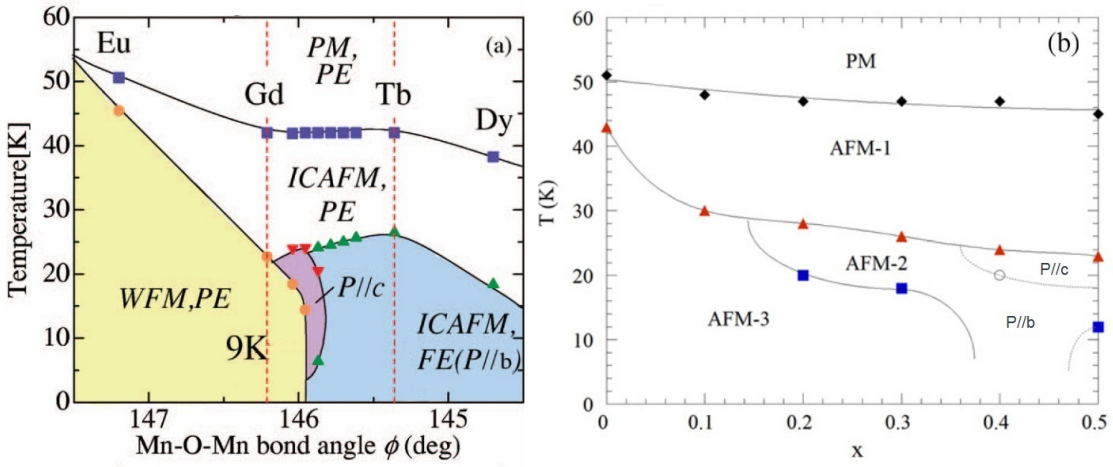

Figure 1.23: (x, T) phase diagrams of the (a) $Gd_{1-x}Tb_xMnO_3$ ($0 \leq x \leq 1$) and (b) $Eu_{1-x}Y_xMnO_3$ ($0 \leq x \leq 0.5$) systems. Adapted from [64] and [70]. In both cases a re-entrant *ac*-cycloidal structure, with polarization along the *c*-axis is found, not seen in the pure RMnO$_3$ phase diagram.

factor. It was also known that only $TbMnO_3$ and $DyMnO_3$ have the necessary tilt distortion to promote, at low temperatures, the spin cycloidal structure that allows the emergence of the polar properties. Having this in mind, the first studies with chemical substitution started by the solid solution $Gd_{1-x}Tb_xMnO_3$, consisting in taking the $GdMnO_3$, the closest paraelectric neighbor (cf. Figure 1.13), and substituting it with $TbMnO_3$, in order to better determine the border between magnetically-induced to spontaneous multiferroics [64]. The phase diagram obtained for this solid solution is presented in Figure 1.23(a). Surprisingly at that time, from polar and dielectric measurements, a re-entrant magnetic phase with a spin cycloidal structure along the *ac*-plane, originating a polarization along the *c*-axis, was found. The range of tilt distortion where this phase can be obtained is only around 0.3 degrees, and was absent on the phase diagram of the unsubstituted materials. Later on, many similar works have been published concerning the effect of the A-site substitution in $GdMnO_3$ and $EuMnO_3$, the closest ones to the ferroelectric phase boundary (cf. Figure 1.13). These works report on the isovalent substitution of Gd^{3+} and Eu^{3+} by smaller cations, such has Y [56, 67–76], Lu [77, 78] and Ho [79, 80]. As an example, Figure 1.23(b) shows the phase diagram of $Eu_{1-x}Y_xMnO_3$, for $x \leq 0.5$ (as the *Pnma* phase is lost afterward) [70].

In this solid solution, a re-entrant *ac*-cycloidal spin structure is established for concentrations of 0.2 and 0.3, with ferroelectricity along the *b*-axis (AFM-2 in Figure 1.23(b)) [70]. Increasing Y-concentration to 0.4 and 0.5, another magnetic structure is found to be stable between T_{lock} and 18 K, exhibiting an electric polarization along the *c*-axis. On further temperature decreasing, a flop of the cycloidal plane is observed, with a consequent change of polarization direction to the *b*-axis [70]. The results of these works were not only of experimental nature, but also they allowed some theoretical models such as the one from Mochizuki and Furukawa to be improved, in a attempt to describe all the recent discovered physics [81].

The chemical substitution on the B-site concerns another kind of distortions. In the special case where the B-site cation is Jahn-Teller active, as it is the case of RMnO$_3$, the chemical substitution by non-active Jahn-Teller cations tune the amplitude of the octahedra distortions and asymmetry. The *B*-site substitution in RMnO$_3$ can be easily achieved using different transition metal cations. In order to avoid changing other distortions other than the Jahn-Teller distortion, the most suitable choice is the Fe^{3+}, as this cation has exactly the same ionic radius of 0.645 Å the Mn^{3+}, considering the high spin configuration and the 6th coordination [82]. As mentioned before, in this case the physical properties will be simultaneously altered both by the

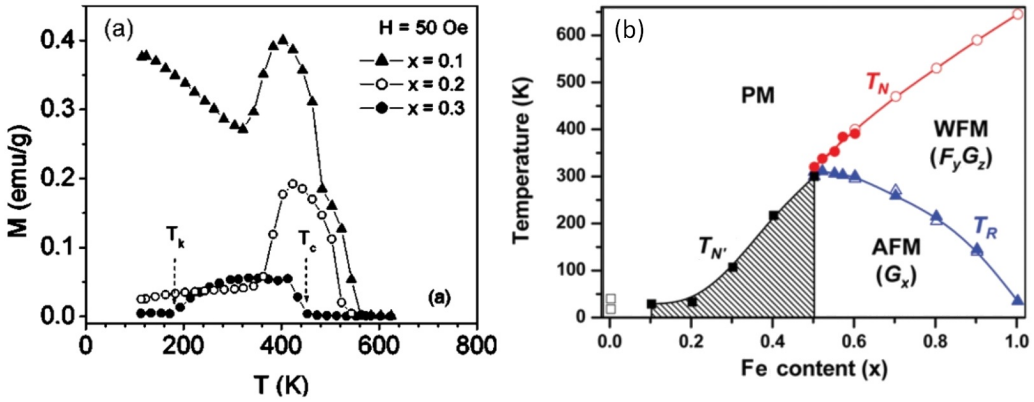

Figure 1.24: (a) Magnetic response as a function of temperature for $SmFe_{1-x}Mn_xO_3$, with $x = 0.1$, 0.2 and 0.3, and (b) (x, T) magnetic phase diagram of the $DyMn_{1-x}Fe_xO_3$ solid solution. Adapted from [84].

structural distortions and the effective magnetic moment variation. While in rare-earth manganites the Mn^{3+} ion only orders magnetically below 100 K, in the ferrites, the Fe^{3+} orders at a much higher temperature, around 650 K [34]. The effect of this B-site substitution has been less explored, and a brief summary of the available works will be given in the following.

First, only the effect of a partial substitution of Fe^{3+} by Mn^{3+} (less than 30%) on the magnetic properties of $SmFeO_3$ was published by Bouziane *et al.* [83]. Figure 1.24(a) summarizes the main results. From the magnetic measurements, the paramagnetic to weak-ferromagnetic transition at T_c and the spin-reorientation to the antiferromagnetic phase at T_k of $SmFeO_3$ both decrease with Mn-concentration. Although they find that the magnetism of the solid solution is strongly dependent on the substitution ratio, which is an interesting result, they present rather speculative explanations without resorting to results from other experimental techniques. They assume that the interactions Mn-Mn are ferromagnetic and the Mn-Fe antiferromagnetic, and also that the Sm^{3+} spins give different magnetic contributions due to internal magnetic fields generated by the Mn^{3+} ions [83].

Only more recently the effect of the substitution of Mn^{3+} by Fe^{3+} on its complete range (0 to 100%) was published by two independent studies in the solid solution of $DyMn_{1-x}Fe_xO_3$, towards a first (x, T) magnetic phase diagram [84, 85]. In both works, x-ray diffraction is used to inspect the structural alterations caused by the chemical substitution. From its analysis, it is concluded that for $x < 0.2$, the Jahn-Teller distortion is not much altered, though for $x > 0.5$ the Jahn-Teller distortion seems to be already suppressed. Regarding the physical properties of $DyMn_xFe_{1-x}O_3$, both studies focus again on the magnetic response as a function of Fe-concentration and temperature, from which the phase diagram shown in Figure 1.24(b) was drawn. They start with $x = 0.1$, finding that the multiferroic properties the $DyMnO_3$ were already suppressed [84, 85]. They conclude this not from polar measurements, but from the weak-ferromagnetic character of the magnetic phase, contrasting with the pure antiferromagnetic character of the spin cycloidal structure needed for the emergence of ferroelectricity[84, 85]. As the Fe-concentration increases, T_N also increases, as expected [84, 85]. Between $x = 0.1$ and up to 0.5, only one phase transition is reported into a magnetic phase where the spins are antiferromagnetically arranged on the ac-plane, with canting along the b-axis. For $x \geq 0.5$, two phase transitions are found, as a spin-reorientation occurs for $T_R < T_N$. As x increases, T_R decreases from 300 K for $x = 0.55$ until around 10 K for $x = 1$ [84, 85]. Though, different magnetic phases are identified, including temperature induced spin-reorientations, making this solid solution interesting for the tuning of different magnetic orderings, details on the (x, T) phase diagram are still missing, being absent for $x < 0.1$, where no connection to the multiferroic properties of $DyMnO_3$ is made.

Later, three different works were exclusively focused on identifying the magnetic structures and magnetic phase transitions temperatures of $TbMn_{1-x}Fe_xO_3$ by using the neutron diffraction technique. Hong *et al.* studied the composition range $0.1 \leq x \leq 0.3$ [86]. They have concluded that, similarly to $DyMn_{1-x}Fe_xO_3$, the cycloidal magnetic ordering is already collapsed for $x = 0.1$ [86]. However, they were able to identify that a canted G-type antiferromagnetic ordering (G_x) develops as x increases above 0.3. Moreover, they find a new spin-reorientation at T_{SR} in this x-range with $F_y + G_z$ structure, not seen in $DyMn_xFe_{1-x}O_3$ [86]. They draw a (x, T) magnetic phase diagram (see 1.25(a)) from the found critical temperatures, identifying that T_N increases, while T_{SR} only slightly decreases, with Fe-concentration [86]. The spin structure of each phase is shown in Figure 1.25(b) and (c), respectively. Nair *et al.* focused solely on the composition of $x = 0.5$ [87]. They have found that for this composition the Mn/Fe spins order below 295 K, identifying the magnetic structure of the type G_z (see Figure 1.25(d)), and not G_x as reported by Hong *et al.* [86]. They have also found that below 250 K a mixed-domain structure is seen, remaining stable until the spin-reorientation temperature of 26 K, below which the magnetic structure is again of the type G_z, as shown in Figure 1.25(f) [87]. Fang *et al.* have performed neutron magnetic diffraction in the $0.4 \leq x \leq 0.9$ composition range, in order to unravel their magnetic structure [88]. The results obtained for the case of $x = 0.75$ is summarized in Figure 1.25(d) to (f) [88]. They have also studied in further detail the spin-reorientation as a function of x. They have shown that the temperature at which the spin-reorientation occurs can be tuned by the Fe-concentration, from 180 K to $x = 0.9$, to 300 K for x =0.5 and 0.6 [88]. They have suggested that this rich magnetic phase diagram should be further studied, such compositions being promising for applications such as magnetic refrigerants and spin-switching devices [88]. To the best of our knowledge, no work has been reported studying the complete range of concentrations from $x = 0$ up to 1 in $TbMn_{1-x}Fe_xO_3$. Moreover, no work addressed to date the multiferroic and magnetoelectric properties found on the RMnO$_3$ side.

1.5 Aim of the Thesis

In this thesis we aim to study the structural distortions and the physical properties (magnetic, polar and magnetoelectric) of the orthorhombic perovskites RMnO$_3$ and RFeO$_3$ series and of their solid solution $RMn_{1-x}Fe_xO_3$ (R = Tb).

We start by addressing the remaining open issues in the pure compounds of the RMnO$_3$ and RFeO$_3$ series. On one hand, though the RMnO$_3$ series is extensively studied by altering chemical composition, temperature and hydrostatic pressure, the behavior of the Jahn-Teller distortion under pressure is scarcely known. On the other hand, the study of the structure and lattice dynamics of the RFeO$_3$ series by varying both temperature and pressure is not systematically carried out. After presenting these two issues, we have thus the basic tools to embrace the study of the $TbMn_{1-x}Fe_xO_3$ solid solution, encompassing both the structural distortions and physical properties. In the case concerning the emergence of magnetoelectricity, we will focus on the range of low iron concentrations, below 6%. In the last part of the thesis, we will focus on the study performed in single crystals to explore how the anisotropy acts on the physical properties of $TbMn_{0.98}Fe_{0.02}O_3$ using neutron and electric polarization data, measured as a function of temperature and magnetic field.

We will now describe the specific goals of each experimental study presented in this thesis.

We dedicate the first study to the unknown behavior of the Jahn-Teller distortion under pressure of the $GdMnO_3$ and $DyMnO_3$. For this, we complement the existent high-pressure x-ray diffraction and Raman scattering studies with x-ray absorption spectroscopy of the Mn^{3+} ion. This technique is more sensitive to local environments, in this case, the oxygen octahedra surrounding the Mn^{3+} ion.

As we have seen, the octahedra tilt is an important distortion of oxide perovskites. Yet, to determine the tilt angles from the oxygen positions are chronically difficult to reach by x-ray diffraction under external parameters, namely hydrostatic pressure. Raman scattering as been used to follow the octahedra tilts in

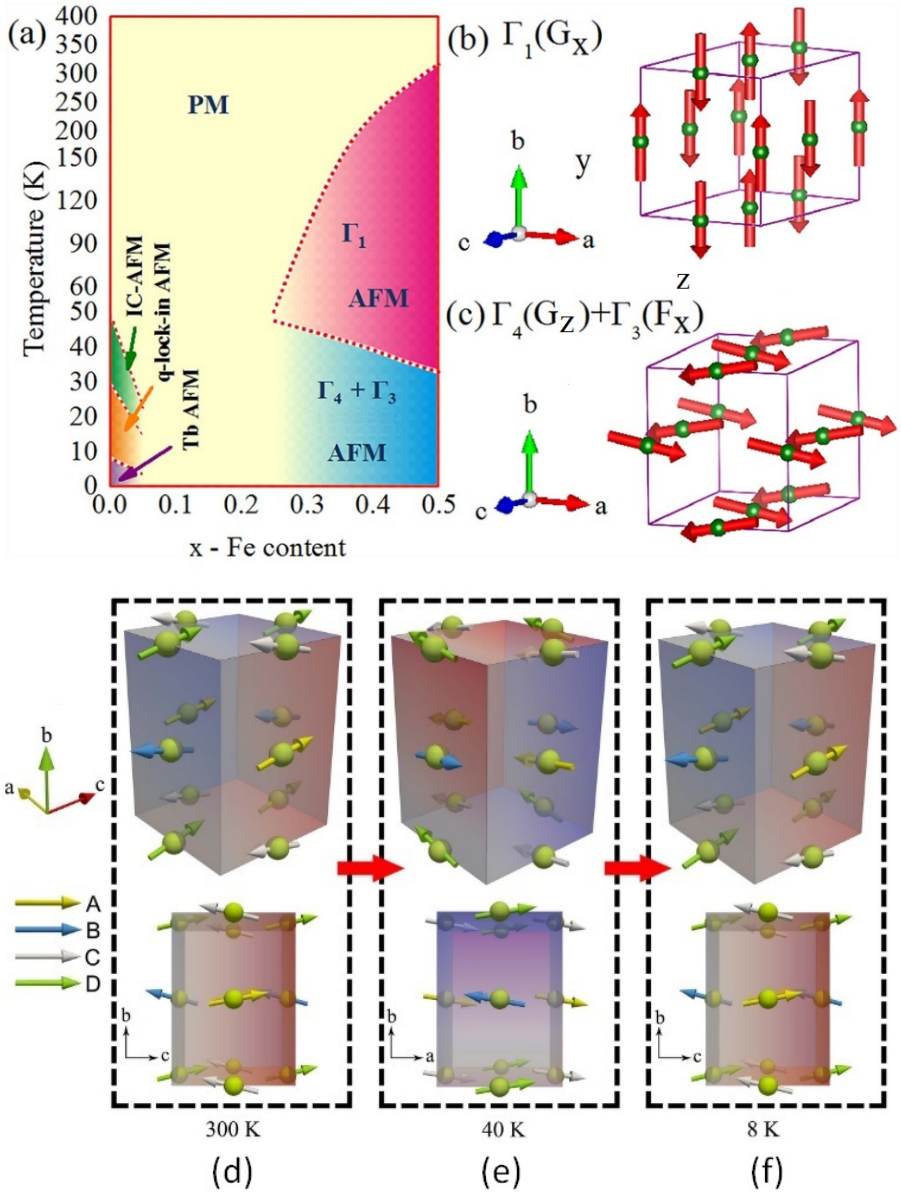

Figure 1.25: (a) (x, T) magnetic phase diagram of $TbMn_{1-x}Fe_xO_3$, (b) and (c) respective magnetic structures. Adapted from [86]. Evolution of magnetic phases for $TbFe_{0.75}Mn_{0.25}O_3$: (d) Γ_4 phase at T = 300 K, (e) Γ_1 phase at T = 40 K, and (f) Γ_4 phase at T = 8 K. Arrows of A to D represent four kinds of spin moments of the Fe^{3+}/Mn^{3+} ions. Adapted from [88].

systems like the $R\mathrm{MnO_3}$ and the $R\mathrm{CrO_3}$. However, the Raman spectra dependence on the rare-earth ionic radius, and the respective mode assignment, is yet to be established for the $R\mathrm{FeO_3}$. Thus, we have performed a systematic Raman scattering study of the $R\mathrm{FeO_3}$ (R = La to Dy) and developed a DFT based complete mode assignment for the Raman-active phonons, establishing how they can be used as probes for the structural distortions.

Due to the difficulty to probe the octahedra distortions by x-ray diffraction, the studies of the $R\mathrm{FeO_3}$ under high-pressure up to now only characterize how volume reduces with the applied pressure, and report the emergence of a pressure-induced insulator-to-metal transition. So far, it remains to be learned how the pressure dependence of the structural distortions, namely of the octahedra tilts, and what role they might play on the insulator-to-metal transition. To give answers to these questions, we follow the structural distortions of $R\mathrm{FeO_3}$ under hydrostatic pressure, using the probes of Raman scattering established in the first study and synchrotron x-ray diffraction.

Physical properties are often coupled to the lattice. In the case of the magnetic properties, this coupling is ensured via the magnetoelastic coupling, also designated as spin-lattice coupling. This feature allows the use of structural probes, such as Raman modes, also as local probes for the magnetic interactions, as it was successfully carried out in the past for the $R\mathrm{MnO_3}$ and $R\mathrm{CrO_3}$ systems. Thus, we study the temperature dependence of the optical phonon modes of $R\mathrm{FeO_3}$ (R = Sm to Tb), to provide insight on the magnetic interactions.

As it was mentioned, the chemical substitution on the A-site, to tune the octahedra tilt and the associated physical properties, has been extensively studied. However, the chemical substitution on the B-site that allows the tune of the octahedra deformation, namely the Jahn-Teller distortion, is far less explored. For this reason, we have chosen the specific solid solution of $\mathrm{TbMn_{1-x}Fe_xO_3}$, $0 \leq x \leq 1$, where we are able to control the magnitude of the Jahn-Teller distortion by chemical substitution, understanding how it is connected with the octahedra tilt distortion and the associated Raman modes, through x-ray diffraction and Raman scattering studies at room conditions.

The substitution of $\mathrm{Mn^{3+}}$ by $\mathrm{Fe^{3+}}$ in $Tb\mathrm{MnO_3}$, causes a strong change in its magnetic properties. Some parts of the associated (x, T) magnetic phase diagram have been reported, though often incomplete. We thus perform an exhaustive study of the magnetic phases of this solid solution, towards the drawing of a complete (x, T) magnetic phase diagram. To this end, we measure the DC and AC magnetic response and the specific heat as a function of temperature and chemical substitution.

To the best of our knowledge, no published studies addressed the multiferroic and magnetoelectric properties of the substitution of $\mathrm{Mn^{3+}}$ by $\mathrm{Fe^{3+}}$ in neither $\mathrm{TbMnO_3}$ nor $\mathrm{DyMnO_3}$. What is now known is that these properties are already lost for 10% of Fe-concentration. In order to unravel the evolution of the multiferroic and magnetoelectric properties and their range of stability with this chemical substitution, we studied the $\mathrm{TbMn_{1-x}Fe_xO_3}$ solid solutions with small increments of Fe-concentration up to 5%. This study was done by specific heat and polar measurements as a function of Fe-concentration, temperature and applied magnetic field.

Finally, it is known these multiferroic rare-earth manganites present highly anisotropic magnetoelectric effects, where the spin cycloidal structure can flop from the ab- to the ac-plane, causing the electric polarization to go from the b- to the c-axis, if a high enough magnetic field is applied along the a-direction. This knowledge is of most importance to understand the underlying mechanisms of the magnetoelectric properties behavior. Since these effects are completely hindered in ceramic samples studies, single crystals sample of $\mathrm{TbMn_{0.98}Fe_{0.02}O_3}$ were grown and oriented. With these single crystals we were able to study the effect of a magnetic field applied along the a-direction on the spin cycloidal structure and on the electric polarization. These studies were carried out using neutron diffraction and electric polarization measurements as a function of temperature and applied magnetic field.

Chapter 2

Experimental Techniques

This Chapter addresses the description of the used experimental parameters towards sample preparation and characterization techniques. No new experimental technique was devised during the development of this thesis. All the experimental work was carried out by the author, except when stated otherwise.

Sample Processing and Chemical and Structural Characterization

Ceramic samples of $R\mathrm{FeO_3}$, $R\mathrm{MnO_3}$ and $\mathrm{TbMn_{1-x}Fe_xO_3}$, were supplied by Pedro Tavares and Eugénia Queirós, from the Centro de Química de Vila Real, Univesidade de Trás-os-Montes e Alto Douro. Both ceramic and single-crystals of $\mathrm{TbMn_{1-x}Fe_xO_3}$ were supplied by the group of Marian Mihalik, from the Experimental Physics Slovak Academy of Sciences, Kosice, Slovak Republic. Ceramic samples were produced following the sol-gel combustion method. Details of the ceramic processing can be found in Refs [89]. All ceramic samples were previously characterized from the chemical and structural point of views by x-ray diffraction, Fourier transform Infrared spectroscopy, scanning electron microscopy and Raman scattering. The quality of the single crystals was checked by x-ray diffraction and energy dispersion s-ray spectroscopy. In all cases, no spurious phases could be detected within the limit of sensibility of the experimental techniques. The results ensure stoicheometric and single phase perovskite samples used in this thesis.

X-ray Diffractometry

X-ray powder diffraction was used to obtain the lattice parameters and atomic positions at room conditions. X-ray powder diffractograms were recorded using the X'Perto Pro, PANalytical diffractometer of the Electron Microscopy Unit in Centro de Química, at University of Trás-os-Montes and Alto Douro in Vila Real, Portugal, in the Bragg-Bentano geometry, by Pedro Tavares and Eugénia Queirós (Chapter 7). The measurements were performed using the $K_{\alpha 1}$ and $K_{\alpha 2}$ doublet emitted by the Cu cathode, with wavelengths 1.540598 Å and 1.544426 Å, respectively. The diffractometer uses a X'Celerator detector, with a Ni filter to minimize the K_β radiation and a secondary monocromator. An acceleration voltage of 50 kV and a current of 40 mA were used. The diffraction patterns were measured in the 10^o to the 70^o 2θ range, with a step of 0.017^o and an acquisition time of 100 s.step^{-1}. The calibration and alignment of the diffractometer were made by polycrystalline silica as external standard. Detailed information of the principles of the x-ray diffraction technique can be found in [90].

The lattice parameters of $R\mathrm{FeO_3}$ at high-pressure were obtained using angle dispersive synchrotron x-ray diffraction experiments, at the European Synchrotron Radiation Facility (ESRF) on the ID27 high-pressure

beam line. The beam time resulted from the acceptance of Proposal HC-2153. X-ray diffraction patterns were collected on a Mar charge coupled device detector with a focused monochromatic beam at $\lambda = 0.3738$ Å. Complete diffractograms were obtained with 5 to 10 seconds integration time. The powder was milled on a agate mortar to obtain the smallest grains possible. High-pressure was obtained by loading the powder sample in a diamond anvil cell with diamond tips of diameter 300 μm and with helium as a pressure-transmitting medium. Helium is the most suitable medium for pressures above 15 GPa, as it is able to maintain hydrostatic conditions, while others like mixtures of ethanol and methanol are not. The value of the applied pressure was obtained by measuring the fluorescence of a ruby inside the diamond anvil cell, using a He-Ne laser at 633 nm (Chapter 5).

The obtained x-ray diffraction patterns were analyzed either using both Jana2006 or Fullprof programs. The Rietveld refinment method was used for the determination of the lattice parameters and atomic positions from the diffffraction patterns,which is simulated by structural data. Details regarding the Rietveld refinement method can be found in [90].

X-ray Absorption Spectroscopy

X-ray absorption spectroscopy was used to inspect the MnO_6 octahedra of RMnO$_3$, under pressure, to disentangle the behavior of the Jahn-Teller distortion, at the BM23 beamline of the ESRF in Grenoble, France. Beam time was obtained from the HC-2730 and HC-3040 accepted proposals. At high-pressures, the x-ray diffraction patterns have poor quality, which hinder the possibility to reliably obtain the position of small atoms, such as the oxygens. X-ray absorption produces the emission of a photoelectron, whose propagating wave autointerferes as it is reflected by the surrounding atoms, producing oscillations in the absorption spectra after the absorption edge. Detailed information of the fundamentals of the x-ray absorption spectroscopy can be found in [91]. Only $DyMnO_3$ and $GdMnO_3$ were studied, since most of the other rare-earths have an absorption edge too close to the Mn K-edge, hindering their correct measurement.

X-ray absorption measurements at the Mn K-edge ($E_0 \simeq 6552$ eV) as a function of pressure up to 30 GPa were carried out with a Si(111) double-crystal monochromator and a Kirkpatrick−Baez mirrors to focus the monochromatic x-ray beam down to 5 x 5 μm^2, with a Pt coating and set at an angle of 7.5 mrad to reject high order harmonics. The spectra were recorded from 6400 to 7088 eV, with 8 seconds integration time per point. The powdered sample was charged on a nano-polycrystalline diamond anvil cell (to avoid glitches from the anvils) [92], with ruby chips as pressure markers. Furthermore, the usage of a partially perforated anvil facing a thin mini-anvil glued on a totally perforated diamond, turned out to be an ideal solution for the low energy Mn K-edge x-ray absorption measurements under pressure on a bending magnet beamline [93]. A mixture of methanol:ethanol (4:1) was used as pressure transmitting medium. Although He would be a better choice, the nano-polycrystalline diamond anvil cell is not able guarantee that leaks would not appear. Moreover, since x-ray absorption spectroscopy is a local probe, unlike the long-range of the x-ray diffraction, it is not so sensitive to the the loss of hydrostatic conditions.

The extended x-ray absorption fine-structure (EXAFS) spectra, $\chi(k)$ are obtained by isolating these oscillations for the k range 2.4 and 10.5 cm^{-1} ($\Delta k = 0.5$ cm^{-1}) using a sinus window, after removing the normalized to unity jump at the edge E_0, and subtracting the pre-edge and post-edge splines with the Athena software of Demeter package. The FEFF-6 code of Artemis software of Demeter package assumes a spherical wave for the propagation of the photoelectron multiplied by a damped wavefunction and fits the following equation to the spectra [94]:

$$\chi(k) \propto \sum_j N_j \frac{f_j(k)}{kR_j^2} e^{-2R_j/\lambda(k)} e^{-2k^2\sigma_j^2} sin\left[2kR_j + \delta_j(k)\right] , \tag{2.1}$$

where j refers to each surrounding atom, N_j is the coordination number, $f_j(k)$ and $\delta_j(k)$ are photoelectron scattering properties, R_j is the distance, σ_j is the mean-square disorder of the jth atom and $\lambda(k)$ is the photoelectron mean free path.

The corresponding structures at ambient pressure were used as a starting point, summing for all atoms within a cluster radius of 3 Å to include only the simple scattering paths to the first oxygen coordination shell. This procedure was chosen as we only focused on the Mn-O distances inside the MnO_6 octahedra. Thus, the minimum quantity of parameters to described it was used. The same referred E_0 parameter and fitting sinus windows between 1 and 2.5 Å (Δr = 0.2 Å) were used for all spectra, in order no to induce artifacts into the fits. To describe the distorted MnO_6 octahedra, we chose 3 different $\triangle r$ for the 3 different values of the Mn-O bond lengths, and the Debye-Waller factor for thermal disorder.

Detailed information regarding the fitting software and procedure can be found in [94].

Raman Scattering

To characterize the lattice dynamics and associated structural distortions, the Raman scattering was measured in RFeO$_3$ and TbMn$_{1-x}$Fe$_x$O$_3$ samples, at room conditions. For the case of RFeO$_3$, a similar study was carried out at high-pressure. To study the spin-phonon coupling of RFeO$_3$, the Raman scattering was measured as a function of temperature. In these studies T64000 Jobin-Yvon and inVia Renishaw Reflex Raman spectrometers were used. Each measurement was always carried out at fixed temperature/pressure, and the effect of the laser power on the Raman spectra was studied, previously to each measurement, in order to prevent self-heating of the sample (typically below 5 mW).

The Wyckoff positions of the studied materials with *Pnma* structure present 60 normal modes at the Γ-point, from which 24 are Raman-active vibrational modes [95], which decompose into $\Gamma_{Raman} = 7A_g + 5B_{1g} + 7B_{2g} + 5B_{3g}$, according to the irreducible representations of the *mmm* point group.

For the Raman scattering measurements in Chapters 7 and 6, the scattered light was analyzed using a T64000 Jobin-Yvon spectrometer at IFIMUP, University of Porto equipped with liquid nitrogen cooled charge-coupled device and photon-counting device. These works were performed with the help of Daniel Passos and Barbara Mota. Using 1800 lines.mm^{-1} holographic gratings and taking into account the 3 mm × 640 mm focal length, the spectral resolution is 0.5 cm^{-1}. The unpolarized Raman spectra was measured in the pseudo-backscattering geometry, both at room temperature and on heating runs. The 514.5 nm polarized line of an Ar^+ laser was used. In order to ensure reliable results, all of the Raman spectra were recorded at fixed holographic gratings positions and identical conditions were maintained for all scattering measurements. The Raman-scattering studies as a function of temperature (Chapter 6) were performed in pellets with dimensions around 1 cm^3, placed either in a closed-cycle helium cryostat, with a temperature range from 9 to 300 K, with a temperature stability of about 0.2 K, or in a Linkam THS 600 stage, with a temperature range from 80 K to 900 K, and a temperature stability of about 0.1 K. In the closed-cycle helium cryostat, the temperature homogeneity of the samples was achieved with a cooper mask setup and the temperature of the sample was estimated to differ by less than 1 K from the temperature measured with a silicon diode attached to the sample holder.

For the high-pressure Raman-scattering studies (Chapter 5) a similar T64000 Jobin-Yvon spectrometer was used, at Institut Néel, Grenoble, France, with a similar diamond-anvil-cell as described above (Chapter 2).

Raman scattering measurements were also performed in collaboration with Mads Weber in an inVia Renishaw Reflex Raman Microscope, in micro-Raman mode, with an excitation laser of a He-Ne laser at 633 nm and a spectral cutoff at 70 cm^{-1}. The polarized Raman spectra were measured using particular configurations of incident and scattered light polarizations with respect to the orientation of the crystal, to selectively probe the Raman modes of a given symmetry. The experimental configurations are expressed in Porto's notation [96]. Samples were cooled to liquid nitrogen temperature in a Linkam THMS600 stage in order to reduce thermal

broadening of the spectra and ease the identification of Raman bands (Chapter 4). For the case of $NdFeO_3$ in Chapter 6, a similar Linkam THMS600 stage was used in the inVia Renishaw Reflex Raman spectrometer at IFIMUP, University of Porto.

The obtained Raman spectra were analyzed using either the commercial Igor Pro program or an automated Python based algorithm, developed in collaboration with Catarina Dias. They both simulate the Raman spectra by using a sum of damped oscillators, according to the following equation [97]:

$$I(\omega, T) = [1 + n(\omega, T)] \sum_{j=1}^{N} A_{oj} \frac{\omega \Omega_{oj}^2 \Gamma_{oj}}{(\Omega_{oj}^2 - \omega^2)^2 + \omega^2 \Gamma_{oj}} , \tag{2.2}$$

where $n(\omega, T)$ is the Bose-Einstein factor, A_{oj} is the strength, Ω_{oj} is the wavenumber and Γ_{oj} is the damping coefficient of the jth oscillator. For more details concerning the Raman scattering technique and the fit procedure, see [98].

Complex Electric Permittivity

The dielectric characterization of the $TbMn_{1-x}Fe_xO_3$ samples was done by calculating the complex electric permittivity ($\varepsilon'(\omega)$ is the real part and $\varepsilon''(\omega)$ the imaginary part) from the measured capacitance and dielectric loss in an HP4284A impedance analyzer at IFIMUP, University of Porto.

The samples were prepared to have large enough parallel areas with sputtered gold electrodes and a constant thickness between these areas. The measurements were carried out in the temperature range from 8 K to 300 K, both in cooling and heating runs, with a temperature rate of 0.5 $K.min^{-1}$, and an accuracy better than 0.1 K. The measurements were performed under an AC electric field of amplitude around 1 $V.cm^{-1}$ in the frequency range from 1 kHz to 1 MHz.

The measured quantities are associated with the complex electric permittivity:

$$\varepsilon = \frac{D(\omega)}{E(\omega)} e^{i\delta} \Leftrightarrow \varepsilon'(\omega) + i\varepsilon''(\omega) = \frac{D(\omega)}{E(\omega)} [cos(\delta) + isin(\delta)] , \tag{2.3}$$

where $C = \frac{D(\omega)}{E(\omega)} \frac{A}{d} = \varepsilon_0 \varepsilon_r(\omega) \frac{A}{d}$, $tg(\delta) = \frac{\varepsilon''(\omega)}{\varepsilon'(\omega)}$, $D(\omega)$ is the electric displacement field, $E(\omega)$ is the electric field, ε_0 is the vacuum permittivity, A is the electrode area, d is the sample thickness, $\varepsilon'(\omega)$ is the real part and $\varepsilon''(\omega)$ the imaginary part of the complex electric permittivity.

Thermally Stimulated Depolarizing Currents

The polar characterization of the $TbMn_{1-x}Fe_xO_3$ was obtained through the measurement of the thermally stimulated depolarizing currents as a function of temperature. For this, a standard short-circuit method was used, with a Keithley 617 electrometer at IFIMUP, University of Porto. In this method, the voltage drop at a reference resistance in parallel with the sample is used to calculate the thermally stimulated depolarizing current. The value of the reference resistance must be 10^1 to 10^2 times lower than that of the sample. The change on electric polarization is obtained by integrating the current in time.

The samples were prepared to have large enough parallel areas with sputtered gold electrodes and a constant thickness between these areas. The measurements were carried out in the temperature range from 8 to 300 K, with a resolution of 0.5 pA, while keeping a fixed temperature rate for each measurement. The sample temperature was measured with an accuracy better than 0.1 K. To study the origin of the measured thermally stimulated depolarizing currents, the temperature rates ranged from 2 to 10 $K.min^{-1}$. For the case of critical phenomena, such as ferroelectricity, the temperature at which changes of the electric polarization are observed

is independent of the temperature rate. For the case of relaxation phenomena, this is not the case. The magnitude of the resistance used was $10^{10}\Omega$. We used this very high resistance in order to have the maximum resolution, as the currents to measure were rather small. The study of thermally stimulated depolarization currents was carried out in heating runs, without applied electric field. A polling electric field was applied with different magnitudes and at different fixed temperatures. Thereafter the sample was cooled down under the polling field to reach dipole alignment. The polling electric field was kept to a maximum of 500 V/cm to avoid induce non-spontaneous phenomena. The temperature dependence of the corresponding polarization was obtained by the time integration of the current density.

Further information concerning the experimental techniques to measure the complex dielectric permittivity and thermally stimulated depolarizing currents refer to [98].

Magnetic Properties

The magnetic properties were studied in similar Quantum Design Superconducting Quantum Interference Devices (SQUID) magnetometers. One at IFIMUP, University do Porto, used in the temperature range from 5 K to 300 K. Another at the Institute of Experimental Physics Slovak Academy of Sciences, in Košice, Slovak Republic, by the group of Marian Mihalik, used in the temperature range from 2 K to 400 K. The resolution in the magnetization measurements is better than 5×10^{-7} emu. The samples used were firmly attached to the SQUID insert, with temperature controlled by liquid helium flux. Detailed information concerning the SQUID magnetometer is available in [98]. The magnetic properties above 400 K were studied in a Quantum Design Physical Properties Measuring System apparatus with installed VSM oven option at the Institute of Experimental Physics Slovak Academy of Sciences, in Košice, Slovak Republic, by the group of Marian Mihalik. The resolution of these measurements is better than 1×10^{-6} emu. For these experiments, bulk polycrystalline samples were used which were directly cleaved from the grown ingots. The samples were fixed to the oven holder by Zircar cement.

The low field temperature dependence of the magnetization was measured in heating runs. The measurements were made in zero-field-cooled (ZFC) and field-cooled conditions (FC), where the applied magnetic field was between 40 and 100 Oe.

Isothermal magnetic hysteresis loops measurements, M(H), were performed for different fixed temperatures, as a function of the applied magnetic field, which varied from -5 to 5 T.

The internal dynamics of the magnetic properties were studied by complex magnetic AC susceptibility measurements. The used driving frequencies varied from 1 to 1000 Hz.

Magnetoelectric Effect

To characterize the magnetoelectric properties, the inverse magnetoelectric effect was measured, i.e. the effect of an applied magnetic field on the electric polarization. This was done using the already described thermally stimulated depolarizing currents under a perpendicularly and constant applied magnetic field. For this, an existing insert with electric contacts for the SQUID magnetometer was used both on one at IFIMUP, University of Porto and another identical at the group of Margarida Godinho, Faculty of Sciences , University of Lisbon. Figure 2.1 depicts a scheme of the sample holder and relative directions of the electric and magnetic fields. A LabView program for the acquisition was made in collaboration with Bernardo Bordalo. In this case, the DC poling tension is limited to 50 V and the applied magnetic field to 5.5 T due to limitations imposed by the SQUID magnetometer.

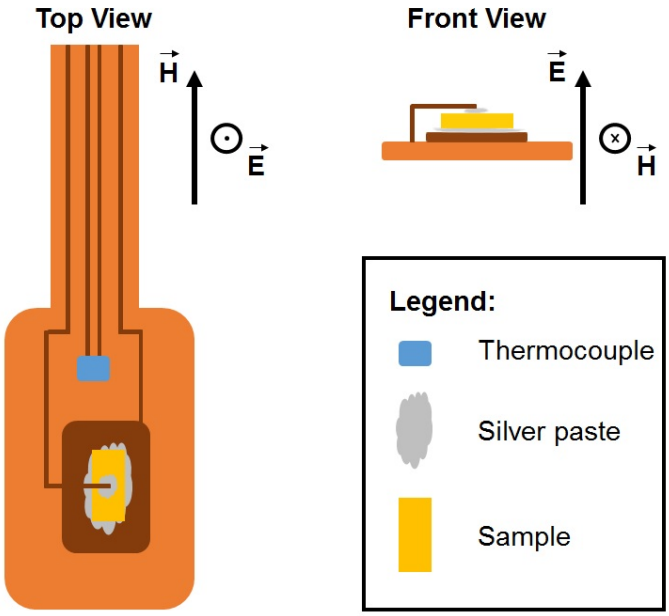

Figure 2.1: Scheme of the configuration used in the SQUID magnetometry to measure the inverse magnetoelectric effect.

Specific Heat

The specific heat was measured by the relaxation method on bulk samples in a Quantum Design Physical Properties Measuring System apparatus at the Institute of Experimental Physics Slovak Academy of Sciences, in Košice, Slovak Republic, by the group of Marian Mihalik. The samples were put in a helium bath and measured in the temperature range from 2 to 300 K.

Neutron Diffraction

To characterize the spin structure of the magnetic phases of $TbMn_{0.98}Fe_{0.02}O_3$ under applied magnetic field we used the single-crystal neutron diffraction technique. This was done at the WISH (wide angle in a single histogram) beam line Target Station 2 of Isis pulsed neutron spallation source of the Rutherford Appleton Laboratory in Oxfordshire, United Kingdom. The beam time was obtained through the Proposal RB1620115.

The magnetic neutron diffraction technique is analogous to x-ray diffraction. The advantage is that, due to the magnetic dipole of the neutrons, it is also sensible to both the magnetic and lattice symmetries. From the available beam lines at Isis, the WISH was chosen as it is a long-wavelength diffractometer. This means that it is most suitable for magnetic diffraction at long d-spacing in magnetic and large unit cell systems, as is the case of the long-range modulated spin structures of $TbMn_{0.98}Fe_{0.02}O_3$.

Cold-neutrons were used for highest resolutions, over a d-spacing range from 0.7-17 Å with a single frame bandwidth of 8 Å. WISH uses pixellated time-of-flight ^{3}He detectors covering scattering angles from 10 to 170 degrees. High-magnetic field magnets were used perpendicular to the neutron beam. The sample was aligned with the a-axis parallel to the applied magnetic field. A schematic view of this alignment is shown in Figure 2.2. However, the used high-magnetic field magnets covered many sections of these detectors, limiting the measurements up to 15 degrees out of plane. More information regarding magnetic neutron diffraction at WISH can be obtained at [99].

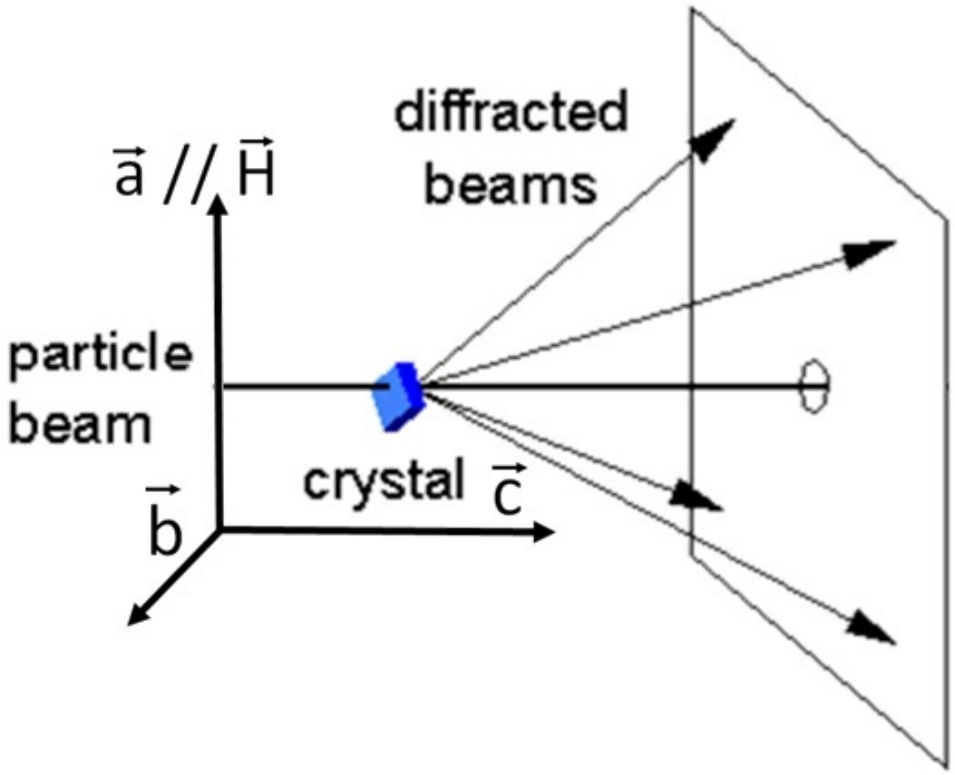

Figure 2.2: Schematic view of the crystal and magnetic field alignment of the neutron diffraction experiments.

Density Functional Theory

The density functional theory (DFT) calculations in Chapter 3 were performed by Rui Mário at IFIMUP, using the Linearized/Augmented Planewave plus local orbital (LAPW+lo) method implemented in WIEN2k [100]. The functional adopted for the exchange correlation interaction was the modified Becke-Johnson (mBJ) [101], because it proves to be more precise in calculating the band gap than LDA and GGA functionals, which are known to underestimate it in semiconductors and insulators. An AFM configuration was assumed to describe reasonably well the PM state and for that a 2x2x2 supercell was constructed. The simulations were converged with a $RK_{max} = 7$ and 36 k points in the irreducible part of the first Brillouin zone.

The DFT calculations in Chapter 4 were performed by Jorge Íñiguez group, within the generalized gradient approximation revised for solids [102], as implemented in the Vienna ab initio simulation package (VASP) [103, 104]. For a better treatment of iron's $3d$ electrons, we used the Hubbard-like correction proposed by Dudarev et al. [105], with $U_{eff} = 4$ eV. The ionic cores were treated within the projection augmented approximation (PAW) [106], and the following electrons were explicitly solved in the simulations: O's $2s^2 2p^4$; Fe's $3p^6 3d^7 4s^1$; $5p^6 5d^1 6s^2$ for Eu, Gd, Tb, and Dy; $5s^2 5p^6 5d^1 6s^2$ for Sm and La. Note that, for the generation of the PAW potentials of the rare-earth species, a 3^+ ionization state was assumed and the remaining $4f$ electrons were considered to be frozen in the ionic core. We explicitly checked in one case ($GdFeO_3$) that this approximation has a very small impact on the phonon frequencies and eigenvectors of interest in this work. Electronic wave functions are described in a basis of plane waves cutoff at 500 eV; reciprocal space integrals in the Brillouin zone of the 20-atom *Pnma* cell were computed in a mesh of $4 \times 3 \times 5$ k points. Structural optimization was performed until residual atomic forces were smaller than 0.01 eV/Å and phonon spectra were computed by the finite difference method.

Part II

Structural Distortions

Chapter 3

Unraveling the role of Jahn-Teller distortion in $R\mathrm{MnO_3}$ at high-pressure

The Jahn-Teller distortion has been referred as an important ingredient for the physical properties of rare-earth manganites under high-pressure. However, despite the intensive research on $R\mathrm{MnO_3}$, namely on the role played by the Jahn-Teller distortion, contradictory results and interpretations were published and, till now, no definitive answer is known [16, 59]. So, the pressure dependence of the Jahn-Teller distortion in $R\mathrm{MnO_3}$ was studied to understand its role in the stabilization of the high-pressure structural phase. In this context, the use of x-ray absorption spectroscopy is crucial, as it is more sensitive to the electronic and geometrical structure around the Mn^{3+} ions than x-ray diffraction [107].

3.1 Experimental data analysis

The x-ray absorption near-edge (XANES) spectra for $RMnO_3$ are shown in Figure 3.1 for $\mathrm{GdMnO_3}$ and $\mathrm{DyMnO_3}$, respectively, at different applied pressures. The ambient pressure value of the K-edge (maximum of the derivative of the spectra) is E_0 = 6552.0 and 6551.6 eV , for $\mathrm{GdMnO_3}$ and $\mathrm{DyMnO_3}$. This small but significant mismatch of 0.4 eV comes from a energy miscalibration at the beamline. Actually, the E_0 parameter is almost pressure independent on the entire range, and we only found a shift below 1 eV at the highest pressures, due to the structural compression. The pre-edge region shows two differentiated structures (see inset of Figure 3.1), as seen in similar compounds at ambient pressure [108]. These structures do not visibly change as pressure is applied. This is in agreement with previous x-ray diffraction and Raman scattering measurements that have shown no evidence for the change of the formal valence of the Mn^{3+} ion [57, 58].

Figures 3.2(a) and (b) show the $k^2\chi(k)$ extended x-ray absorption fine-structure (EXAFS) spectra and the respective $|\chi(R)|$ Fourier Transform for $\mathrm{GdMnO_3}$ and $\mathrm{DyMnO_3}$, recorded at different applied pressures. An example of the fitting $k^2\chi(k)$ and its Fourier transform modulus in real-space based on Equation 2.1 is shown in Figure 3.2(c) for $\mathrm{GdMnO_3}$ at P = 9.5 GPa . From these fits the Δr values were obtained, from which the Mn-O distances calculated, as explained in the previous Chapter. The R-factors of the fits were mostly around 0.02.

3.2 Pressure-dependence of the Jahn-Teller distortion

Figure 3.3(a) depicts the pressure dependence of the three Mn-O bond lengths for $\mathrm{GdMnO_3}$ and $\mathrm{DyMnO_3}$. Below 6 GPa, both Mn-O1 and Mn-$\mathrm{O2_{long}}$ bond lengths decrease in the two compounds, and between 6 and

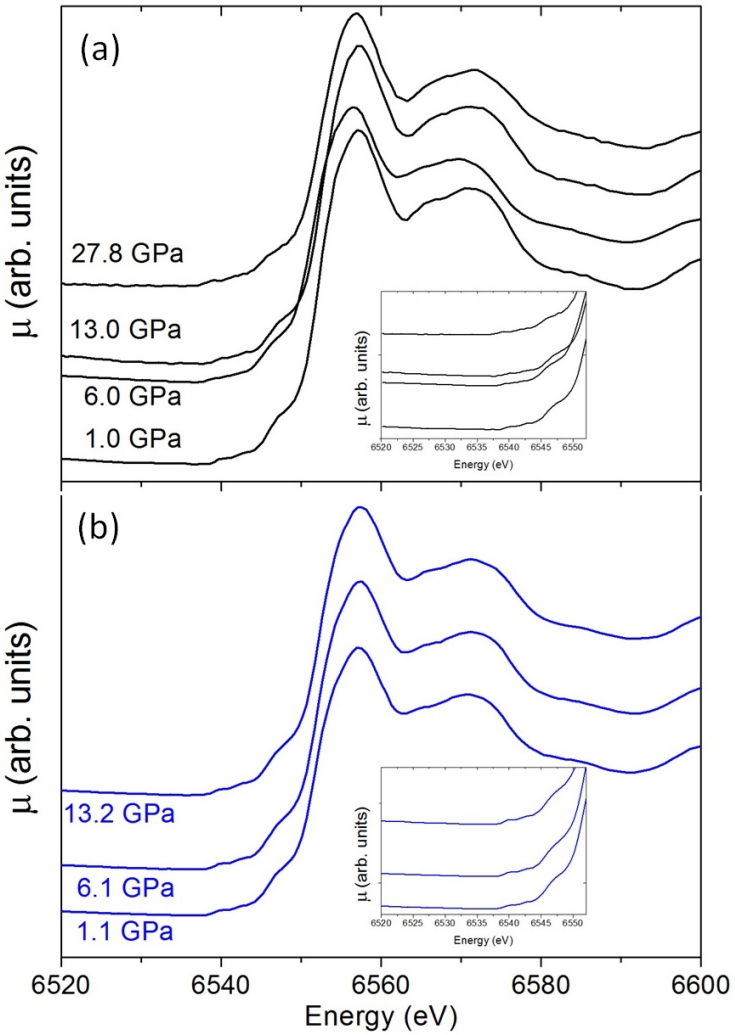

Figure 3.1: Normalized x-ray absorption near-edge spectra at Mn K-edge from (a) $GdMnO_3$ and (b) $DyMnO_3$ at selected pressures. Inset: zoom of the pre-edge region.

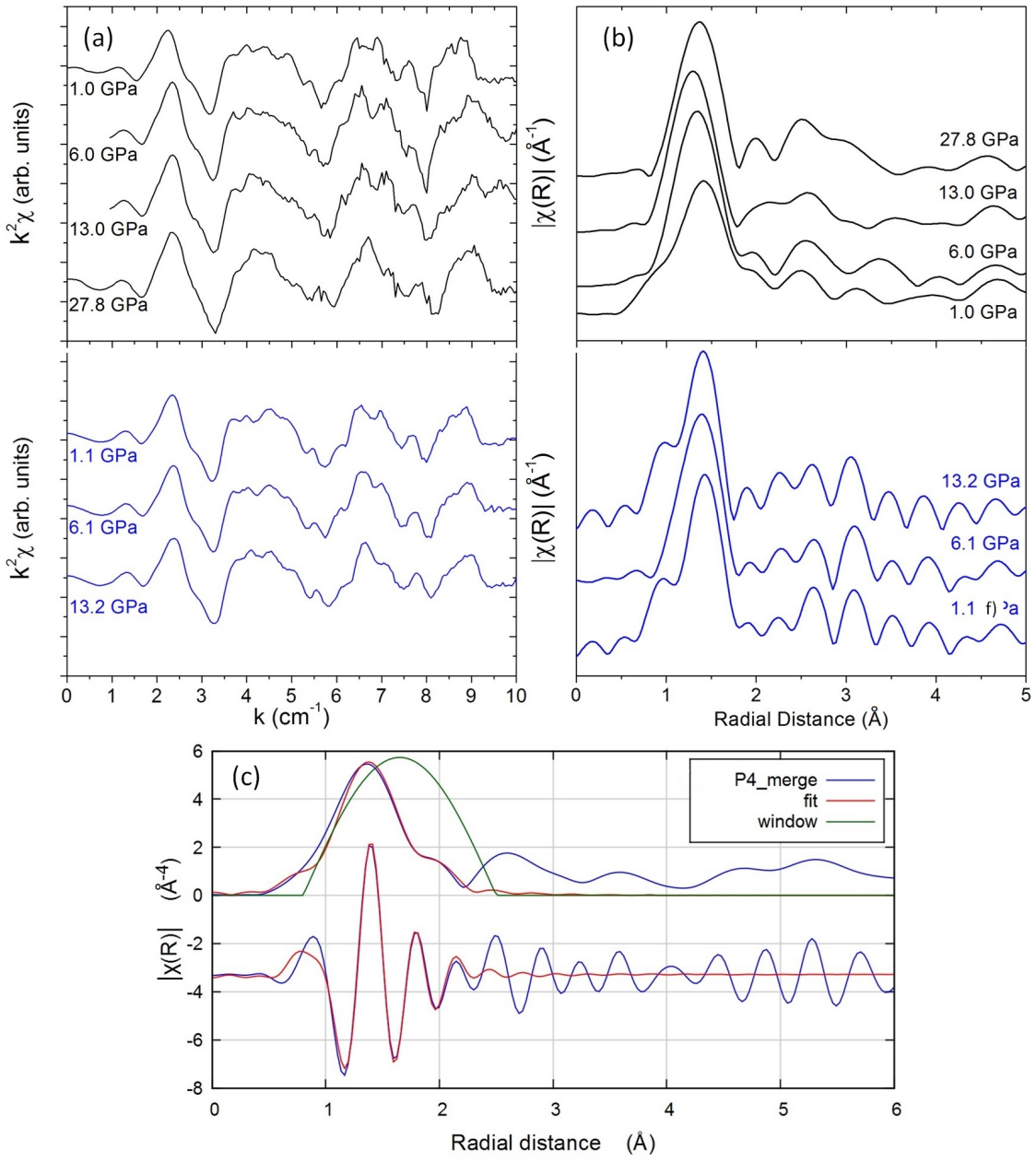

Figure 3.2: Representative $k^2\chi(k)$ extended x-ray absorption fine-structure spectra and respective Fourier Transform of $|\chi(R)|$ for (a) $\mathrm{GdMnO_3}$ and (b) $\mathrm{DyMnO_3}$ (blue), for different applied pressures. (c) Example of spectra fitting in $k^2\chi(k)$ along with its Fourier transform modulus in the real space for $GdMnO_3$ at P = 9.5 GPa.

15 GPa they become pressure independent. Contrarily, the Mn-$O2_{short}$ bond length increases as the pressure increases up to 6 GPa, and above this pressure, both Mn-O1 and Mn-$O2_{short}$ bond lengths take similar values, separated by a magnitude less than the technique resolution (around 0.05 Å), and are pressure independent up to the highest measured pressure of 30 GPa. When the Mn-O1 and Mn-$O2_{short}$ bond lengths take similar values, the algorithm produces error bars with no physical meaning, and thus the estimated error bars from data scattering were used. A possible alternative would be to impose the same value for both bond-lengths (i.e. using only 2 different Δr fit parameters), but we preferred not to introduce that constraint, allowing them to reflect more effectively the experimental data.

The variation of the total distortion of the MnO_6 octahedra is best described using the variance of the distances, expressed as:

$$\Delta d = \frac{1}{6}\sum_{i=1}^{6}\left(\frac{d_i - < d >}{< d >}\right)^2 , \tag{3.1}$$

where d_i are the six MnO_6 distances and $< d >$ is their average value. The pressure variation of Δd is shown in Figure 3.3(b) for both compounds. The results present similar pressure evolution in both compounds. The parameter Δd, associated with the distortion of the MnO_6 octahedra, decreases around 30% between 0 and 6 GPa, while above this pressure, it stabilizes in a constant value of 0.0045 and 0.0055 for $GdMnO_3$ and $DyMnO_3$, respectively.

In order to further confirm this result and discard any possible spurious contributions, we have calculated the Δd parameter using available data from x-ray diffraction at high-pressure from the works of Oliveira *et al.* for $GdMnO_3$ [58] and Chen *et al.* for $TbMnO_3$ [109]. These works present the Mn-O bond lengths up to 15 and 8 GPa, respectively. Due to the high scattering of the the Mn-O bond lengths obtained through the Rietveld structure refinement to the x-ray diffraction patterns in those works, the respective authors did not address the changes in behavior around 6 GPa that we have found. The Δd values presented in Figure 3.3(b), along with the Δd values calculated from data presented in Refs. [58] and [109], are shown in Figure 3.4. A similar pressure dependence of the Δd parameter is clearly observed for the three compounds, though a larger scattering is obtained for the results from x-ray diffraction.

From the results presented to above, a rather similar pressure evolution of the Jahn-Teller distortion is unraveled for all these compounds: as the pressure increases towards 6 GPa, the MnO_6 distortion reduces and keeps a constant value above 6 GPa. It is worth to note that the mismatch between the absolute distances obtained from x-ray diffraction and absorption is common, as the former is most suitable for absolute distances while the latter for relative variations of these distances.

The magnitude of the deformations Δd above 6 GPa, though smaller than that at ambient pressure, is still one order of magnitude higher than the 0.0005 Å found for the same $R FeO_3$ at ambient conditions, where the Jahn-Teller distortion is absent (note that the octahedra deformation in $R FeO_3$ is expected to be independent of applied pressure). With such large values of Δd, we conclude that the $R MnO_3$ system still presents Jahn-Teller distortion above 6 GPa, which was weakened by about a third of its value. This implies that there is no electronic reconfiguration that makes the Jahn-Teller effect disappear. Instead, the applied pressure simply decreases its magnitude at low pressures. Since Δd was found to be constant between 6 GPa up to the highest measured pressure of 30 GPa in $GdMnO_3$, we conclude that the Jahn-Teller effect is maintained up to this pressure, though it is still unclear whether it vanishes for pressures below critical pressure for the insulator to metal phase transition.

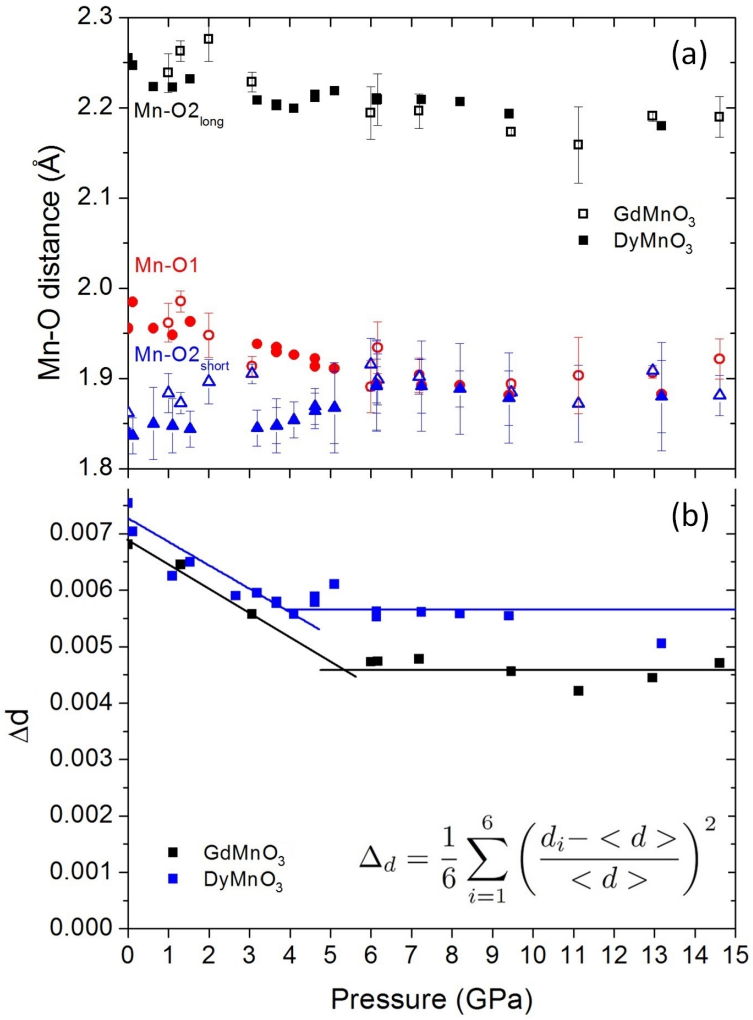

Figure 3.3: (a) Mn-O bond-lengths and (b) Δd parameter of GdMnO$_3$ (open symbols) and DyMnO$_3$ (closed symbols) as a function of applied pressure.

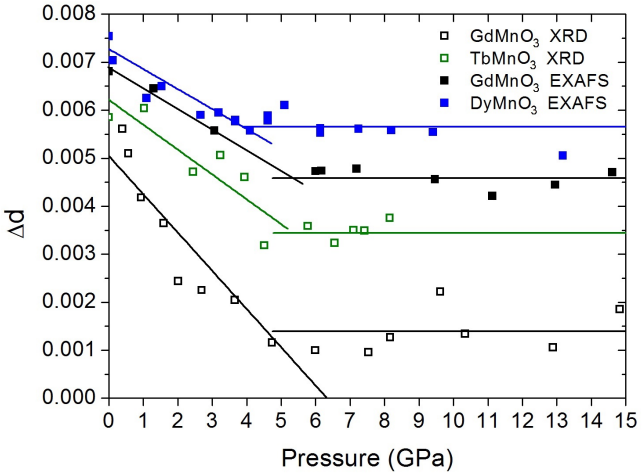

Figure 3.4: Δd parameter of $GdMnO_3$ and $TbMnO_3$ obtained by Rietveld structure refinement of x-ray diffraction patterns, taken from Refs. [58] and [109], as a function of applied pressure, superimposed with data shown in Figure 3.3(b).

3.3 DFT Band Structure Calculations in $GdMnO_3$

To confirm whether there is still a weakened Jahn-Teller distortion above 6 GPa, DFT theoretical calculations were performed by Rui Mário at IFIMUP, to calculate the electronic density of states, wherein the atomic positions of $GdMnO_3$ obtained by x-ray diffraction for the different applied pressures from Oliveira *et al.* work were used [58]. The results of the Mn^{3+} ion $3d$ e_g-orbitals are shown in Figure 3.5. Close to room pressure (Figure 3.5(a)), the obtained result is the expected one. The band structure presents the signature of the orbital ordering due to the Jahn-Teller distortion, causing the d_{z^2}-orbital to be completely filled and the $d_{x^2y^2}$-orbital completely empty. The calculations performed for the structures above 6 GPa, always present the same signature of the orbital ordering due to the Jahn-Teller distortion on the obtained band structure. Figure 3.5(b) shows a representative result obtained at 10.3 GPa. It can be noticed that, as pressure increases from 0.4 to 10.3 GPa, the energy gap between these e_g-orbitals decreases from 1.8 eV to only 0.75 eV. This outcome confirms the reduction of the MnO_6 deformation, which can be associated with the reduction of the Jahn-Teller distortion magnitude referred to above.

3.4 Summary

We have demonstrated that the Jahn-Teller distortion is steeply weakened with applied pressure, up to 6 GPa. Above 6 GPa, the magnitude of the Jahn-Teller distortion becomes constant and persists up to 30 GPa. Moreover, such behavior is apparently common to $RMnO_3$, with R = Dy, Tb and Gd.

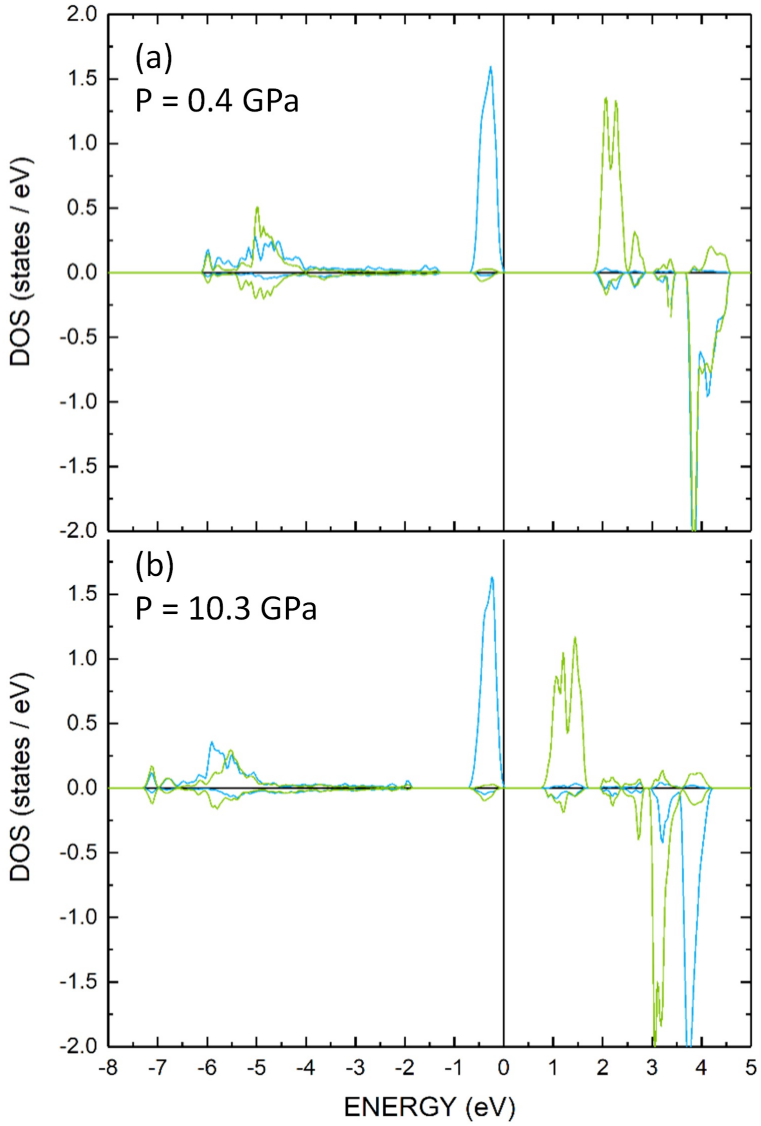

Figure 3.5: Density of states of e_g-orbitals d_{z^2} (blue) $d_{x^2y^2}$ (green) and as a function of energy for GdMnO$_3$ at (a) 0.4 GPa and (b) 10.3 GPa. The d_{z^2}-orbital is filled while the $d_{x^2y^2}$-orbital is empty, with an electronic band gap of 1.8 and 0.75 eV at 0.4 and 10.3 GPa, respectively.

Chapter 4

Lattice Dynamics of $R\mathrm{FeO_3}$

The *Pnma* structure of the rare-earth ferrites is long known by x-ray diffraction [32]. Yet, for structural studies under external parameters, such as temperature or hydrostatic pressure, the x-ray diffraction, carried out even in synchrotrons, is usually unsuitable to follow the oxygen positions, due to their low scattering cross section. This is an important drawback since the oxygens positions are crucial to determine the tilt angles, which affect the magnetic interactions and thus their physical properties. In order to circumvent this handicap, is highly appropriated to face the structural data with those obtained using Raman scattering.

It is a well-known that Raman scattering is able to follow tilt-driven soft-mode phase transitions [110–112], and to investigate lattice distortions, in particular minor changes in octahedra distortions [30, 113–115]. Moreover, Raman scattering is suitable for investigating spin-phonon coupling [116–120]. Thus, by combining Raman scattering and x-ray diffraction, a deeper understanding of the underlying mechanisms driving the physical properties of the $R\mathrm{FeO_3}$ series will be provided. This objective will be better reached whenever it can be guaranteed that this investigation relies on thorough reference spectra, solid knowledge of the relations between structural distortions and phonons, and on a proper band assignment of vibrational bands in terms of symmetry and atomic displacement patterns.

This Chapter embraces the investigation carried out both experimentally and theoretically on a set of rare-earth ferrites proposing a consolidated view of our results along with available literature data on other members of the series. The results obtained will provide new insights into the relations among structural order parameters, associated phonon frequencies, and steric effects driven by the R-cation. Furthermore, the outcomes of this Chapter will be used as basis for the following ones, where the pressure-dependence of the structural distortions and the temperature-dependent spin-phonon coupling are addressed.

4.1 Structural properties of the $R\mathrm{FeO_3}$

In the rare-earth ferrites series, the size of the rare-earth impacts on the distortions of the structure, as measured for example by the tilt angles or the strains, which can be tuned by R-cation chemical substitution. At room conditions, the octahedral rotations are reliably calculated from atomic positions following the formalism given in Ref. [121]. Marezio *et al.* obtained these atomic positions by the Rietveld structure refinement to the respective x-ray diffraction patterns [32, 122]. Table 4.1 summarizes the structural characteristics of all members of the $R\mathrm{FeO_3}$ family. Some of these characteristics were already shown in Figures 1.6, 1.7 and 1.8 of Chapter 1. Figure 4.1 presents the ionic radius dependence of the amplitudes of the symmetry-adapted mode distortions, calculated from the atomic positions already available in the literature, using the Amplimodes tool of the Bilbao Crystallographic Server [22, 123]. This is a more practical alternative to view the structural distortions evolution in the $R\mathrm{FeO_3}$ series. The R4+ and M3+ distortions, associated with the tilts, are the

	r_R	a (Å)	b (Å)	c (Å)	V (Å^3)	t	ϕ or $[010]_{pc}$ (°)	θ or $[101]_{pc}$ (°)
$LaFeO_3$	1.160	5.563	7.867	5.553	243.022	0.934	7.3	12.2
$PrFeO_3$	1.126	5.578	7.786	5.482	238.085	0.921	9.6	13.6
$NdFeO_3$	1.109	5.584	7.768	5.453	236.532	0.915	10.0	14.5
$SmFeO_3$	1.079	5.584	7.768	5.400	234.233	0.904	11.2	15.6
$EuFeO_3$	1.066	5.606	7.685	5.372	231.437	0.899	11.6	16.0
$GdFeO_3$	1.053	5.611	7.669	5.349	230.172	0.894	11.9	16.2
$TbFeO_3$	1.040	5.602	7.623	5.236	227.442	0889	12.1	16.9
$DyFeO_3$	1.027	5.598	7.623	5.302	226.255	0.884	12.6	17.3
$HoFeO_3$	10.15	5.598	7.602	5.278	224.611	0.880	12.7	17.7
$ErFeO_3$	1.004	5.582	7.584	5.263	222.803	0.876	12.9	18.2
$TmFeO_3$	0.994	5.576	7.584	5.251	222.056	0.872	12.9	18.6
$YbFeO_3$	0.985	5.557	7.570	5.233	220.134	0.869	13.4	19.0
$LuFeO_3$	0.977	5.547	5.565	5.213	218.753	0.866	13.2	19.5

Table 4.1: Structural characteristics of RFeO$_3$ samples: R ionic radii (r_R values given in an eightfold coordination [82], lattice parameters, tolerance factor (t) and octahedra tilt angles (ϕ or $[010]_{pc}$, θ or $[101]_{pc}$) calculated from the atomic coordinates. The data for the crystal structures are from Refs. [32, 122].

largest. The X5+ and R5+ distortions, associated with the rare-earth shifts, are also significant, while the M2+ distortion, associated with the FeO_6 deformation, has the smallest amplitude. The sketches of these distortion modes was presented in Figure 1.4. All these distortions increase linearly as the ionic radius decreases. Only the case of $LaFeO_3$ deviates from this linear behavior, as it is very close to the cubic symmetry (t closest to 1).

When the refinement of the atomic coordinates is not possible on studies under external parameters, as it is the case of hydrostatic pressure, the Amplimodes refinement of the diffraction patterns is also suitable for the symmetry conditions that it establishes in the atomic coordinates [22, 123]. During the Amplimodes refinement, instead of allowing the atomic positions to vary in the 3D space without restriction to find the global minimum, they are described as the sum of the symmetry-adapted distortions, enabling the structure refinement in these particular cases [123]. In the following Chapter we will use this kind of refinement for a high-pressure structural characterization.

It is also possible to estimate the tilt angles simply from the lattice parameters, if the oxygen octahedra are not much distorted [20, 121]. This estimation was introduced by Megaw *et al.* using the following equations [20, 121]:

$$\theta = cos^{-1}\left(\frac{c}{a}\right) \ , \ \phi = cos^{-1}\left(\frac{\sqrt{2}c}{b}\right) \ , \tag{4.1}$$

where θ stands for the anti-phase tilt angle around $[101]_{pc}$ and ϕ stands for the in-phase tilt angle around $[010]_{pc}$. These formulae assume that the change of the unit cell volume is originated by the octahedral tilting, and no significant additional octahedra distortion occurs [20, 121]. For example, they are not applicable to the RMnO$_3$ due to the Jahn-Teller distortion. Moreover, this formulae are more suitable for larger tilts than for smaller tilts, where other contributions to the change of the unit cell volume may be comparable to the contribution from the tilts [20, 121]. Therefore, for RFeO$_3$ compounds, the estimation using Megaw's formula is better for the anti-phase tilt around the $[101]_{pc}$ axis than for the in-phase tilt around $[010]_{pc}$ axis, and for smaller tolerance factors than for larger ones. The reliability of this approach was assessed by comparing the results to the values of the tilt angles obtained at room conditions using the Megaw' formula with their reference values obtained from the refinement of the atomic positions (see Figure 4.1(b)). This procedure will be also used to estimate the tilt evolution on the RFeO$_3$ under pressure on the next Chapter.

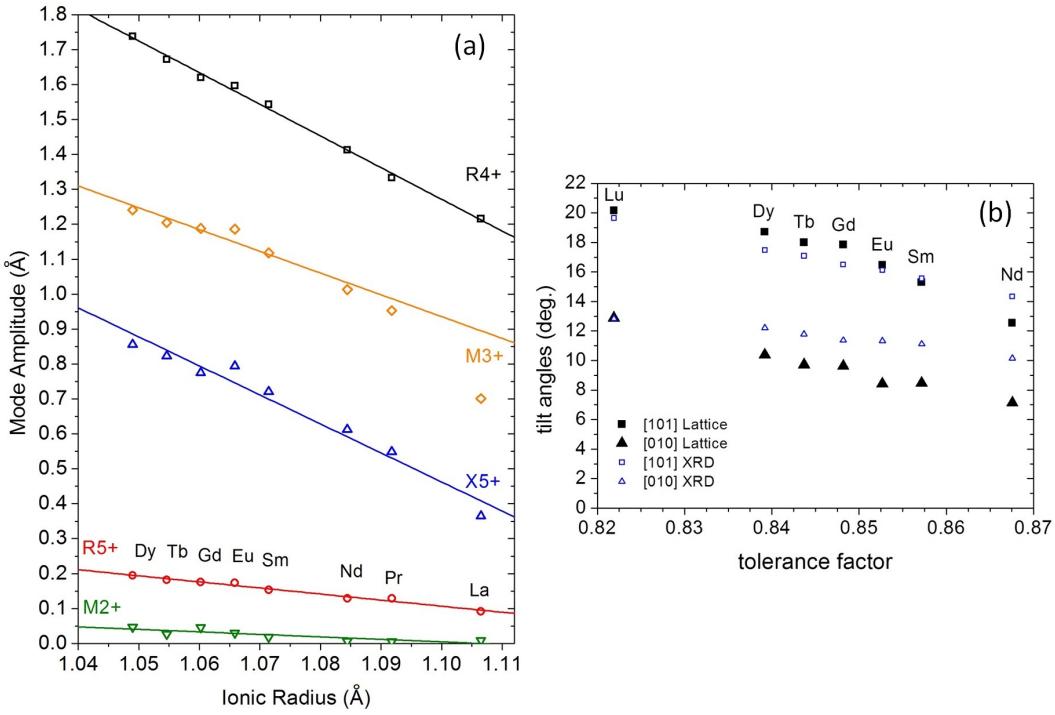

Figure 4.1: Variation of the distortion mode amplitudes as a function of the R^{3+} ionic radius. (b) Comparison of tilt angles estimated from the lattice parameters (closed symbols) with the values obtained from the atomic positions (open symbols).

4.2 Raman spectra and mode assignment

The orthorhombic *Pnma* structure gives rise to 24 Raman-active vibrational modes, as explained in Chapter 2 [95]. Figure 4.2 shows the unpolarized Raman spectra of six rare-earth ferrites RFeO$_3$ (R = Sm, Eu, Gd, Tb, Dy), all measured at 10 K, in order to reduce thermal broadening, thus improving the band identification and reducing the thermal expansion effects for the comparison with the DFT calculations carried out at 0 K. As the samples are all magnetic below 600 K, spin-phonon couplings might arise for some phonons. However, these effects are typically small (below 15 cm^{-1} as we will see in Chapter 6), not preventing the correct mode identification. Thanks to well-defined spectra, we identify between 18 and 21 vibration bands, depending on the compound, summarized in Table 4.2. The remaining predicted modes are either masked by band overlap or their intensity is below the detection limit. The Raman spectra of SmFeO$_3$, EuFeO$_3$, GdFeO$_3$, TbFeO$_3$ and DyFeO$_3$ present a similar overall shape which allows us to follow the evolution of particular bands throughout the series.

In order to go further in the mode assignment, Mads Weber performed a polarized Raman scattering study of SmFeO$_3$ oriented single crystals at room conditions [31]. Polarized Raman scattering on well-oriented single crystals allows identifying the symmetries of phonon bands. In the following, we use the previously defined Porto's notation with X//a, Y//b and Z//c. Figure 4.3(a) shows the Raman spectra for A_g configuration modes, while spectra exhibiting B_{1g}, B_{2g}, or B_{3g} modes are presented in Figure 4.3(b). In total, we identify all the seven A_g modes, six out of seven B_{2g} modes, and four out of five B_{1g} and B_{3g} modes (see Table 4.2). In a next step, DFT calculations were performed by the group of Íñiguez to assign the atomic motions to the observed Raman bands, for all measured rare-earth ferrites, in order to confirm the mode symmetries and associate a vibrational pattern to each mode [31]. A summary of all theoretical and experimental band frequencies with their symmetry and characteristic atomic motions are given in Table 4.2. The calculated

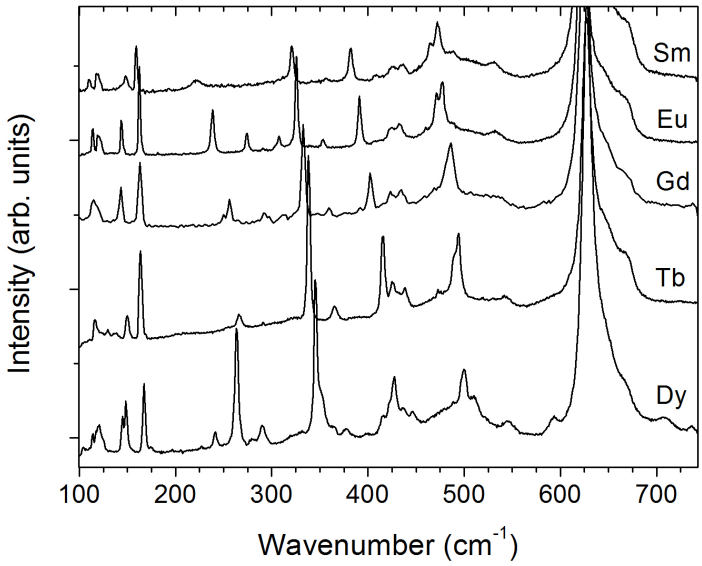

Figure 4.2: Raman spectra at 10 K of several RFeO$_3$ (R = Sm, Eu, Gd, Tb, Dy).

frequencies are in very good agreement with our experimental values and the continuous evolution of the spectral signature.

The vibration modes below 200 cm^{-1} are mainly characterized by displacements of the heavy rare-earth ions. Above 300 cm^{-1}, motions of the oxygen ions dominate, and in the intermediate frequency range (200 to 300 cm^{-1}) vibration patterns involve both ions. Note that iron ions occupy centers of inversion in the *Pnma* structure and, therefore, vibrations involving it are not Raman active. The band between 600 and 650 cm^{-1} in Figure 4.3(a) shows a peculiar behavior and needs a specific discussion. First, as can be seen in Figure 4.2, its frequency seems to be independent of the rare-earth. Besides, it shows a strong asymmetry. Figure 4.3 shows that these bands appear with very low intensity in crossed polarization but are strongly visible in parallel configuration, which would point to an A_g symmetry. However, as can be seen in Table 4.2, the calculations predict two bands of B_{2g} and B_{3g} symmetry in this region, but no A_g Raman mode, and all A_g modes are already conclusively attributed. We therefore conclude that this band is not a first-order Raman mode. A precise interpretation for this band is beyond the scope of this thesis, but we note that similar features have been described for other perovskite oxides, with unclear assignments and conflicting reports. As an example, Iliev *et al.* discussed this issue for $LaCrO_3$ and demonstrated that its intensity can be reduced by annealing the sample in vacuum [124]. Therefore it seems likely that it is associated with chemical defects of the lattice [124]. Nevertheless, no consequences arising from such defects were detected on the structural and physical properties.

The dependence of the Raman wavenumbers on the rare-earth ionic radius is presented in Figure 4.4. Overall, Raman bands shift to lower frequencies with increasing r_R , which naturally correlates with the volume increase and, therefore, of the R-O bond lengths. It can be seen that the frequencies of the Raman modes are differently sensitive to the change of rare-earth. The Raman modes associated with the rare-earths motions are "hard modes", in the sense that their wavenumber only slightly decreases as the ionic radius increases. The Raman rotation modes associated with the tilt angles are the "soft modes", as they present the largest wavenumber shift. This is usual when the vibrational displacement is directly associated with the order parameter, and are commonly used as structural probes.

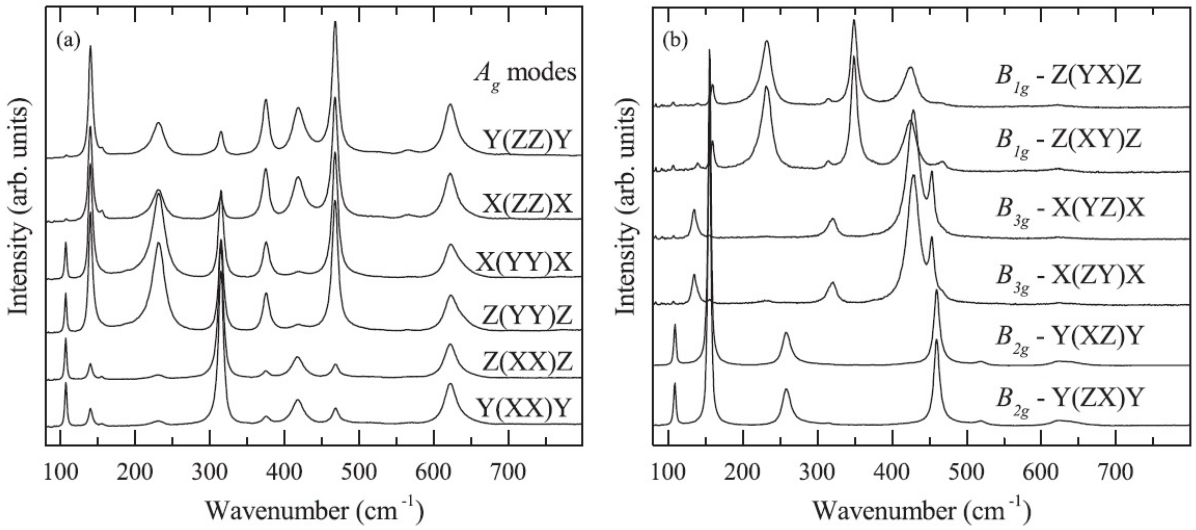

Figure 4.3: Polarized Raman spectra of a $SmFeO_3$ crystal at ambient conditions, performed by Mads Weber. The measurement configurations are given in Porto's notation, in (a) for the vibration modes of A_g symmetry and in (b) for the vibration modes of B_{1g}, B_{2g}, and B_{3g} symmetries. X, Y, and Z correspond to the orthorhombic axes a, b and c, respectively, in the $Pnma$ space group.

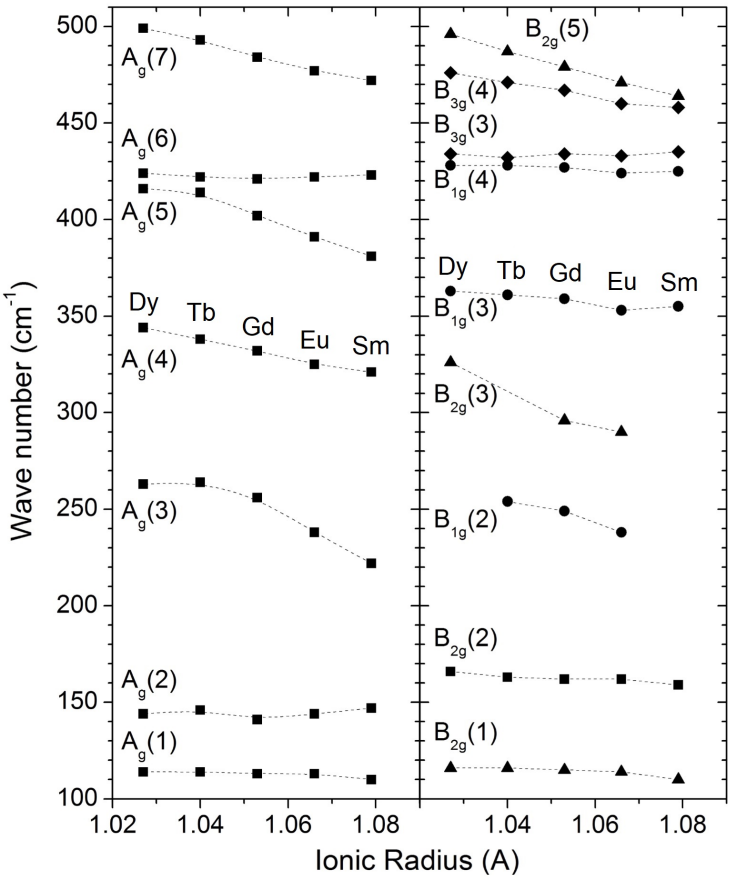

Figure 4.4: Wavenumber of the Raman-active modes RFeO$_3$ as a function of the rare-earth ionic radius. All lines are guides to the eye.

	$SmFeO_3$			$EuFeO_3$			$GdFeO_3$			$TbFeO_3$			$DyFeO_3$			
Symm.	10 K	calc.	300 K	10 K	calc.	300 K	10 K	calc.	300 K	10 K	calc.	300 K	10 K	calc.	300 K	Main atomic motion
A_g (1)	110	109		113	112	112	113	111		114	112	114	114	112	118	R(x), in-phase in xz, out-of-phase in y
A_g (2)	147	138	139	144	140	143	141	137	140	146	136	143	144	135	143	R(z), out-of-phase
A_g (3)	222	244	230	238	252	239	256	255		264	259	260	263	262	265	$[010]_{pc}$ FeO_6 rotation, in-phase
A_g (4)	321	320	314	325	325	322	332	330	326	338	330	334	344	332	340	O1 xz-plane
A_g (5)	381	383	374	391	397	387	402	405	395	414	410	410	424	422	422	$[101]_{pc}$ FeO_6 rotation, in-phase
A_g (6)	423	413	418	422	414	423	421	416	420	422	416		416	415		Fe-O2 stretching, in-phase
A_g (7)	472	468	467	477	476		484	480		493	484		499	490		O1-Fe-O2 scissor-like bending
B_{1g} (1)		151	159		149			143			139			135		R(y) in-phase in xz, out-of-phase in y
B_{1g} (2)		233	232	238	243	272	249	244	246	254	248			250		$[010]_{pc}$ FeO_6 rotation, out-of-phase
B_{1g} (3)	355	352	349	353	356	352	359	356	353	361	356	360	363	359	361	$[101]_{pc}$ FeO_6 rotation, out-of-phase
B_{1g} (4)	425	422	424	424	424		427	426	426	428	425		428	427	429	Fe-O2 stretching, out-of-phase
B_{1g} (5)		594			597			595			592		594	593		Fe-O1 stretching
B_{2g} (1)	110	109	108	114	111	114	115	109	111	116	109	118	116	109	114	R(z), in-phase in xz, out-of-phase in y
B_{2g} (2)	159	159	155	162	163	160	162	161	160	163	161	162	166	161	164	R(x), out-of-phase
B_{2g} (3)		278	259	290	291		296	299	289		305	300	326	311	316	$[101]_{pc}$ FeO_6 rotation, in-phase
B_{2g} (4)		346			348			349			349			351		O1 xz-plane
B_{2g} (5)	464	460	459	471	469	472	479	474	476	487	478	488	496	482	494	O1-Fe-O2 scissor-like bending
B_{2g} (6)	530	513	517	531	521	524	438	528		542	528	540	544	534	544	O2-Fe-O2 scissor-like bending, in-phase
B_{2g} (7)	623	610	622	623	613	626	624	612	623	627	611	627	627	612	630	Fe-O2 stretching, in-phase
B_{3g} (1)	146	135	134		134			129		129	126		125	123		R(y) out-of-phase in xz, y
B_{3g} (2)		313	319		315			312			311			311		O1-Fe-O2 in-phase
B_{3g} (3)	435	424	428	433	424	430	434	426		432	422	430	434	424		FeO_6 octahedra squeezing in y
B_{3g} (4)	458	447	453	460	452		467	455	456	471	457	471	476	460	474	O2-Fe-O2 scissor-like bending, out-of-phase
B_{3g} (5)		641			643			640			637			637		FeO_6 breathing

Table 4.2: Experimental and theoretical band positions, the corresponding symmetry assignment and main atomic motions of the observed Raman modes in $R$$FeO_3$. The main atomic motions are identified from DFT calculations performed by Íñiguez group.

4.3 Raman-active phonons vs ionic radii and octahedra tilt angles

The ionic radius dependence of the Raman octahedra rotation modes associated with the tilt angles is understood in the context of the structural instabilities in the *Pnma* structure. In the framework of Landau theory, the two octahedra tilts represent the two principal order parameters for a phase transition from the high-symmetry parent cubic perovskite phase. To obtain a quantitative relation between these quantitites, we may follow the model with a Landau-like potential connecting all the relevant ingredients, developed by the group of Mael Guennou [31]. Let Q denote the relevant structural order parameter, corresponding to either anti-phase or in-phase FeO$_6$ tilts in the case of rare-earth ferrites. Also, let η be the isotropic strain of the material, with $Q = \eta = 0$ corresponding to the ideal cubic perovskite. Then, the Landau free energy is written as [31]:

$$\triangle F\left(Q,\eta\right) = \frac{1}{2}A'\left(T - T_t\right)Q^2 + \frac{1}{4}BQ^4 + \frac{1}{2}C\eta^2 + \gamma\eta Q^2\,, \tag{4.2}$$

where A' and B define the potential well associated to the Q instability, and we have assumed the simplest temperature (T) dependence of the quadratic term as customarily done in Landau theory. We want to focus on the behavior of the material at temperatures well below the structural transition between the assumed prototype high-temperature cubic phase and the known orthorhombic phase. This means that at room-temperature, and below, the tilt order parameters are already saturated. From this model, they arrive to the result for the associated soft-mode frequency [31]:

$$\omega = \sqrt{\frac{2B}{m}}Q_{eq}\,, \tag{4.3}$$

where m is a characteristic mass of the lattice mode associated with the Q order parameter and Q_{eq} is its equilibrium value. For the FeO$_6$ octahedra tilts cases, this reduces to the mass of the oxygen atom. Thus, a linear relation between order parameter Q and the corresponding soft-mode frequency ω is expected [31].

In order to apply this relation to the rare-earth ferrites family, the identification of the soft modes is crucial. An order parameter may give rise to several soft modes which do not necessarily need to be Raman active. However, using the group theoretical formalism of Landau theory, Birman [128] and Shigenari [129] demonstrated that one of the soft modes associated with an order parameter has a Raman-active A_g symmetry. In the *Pnma* structure it is therefore common to focus on the A_g soft-modes. From the DFT calculations leading to the assignment of the bands to the respective vibrational pattern (see Table 4.2), we find that $A_g(3)$ and $A_g(5)$ are the soft-modes corresponding to the order parameters of the *Pnma* structure representing the octahedra tilts around the $[010]_{\mathrm{pc}}$ (in-phase) and the $[101]_{\mathrm{pc}}$ (anti-phase) axes, respectively denoted by $Q_{[010]_{\mathrm{pc}}}$ and $Q_{[101]_{\mathrm{pc}}}$. The assignment of the $A_g(3)$ as a soft-mode is at variance with earlier work by Todorov and co-workers [30] and underlines the importance of precise calculations to gain full understanding of the experimental findings.

Figure 4.5 presents the evolution of the soft-modes $A_g(3)$ and $A_g(5)$ against the corresponding tilt angle. For completeness and in order to test the general validity of this model, we extend our graph with literature data to rare-earth ferrites with R = Lu, Tm, Er, Ho, Nd, and La [45, 125–127, 130]. The tilt angle dependencies of these modes wavenumbers show the expected linear relation between the vibrational frequencies and the tilt angles of the RFeO$_3$. This adds further support to the proposed soft-mode-like relation of tilt mode wavenumber and size of the rare earth, not only for the rare-earth orthoferrites, but also for other families where this behavior has been experimentally verified: orthomanganites [113], orthochromates [114], orthoscandates [115], among others [30]. However, at variance with these previous experimental data, our work on rarre-earth ferrites shows two additional features that have to be commented, namely the tilt angle dependencies of these modes wavenumbers. Indeed, the octahedral tilting angles and soft-mode wavenumbers do not present the

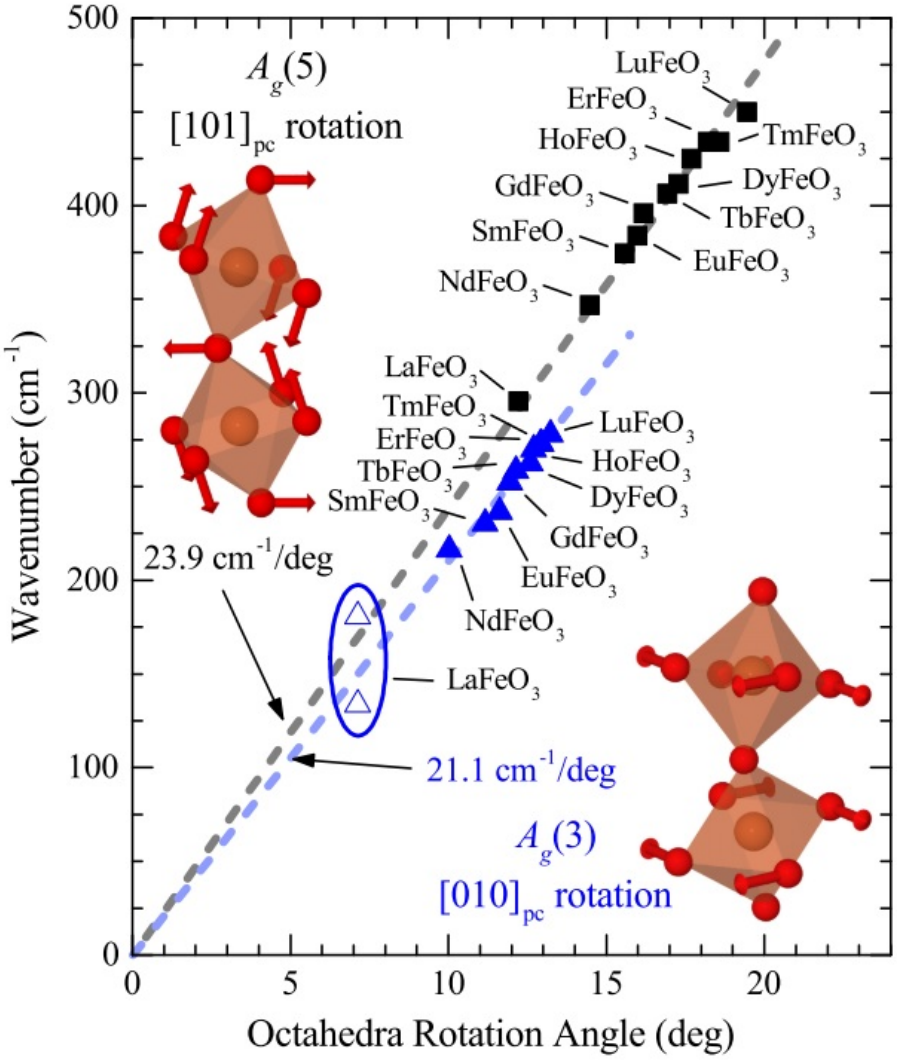

Figure 4.5: RFeO$_3$ soft-mode wavenumbers at ambient conditions as a function of octahedra tilt angles for the $A_g(3)$ and $A_g(5)$ modes. Data from this work are complemented by literature data for LaFeO$_3$ [31], NdFeO$_3$ [125], HoFeO$_3$ and TmFeO$_3$ [45], ErFeO$_3$ [126], and LuFeO$_3$ [127]. The oval and the open symbols point out the mode mixing region of the $A_g(2)$ and $A_g(3)$ modes for LaFeO$_3$, as discussed in the text.

same scaling for the different order parameters. The tilt $Q_{[010]_{pc}}$ about $[010]_{pc}$ reveals a scaling factor of 21.1 cm^{-1}/deg whereas the slope of the tilt $Q_{[101]_{pc}}$ about $[101]_{pc}$ gives 23.9 cm^{-1}/deg. This is expected as the two soft modes are associated with two independent order parameters. The derived relation needs to be separately considered for each of the relevant order parameters (in-phase and anti-phase FeO_6 tilts in our case), and thus it is expected that the values of the coefficients in the Landau potential will be the different for independent order parameters. However, this difference was never pointed out in previous investigations [30, 113–115], probably due to a combination of factors including experimental difficulties in mode assignment and wavenumber determination, scattered data from a more limited number of compounds, and possibly differences in scaling factors coincidentally too small to be resolved experimentally. We realize that a careful (re)investigation of the other series will reveal this difference.

It is still worth to comment on the special case of $LaFeO_3$. For $LaFeO_3$, no A_g Raman mode actually follows the scaling given by the other members of the series. Instead, the $A_g(2)$ and $A_g(3)$ modes, plotted as open triangles in Figure 4.5, fall below and above the scaling line, respectively. On the other hand, the band positions in $LaFeO_3$ differ significantly from the other rare-earth ferrites and do not seem to follow from a continuous evolution of the other spectra. For the smaller cations, the $A_g(2)$ mode is dominated by R^{3+} displacements while $A_g(3)$ is dominated by octahedral rotations, having very distinguishable atomic displacement patterns. In contrast, in $LaFeO_3$, the two modes have significant contributions from both La^{3+} displacement and octahedral rotations. It is therefore no longer possible to identify any of them as the soft mode of interest associated with octahedral tilts only. The soft-mode wavenumber for a hypothetical unmixed state would lie between the two positions. This in turn enables us to understand why the Raman spectrum of $LaFeO_3$ is significantly different as a whole from the others members of the series, since the mode coupling will affect band positions and intensities. This behavior reported by Iliev *et al.* in manganites [113], and also found in the (La, Sm)CrO_3 solid solutions [131], is probably a general phenomenon occurring in orthorhombic *Pnma* perovskites in the limit of small tilt angles, where distortions of the octahedra have to be taken into account [132].

4.4 Summary

We have presented a Raman scattering study of a series of RFeO$_3$ (R = Sm, Eu, Gd, Tb, Dy). A symmetry assignment of the observed modes has been presented on the basis of a single-crystal study of $SmFeO_3$, DFT calculations, and by taking advantage of the continuous changes in the Raman spectra across the whole RFeO$_3$ series. This careful assignment has allowed us to associate most of the vibration modes to their vibrational pattern and symmetries. We have then followed the structural evolution across the series, and namely shown that the $A_g(3)$ and $A_g(5)$ Raman modes are the soft modes of A_g symmetry that are proportional to the in-phase and anti-phase octahedral tilts order parameters, respectively. Furthermore, this proportionality is not the same for both tilts, being 21.1 cm^{-1}/deg for the in-phase tilt and 23.9 cm^{-1}/deg for the anti-phase tilt. This work provides reference data for structural investigation of the RFeO$_3$ series and will be helpful in the following Chapters, as well as, in further studies of phenomena in rare-earth ferrites including structural instabilities, possible ferroelectricity, multiferroicity and rare-earth magnetism at low temperature.

Chapter 5

Pressure evolution of elementary distortions in $R\mathrm{FeO_3}$

Hydrostatic pressure has been increasingly considered in the study of critical phenomena and phase transitions because it allows to modify the inter-atomic distances and promoting distortions to change the interactions to a greater extent than any other external parameters. Among the most studied systems under pressure, the $AB\mathrm{O_3}$ perovskites have been the focus of intense research under pressure, because of their remarkable pressure-induced phase transition sequence, many of them undergoing many structural transformations accompanied by changes on the magnetic, transport and ferroelectric properties [57, 133, 134]. In order to explain and predict the behavior of perovskites under high-pressure, several models and rules have been developed. Some of them are empirical laws, while other are based on theoretical models or DFT calculations. $R\mathrm{FeO_3}$ are particularly interesting because they show (or are predicted to show) different behavior across the series, with a cross-over occurring at definite values of the tilt angles [60].

In this work we carried out high-pressure studies on the $\mathrm{TbFeO_3}$ and $\mathrm{SmFeO_3}$ compounds by synchrotron x-ray diffraction and on from $\mathrm{DyFeO_3}$ to $\mathrm{NdFeO_3}$ by Raman scattering. From the experimental results obtained, we provide a description of how the main structural distortions evolve with pressure as a function of ionic radius, and determine the critical pressure of the isostructural insulator-to-metal transition found in the rare-earth ferrites.

5.1 Experimental results of XRD at high-pressure

Figure 5.1 shows representative x-ray diffraction patterns of $\mathrm{SmFeO_3}$ and $\mathrm{TbFeO_3}$, recorded at different pressures. Figure 5.2 presents the pressure dependence of the pseudocubic lattice parameters and the pseudocubic volume calculated from the primitive cell of the *Pnma* structure of both compounds. These values can be found in Table 5.1.

As the pressure increases, the pseudocubic lattice parameters monotonously decrease and suddenly down shift at 41 GPa for $\mathrm{SmFeO_3}$, and at 46 GPa for $\mathrm{TbFeO_3}$; as a consequence, the pseudocubic volume is reduced 4.3% and 6.6%, respectively. These values provide a clear evidence for a pressure-induced structural phase transition, which we will discuss in detail in the last Section of this Chapter. On further pressure increase, the normal pressure evolution of the pseudocubic lattice parameters is again observed. The symmetry of both low and high pressure phases of $\mathrm{SmFeO_3}$ and $\mathrm{TbFeO_3}$ is found to be *Pnma*. This symmetry has been reported for the high-pressure phase of other rare-earth ferrites [48, 49].

In the low pressure phase, the pressure dependence of the pseudocubic cell volume of $\mathrm{TbFeO_3}$ and $\mathrm{SmFeO_3}$

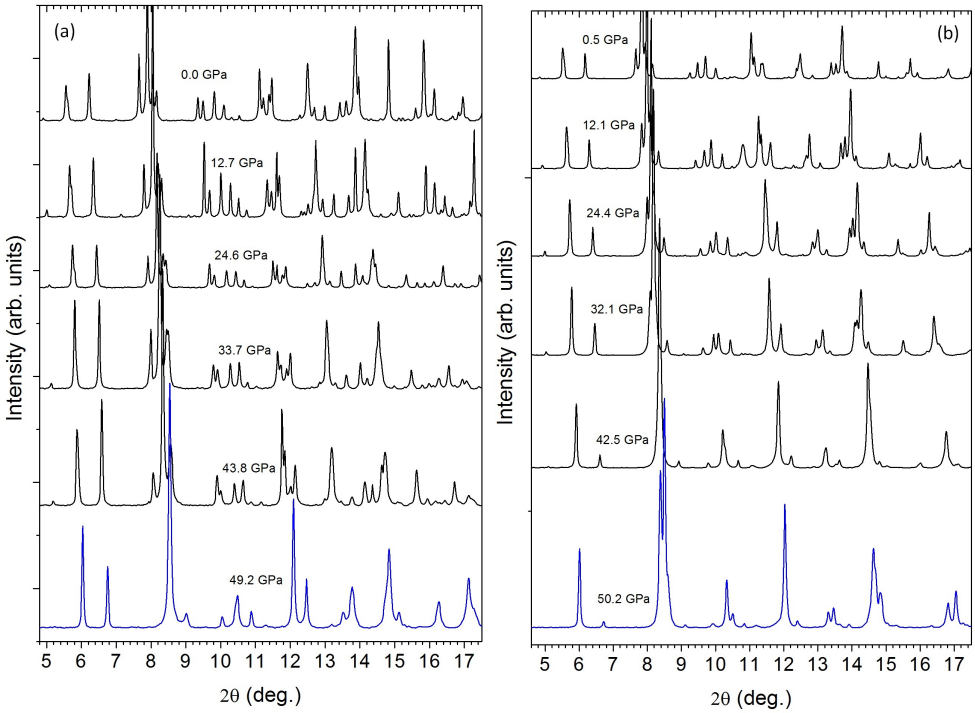

Figure 5.1: Representative x-ray diffraction patterns of (a) $TbFeO_3$ and (b) $SmFeO_3$ recorded at different fixed pressures.

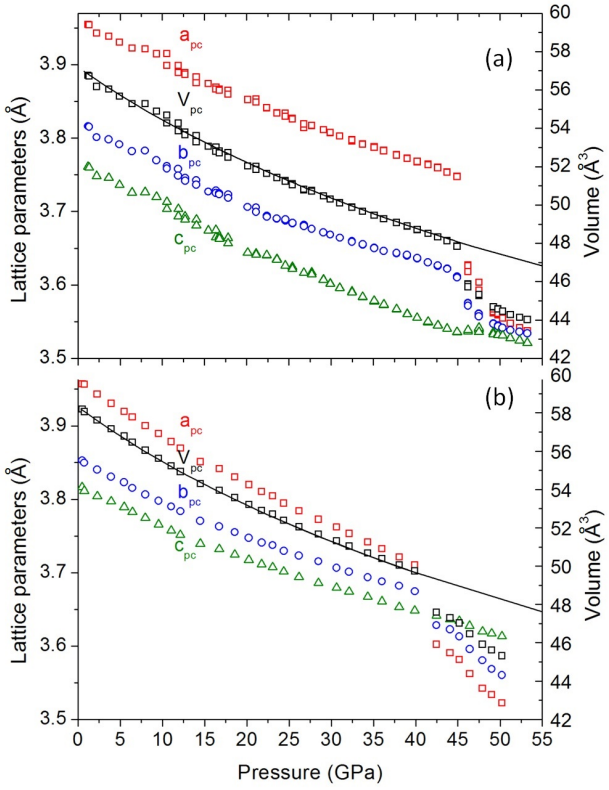

Figure 5.2: Pseudocubic lattice parameters and volume as a function of pressure for (a) $TbFeO_3$ and (b) $SmFeO_3$. Lines are best fit of Equation (5.1) to the pseudocubic volume.

$TbFeO_3$				$SmFeO_3$			
P (GPa)	a_{pc}(Å)	b_{pc}(Å)	c_{pc}(Å)	P (GPa)	a_{pc}(Å)	b_{pc}(Å)	c_{pc}(Å)
1.2	3.9547(3)	3.8162(4)	3.7609(9)	0.5	3.9573(9)	3.852(9)	3.8164(7)
1.3	3.9541(8)	3.8154(5)	3.7600(8)	0.7	3.9569(7)	3.849(8)	3.8115(2)
2.2	3.9428(1)	3.8013(1)	3.7482(8)	2.3	3.9433(9)	3.840(6)	3.8042(3)
3.7	3.9386(2)	3.7982(5)	3.7460(8)	3.9	3.9306(7)	3.830(7)	3.7970(2)
4.9	3.9307(1)	3.7914(5)	3.7362(1)	5.6	3.9197(1)	3.823(1)	3.7893(9)
6.4	3.9225(5)	3.7822(6)	3.7258(8)	6.4	3.9120(7)	3.8154(5)	3.7826(7)
7.9	3.9216(2)	3.7829(6)	3.7263(1)	7.8	3.9005(4)	3.806(5)	3.7747(5)
9.3	3.9147(6)	3.7696(6)	3.7199(6)	9.5	3.8893(7)	3.797(7)	3.7657(7)
10.5	3.8989(7)	3.7585(7)	3.7036(5)	11.0	3.8785(5)	3.790(1)	3.7572(8)
11.9	3.8892(3)	3.7489(7)	3.6936(9)	12.1	3.8699(2)	3.783(6)	3.7515(6)
12.7	3.8867(9)	3.7417(8)	3.6891(4)	14.5	3.8511(2)	3.770(5)	3.7395(3)
14.0	3.8831(2)	3.7426(7)	3.6892(3)	16.7	3.8416(4)	3.763(2)	3.7321(1)
15.4	3.8742(1)	3.7270(1)	3.6744(6)	18.6	3.8306(1)	3.7551(5)	3.7246(1)
16.3	3.8668(2)	3.7252(4)	3.6649(1)	20.2	3.8199(3)	3.747(3)	3.7173(3)
16.7	3.8666(3)	3.7249(1)	3.6664(7)	21.8	3.8107(4)	3.741(1)	3.7115(3)
17.8	3.8650(3)	3.7230(4)	3.6641(3)	23.1	3.8047(3)	3.737(5)	3.7075(7)
20.1	3.8525(5)	3.7060(3)	3.6438(8)	24.4	3.7947(6)	3.7296(5)	3.7014(9)
21.1	3.8490(2)	3.6994(5)	3.6413(3)	26.2	3.7844(4)	3.7232(5)	3.6940(7)
22.4	3.8414(5)	3.6927(9)	3.6408(5)	28.5	3.772(7)	3.7154(5)	3.6857(9)
23.6	3.8341(3)	3.6906(1)	3.6344(7)	30.6	3.7622(3)	3.706(6)	3.6797(1)
24.6	3.8298(2)	3.6891(4)	3.6265(7)	32.1	3.7533(9)	3.701(3)	3.6741(3)
25.4	3.8257(1)	3.6845(5)	3.6219(1)	34.3	3.7417(3)	3.693(5)	3.6670(6)
26.8	3.8191(9)	3.6799(5)	3.6163(8)	36.0	3.7325(3)	3.68(8)	3.660(9)
27.7	3.8171(9)	3.6763(8)	3.6142(7)	38.0	3.7212(2)	3.682(1)	3.653(2)
29.1	3.8114(3)	3.6716(5)	3.6071(1)	39.9	3.7106(1)	3.674(6)	3.6484(6)
29.9	3.8075(5)	3.6686(3)	3.6015(5)	42.5	3.602(2)	3.628(2)	3.641(6)
31.0	3.8027(5)	3.6642(2)	3.5958(5)	44.1	3.590(8)	3.622(8)	3.636(5)
32.5	3.7973(6)	3.6585(3)	3.5900(6)	45.2	3.581(8)	3.613(1)	3.634(2)
33.7	3.7916(1)	3.6553(7)	3.5839(2)	46.4	3.562(1)	3.595(6)	3.627(6)
35.1	3.7872(3)	3.6499(5)	3.5785(3)	47.9	3.542(3)	3.580(6)	3.619(9)
36.2	3.7826(7)	3.6461(7)	3.5732(7)	49.0	3.533(8)	3.568(7)	3.617(3)
37.7	3.7767(1)	3.6435(8)	3.5670(6)	50.2	3.522(6)	3.560(4)	3.613(3)
39.0	3.7724(1)	3.6408(1)	3.5603(8)				
40.2	3.7681(4)	3.636(5)	3.5554(5)				
41.5	3.7637(9)	3.6308(8)	3.5498(8)				
42.6	3.7595(5)	3.6267(3)	3.5448(7)				
43.7	3.7535(5)	3.6218(2)	3.5404(9)				
44.9	3.7475(7)	3.6099(6)	3.5361(2)				
46.2	3.6182(1)	3.5716(2)	3.5387(1)				
47.5	3.5926(4)	3.5603(4)	3.5416(6)				
49.2	3.5632(5)	3.5467(8)	3.5351(2)				
49.8	3.5610(5)	3.5435(5)	3.5320(2)				
50.3	3.5547(8)	3.5414(9)	3.5312(1)				
51.2	3.5479(1)	3.5382(4)	3.5276(7)				
52.3	3.5418(7)	3.5360(7)	3.5245(1)				
53.2	3.5373(2)	3.5342(6)	3.5211(9)				

Table 5.1: Pseudocubic lattice parameters as a function of pressure for $TbFeO_3$ and $SmFeO_3$.

	$V_{pc}(0)$ $\left(\text{Å}^3\right)$	B_0 (GPa)	B_0'
$TbFeO_3$	57.2 ± 0.1	183 ± 9	4.0 ± 0.6
$SmFeO_3$	58.3 ± 0.1	181 ± 3	4.0 ± 0.2

Table 5.2: Pseudocubic volume at room pressure $V_{pc}(0)$, bulk modulus B_0 and its first pressure derivative B_0', obtained from the best fit of the third-order Birch-Murnaghan equation of state (Equation 5.1) to the pseudocubic volume of $TbFeO_3$ and $SmFeO_3$.

could be adequately described by a third-order Birch-Murnaghan equation of state [135]:

$$P = 3B_0 f_E \left(1 + 2f_E\right)^{\frac{5}{2}} \left[1 + \frac{3}{4}\left(B_0' - 4\right) f_E\right] , \tag{5.1}$$

where B_0 is the bulk modulus and B_0' its pressure derivative, all taken at room pressure, and f_E is given by:

$$f_E(P) = \frac{1}{2}\left[\left(\frac{V_{pc}(0)}{V_{pc}(P)}\right)^{\frac{2}{3}} - 1\right] , \tag{5.2}$$

where $V_{pc}(P)$ and $V_{pc}(0)$ are the values of the pseudocubic volume at pressure P and at room pressure, respectively. Table 5.2 presents the values of B_0 and B_0', obtained from the best fit of Equation (5.1) to the experimental data. For the two compounds here studied, the values of the bulk modulus are not much different, taking values around 182 GPa, while the B_0' is about 4, typical of a nearly isotropic compression. In the literature, the reported values for B_0 are quite higher (241 GPa for $LuFeO_3$ and $EuFeO_3$ and 244 GPa for $NdFeO_3$), while B_0' is also around 4 [49, 136]. These values contrast to those found for RMnO$_3$, where the B_0' ranges from 3.7 to 9.7, evidencing a much more anisotropic compression, which may be due to the existence of the Jahn-Teller distortion [57].

5.2 Experimental results of Raman scattering at high-pressure

In this section we will refer to results already presented and discussed in the previous Chapter, namely the mode assignment of the Raman bands and the corresponding atomic displacements. Figure 5.3 shows the unpolarized Raman spectra of RFeO$_3$, with R = Nd, Sm, Eu, Gd, Tb and Dy recorded at different fixed pressures.

For all the studied materials, the Raman spectra exhibit similar trends with increasing pressure: Raman bands shift towards higher wavenumbers, due to an overall pressure-induced bond shortening and volume reduction, and become broader; their intensity reduces and disappear above a certain pressure, dependent on the compound. The later result corroborates the existence of a structural phase transition at high pressures, observed for all the studied compounds. We shall address this issue later on in this Chapter.

In the following, we focus our attention on the Raman-active modes assigned to the FeO_6 octahedra rotations, mirroring the anti-phase and in-phase octahedra tilts, which are the two primary structural distortions, with symmetries given by the irreducible representations R4+ (anti-phase) and M3+ (in-phase) of the high symmetry cubic space group [22]. We also follow the pressure dependence of the Raman band assigned to the R-shift along z-direction, associated with the X5+ distortion [22]. Figure 5.4 presents the pressure dependence of the wavenumber of the aforementioned Raman modes for all the studied RFeO$_3$. The pressure dependence of the wavenumber of the Raman modes does not exhibit anomalous behavior up to the critical pressure, corroborating the *Pnma* structure in the low pressure phase. A linear pressure dependence of the wavenumber of the Raman bands is observed below 20 GPa. From the best fit of a linear function to the data presented in Figure 5.4, we determined the slopes of those linear dependencies, which are also shown.

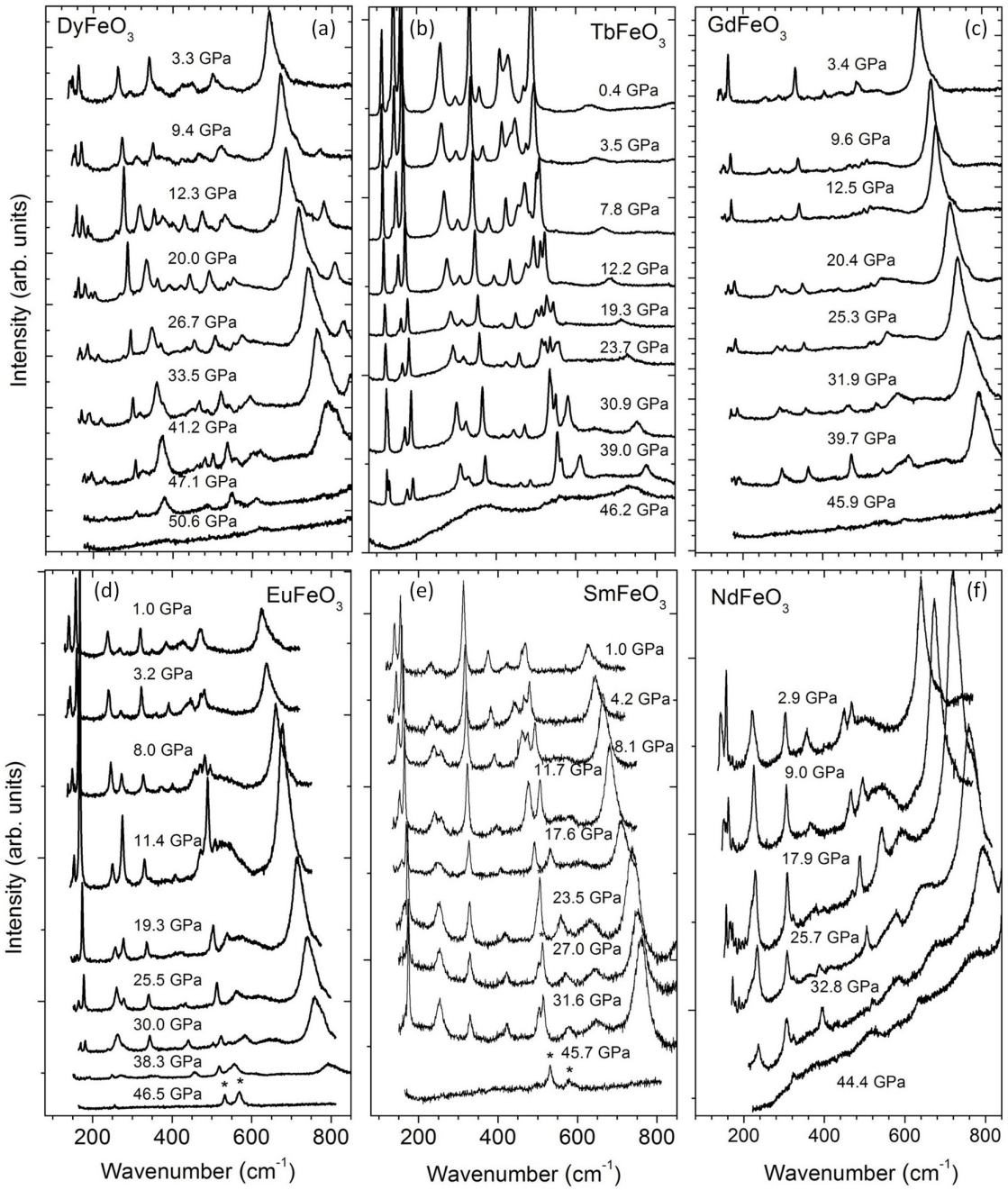

Figure 5.3: Representative Raman spectra of (a) $DyFeO_3$, (b) $TbFeO_3$, (c) $GdFeO_3$, (d) $EuFeO_3$, (e) $SmFeO_3$ and (f) $NdFeO_3$ recorded at different applied pressures. The peaks marked with * correspond to Raman modes arising from impurity solid phases, which were unintentionally introduced as a minor phase in the helium transmitting medium during the diamond-anvil cell preparation procedure.

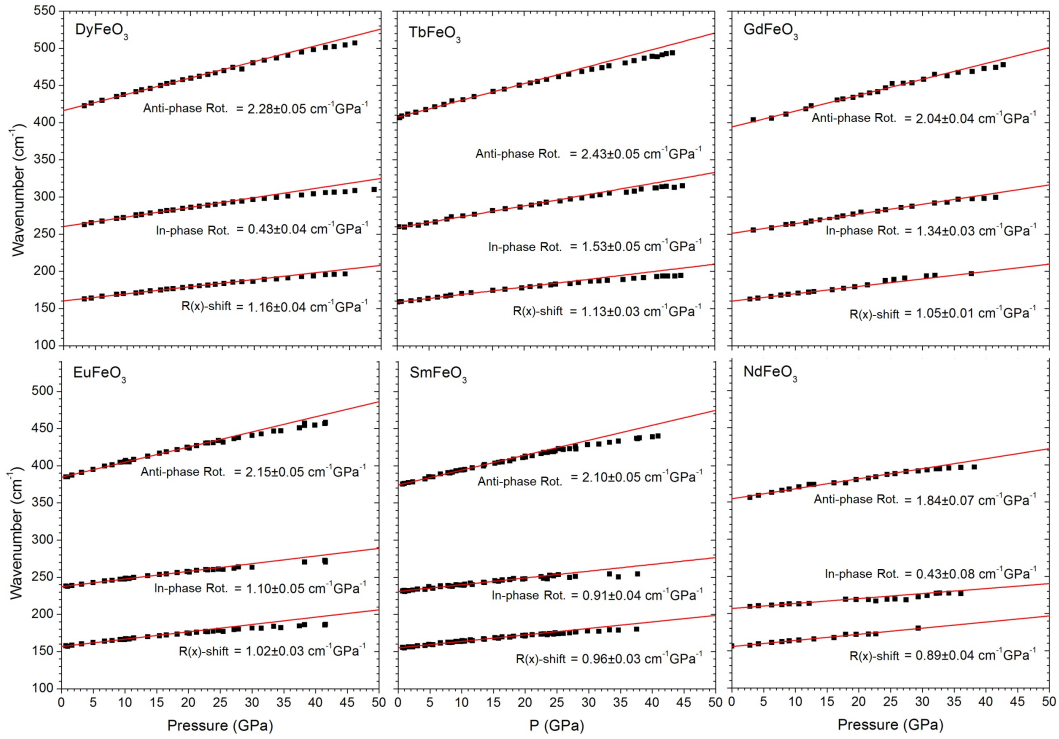

Figure 5.4: Pressure evolution of the Raman in-phase $[010]_{\mathrm{pc}}$ and anti-phase $[101]_{\mathrm{pc}}$ rotation modes wavenumber and Raman R(z)-shifts mode of (a) $DyFeO_3$, (b) $TbFeO_3$, (c) $GdFeO_3$, (d) $EuFeO_3$, (e) $SmFeO_3$ and (f) $NdFeO_3$. The lines were obtained from best linear fits to the data recorded below 20 GPa; the corresponding slopes are presented.

5.3 Pressure behavior of the tilt angles

The quality of the x-ray diffraction patterns obtained at high pressures hinders the full Rietveld refinement of the atomic positions and, so, the calculation of the tilt angles. This has been possible with the Amplimodes refinement, as explained in the previous Chapter [22, 123]. Still, the refined mode amplitudes when plotted versus pressure show dispersion, especially in the modes mainly involving the oxygen motions. This is not surprising since high-pressure powder diffraction presents peak overlapping and the contribution of the oxygen atoms to the diffraction peaks intensity is small compared to the rest of the atoms (that is Sm or Tb, and Fe). The Amplimodes refinements results, especially the octahedral tilts (not shown), should then be contrasted with other observations.

Thus, we have estimated the tilt angles from the lattice parameters, using the equations of Megaw *et al.* [20, 121]. Their pressure behaviors follow similar trends as those found by the Amplimodes analysis, though with much less dispersion. The good agreement between the literature and our experimental observations ensures the validity of this method for other compounds where similar conditions are expected, such as LuFeO$_3$, EuFeO$_3$ and NdFeO$_3$. For the last compounds, we have calculated the tilt angles from the lattice parameters measured at different pressures already published, as these values are relevant for the discussion of how their pressure behavior depends on the rare-earth ionic radius (see following section).

The pressure dependence of the anti-phase tilt angle for R = Nd, Sm, Eu, Tb and Lu, and of the in-phase tilt angle for R = Sm, Eu and Tb are shown in Figures 5.5(a) and (b), respectively. The data regarding the in-phase tilt angle for LuFeO$_3$ and NdFeO$_3$ are not presented because they are too scattered.

For the same compound, both anti-phase and in-phase tilt angles present similar pressure behaviors, but the pressure trend depends on the R-cation. For the compounds with largest rare-earth cations (SmFeO$_3$ and NdFeO$_3$), the applied pressure causes a decrease of both anti-phase and in-phase tilt angles, and thus of the associated symmetry-adapted R4+ and M3+ distortion modes, while the exact opposite behavior is observed for the compounds with smallest rare-earth cations (LuFeO$_3$ and TbFeO$_3$). A similar trend is ascertained for the pressure dependence of the total strain in the same pressure range, which is inherently connected to the two tilts, as shown in Figure 5.5(d). The EuFeO$_3$ case sits exactly in the transition between these two opposite pressure behaviors, where both the tilt angles and, consequently, the total strain are almost pressure independent. Our experimental results point out that pressure weakens both anti-phase and in-phase tilts for compounds with larger rare-earth cations towards a less distorted structure, while it enhances them for compounds with smaller rare-earth cations. Moreover, a remarkable continuous evolution between the two opposite pressure behaviors is experimentally observed.

As stated by Xiang *et al.* [60], the stabilization of the *Pnma* phase of perovskites is predicted to be due to an energy gain coming from a trilinear coupling of both R4+ and M3+ distortions with the X5+ distortion, associated with the displacement of the rare-earth cation [24, 25]. In this theoretical framework, the magnitude of the X5+ distortion mode is predicted to be proportional to the product of both tilt distortions [25]:

$$Z_{xz}^{eq} = -\frac{\beta_{int}}{2k_Z} r_{xz} m_y \,, \tag{5.3}$$

where Z_{xz}^{eq} is the amplitude of the rare-earth distortion, $r = r_{xz}(1,0,1)$ and $m = m_y(0,1,0)$ are the tilt distortions, β_{int} is a material dependent constant and k_Z is a positive constant that gives the proportionality between the amplitude of the rare-earth distortion and its associated energy, $E_Z = k_Z Z_{xz}^2$. If this is the case, then this displacement should follow the same trend as the tilts to which it is coupled with. In fact, the pressure evolution of the X5+ distortion amplitude, which we have obtained by the Amplimodes analysis, experimentally evidences this predicted trilinear coupling, since it mimics the behavior of the tilts for the respective rare-earth, as seen in Figure 5.5(c).

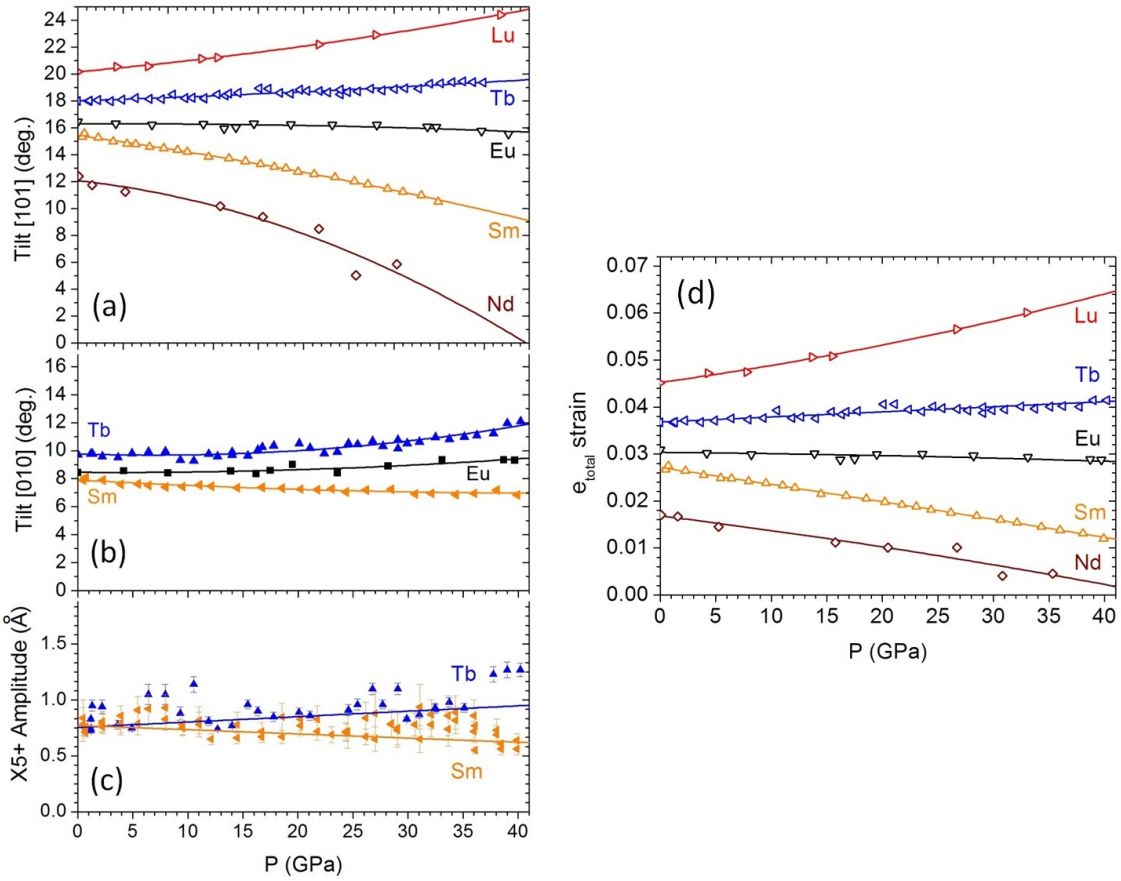

Figure 5.5: Pressure dependence of the (a) anti-phase, (b) in-phase octahedra tilts, calculated from the lattice parameters using the Megaw's formula (Equation 4.1), (c) X5+ distortion calculated from Amplimodes refinement tool and (d) total strain, for the different RFeO$_3$. The solid lines are guides for the eyes. Data of LuFeO$_3$ and EuFeO$_3$ from [49] and NdFeO$_3$ from [137].

5.4 Relation between distortion amplitudes and Raman frequencies

Raman scattering was also used to probe the pressure dependence of both rare-earth shifts and tilt angles. In the last hapter we have defined the proportionality constant between the tilt angles and the the Raman octahedra rotation modes wavenumber for the RFeO$_3$ at room conditions [31]. However, Todorov *et al.* have shown that this proportionality is only constant when similar mean B-O bond lengths are experimentally evidenced [30]. This was the case for the RFeO$_3$ at room conditions, though it is not when pressure is applied, as it shortens all the bond lengths [30]. In their work they show that the Raman octahedra rotation mode wavenumber is actually dependent on the mean B-O bond length, being a function of both the tilt angle and the B-O bond length [30]. In a general approach, the wavenumber of this mode for RFeO$_3$ is written as follows [30]:

$$\omega = (\alpha_1 - \alpha_2 < Fe - O >)\varphi = (m_1 + m_2)\varphi \tag{5.4}$$

where φ is the tilt angle value, <Fe-O> is the mean Fe-O bond length, $\alpha_1 = 109.1$ cm^{-1}/deg, and $\alpha_2 = 42.3$ cm^{-1}/(Å.deg). So, for each Raman octahedra rotation mode, we must take into account that the slope of the pressure dependence of the corresponding wavenumber has two contributions: $m_{total} = m_1 + m_2$, where m_1 stands for the contribution coming from the actual tilt angle change with pressure (α_1), while m_2 is the contribution coming from the isotropic reduction of the FeO$_6$ octahedra volume; i.e., of the average Fe-O distance ($-\alpha_2$<Fe-O>) [30]. In the following, we present an estimation of the m_2 value and how m_1 changes with the rare-earth ionic radius, thus gaining insight on how the mean Fe-O bond length changes with pressure for each rare-earth ferrites.

The rare-earth cation size dependence on the linear pressure relation slopes, in the 0 to 20 GPa range, of the Raman octahedra rotation modes and of the anti-phase and in-phase tilt angles, are depicted in Figures 5.6(a) and (b), respectively. Interestingly, the slope of the Raman mode associated with the R-shift presents the same relative variation with the ionic radius as the tilt angles, seen both by Raman or x-ray diffraction (see Figure 5.6(c)). This outcome further proves the trilinear coupling expected by symmetry considerations, as already seen for the X5+ distortion.

The slopes of the linear pressure dependence of the Raman octahedra rotation modes, presented in Figure 5.6(a), are always positive. The case of EuFeO$_3$ is straightforward because the tilt angles are pressure independent and, thus, $m_1 = 0$ (see Equation 5.4). So, the linear pressure dependence of both Raman octahedra rotation modes in EuFeO$_3$, observed in the 0 to 20 GPa range, comes from the reduction of the <Fe-O> value, and $m_2 = m_{total}$, which is represented by the horizontal dashed lines in Figure 5.6(a). In this case, the wavenumber of the Raman octahedra rotational modes mirrors the reduction of the unit cell volume, due to the decrease of the mean B-O bond lengths with pressure. Thus, a linear relation between the mode wavenumber and volume is experimentally evidenced, as shown in Figure 5.6(e). For TbFeO$_3$/SmFeO$_3$, the upper/down shift of the wavenumber of both Raman rotational modes relatively to the linear dependence on the BO$_6$ volume is observed in Figures 5.6(d)/(f). The observed shifts are a direct consequence of the decrease/increase of the tilt angles with pressure.

In order to unravel the effect of the tilt angles on the pressure dependence of the Raman octahedra rotation modes wavenumbers for the other compounds, the $m_2 = m_{total}$ value calculated for EuFeO$_3$ might not the best reference, since the reduction of the FeO$_6$ octahedra volume may have different values for each compound, as it will be shown. According to Equation 5.4, the pressure derivative of the wavenumber of the Raman octahedra rotation modes is:

$$\frac{d\omega}{dP} = [\alpha_1 - \alpha_2 < Fe - O > (P)]\,\frac{d\varphi}{dP} - \alpha_2\varphi(P)\left[\frac{d < Fe - O >}{dP}\right] . \tag{5.5}$$

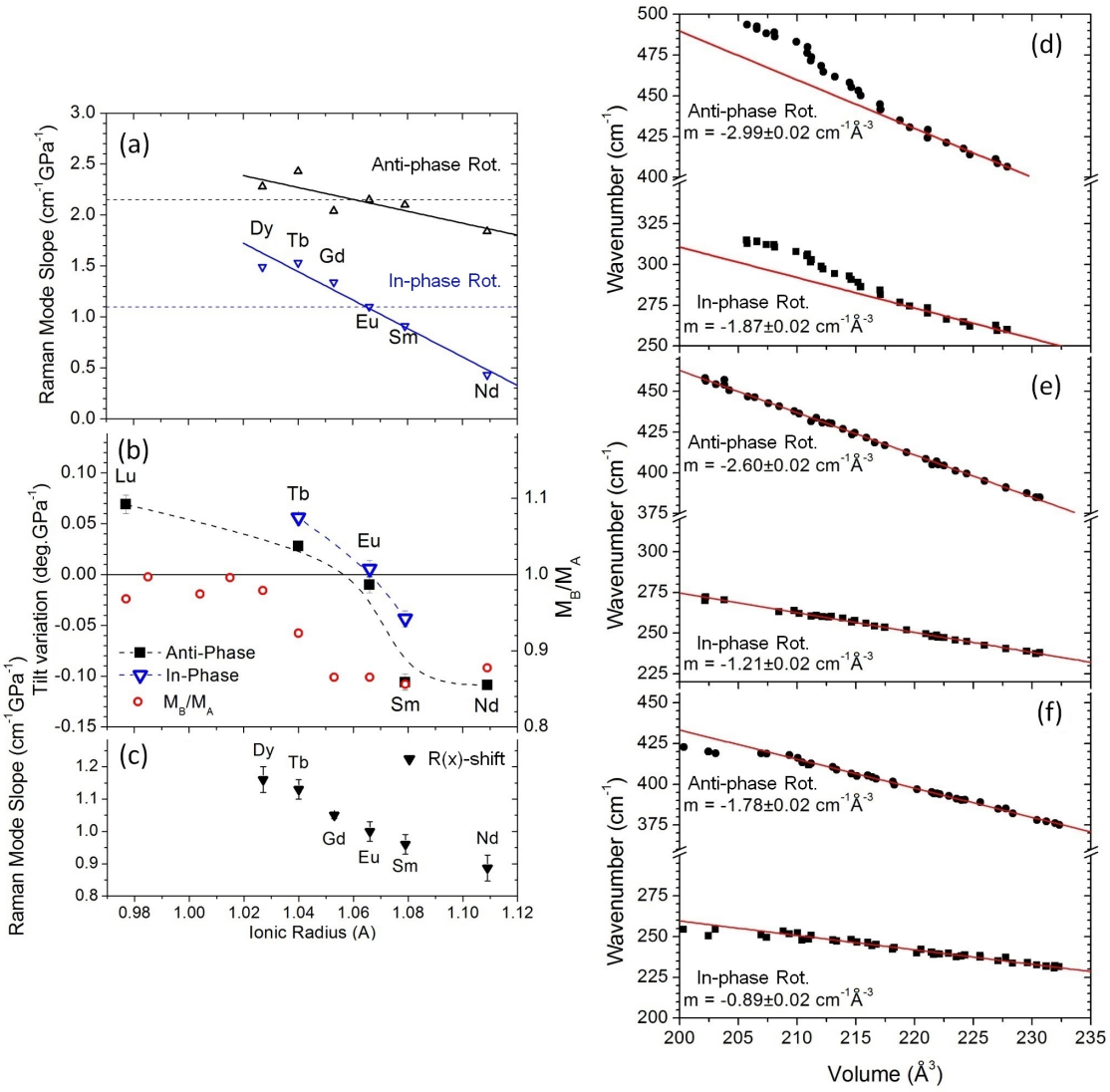

Figure 5.6: Rare-earth cation size dependence of the slopes of the linear pressure relation, in the 0 to 20 GPa range, of the (a) the Raman octahedra rotation modes, (b) of the anti-phase and in-phase tilt angles (c) and of the Raman R-shift mode. Dashed lines in (a) mark the reference value of $EuFeO_3$ for the contribution of the isotropic FeO_6 octahedra volume reduction. For comparison, we also present in (a) the ratio between the compressibilities of the AO_{12} dodecahedra β_A and the FeO_6 octahedra β_B: $\frac{\beta_A}{\beta_B} = \frac{M_B}{M_A}$, from Zhao's *et al.* work [61]. Volume dependence of the frequency of the Raman octahedra rotation modes for (d) $TbFeO_3$, (e) $EuFeO_3$ and (f) $SmFeO_3$.

	$\frac{d<Fe-O>}{dP}$ (Å/GPa)	
Tilt Angle	Anti-Phase	In-Phase
TbFeO$_3$	-0.0023 ± 0.0003	-0.0009 ± 0.0004
EuFeO$_3$	-0.0031 ± 0.0001	-0.0031 ± 0.0001
SmFeO$_3$	-0.0071 ± 0.0003	-0.0058 ± 0.0006
NdFeO$_3$	-0.0082 ± 0.0003	N/A

Table 5.3: $\frac{d<Fe-O>}{dP}$ calculated from Equation 5.5, for the low pressure range, using either the anti- and the in-phase tilt angles, for the different rare-earth ferrites. The values obtained using the anti-phase tilt should be the most accurate.

In the following, we shall consider the values concerning $\frac{d\varphi}{dP}$ and $\frac{d\omega}{dP}$ as the slopes obtained in the 0 to 20 GPa range, shown in Figures 5.6(a) and (b), respectively. For EuFeO$_3$, where $\frac{d\varphi}{dP} = 0$, we have obtained $\frac{d<Fe-O>}{dP} = -0.0031 \pm 0.0001$ Å/GPa, using either anti- or in-phase tilts. For the remaining compounds, we focus our calculation to the linear range on the vicinity of P = 0 GPa, thus taking the values of <Fe-O> and φ at that point. The obtained results for the low pressure range are shown in Table 5.3. The $\frac{d<Fe-O>}{dP}$ values varied only around 0.001 Å/GPa when using the two different tilt modes. It is worth to note that in the previous Chapter we have found different proportionality constants (m_{total}) between and for the anti- and in-phase tilts for the RFeO$_3$ system [31]. The presented value agrees with that obtained by Todorov *et al.* for the anti-phase tilt, but not for the in-phase tilt [30]. Therefore, the most correct value for the actual $\frac{d<Fe-O>}{dP}$ is the one obtained with the anti-phase tilt.

These results evidence that, at low pressures, as the rare-earth ionic radius increases, the pressure rate at which the FeO$_6$ octahedra reduce also increases. For TbFeO$_3$, the average reduction of the Fe-O mean bond length is of -0.0016 Å/GPa, half the value of EuFeO$_3$, and around 5 times smaller than the largest one of -0.0082 Å/GPa for NdFeO$_3$. This is not unexpected, since the tilts provide a mechanism of pressure accommodation. Thus, for the smaller rare-earth cations, where the tilts increase with pressure, the FeO$_6$ octahedra are compressed at lower rates. Conversely, for the larger rare-earths, where the tilts decrease with pressure, the FeO$_6$ octahedra must be compressed at larger rates.

5.5 Crossover for the behavior of tilts in the rare-earth series: experiment and theory

We now focus on the evolution of the tilt angles in the vicinity of zero (atmospheric) pressure across the series. From Figure 5.6(b), we can see that the slope of the linear pressure dependence of both anti-phase and in-phase octahedra tilt angles is positive for compounds with smaller rare-earth cations (R = Lu and Tb), while they are negative for those with larger rare-earth cations (R = Sm and Nd). EuFeO$_3$ stands at the borderline, as for this both slopes are negligibly small. The modulus of the slope of the linear pressure dependence of the in-phase tilt angle is smaller than the anti-phase tilt angle for SmFeO$_3$, while for TbFeO$_3$ it is the opposite. These results show that the way the pressure is accommodated is different for compounds with different rare-earth cationic sizes.

We now compare this compilation of experimental results with predictions made by theoretical approaches for the pressure evolution of tilt angles. A first approach is based on the compressibility of the polyhedra constituting the perovskite structure. In this approach, the ratio of compressibilities β_A/β_B between the AO$_{12}$ and BO$_6$ polyhedra is used as a predictor of the behavior of tilt angles under pressure, and is calculated by a valence bond sum model: tilt angles are expected to increase when this ratio is larger than unity, and decrease otherwise [61]. The case of the rare-earth ferrites has been treated in Ref. [61], and the corresponding

data are reported in Figure 5.6(b) for comparison. The ratio is always positive, but decreases as the ionic radius increases and reaches values very close to unity for the smallest cations [61]. According to this criterion, all compounds in the series should see their tilt angles reduced under pressure, with the exception of $TmFeO_3$ [61]. This is not what is found experimentally, but the overall evolution bears a striking resemblance with the experimental one, up to an overall shift.

More recently, in a DFT-based approach, a set of rules for the evolution of tilts under pressure was proposed [60]. In this paper, the compounds with the smallest A-cations (Lu and Tm), are predicted to exhibit an unusual behavior wherein the two tilt angles behave in the opposite way with pressure: the anti-phase tilts are reduced whereas the in-phase tilts are enhanced [60]. For larger cations, both tilts behave the same way and are reduced as pressure increases. We find here no evidence for this behavior, but instead, both tilt angles behave the same in all investigate compounds. Moreover, Ref. [60] does not predict any case where both tilts increase under pressure.

The discrepancies between theoretical and experimental results seemingly point to a specific difficulty in predicting the tilt behavior for the smallest cations in the series. While we cannot be conclusive at this point about the precise reasons for this discrepancy, we observe that, in both approaches, the predicted tilt changes under pressure reach extremely small values, typically below 0.01°/GPa for LuFeO3 in Ref. [60]. For $EuFeO_3$, which in fact has absolute pressure derivatives below 0.01°/GPa, the slopes for in-phase and anti-phase tilts are of opposite sign (0.006 and -0.01°/GPa, respectively), but with values negligible small that fall in the experimental uncertainty. In that context, it is conceivable that some additional parameters, legitimately neglected for large cations, become relevant and suffice to change the trend from slightly positive to negative or vice versa. In particular, $RFeO_3$ with very small cations (Lu to Er) are known to exhibit some distortions of the AO_{12} polyhedra, so that the classical separation of the 12 A-O bonds into 4 longer bonds and 8 shorter bonds becomes less satisfactory [32]. We hypothesize that this has an influence of the bond valence sum and compressibilities calculated in Ref. [60]. In the DFT approach, where calculations are performed at 0 K, and the behavior of tilts is the result of a delicate balance between the pressure evolution of the Landau parameters, one might question the role of temperature effects. Differences in tilt angles of the order of 0.1degrees between 0 and 300 K – which is reasonable following Ref. [138] – would be equivalent to several tens of GPa and cause significant shifts in the predicted behavior. Altogether, further work will be needed to clarify the picture for small cations, which calls for detailed experimental studies and reexamination of theoretical models.

5.6 High-pressure phase transition

Despite the crossover between enhancement and suppression of the tilt angles on the low-pressure regime, for all the studied compounds a similar isostructural pressure-induced structural phase transition occurs. This implies that the tilts play no major role on triggering this phase transition, nor on the symmetry of the high-pressure phase. This phase transition is clearly evidenced by the changes on the x-ray diffraction patterns, mirroring the sudden changes of the pseudocubic lattice parameters. The structural phase transition reveals itself by the disappearance of the Raman signal above a certain critical pressure. The crystallographic structure of the high-pressure phase of $SmFeO_3$ and $TbFeO_3$ is $Pnma$, as it was reported for other rare-earth ferrites [49]. This structure allows for Raman signal. Therefore, the disappearance of the Raman spectra above the critical pressure suggests the metallic character of the high-pressure phase.

The pressure hysteresis evidenced by the x-ray diffraction patterns of $SmFeO_3$ and $TbFeO_3$, and Raman spectra of all studied compounds, recorded on increasing and decreasing pressure runs (3 to 6 GPa depending on the rare-earth cation), evidences for the first-order character of this structural transition. Taking into account the x-ray diffraction and Raman scattering data together, we can estimate the critical pressure P_{IM}, depicted in Figure 5.7. As it can be observed, the critical pressure linearly increases as the rare-earth cation

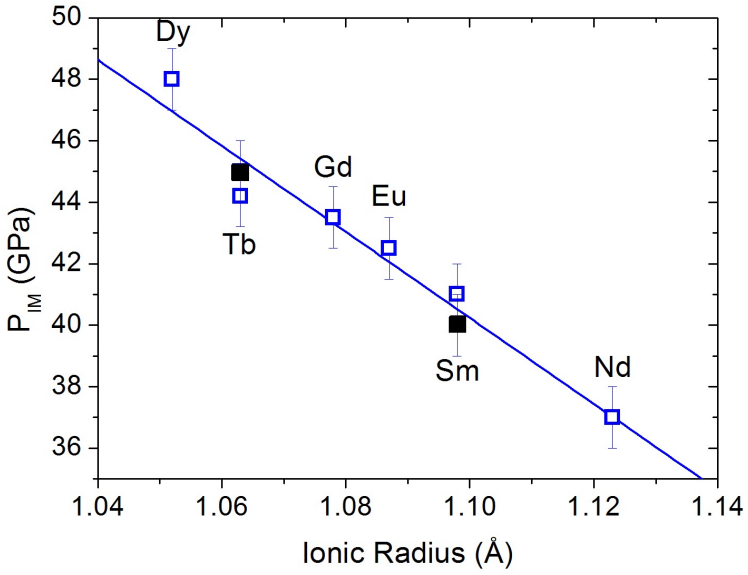

Figure 5.7: Critical pressure P_{IM}, obtained from x-ray diffraction (closed symbols) and Raman scattering (open symbols) data, for RFeO$_3$ as a function of rare-earth ionic radius.

size decreases.

High-pressure Mössbauer experiments give evidences for a transition from high-spin to low-spin configurations occurring at P_{IM} [48]. As the tilts have little impact on this transition, it is sensible to assume that it depends mostly on the chemistry found inside the FeO$_6$ octahedra. We suggest that, as pressure increases and the FeO$_6$ octahedra become smaller, a critical volume of the octahedron is reached where the electronic repulsion between the oxygens p-electrons and the iron e_g-electrons is such, that it triggers this electronic reconfigurations, as it is energetically favorable for the e_g-electrons to pair with the t_{2g}-electrons, avoiding the oxygen p-electrons. The critical volume can be estimated for EuFeO$_3$. As the tilt angles do not change with pressure, there is an isotropic volume reduction of the unit cell, and thus the ratio of the FeO$_6$ octahedron volume with the pseudocubic unit cell volume ($\frac{V_{FeO_6}}{V_{pc}}$) can be assumed pressure-independent. Considering a regular octahedron at room pressure, the ratio $\frac{V_{FeO_6}}{V_{pc}} = 0.189$ is obtained. Using the value of V_{pc} before the critical pressure, the critical volume for EuFeO$_3$ is estimated to be $V_{FeO_6} = 9.5 \pm 0.2$ Å^3.

It is expectable that for larger R-cations, where from Table 5.3 we know the FeO$_6$ octahedra reduce their volume at a larger rate, the aforementioned phenomenon is promoted at a lower critical pressure. Conversely, for the smaller R-cations, as the FeO$_6$ octahedra reduce their volume at a lower rate, they present higher values of critical pressure. This prediction explains the behavior of P_{IM} with the rare-earth size, shown in Figure 5.7. Moreover, one can infer that a similar role is played by the octahedra tilting in the similar pressure-driven phase transition observed in RMnO$_3$ [57]. The critical pressures for RMnO$_3$ have similar dependence on the rare-earth ionic size, being always slightly higher by a constant value of 2 GPa. This difference can be assigned to the Jahn-Teller distortion present in RMnO$_3$, as it provides an additional pressure accommodation mechanism than their respective RFeO$_3$ compounds. It is worth to note that the tilt angles are almost the same, thus allowing for this comparison [26]. This fact also supports the importance of the chemistry inside the octahedra in determining the symmetry of the high-pressure phase. This is because, unlike the isostructural phase transition found for the RFeO$_3$, the RMnO$_3$ present many different symmetries of the high-pressure phase [57].

5.7 Summary

In summary, we have experimentally found that there is a crossover between enhancement and suppression of the *Pnma* main distortions, i.e. octahedra tilting and rare-earth shift, in the $R\mathrm{FeO}_3$, as a function of the rare-earth ionic radius. This peculiar change in behavior is a novelty for such systems. Moreover, we were able to provide an explanation for the change in the critical pressure P_{IM} as a result of the change on the pressure dependence of the tilts. These tilts play an important role on the pressure value at which the critical octahedra volume that triggers the high to low spin reconfiguration at P_{IM}. We also estimate the pressure rate of the FeO_6 volume reduction as a function of the rare-earth ionic radius, as well as a value of the FeO_6 critical volume.

Chapter 6

Spin-Phonon Coupling of $R\mathrm{FeO_3}$

This Chapter begins with a brief summary of the magnetic properties of $R\mathrm{FeO_3}$ (R = La to Lu). The reader can follow this description looking at the phase diagram already present in Figure 1.9(b) of Chapter 1. All compounds undergo a paramagnetic-antiferromagnetic phase transition at high temperatures (T_N $\approx$ 700 K, decreasing as the rare-earth cation size decreases) [35]. This phase transition is associated with the ordering of the Fe^{3+} spin sublattice into the $A_xF_yG_z$ type [35]. The spin structure can be described as a two antiferromagnetically ordered Fe spins, with a spin-canting which allows for a net ferromagnetic magnetization, whose direction is along the b-axis [35]. This structure is kept to the lowest temperatures in the case of R = La, Eu, Gd and Lu [35]. The remaining compounds exhibit a spin-reorientation transition at finite temperature [35]. The case of R = Pr, Nd, Sm, Tb, Ho, Er, Tm and Yb the spin-reorientation goes continuously from $A_xF_yG_z$ into $C_xG_yF_z$, in a certain temperature range strongly dependent on the rare-earth cation [35]. During this transition, the magnetization flips from the b-axis to the c-axis. For the case of R = Ce and Dy the spin-reorientation changes the Fe^{3+} structure into the $G_xC_yA_z$ [35].

For R = Sm, Nd and Er, it is currently accepted that the anisotropic interactions between the two antiferromagnetically coupled Fe- and R-sublattices, with opposite net ferromagnetic moment, underlie the spin-reorientation transition. Just below the lower temperature limit of the spin-reorientation transition, a decrease of the net magnetization is ascertained, and eventually it vanishes at finite temperatures depending on the rare-earth cation, and, then, it reverses sign, as shown in Figure 6.1(a) for $NdFeO_3$. This result is a consequence of the reinforcement of the R-R interactions as temperature lowers. The R-sublattice orders in opposite direction regarding the Fe-sublattices. On other compounds, such as $TbFeO_3$, there is a monotonous increase of the magnetization as temperature lowers (see Figure 6.1(b)).

In this Chapter, we will present and discuss the experimental results concerning the Raman-active magnetic excitations and lattice dynamics of $R\mathrm{FeO_3}$, with R = Nd, Eu, Gd and Tb. Our purpose is to get deeply knowledge about how the phonons mirror the magnetic transitions and interactions in these materials. The mode assignment was already presented in Chapter 4.

This Chapter is organized as follows. First, the results obtained in compounds exhibiting spin-reorientation transition ($NdFeO_3$ and $TbFeO_3$) are presented and compared with results already published in other materials undergoing similar magnetic transformation. Then, we will present and discuss the results obtained in $EuFeO_3$ and $GdFeO_3$ that have no phase transition other than the high temperature one.

6.1 Experimental results

Figures 6.2(a) to (d) show representative unpolarized Raman spectra of $R\mathrm{FeO_3}$, R = Nd, Eu, Gd and Tb, recorded at different fixed temperatures, in the 100 to 450 cm^{-1} spectral range, where the modes that will

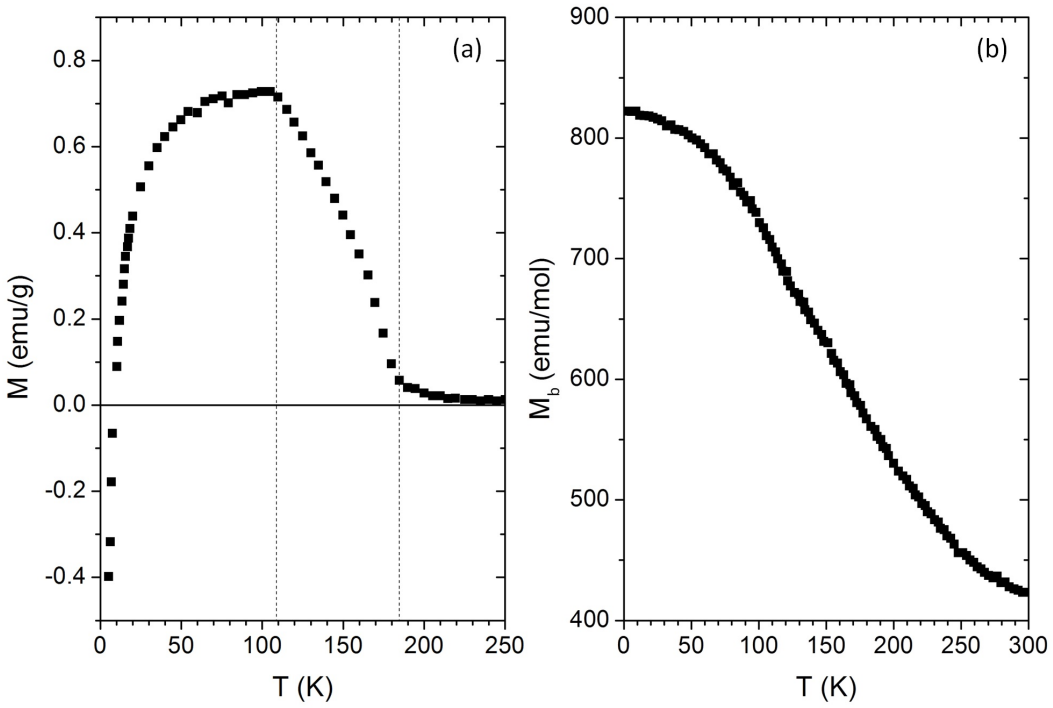

Figure 6.1: Magnetic response as a function of temperature for (a) $NdFeO_3$ and (b) $TbFeO_3$. Vertical dashed lines in (a) mark the spin-reorientation temperature range. Data from Refs. [139, 140].

be discussed in this Chapter are observed. The mode assignment of the bands observed at 10 K is also presented. Among the Raman–active modes, we have focused our attention on phonons which involves the R-shifts and oxygen octahedra rotations that best sense the R-Fe and R-R magnetic interactions. These are the Raman out-of-phase R-oscillations along the z-axis (R(z)) and x-axis (R(x)) modes, the Raman in-phase $[010]_{\mathrm{pc}}$ octahedra rotation (IP Rot) and anti-phase $[101]_{\mathrm{pc}}$ octahedra rotation (AP Rot) modes and the Raman O1 in-phase oscillations in the xz-plane mode (O1(xz)) mode.

Common features can be observed in the temperature evolution of the Raman spectra. As temperature decreases, the Raman bands become better resolved and many bands shift to higher frequencies due to volume contraction. No well-defined activated Raman bands could be detected in the 10 to 875 K temperature range. The temperature dependence of all Raman active modes does not exhibit anomalous behavior at the Néel temperature. This result shows that the high temperature magnetic phase transition does not involve structural changes. However, a detailed analysis of the Raman spectra reveals interesting temperature dependencies of the wavenumbers of the Raman rare-earth shifts and octahedra rotations modes, which this Chapter will focus on.

The wavenumber temperature dependence of the most intense Raman modes was obtained by the best fit of a sum of damped oscillators. The wavenumber temperature dependence of the analyzed modes, in the temperature range where no anomalous behavior is observed, was described by the normal anharmonic temperature effect due to volume contraction as temperature decreases [141]:

$$\omega_{anh}(T) = \omega_0 + C\left[1 + \frac{2}{e^x - 1}\right] + D\left[1 + \frac{3}{e^y - 1} + \frac{3}{(e^y - 1)^2}\right], \tag{6.1}$$

where ω_0, C and D are model constants, x is given by $x = \frac{\hbar\omega_0}{2k_BT}$, y is given by $y = \frac{\hbar\omega_0}{3k_BT}$, where $\hbar$ is the reduced Planck constant, k_B is the Boltzmann constant and T is the temperature.

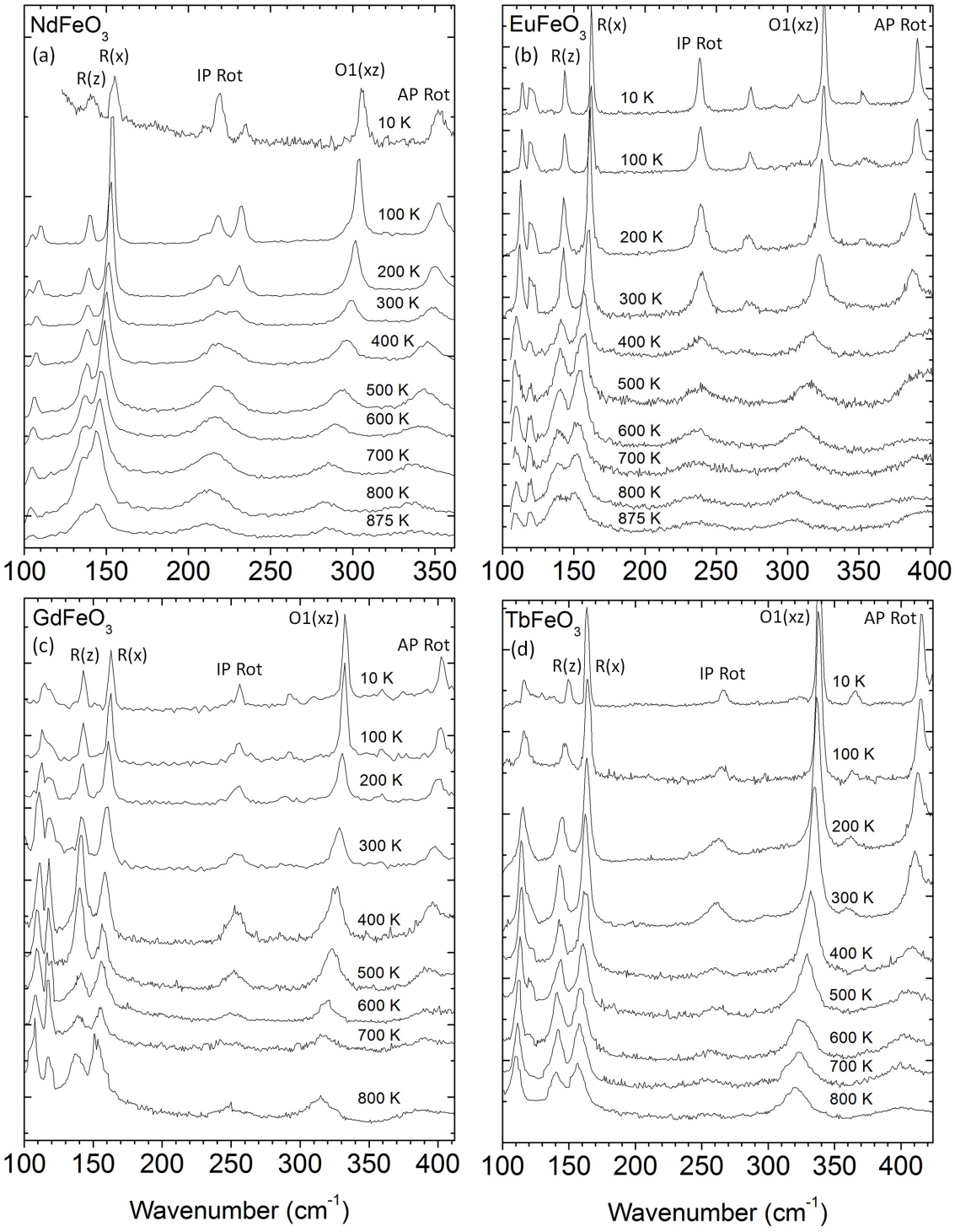

Figure 6.2: Representative Raman spectra of (a) $NdFeO_3$, (b) $EuFeO_3$, (c) $GdFeO_3$ and (d) $TbFeO_3$ recorded at different fixed temperatures. R(z) and R(x) stand for the Raman R-shifts along the z-axis and x-axis modes, respectively, IP and AP Rot for the Raman in-phase $[010]_{pc}$ octahedra rotation and anti-phase $[101]_{pc}$ octahedra rotation modes, respectively, and O1(xz) for the Raman O1 oscillations in the xz-plane mode.

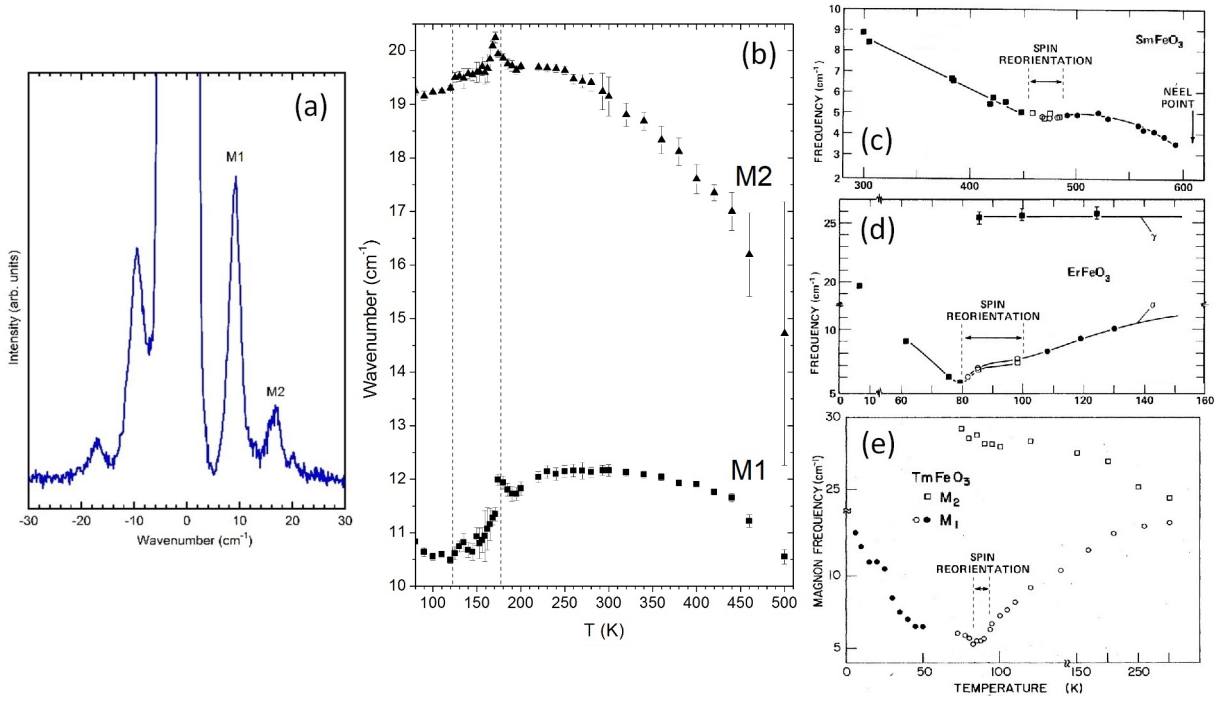

Figure 6.3: (a) Unpolarized Stokes and anti-Stokes Raman spectra of $NdFeO_3$ between -30 and 30 cm^{-1}. M1 and M2 identify the two magnon bands. Wavenumber temperature dependence of the magnon bands of (b) $NdFeO_3$, and for comparison of (c) $SmFeO_3$, (d) $ErFeO_3$ and (e) $TmFeO_3$ from Refs. [45, 142]. Vertical lines in (b) to (d) mark the spin-reorientation temperature range.

6.2 Magnetic excitations and lattice dynamics of $NdFeO_3$

Figure 6.3(a) shows a representative unpolarized Stokes and anti-Stokes components of the Raman spectra of $NdFeO_3$ between -30 and 30 cm^{-1}, recorded at room temperature. Two magnon bands are clearly observed, in good agreement with other rare-earth ferrites [46, 142]. The lower frequency band is assigned to the motion of the magnetization vector of the Fe-sublattice along a narrow elliptical orbit within the *ac*-plane, giving rise to a net magnetization oscillating at a characteristic wavenumber. As the spin-reorientation transition involves the rotation of the net magnetization in the *ac*-plane [35], this mode exhibits a characteristic instability at the spin-reorientation transition. The higher band is assigned to the motion of the magnetization vectors of each Fe spin sublattice along an elliptical orbit whose major axis is in the *b*-axis. The spin-reorientation does not affect this net magnetization, thus this mode is expected to be weakly sensitive to that transition. At room temperature, the lower wavenumber band peaks at 12 cm^{-1} while the other peaks at 19 cm^{-1}. Figures 6.3(b) show the temperature dependence of the wavenumber of both magnons in the 80 to 500 K temperature range (our experimental setup did not allow low-wavenumber measurements below this temperature).

Both magnons are observed below 675 K, although the higher wavenumber magnon is not well resolved, so that, its wavenumber was not accurately determine. This is the unique experimental evidence for the high temperature magnetic phase transition in $NdFeO_3$. Below 550 K and down to 300 K their wavenumber monotonously increase. Below 240 K, the lower wavenumber magnon (M1) softens on approaching the upper temperature of the spin-reorientation region, although its wavenumber stays finite. Its temperature dependence also exhibits anomalous behavior in the limits of the spin-reorientation region. The wavenumber of the higher wavenumber magnon (M2) behaves in a different way. Its wavenumber monotonously increases down to 220 K. Then, a clear cusp like anomaly emerges at 170 K and a sudden downward jump at 124 K is observed. Below 100 K, the frequency of both magnons exhibit an increasing trend on further cooling. This result evidences

that the interactions between the rare-earth and the iron spins affect the spin dynamics and the role played by the M1 magnon on the spin-reorientation mechanisms.

It is worth to compare the result here obtained with the temperature dependence of the magnons observed in other compounds with spin-reorientation transitions, which are shown in Figures 6.3(c) to (e) [45, 142]. The temperature dependence of the magnon wavenumbers in NdFeO$_3$ sharply contrast with SmFeO$_3$. In addition to observe only one magnon in SmFeO$_3$, no significant softening of its wavenumber could be observed on approaching the spin-reorientation transition from higher temperatures [45, 142]. In this case, just below the lower temperature limit of the spin-reorientation region, a monotonously increase of wavenumber is observed. The temperature behavior of the lower wavenumber magnon in NdFeO$_3$ is more similar to those observed in both ErFeO$_3$ and TmFeO$_3$ [45, 142]. In these two compounds, the lower wavenumber magnon partially softens as temperature approaches the upper limit of the spin-reorientation region by higher values. No anomalies in the temperature dependence of the wavenumber of magnons in ErFeO$_3$ and TmFeO$_3$ could be ascertained [45, 142].

The magnetic interactions involved in the spin-reorientation process and the decrease of net magnetization also reveal themselves by anomalies in the temperature dependence of several lattice modes, via the spin-phonon coupling. Figures 6.4(a) to (e) show the wavenumber temperature dependence of the Raman anti-phase $[101]_{\mathrm{pc}}$ octahedra rotation, O1 xz-plane oscillation, in-phase $[010]_{\mathrm{pc}}$ octahedra rotation, R(x)-shift and (e) R(z)-shift modes, respectively. Above 200 K, the modes follow the expected temperature dependence due to anharmonic effects arising from volume contraction (solid curve) [141].

The spin-reorientation transition reveals itself on most of the presented Raman modes, most clearly by the upward deviation of the Raman in-phase $[010]_{\mathrm{pc}}$ octahedra rotation mode wavenumber from the extrapolated high temperature dependence, as seen in Figure 6.4(c). Below the lower temperature limit of the spin-reorientation region and on further cooling, the wavenumber of this mode increases linearly with decreasing temperature down to 10 K, and no hints of saturation is observed. This is likely associated with the effect of strong interactions of the Nd-sublattice, which orders at 100 K. At 150 K there is a kink on the wavenumber temperature dependence of the Raman R(z)-shift mode (Figure 6.4(e)), while the Raman R(x)-shift mode has a downward deviation below this temperature (Figure 6.4(d)). The wavenumber of the Raman anti-phase $[101]_{\mathrm{pc}}$ octahedra rotation and O1 xz-plane oscillation modes follow the extrapolated expected temperature dependence down to 90 K, presenting an upward deviation below (see Figures 6.4(a) and (b)).

As the Raman O1 xz-plane oscillation mode actually also involves the Nd oscillation in the same plane, we have analyzed the relationship between the corresponding wavenumber deviations ($\Delta\omega$), calculated by the difference from the actual experimental wavenumber values of the two aforementioned modes and the extrapolated tendency expected from Equation 6.1. Figure 6.5(a) shows the result for temperatures below 90 K, where a linear relationship between the anomalous decrease/increase frequency is ascertained. This result clearly evidences for a coupling between these two modes, which reflects the magnetic interaction of the Nd- and Fe-sublattices, via oxygen atoms. Indeed, it is accepted that the magnetic interactions of the Nd- and Fe-sublattices is mediated by superexchanges involving the oxygen atoms [35]. Moreover, we have analyzed the relation between the $\Delta\omega$ and the difference of net magnetization relatively to its maximum value attained at 100 K (ΔM), shown in Figure 6.5(b). The difference of magnetization comes from the ordering of the Nd-sublattice in opposite sense to the Fe-sublattice [139]. A linear relationship between the $\Delta\omega$ of the Raman O1 xz-plane oscillation mode and the ΔM is ascertained in the 40 to 90 K range, pointing for a coupling between this phonon and the Nd-sublattice magnetization. As the temperature decreases from 100 K towards 40 K, the $\Delta\omega$ of the Raman O1 xz-plane oscillation mode becomes sensitive to the increasing of the Nd-Nd interaction strength.

It is challenging to compare the results here described with those of SmFeO$_3$. The temperature dependence of the Raman modes on SmFeO$_3$ was already studied by Mads Weber [130]. SmFeO$_3$ presents a similar

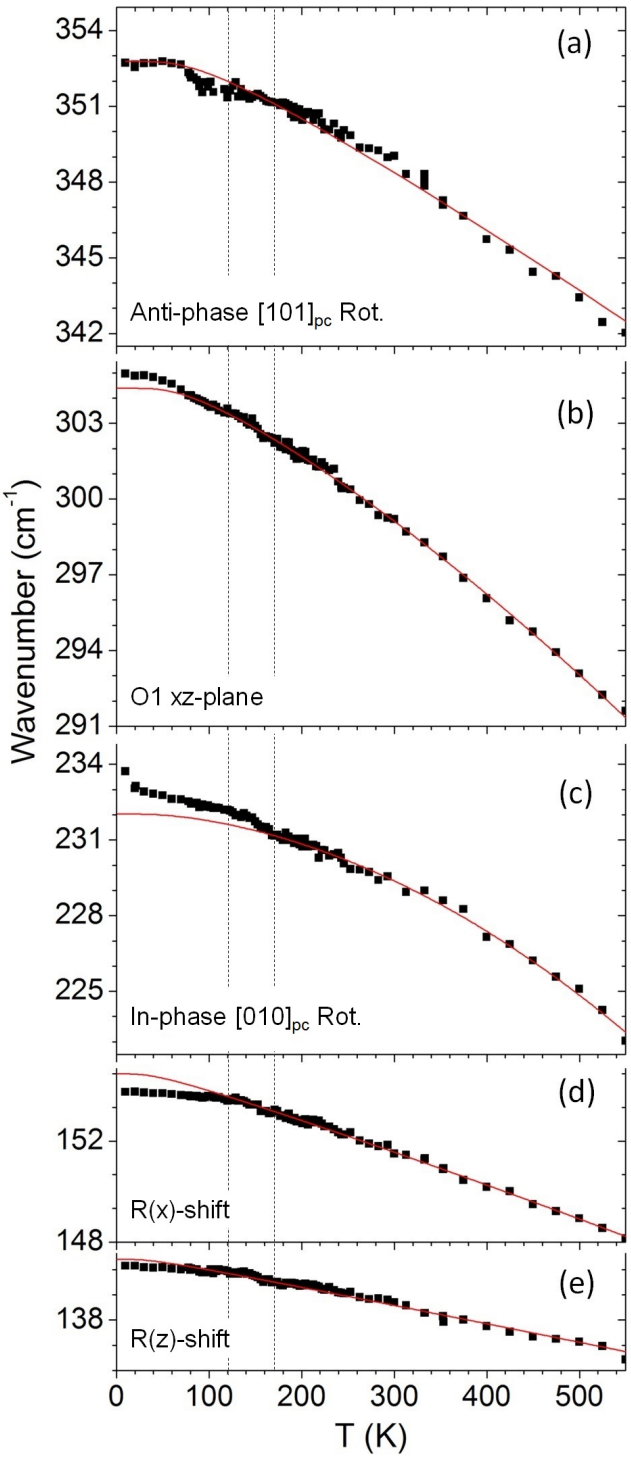

Figure 6.4: Wavenumber temperature dependence of (a) Raman anti-phase $[101]_{pc}$ octahedra rotation, (b) O1 xz-plane oscillation, (c) in-phase $[010]_{pc}$ octahedra rotation, (d) R(x)-shift and (e) R(z)-shift modes. The solid line was determined by the best fits of Equation 6.1 above 200 K and its extrapolation down to 10 K, for $NdFeO_3$.

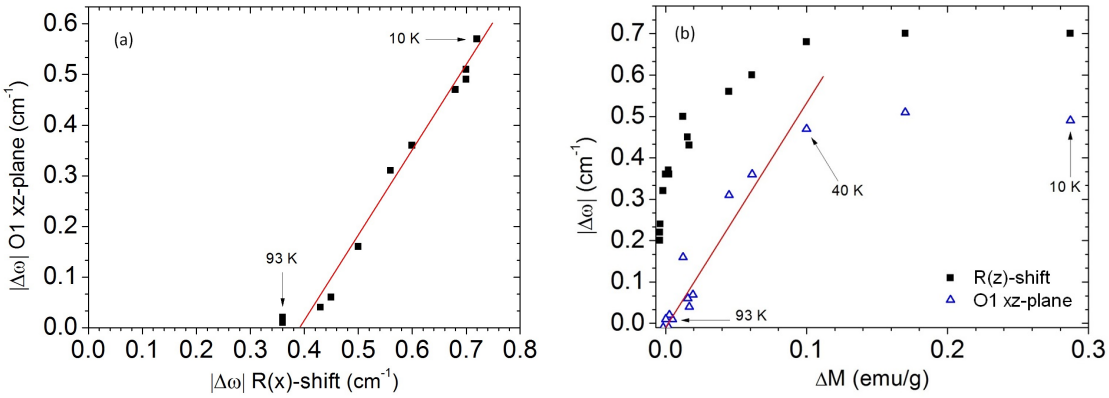

Figure 6.5: (a) Modulus of the wavenumber deviations ($\Delta\omega$) of Raman O1 xz-plane oscillation mode versus $\Delta\omega$ of Raman R(z)-shift mode, and (b) $\Delta\omega$ of both Raman modes as a function of the difference of net magnetization relatively to its maximum value for NdFeO$_3$.

spin-reorientation process, with the same mechanics of anti-parallel alignment of the Sm^{3+} spins. However, in SmFeO$_3$ the interaction between rare-earth and iron spins is the strongest in the RFeO$_3$ series [139]. Thus, in SmFeO$_3$, deviations below the spin-reorientation were also seen by Mads Weber, though stronger than in NdFeO$_3$ (up to 15 cm^{-1}) [130]. Namely, the Raman in-phase $[010]_{pc}$ octahedra rotation mode has a strong negative deviation, while the Raman R-shift modes have strong positive deviations [130]. Like in NdFeO$_3$, a coupling between these two modes could be ascertained in SmFeO$_3$.

6.3 Lattice dynamics of TbFeO$_3$

Since the Raman-active magnetic excitations were already studied in TbFeO$_3$ as a function of temperature, our attention turns to the temperature dependence of lattice modes. The spin-reorientation transition in TbFeO$_3$ only takes place at 6 K, below the minimum temperature that our cryogenic system can reach. Still, interesting temperature dependencies of some phonons can be studied using our Raman scattering data. Figures 6.6(a) to (e) show the wavenumber temperature dependence of the Raman anti-phase $[101]_{pc}$ octahedra rotation, O1 xz-plane oscillation, in-phase $[010]_{pc}$ octahedra rotation, R(x)-shift and R(z)-shift modes, respectively. Above 300 K, these modes wavenumbers follow the expected temperature dependence due to anharmonic effects arising from volume contraction (solid curve) [141].

The temperature behavior of the Raman anti-phase $[101]_{pc}$ octahedra rotation mode wavenumber exhibits a small upward deviation below 100 K, relatively to the extrapolated high temperature anharmonic trend (Figures 6.6(a)). However, no significant temperature anomalous behavior can be clearly observed for the Raman O1 xz-plane oscillation mode wavenumber. It is worth to stress that in NdFeO$_3$ the wavenumber temperature dependence of the Raman modes assigned to the same atomic motions display anomalous behavior at the temperature where the magnetization starts to decrease, mirroring the strong interplay between Nd- and Fe-sublattices in this compound.

Below 300 K, the Raman in-phase $[010]_{pc}$ octahedra rotation and R(z)-shift modes show a large upward deviation, relatively to the extrapolated high temperature behavior (Figures 6.6(c) and (e), respectively). Also, below 150 K, the Raman R(x)-shift mode presents a downward deviation (Figure 6.6(d)). We interpret the the set of results here presented as manifestation of the magnetic interaction between the Tb- and Fe-sublattices, although weaker than in the case of NdFeO$_3$. This assumption is corroborated by the rather low temperature

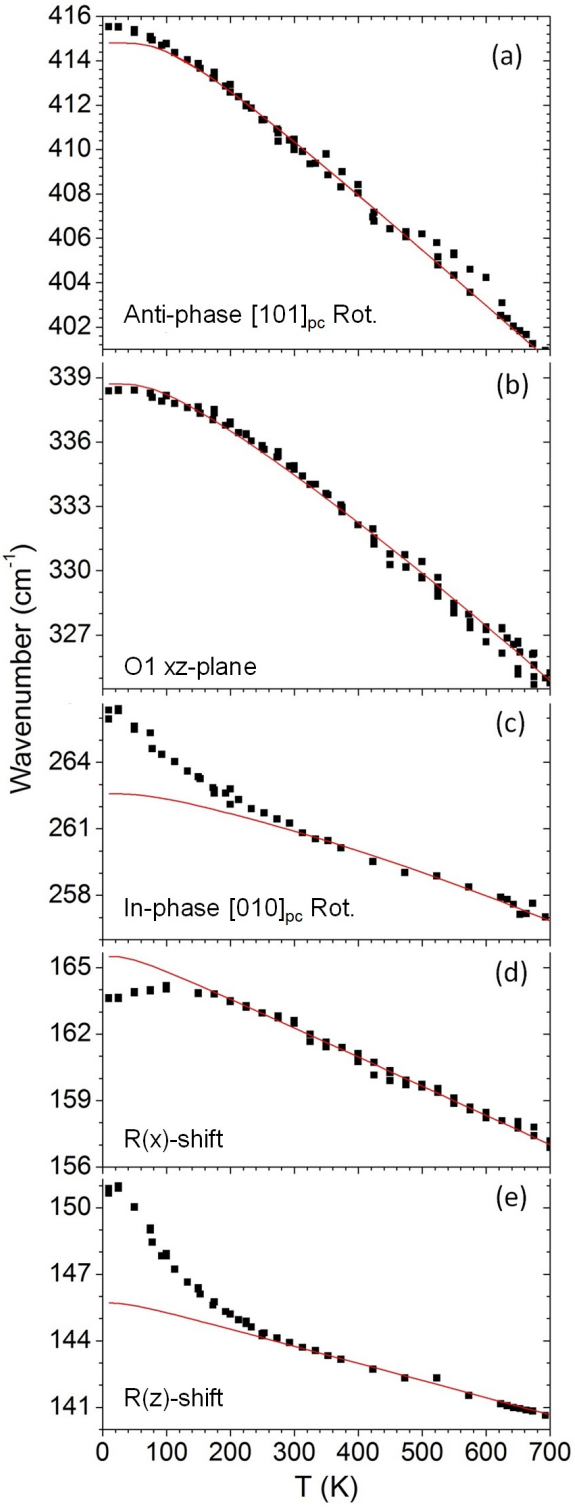

Figure 6.6: Wavenumber temperature dependence of (a) Raman anti-phase $[101]_{pc}$ octahedra rotation, (b) O1 xz-plane oscillation, (c) in-phase $[010]_{pc}$ octahedra rotation, (d) R(x)-shift and (e) R(z)-shift modes. The solid line was determined by the best fits of Equation 6.1 above 300 K and its extrapolation down to 10 K, for $TbFeO_3$.

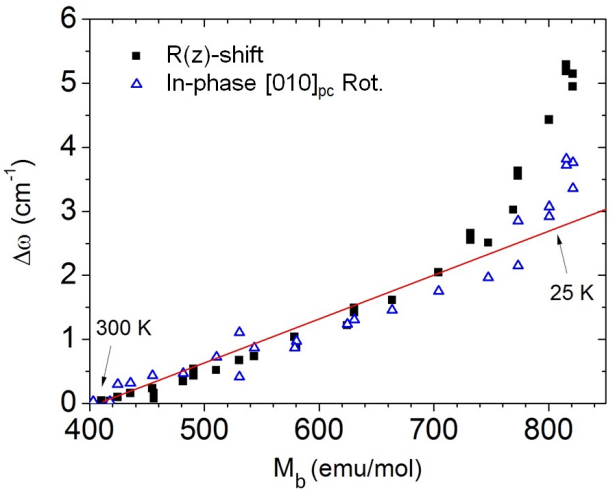

Figure 6.7: Wavenumber deviation ($\Delta\omega$) of Raman in-phase $[010]_{\rm pc}$ octahedra rotation (open triangles) and R(z)-shift (closed squares) modes as a function of magnetization along the b-axis (M_b) for TbFeO$_3$.

where the spin-reorientation transition takes place in TbFeO$_3$. To go further in this analysis, we have studied the correlation between the anomalous wavenumber deviation $\Delta\omega$ of the Raman in-phase $[010]_{\rm pc}$ octahedra rotation and R(z)-shift modes and the magnetization $M(T)$ in TbFeO$_3$. The magnetization has been found to be parallel to the b-axis and monotonously increases as temperature decreases below 300 K (cf. Figure 6.1(b)).

Figure 6.7 shows the anomalous wavenumber deviation ($\Delta\omega$) of the Raman in-phase $[010]_{\rm pc}$ octahedra rotation and R(z)-shift modes as a function of the magnetization along the b-axis (M_b). A linear dependence between $\Delta\omega$ and M_b could be ascertained for both these Raman modes. This last result corroborates the coupling between the oxygen octahedra rotations and the rare-earth against oxygen movements with the magnetism in TbFeO$_3$. It has been accepted that the magnetism in TbFeO$_3$ can be understood in terms of Fe-Fe and Fe-Tb interactions, the later involving significant van Vleck mechanism of the low lying electronic levels of Tb^{3+} ion. We interpret the anomalous temperature behavior of the Raman R(z)-shift mode below 300 K as a manifestation of the effect of the effective field created by the ordered Fe-sublattice on the Tb^{3+} spins. Our results here presented show that the Raman R(z)-shift mode are sensitive to the Tb-Fe interactions, although in this compound, these interactions are of the weakest among the RFeO$_3$ series, as the spin-reorientation occurs at much lower temperatures than PrFeO$_3$, NdFeO$_3$, SmFeO$_3$ and others [139].

6.4 Lattice dynamics of EuFeO$_3$ and GdFeO$_3$

Figures 6.8(a) to (j) show the wavenumber temperature dependence of the Raman anti-phase $[101]_{\rm pc}$ octahedra rotation, O1 xz-plane oscillation, in-phase $[010]_{\rm pc}$ octahedra rotation, R(x)-shift and R(z)-shift modes for GdFeO$_3$ and EuFeO$_3$. Except for the cases of the Raman in-phase $[010]_{\rm pc}$ octahedra rotation mode, the temperature dependence of the wavenumber of the remaining modes follow the normal anhamonic behavior from 10 to 875 K (solid curves) [141]. The absence of anomalous temperature behavior of all other Raman modes on both compounds sharply contrast with the results observed in NdFeO$_3$ and TbFeO$_3$. We interpret the lack of anomalies in the temperature dependence of the wavenumber of the aforementioned modes as a reflection of the the absence of a spin-reorientation transition in GdFeO$_3$ and EuFeO$_3$ and the weak or even absence of magnetic interactions between the Eu/Gd and Fe spins.

Surprisingly, the Raman in-phase $[010]_{\rm pc}$ octahedra rotation mode of GdFeO$_3$/EuFeO$_3$ temperature depen-

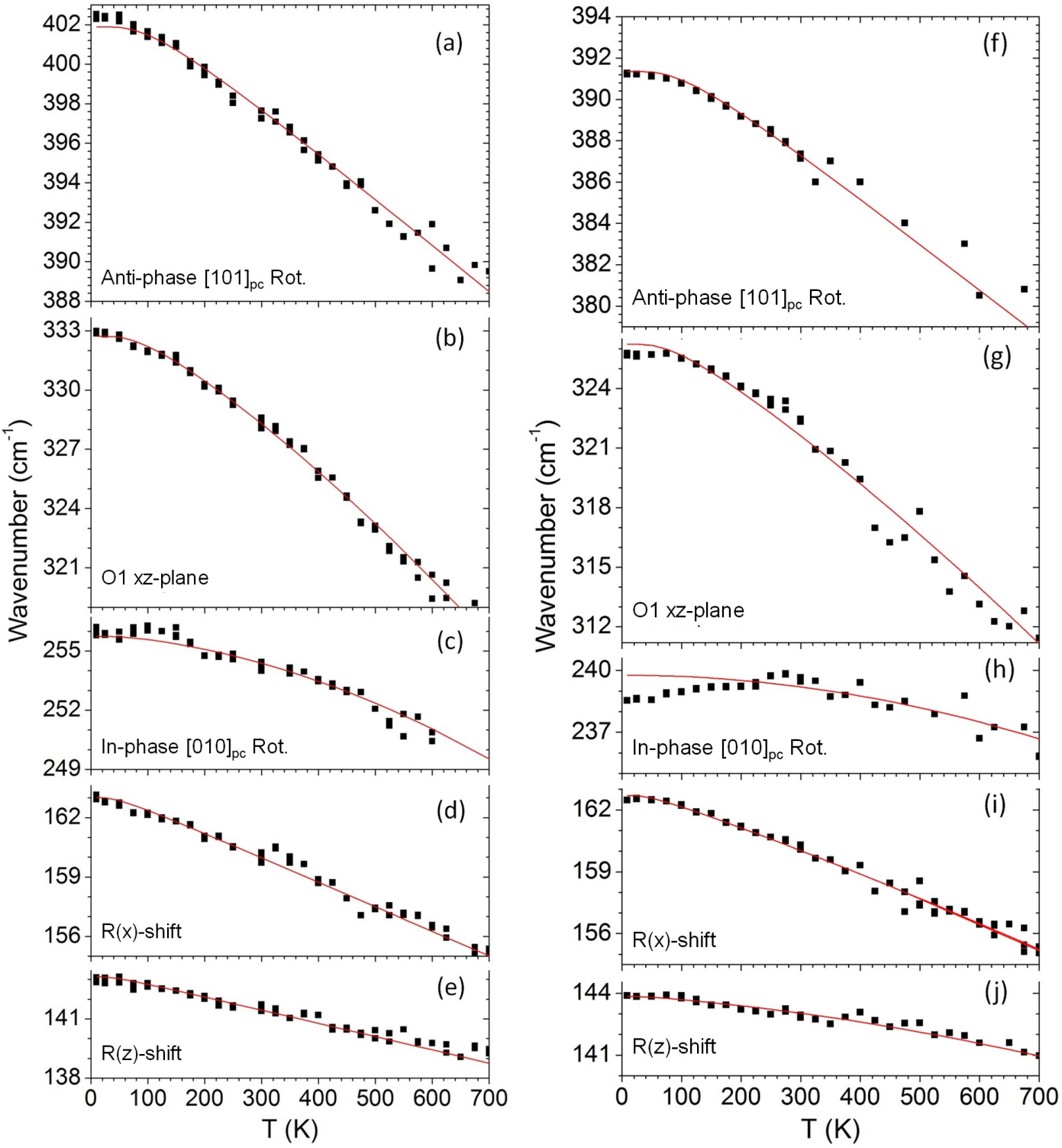

Figure 6.8: Wavenumber temperature dependence of (a)/(f) Raman anti-phase $[101]_{pc}$ octahedra rotation, (b)/(g) O1 xz-plane oscillation, (c)/(h) in-phase $[010]_{pc}$ octahedra rotation, (d)/(i) R(x)-shift and (e)/(j) R(z)-shift modes, with best fits of Equation 6.1 above 300 K and its extrapolation down to 10 K, for $GdFeO_3/EuFeO_3$.

dence exhibits a upward/downward deviation relatively to the extrapolated high temperature behavior below 200/300 K, as shown in Figure 6.8(c)/(h). The anomaly is more pronounced in the case of $EuFeO_3$ than in $GdFeO_3$. These anomalies do not match with any anomalous temperature behavior of the magnetization in both compounds, so a correlation between magnetic ordering and phonons cannot be reasonable. The anomaly referred to above is actually assigned to a change of structure associated with a tilt of the FeO_6 octahedra without any expression on the magnetic properties of $GdFeO_3$ and $EuFeO_3$ related with the Fe-sublattice. This issue deserves further research through temperature dependent x-ray or neutron diffraction to rule out the structural distortions occurring at low temperature.

6.5 Summary

In summary, we have shown the temperature evolution of the main Raman active modes in RFeO$_3$ from 10 to 875 K. From it, we have ascertained that when a spin-reorientation process occurs, most of the Raman modes are sensitive to it, as in the case of $NdFeO_3$. In $TbFeO_3$, where we did not reach the spin-reorientation temperature, we were still able to see the spin-phonon coupling in some of the Raman modes. Despite $GdFeO_3$ and $EuFeO_3$ not having any spin-reorientation process, the Raman in-phase $[010]_{pc}$ octahedra rotation mode still present anomalous deviations below 200 and 300 K, respectively. These deviations could not be attributed to any known phenomena, thus suggesting that these compounds should be further investigated.

Chapter 7

Suppression of Jahn-Teller distortion on $TbMn_{1-x}Fe_xO_3$ system

Up to this Chapter, we have focused our attention on the structural aspects of rare-earth manganites and ferrites. In this Chapter, we will address the structural study of the $TbMn_{1-x}Fe_xO_3$ solid solution, with $0 < x < 1$. It will offer the opportunity to adequately study structural distortions, in particular, Jahn-Teller distortion through the controlled substitution of Mn^{3+} by Fe^{3+}. The advantage arises from the fact that these cations have the same ionic radius for the high-spin configuration in the same coordination, though Mn^{3+} is Jahn-Teller active and Fe^{3+} inactive.

As it was clearly demonstrated in the last Chapters, Raman scattering has been amply used to study these distortions in the rare-earth manganites and ferrites and to monitor them as a function of temperature, pressure, chemical substitution, etc. [57, 75, 116]. The specific vibration modes, associated with the BO_6 rotations in particular, have been identified and studied in detail. In the case of the $R\mathrm{MnO}_3$, it was shown that the wavenumber of the Raman in-phase $[010]_{\mathrm{pc}}$ and anti-phase $[101]_{\mathrm{pc}}$ octahedra rotation modes scale linearly with the respective tilt angles [113]. This was observed later in a wide variety of *Pnma* perovskites [30], namely in the rare-earth ferrites, presented in Chapter 4, where a rationale was proposed in terms of a simple and general Landau model that clarifies why the Raman octahedra rotation modes wavenumber can be taken as a measure for the tilt angle itself [31]. However, the specific effect of the cooperative Jahn-Teller distortion has so far been ignored in these approaches. It is the aim of this study to fill this gap by examining the evolution of the Raman octahedra rotation modes in a system where the Jahn-Teller distortion is continuously tuned.

This Chapter addresses the structural changes induced by substituting the Jahn-Teller-active Mn^{3+} ion by the Jahn-Teller-inactive Fe^{3+}. For this study, we have chosen the rare-earth to be Tb, being the studied system $TbMn_{1-x}Fe_xO_3$, since $TbMnO_3$ is a well known multiferroic, whose low-temperature magnetoelectric properties will be addressed in the next Part of this thesis. We follow the x-dependency of the Jahn-Teller distortion amplitude from $x = 0.0$ to 1.0. We also correlate this evolution with the behavior of the Raman modes across the solid solution. In particular, we investigate the sensitivity of the Raman octahedra rotation modes wavenumber to the amplitude of the Jahn-Teller distortion.

7.1 Experimental results of XRD and Raman Scattering

Figure 7.1(a) shows representative x-ray diffraction patterns obtained at ambient conditions for some compounds of the $TbMn_{1-x}Fe_xO_3$ series, from $x = 0$ to 1, in the 20 to 35 degrees in 2θ range. The x-ray

diffraction patterns reveal good crystallinity of the samples. Figure 7.1(b) shows the full Rietveld refinement for the composition $x = 0.6$, as a representative result.

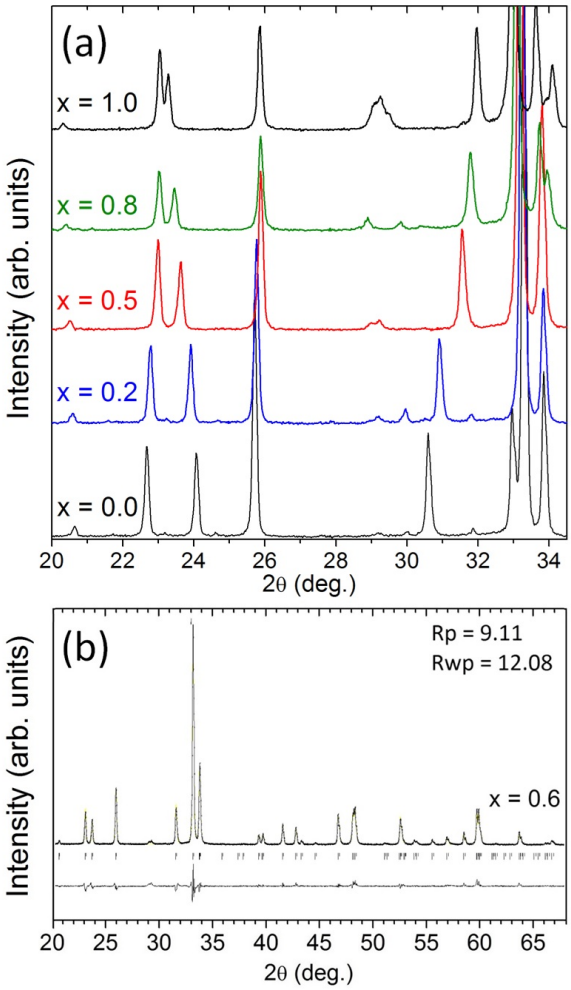

Figure 7.1: (a) Representative x-ray diffraction patterns of $TbMn_{1-x}Fe_xO_3$, for x = 0.0, 0.2, 0.5, 0.8, and 1.0 at ambient conditions. (b) Representative example of Rietveld refinement for $x = 0.6$. Measurements and Rietveld refinement done by Pedro Tavares group.

The substitution of Mn^{3+} by Fe^{3+} promotes regular changes in the x-ray diffraction pattern profile throughout the series, and matches the expected *Pnma* space group of the end members for the entire solid solution. Table 7.1 present the obtained atomic coordinates from the refinement for x = 0 to 1.

Figure 7.2(a) shows the Raman spectra of $TbMn_{1-x}Fe_xO_3$ (for x = 0.0, 0.2, 0.5, 0.8, and 1.0), recorded at ambient conditions. The predicted Raman-active vibration modes are the same throughout the entire series since the space group and site symmetries of the atoms are maintained. Out of the possible 24 Raman-active modes, we were able to identify 14 to 18 bands for the end members $TbMnO_3$ and $TbFeO_3$, respectively, in agreement with previous studies, such that of Chapter 4 [31, 113].

Interestingly, the spectral weight is changing throughout the series. While we find bands of similar intensity in the spectra of iron-rich compounds, high wavenumber bands (above 350 cm^{-1}) dominate the spectra of Mn-rich components. As the Fe content increases from $x = 0$ up to 0.7, a continuous increase of the linewidth and a decrease of the band intensity is ascertained from Figure 7.2(a), resulting in very broad bands, especially in the concentration range of x = 0.5 to 0.7. This feature prevented us from accurately determining

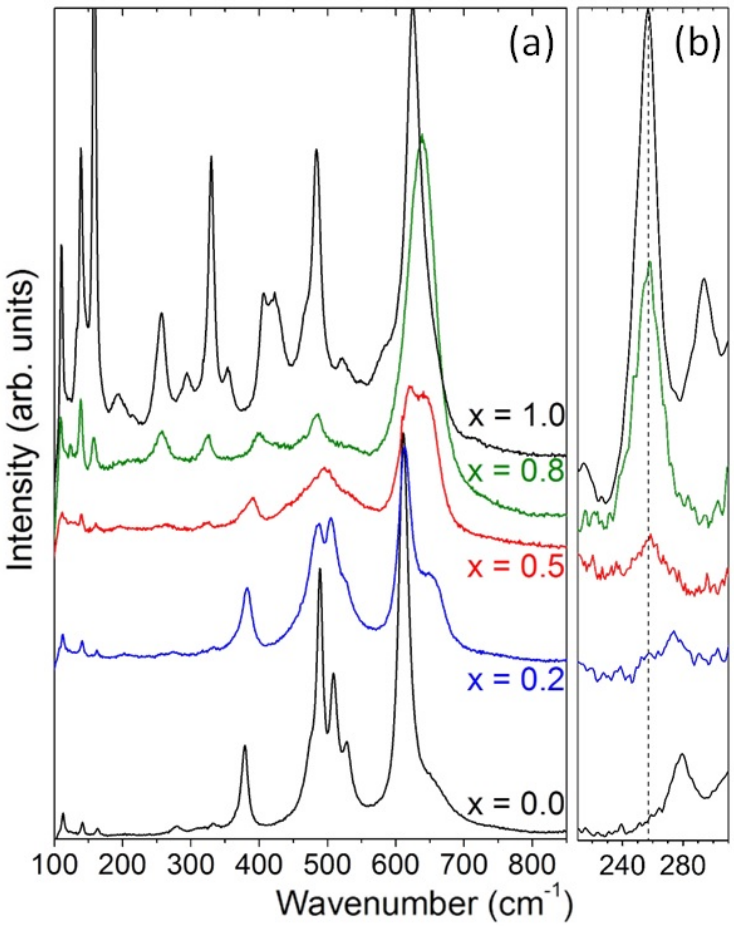

Figure 7.2: (a) Raman spectra at ambient conditions of the $TbMn_{1-x}Fe_xO_3$, for x = 0.0, 0.2, 0.5, 0.8 and 1.0. (b) Enlarged view of the 220 to 300 cm^{-1} spectral range.

Composition (x)	Cell parameters (Å)	Atom	x-position	y-position	z-position
0.0	a = 5.849(4)	Tb	0.06812(6)	0.25000	-0.01690(6)
	b = 7.402(1)	Mn	0.00000	0.00000	0.50000
	c = 5.299(6)	O1	0.47743(8)	0.25000	0.09748(6)
	V = 229.4(6)	O2	0.18909(8)	0.54911(7)	0.20266(3)
0.1	a = 5.820(4)	Tb	0.0789(1)	0.25000	-0.01584(1)
	b = 7.428(6)	Mn/Fe	0.00000	0.00000	0.50000
	c = 5.301(1)	O1	0.4479(4)	0.25000	0.1941(8)
	V = 229.2(1)	O2	0.1777(5)	0.5557(5)	0.1941(8)
0.2	a = 5.792(6)	Tb	0.07883(4)	0.25000	-0.01689(9)
	b = 7.453(5)	Mn/Fe	0.00000	0.00000	0.50000
	c = 5.304(2)	O1	0.4704(6)	0.25000	0.1064(8)
	V = 229.0(1)	O2	0.1849(7)	0.5517(7)	0.2026(5)
0.3	a = 5.765(1)	Tb	0.07303(8)	0.25000	-0.01643(2)
	b = 7.479(5)	Mn/Fe	0.00000	0.00000	0.50000
	c = 5.305(3)	O1	0.466(2)	0.25000	0.1040(3)
	V = 228.7(6)	O2	0.1822(3)	0.5488(7)	0.1973(2)
0.4	a = 5.736(8)	Tb	0.07318(5)	0.25000	-0.01644(7)
	b = 7.505(7)	Mn/Fe	0.00000	0.00000	0.50000
	c = 5.308(4)	O1	0.4697(2)	0.25000	0.10364(4)
	V = 228.5(7)	O2	0.1831(6)	0.5477(8)	0.19780(5)
0.5	a = 5.707(5)	Tb	0.07084(1)	0.25000	-0.0170(5)
	b = 7.534(6)	Mn/Fe	0.00000	0.00000	0.50000
	c = 5.311(8)	O1	0.46565(9)	0.25000	0.09827(8)
	V = 228.4(3)	O2	0.18794(7)	0.54832(1)	0.18980(6)
0.6	a = 5.683(5)	Tb	0.07068(5)	0.25000	-0.01736(8)
	b = 7.557(8)	Mn/Fe	0.00000	0.00000	0.50000
	c = 5.314(9)	O1	0.4716(2)	0.25000	0.1017(8)
	V = 228.3(1)	O2	0.1922(7)	0.5498(3)	0.1981(2)
0.7	a = 5.659(3)	Tb	0.06648(3)	0.25000	-0.01691(6)
	b = 7.580(1)	Mn/Fe	0.00000	0.00000	0.50000
	c = 5.318(6)	O1	0.45941(2)	0.25000	0.09016(8)
	V = 228.1(6)	O2	0.1918(8)	0.5564(4)	0.1911(7)
0.8	a = 5.637(9)	Tb	0.06540(5)	0.25000	-0.01598(1)
	b = 7.600(1)	Mn/Fe	0.00000	0.00000	0.50000
	c = 5.321(5)	O1	0.4573(1)	0.25000	0.10780(5)
	V = 228.0(2)	O2	0.4573(1)	0.5585(9)	0.1869(5)
0.9	a = 5.611(2)	Tb	0.0661(2)	0.25000	-0.01721(3)
	b = 7.626(2)	Mn/Fe	0.00000	0.00000	0.50000
	c = 5.327(2)	O1	0.4759(7)	0.25000	0.0955(2)
	V = 227.9(5)	O2	0.1918(4)	0.5477(9)	0.2003(2)
1.0	a = 5.598(4)	Tb	0.06430(2)	0.25000	-0.01638(0)
	b = 7.641(5)	Fe	0.00000	0.00000	0.50000
	c = 5.328(1)	O1	0.4876(5)	0.25000	0.0953(2)
	V = 227.9(4)	O2	0.1862(2)	0.5506(1)	0.1913(6)

Table 7.1: Cell parameters and atomic fractional coordinates obtained from the Rietveld refinement of $TbMn_{1-x}Fe_xO_3$ x-ray diffraction patterns.

	$TbMnO_3$		$TbFeO_3$		
Symm.	Exp.	Exp.	Exp.	Calc.	Main atomic motion
A_g	113	N/A	111	112	Tb(z), in-phase in x-z, out-of-phase in y
A_g	141	N/A	139	136	Tb(z), out-of-phase
B_{2g}	164	N/A	159	161	Tb(x), out-of-phase
A_g	280	280	257	259	$[010]_{pc}$ BO_6 rotation, in-phase
A_g	379	378	406	410	$[101]_{pc}$ BO_6 rotation, out-of-phase

Table 7.2: Symmetry, wavenumber (in cm^{-1}), and atomic motions of the Raman bands assigned to the Tb^{3+} motions and BO_6 rotation motions in $TbMnO_3$ and $TbFeO_3$, along with expected values after Refs. [31, 113].

the wavenumber of the A_g-symmetry doublet located around 500 cm^{-1}, assigned to B-O-B bending-type vibration and the asymmetric stretching Jahn-Teller-type vibration, which may cross with the B_{2g} symmetry shoulder-like bands [31, 113]. For higher Fe content, the bands sharpen again as the disorder decreases. The nature of the band located at around 645 cm^{-1}, whose intensity strongly depends on Fe concentration, was already discussed in Chapter 4 and we will skip it in this Chapter. The symmetric stretching Jahn-Teller-type vibration of the BO_6 octahedra with symmetry B_{2g} is located at 620 cm^{-1} for the $TbMnO_3$ [31, 113]. So, it is difficult to disentangle the Jahn-Teller-sensitive B_{2g} band from the other higher-frequency spectral contribution. However, none of this is a problem for the objectives of this work, which is focused on the purely rigid Raman octahedra rotation modes [30, 31, 113]. Table 7.2 summarizes the symmetry, wavenumbers (experimental and calculated), and the main atomic motions involved in the vibrations that will be discussed in this work, concerning the $TbMnO_3$ and $TbFeO_3$. Figure 7.2(b) shows an enlarged view of the 220 to 300 cm^{-1} spectral range that will be discussed below.

7.2 Suppression of the cooperative Jahn-Teller distortion

Figure 7.3(a) shows the x-dependence of the pseudocubic lattice parameters and cell volume for the entire series, obtained from the Rietveld analysis of the x-ray diffraction patterns. The total volume variation across the whole substitution range is of 0.7%, which is the known value for the total suppression of the Jahn-Teller distortion [21]. The lattice parameters follow linear x-dependencies between the two end members. Figure 7.33(b) shows the x-dependence of the three symmetry-inequivalent mean bond lengths of the B-site cation (Mn^{3+} or Fe^{3+}) to the surrounding oxygen ions throughout the series. For clarity, Figure 7.3(c) shows a schematic c-axis view of the pseudocubic cell of $TbMnO_3$, where s, m, and l denote the short, medium, and long B-O bonds, respectively. For $x < 0.5$, three distinct values of the mean B-O bond lengths are found, which is typical for Jahn-Teller-distorted systems [33]. The mean B-O bond lengths get closer to each other; i.e., the total distortion decreases as the compound becomes Fe^{3+} richer up to $x = 0.5$. Thereafter, it becomes almost x-independent, with the medium and short bond lengths stabilizing into a similar value, but different from the long bond one. This is typically found in rare-earth ferrites [33]. The remaining difference emerges simply from the intrinsic octahedra distortion due to the existence of two anti-phase tilts, always present in $Pnma$ perovskites [18]. The significant x-dependence of the short and long mean B-O2 bond lengths indicates that the distortions mainly occur in the ac-plane.

As an alternative way to get insight into the structure evolution, we performed a symmetry-adapted mode decomposition of the distortions present in the $Pnma$ structure with respect to their associated irreducible representations of the $Pm\bar{3}m$ parent structure, using the Amplimodes tool of the Bilbao Crystallographic Server [22, 123]. As discussed on Chapter 4, the decomposition yields five symmetry-adapted modes, associated with octahedral tilts about the $[101]_{pc}$ and $[010]_{pc}$ axes (with R4+ and M3+ symmetries, respectively), anti-polar displacements of Tb and O in the ac-plane (with X5+ symmetry), Tb displacements (with R5+

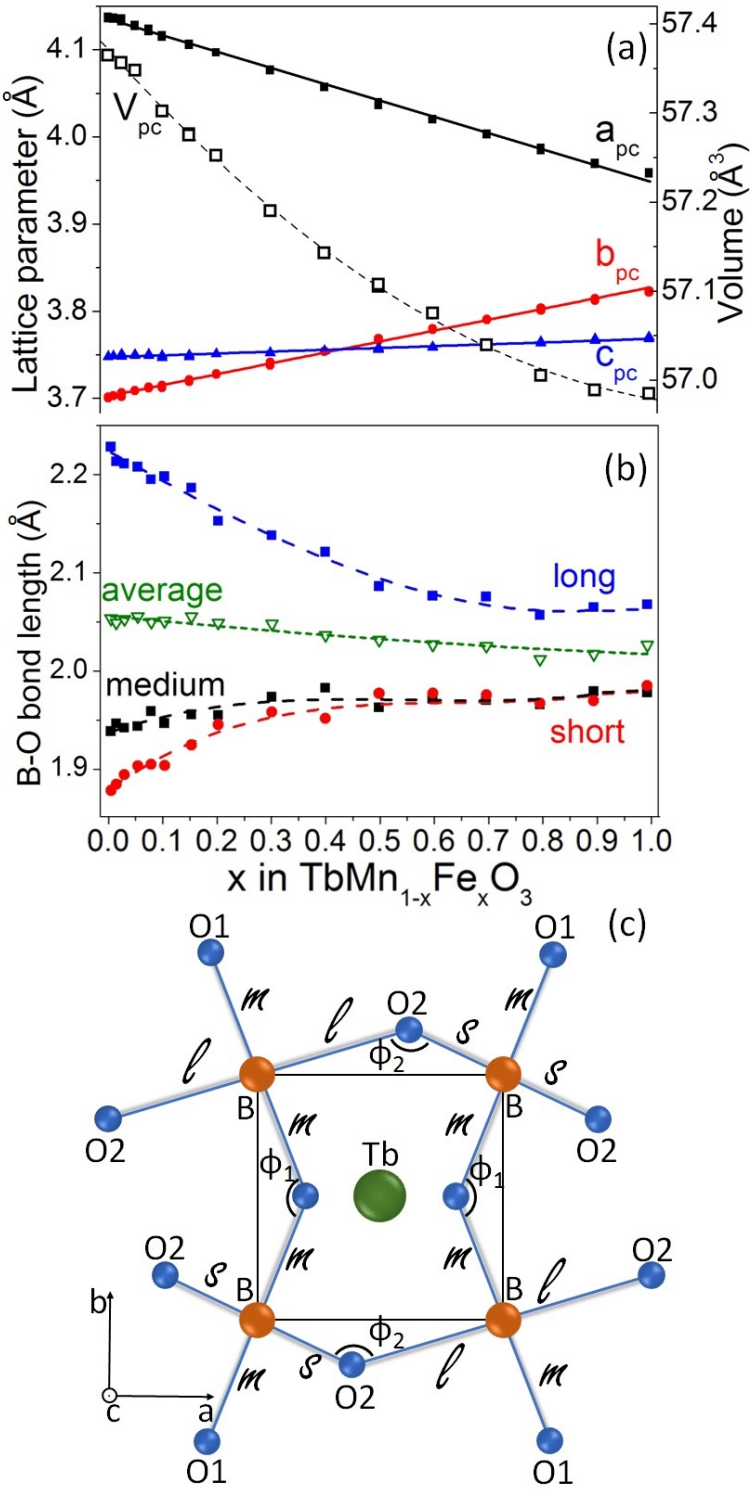

Figure 7.3: (a) x dependence of the pseudocubic lattice parameters (closed symbols) and volume (open symbols), and (b) of the three symmetry-inequivalent mean B-O bond lengths (closed symbols) and their average (open symbols). (c) c-axis view of the pseudocubic cell of $TbMnO_3$. s, m, and l stand for the short, medium, and long B-O bonds, whereas ϕ_1 and ϕ_2 correspond to the $[101]_{pc}$ and $[010]_{pc}$ tilt angles, respectively.

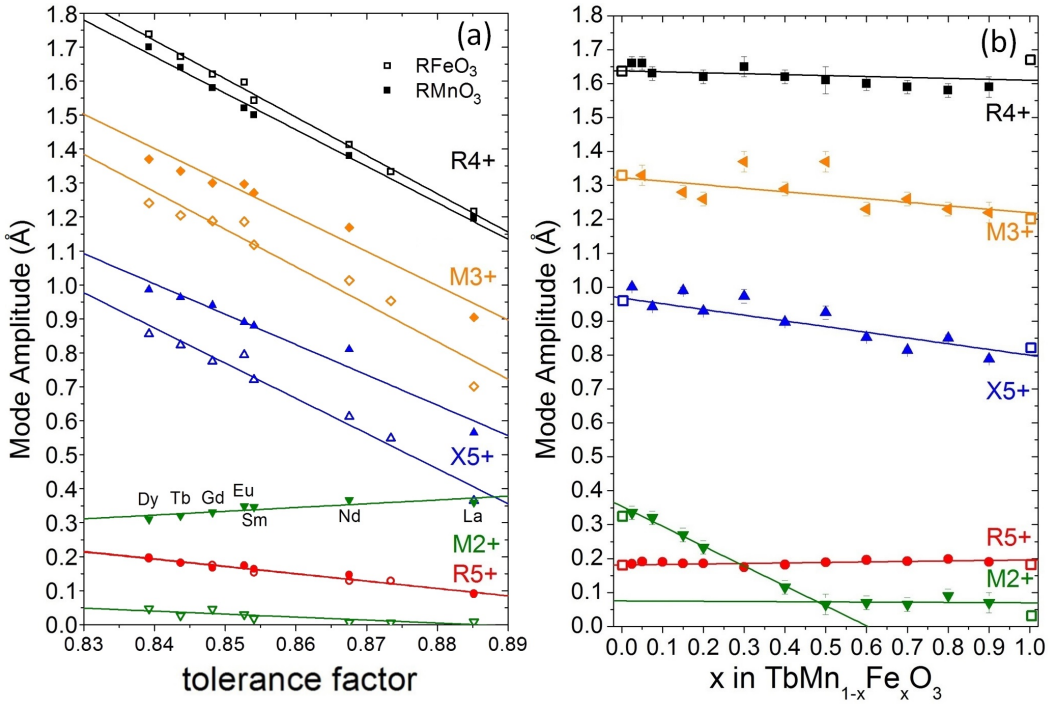

Figure 7.4: (a) Tolerance factor and (b) x-dependencies of the amplitude of the five symmetry-adapted modes in RMnO$_3$, RFeO$_3$ and $TbMn_{1-x}Fe_xO_3$ series. Open symbols in (b) are reference values of parent compounds shown in (a).

symmetry), and octahedra distortion (with M2+ symmetry), whose sketch was presented in Figure 1.4.

Figure 7.4(a) presents the tolerance factor dependence of the five symmetry-adapted modes for the RMnO$_3$ and RFeO$_3$ series. The values and their evolution are the same in both families for most distortions, namely the R4+ and M3+ ones, associated with the octahedra tilts, except for the case of the M2+ one. This is because the M2+ reflects the deformation of the BO_6 octahedra, which is much larger in RMnO$_3$ than in RFeO$_3$, due to the Jahn-Teller effect.

To study the distortions evolution from RMnO$_3$ to RFeO$_3$, Figure 7.4(b) presents the x-dependence of the five symmetry-adapted modes for $TbMn_{1-x}Fe_xO_3$. The x dependence of the amplitude of the M2+ distortion, associated with the BO_6 octahedra deformation, corroborates the conclusions drawn from the x-dependence of the B-O bond lengths. Its amplitude decreases from 0.35 Å as x increases up to 0.5, stabilizing below 0.10 Å above this value. The larger amplitudes obtained for $x < 0.5$ give evidence for a larger octahedra deformation arising from the Jahn-Teller distortion, while for $x > 0.5$ the rather small amplitudes are of the order of the ones observed in non-Jahn-Teller systems, such as the RFeO$_3$, shown in Figure 7.4(a).

The x-dependencies of the three symmetry-inequivalent mean B-O bond lengths and the amplitude of the symmetry-adapted mode associated with octahedra distortion (M2+) are self-consistent and allow us to ascertain that the cooperative Jahn-Teller distortion in the solid solution decreases up to $x = 0.5$, above which the cooperative distortion is suppressed. This critical value of $x = 0.5$ is remarkably similar to the values found in previous studies of $DyMn_{1-x}Fe_xO_3$ and $LaMn_{1-x}Ga_xO_3$ [84, 107], and so far appears as a common behavior for these solid solutions.

7.3 Jahn-Teller distortion and Raman octahedra rotation modes

Figure 7.5(a) shows the x-dependence of the wavenumber of the Raman-active vibration modes assigned to Tb^{3+} translations and rigid octahedra rotations over the full solid solution. Two types of x-dependencies of the Raman modes wavenumbers can be ascertained. The wavenumber of the Raman modes involving Tb^{3+} motion behaves linearly with x, decreasing as x increases. This evidences the weakening of the interactions between those ions and the neighboring oxygen ions, pointing at a decrease of the AO_{12} dodecahedra deformation. This feature is also reflected in the amplitude of the associated X5+ distortion, due to the average decrease of the BO_6 octahedra deformation.

The wavenumbers of the Raman octahedra rotation modes exhibit more complex x-dependencies, with a kink located close to $x = 0.6$. The wavenumber behavior below and above this concentration limit is linear, but with different slopes. The wavenumber of the Raman anti-phase $[101]_{pc}$ octahedra rotation mode increases with x, but the slope of the linear relation changes from 19 ± 1 cm^{-1} in the first x range to 39 ± 2 cm^{-1} in the second. On the other hand, the wavenumber of the Raman in-phase $[010]_{pc}$ octahedra rotation mode is a decreasing linear function for $x < 0.6$, and is almost constant on further increasing x, exhibiting a drastic change of slope near $x = 0.6$, whose modulus decreases from 39 ± 3 to 3 ± 2 cm^{-1}.

Considering that the kinks in the x-dependencies of the Raman octahedra rotation modes wavenumbers occur nearly at the composition wherein the cooperative Jahn-Teller distortion is suppressed, we propose that these Raman modes do not exclusively mirror the tilts, but also the octahedra distortions. The correlation is particularly striking for the Raman in-phase $[010]_{pc}$ octahedra rotation mode, whose wavenumber scales directly with the extent of the octahedra deformation as measured by the amplitude of the associated M2+ distortion (Figure 7.5(b)). Qualitatively, the strong coupling between the BO_6 distortion and this particular Raman mode can be understood by recalling that the latter essentially involves motions of the oxygen ions that are associated with the cooperative Jahn-Teller distortion (see sketch in Figure 7.5(b)). It is not clear how to interpret the small difference in the critical x-values found in x-ray diffraction and Raman scattering ($x = 0.5$ and 0.6, respectively). It could be a result of experimental uncertainty, and difficulty of fitting Equation 2.2 to the Raman modes in this Fe-concentration region. It might also emerge from the fact that x-ray diffraction and Raman scattering probe materials at different coherence lengths, so that Raman scattering would still feel the cooperative Jahn-Teller distortion in a slightly broader range than x-ray diffraction [143].

The solid solution, at room temperature, goes from paramagnetic for $TbMnO_3$ to antiferromagnetic for $TbFeO_3$, which might influence the Raman wavenumbers via spin-phonon coupling. However, taking into account the data available in literature for RMnO$_3$[113],and in Chapter 4 of this thesis for RFeO$_3$, it cannot justify the 20 cm^{-1} deviation away from a simple linear behavior [116].

It is thus clear that the wavenumbers of the two Raman octahedra rotation modes cannot simply scale linearly with the tilt angles over the whole composition range, since the tilt angles behave linearly throughout the series, as measured by the amplitudes of the associated M3+ and R4+ distortions (cf. Figure 7.4(b)). However, in this case, the mean B-O bond length is constant in all the series and a unique linear relation of the wavenumber of the Raman octahedra rotation modes with x is not observed (cf. Figure 7.3(b)).

7.4 Relation to Landau theory

The linear relation between the octahedra tilt angles and the wavenumbers of their corresponding Raman octahedra rotation modes, observed experimentally in a plethora of *Pnma* perovskites, was recently given physical foundation in a simple and general Landau model in Chapter 4 [31]. This model only takes into account the basic relevant ingredients with primary order parameters associated with the octahedra tilts, but it does not take into account the possibility of cooperative Jahn-Teller distortion. Thus, it cannot be applied

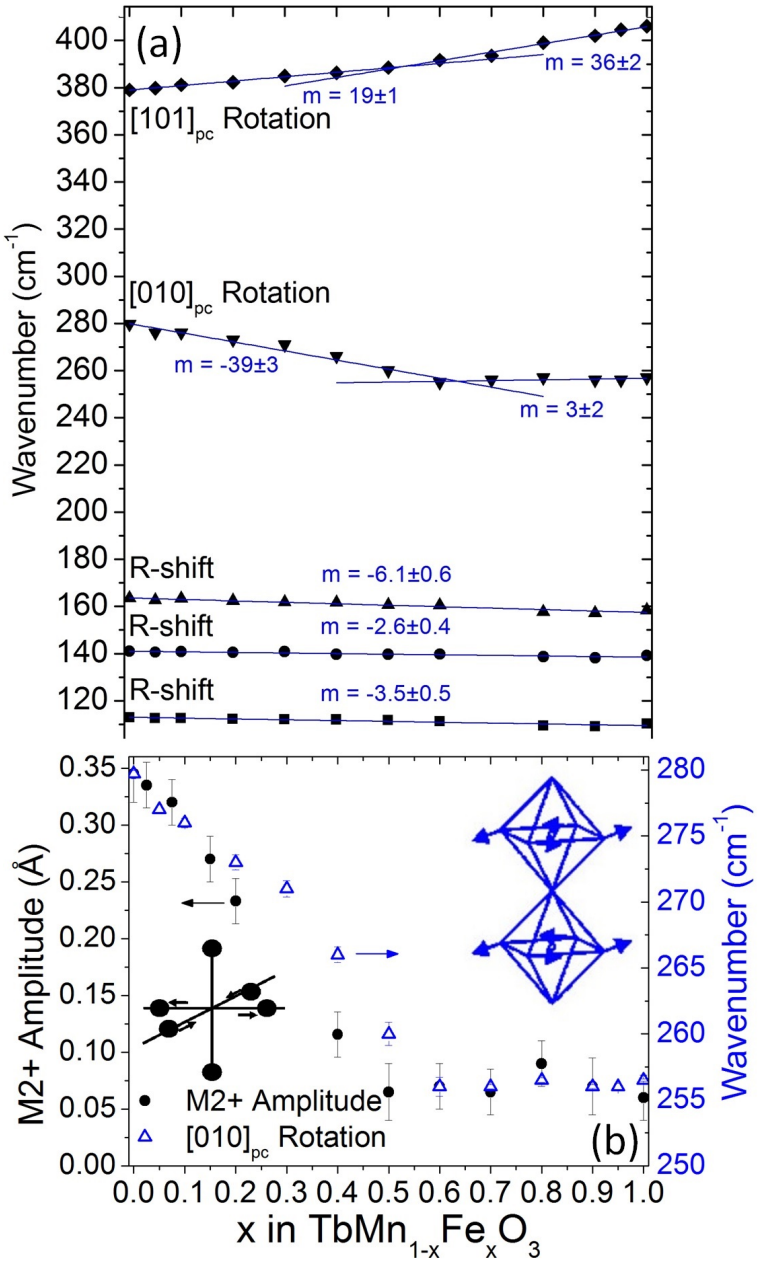

Figure 7.5: (a) Wavenumber of the Raman R-shifts modes and Raman in-phase $[010]_{pc}$ and anti-phase $[101]_{pc}$ octahedra rotation modes as a function of x. The error bars are smaller than the symbols. Slopes of linear relations also displayed. (b) Raman in-phase $[010]_{pc}$ octahedra rotation mode wavenumber (open symbols) and M2+ distortion amplitude (closed symbols) x-dependencies.

directly to solid solutions, as it is in the case of $TbMn_{1-x}Fe_xO_3$, in which this distortion varies. As we have just demonstrated that the cooperative Jahn-Teller distortion does have a sizable influence on the Raman octahedra rotation mode wavenumbers, it is necessary to slightly modify this model to fully understand this behavior.

In order to take into account the influence of Jahn-Teller distortion to the model referred on Chapter 4, we have to add to the Landau expansion the relevant energy terms as:

$$\alpha_{JT} Q_{JT}^2 + \lambda_{JT-tilt} Q_{JT}^2 Q_{tilt}^2 \,, \tag{7.1}$$

where the latter is a coupling term between the tilt-order parameters with either R4+ or M3+ symmetry and the cooperative Jahn-Teller distortion, with symmetry M2+. In all cases, the coupling term is biquadratic [23]. This makes the soft-mode (the rotation mode wavenumber in our case) dependent on the equilibrium value of the cooperative Jahn-Teller distortion strength, which qualitatively explains our observation. On the other hand, it is important to point out that this coupling is by no means specific to the tilts: the Jahn-Teller order parameter may couple biquadratically with the other secondary distortions. For example the X5+ associated with the antiparallel motion of Tb^{3+} cations, and thus, there is no symmetry reason determining which Raman modes will behave linearly and which will not. Instead, the differences in behaviors must be interpreted as originating from differences in coupling strengths. For that reason, it is delicate to extrapolate our results to other similar solid solutions, even though similar behaviors may be expected.

With this in mind, we can now clarify the role of Jahn-Teller distortions in the Raman spectra of $R MnO_3$. The linear scaling between tilt angle and Raman octahedra rotation mode wavenumber [31], according to our findings, only holds because the equilibrium value of Jahn-Teller distortion is maintained, as it is shown in Figure 7.4(a). A reinvestigation of this archetypal case in the light of the recent developments might be useful to refine this interpretation.

7.5 Summary

In summary, we have studied the changes on the structure and lattice dynamics for the $TbMn_{1-x}Fe_xO_3$ solid solution, by x-ray diffraction and Raman scattering. First, we have shown that substitution of the Jahn-Teller-active Mn^{3+} ion by the Jahn-Teller-inactive Fe^{3+} results in a suppression of the cooperative Jahn-Teller distortion for $x > 0.5$. This result appears to be a universal behavior, at least at the level of the long-range structure, for solid solutions between a Jahn-Teller-distorted and a non-Jahn-Teller-distorted perovskite of otherwise similar structures. Second, we have ascertained that Raman mode wavenumbers show different x-dependencies. The wavenumber of the Raman octahedra rotation modes exhibits non-unique linear evolution in the whole x-range. This cannot be simply due to the linear scaling between wavenumber and tilt angle, even when the average B-O distance is taken into account. We have shown that the Raman octahedra rotation modes wavenumber correlates with the amplitude of Jahn-Teller distortion. This calls for some care in the interpretation of the Raman studies of Jahn-Teller-distorted perovskites.

Having embraced the structural properties and dynamics of the parent compounds ($R MnO_3$ and $R FeO_3$) and of the solid solution $TbMn_{1-x}Fe_xO_3$, we will address in the following the physical properties at low temperatures of $TbMn_{1-x}Fe_xO_3$.

Part III

Physical Properties

Chapter 8

Magnetic properties and phase diagram of $TbMn_{1-x}Fe_xO_3$ system

Once presented a deeply study of the structure and lattice dynamics of rare-earth manganites, rare-earth ferrites under external parameters, and $TbMn_{1-x}Fe_xO_3$ mixed system, we will focus our attention on the physical properties of the $TbMn_{1-x}Fe_xO_3$ on the second part of this thesis. The phase diagrams of both rare-earth manganites and rare-earth ferrites are well established in the literature. However, the phase diagrams of $RMn_{1-x}Fe_xO_3$ solid solutions are incomplete or still missing. A first attempt of the magnetic phase diagram of $TbMn_{1-x}Fe_xO_3$ solid solution was recently reported in the concentration range $0 \leq x \leq 0.5$ by Hong et al. [86].

In this Chapter we will address to the magnetic phase diagram of the $TbMn_{1-x}Fe_xO_3$ solid solution in a much larger concentration range from $x > 0.05$. The $0 \leq x \leq 0.05$ region will be touched on in the following Chapters, as the compounds in this concentration range exhibit multiferroic properties at low temperatures, which deserve a different experimental approach. The presented magnetic phase diagram is traced by considering the anomalies observed in the temperature dependence of both specific heat and magnetization.

For easiness, this Chapter is divided into sections dealing with concentration ranges that present the same phase sequence. The last section deals with the construction of the magnetic phase diagram from all obtained experimental data, including already published results of magnetic structures determined by neutron diffraction measurements. This is the main goal of this Chapter.

8.1 Concentration range $0.05 < x < 0.2$

The temperature dependence of the specific magnetization is shown in Figures 8.1(a) and (b) show, measured in zero-field cooling (ZFC) and field-cooling (FC) conditions under a magnetic field of 0.004 T, for $x = 0.05$ and 0.1, respectively. The M(T) curves point for the existence of a weak spontaneous magnetization at low temperatures evidenced from the deviation to higher magnetization values of the curve measured under FC relatively to that measured under ZFC conditions. This magnetization likely emerges due to spin canting, which points to the stabilization of a canting-antiferromagnetic phase. Figures 8.1(c) and (d) show the temperature dependence of the H/M(T) for the same compounds. Above a certain temperature, which is strongly dependent on the Fe-content, the H/M(T) follow a linear temperature behavior. The temperature below which the H/M curves deviates from the linear temperature behavior defines the Néel temperature at 45 and 50 K, for $x = 0.05$ and 0.1, respectively. The linear temperature behavior of H/M(T), above the Néel temperature, is well described by a Curie-Weiss law:

$$\chi = \frac{C}{T - \theta_p}\,, \tag{8.1}$$

where C and θ_p stand for the Curie-Weiss constant and the Curie-Weiss temperature, respectively. From the best fits above the Néel temperature, extrapolated to negative temperatures, the obtained values of θ_p were of -30 and -31 K, with a magnetic moment of 10.50 and 9.24 μ_B, for $x = 0.05$ and 0.1, respectively.

Figure 8.1(e) shows the temperature dependence of the specific heat of $TbMn_{1-x}Fe_xO_3$, with $x = 0.075$ and 0.1, measured by Mihalik's Group. Two anomalies in the temperature dependence of the specific heat can be observed. The highest temperature anomaly occurs at 30 and 32 K, for $x = 0.075$ and 0.1, respectively. Taking into account the results obtained in $DyMn_{1-x}Fe_xO_3$ systems, we assign the first anomaly to the paraelectric modulated antiferromagnetic phase transition [84, 85]. This result clearly points out that the Néel temperature decreases from 42 K for $TbMnO_3$ to 33 K in $TbMn_{0.9}Fe_{0.1}O_3$, pointing out that the substitution of Mn by Fe destabilizes the sinusoidal collinear incommensurate antiferromagnetic phase. The second anomaly is observed at 6.5 K for both compounds. Based on neutron diffraction and specific heat data, Aliouane *et al.* reported the ordering of the Tb^{3+}-sublattice in $TbMnO_3$ at 7 K [144]. Thus, we also assign the anomaly observed in our specific data to the same process for concentrations $x > 0$. It is worth to note that no other anomaly could be observed in the temperature dependence of the specific heat, so we conclude that the lock-in transition is absent for $x = 0.075$ and 0.1. This result means that the ferroelectric phase is no longer stabilized in these compounds. We shall come back to this issue in the next Chapters.

8.2 Concentration range $0.2 \leq x < 0.5$

Figures 8.2(a) and (b) show the temperature dependence of the specific magnetization, measured in ZFC and FC conditions, also under a magnetic field of 0.004 T, for $x = 0.2$ and 0.3, respectively. In these cases, the M(T) curves also evidence the existence of a weak spontaneous magnetization at low temperatures, as for $x = 0.05$ and 0.1, which we assume to be associated with stabilization of the same canted-antiferromagnetic phase. The temperature below which the H/M curves deviates from the linear temperature behavior defines the Néel temperature at 35 and 92 K, for $x = 0.2$ and 0.3, respectively, as seen in Figures 8.2(d) and (e). From the best fits above the Néel temperature and their extrapolation to negative temperatures, the obtained values of θ_p were of -24 and -21 K, with a magnetic moment of 9.88 and 9.17 μ_B, for $x = 0.2$ and 0.3, respectively.

The H/M(T) curve of $x = 0.2$ exhibits another anomaly at 20 K, which is associated with the separation of the M(T) curves measured in ZFC and FC conditions. For the case of $x = 0.3$, H/M(T) curves shows another anomaly at 37 K, where the separation between the curve measured in ZFC and the measured in FC conditions reaches a minimum. We assign these anomalies to change of the Mn/Fe spins structure. Unfortunately, the temperature dependence of the specific heat, presented on the inset of Figure 8.2(b), does not exhibit any anomaly, other than that at 6 K, which marks the ordering temperature of the Tb^{3+} spins.

The case of $x = 0.4$, whose M(T) and H/M(T) curves are shown in Figures 8.2(c) and (f), respectively, deserves a carefully analysis. First, the M(T) curve measured under ZFC conditions evidences for a ferromagnetic response, in contrast with what was observed for the $x = 0.2$ and 0.3 compounds. The H/M(T) curve deviates from the linear temperature dependence described by the Curie-Weiss law at 198 K, from which a θ_p of -24.5 K and a magnetic moment of 10.16 μ_B were obtained. Furthermore, M(T) exhibits anomalous behavior at 33 K, whose shape changes accordingly the FC and ZFC measurement conditions. We also assign this anomaly the a change of spin structure, though we must stress that despite this composition displays a similar phase sequence, the magnetic character appears to be different relatively to the compound with $x = 0.2$ and 0.3. So, the results obtained for $TbMn_{0.6}Fe_{0.4}O_3$ compound are not enough to unequivocally define its phase sequence. This issue will be addressed in future work.

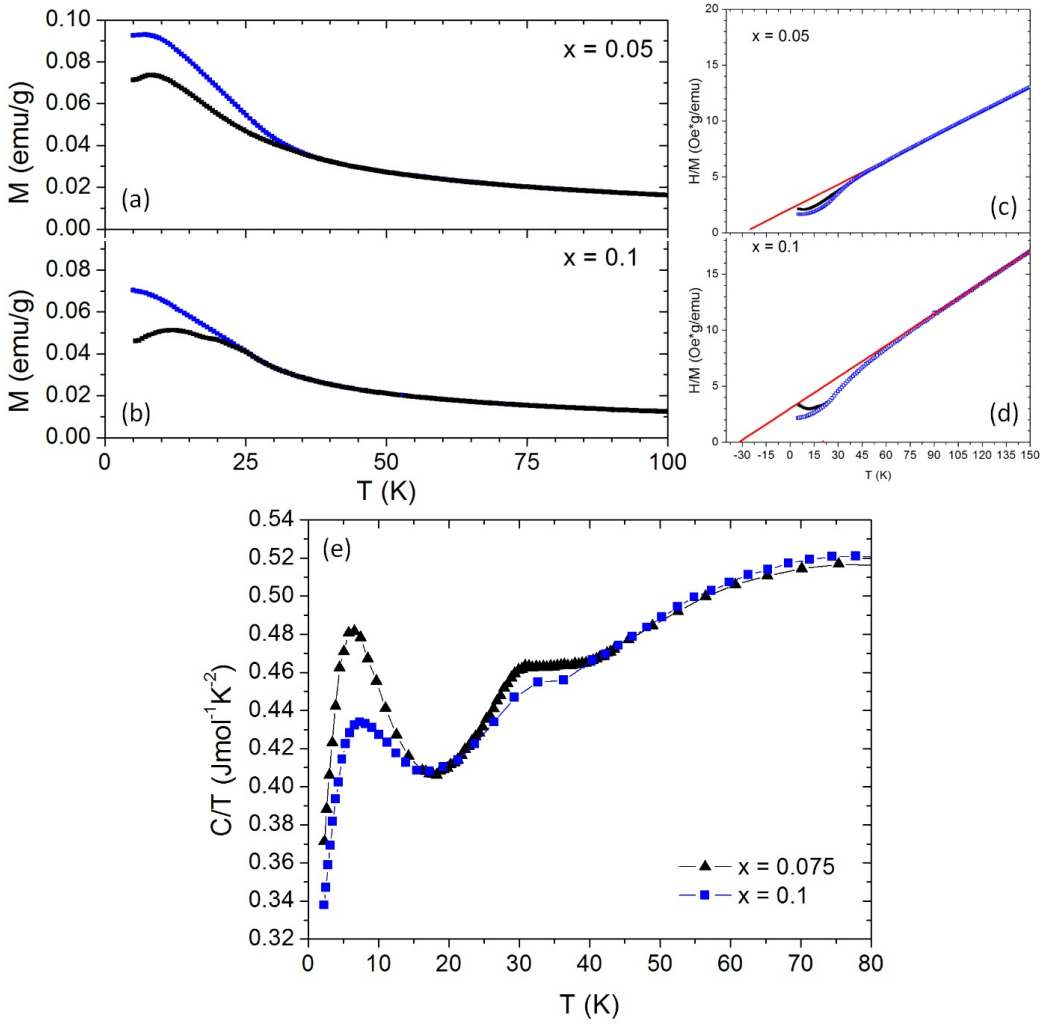

Figure 8.1: M(T) and H/M(T) curves under ZFC and FC conditions for (a)/(c) $x = 0.05$, and (b)/(d) 0.1, respectively. (e) C/T(T) curves for $x = 0.075$ and 0.1, measured by Mihalik's Group.

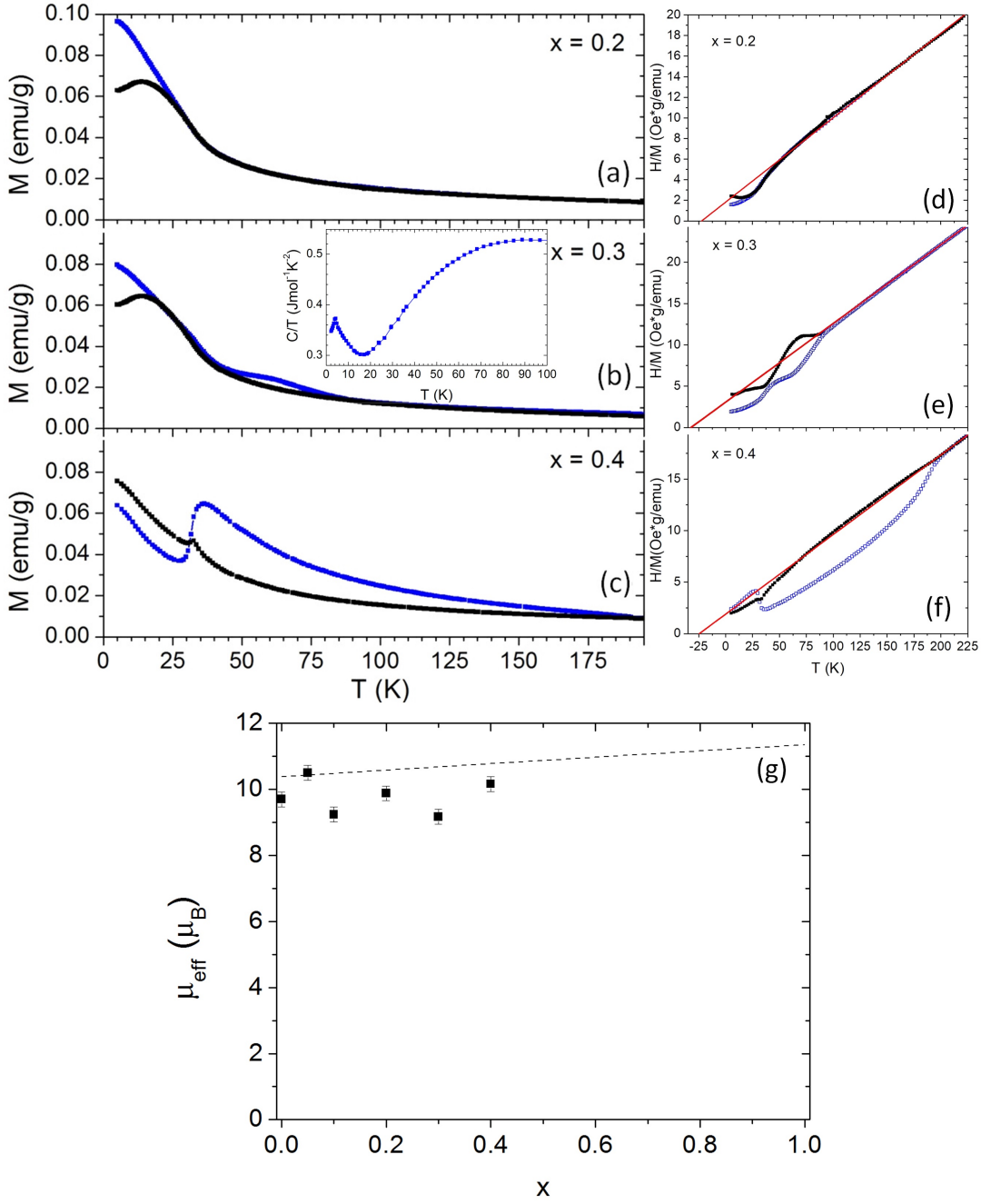

Figure 8.2: M(T) and H/M(T) curves under ZFC (black) and FC (blue) conditions for (a)/(d) $x = 0.2$, (b)/(e) 0.3 and (c)/(f) 0.4, respectively. The data were measured with applied magnetic field μ_0H = 0.004 T. Inset of (b) shows the C/T(T) curve for $x = 0.3$. (g) x-dependency of the magnetic moment obtained from the best fit of the Curie-Weiss law. Dashed line in (g) marks the expected theoretical values.

Figure 8.2(g) shows the Fe-concentration dependence of the magnetic moment obtained from the best fit of the Curie-Weiss law for the presented samples up to $x = 0.4$, along with the dashed line for the expected theoretical values, namely of 10.3 and 11.3 μ_B for $TbMnO_3$ and $TbFeO_3$, respectively. The obtained magnetic moment for $TbMnO_3$ was 9.7 μ_B, and as Fe is introduced, this value presents a random variation between 9.2 and 10.5 μ_B, with no significant trend. Moreover, the obtained values are always slightly lower than those expected. This result suggests that no significant changes are occurring on the paramagnetic interactions by the chemical substitution in this x-region.

8.3 Concentration range $0.5 \leq x \leq 0.7$

Figures 8.3(a) to (c) show the temperature dependence of the specific magnetization of the compound with $x = 0.5$, 0.6 and 0.7, respectively, measured in ZFC and FC conditions. The temperature dependence of the specific magnetization displays anomalous behavior at 300 K ($x = 0.5$), 366 K ($x = 0.6$) and 494 K ($x = 0.7$), defining the Néel temperature. These values are consistent with the value already reported for $TbMn_{0.5}Fe_{0.5}O_3$ ($T_N = 550$ K). Below the Néel temperature, the magnetization of the compositions $x = 0.6$ and 0.7 increase as temperature decreases down 297 and 250 K, respectively, where a decrease of the magnetization occurs. The increase of the separation between both M(T) curves, measured in ZFC and FC conditions, evidences for a ferromagnetic behavior, likely due to a spin canting (this separation does not occur for $x = 0.7$ since a high to low temperature continuous measurement in FC conditions could not be experimentally done). Taking into account Mössbauer spectroscopy data, which clearly evidences a change in the spin-structure for $x = 0.75$, we attribute this decrease of the M(T) curves to the same process , emerging for $x > 0.5$ [145].

For $x = 0.5$, the paramagnetic to magnetically ordered phase transition is marked by a small anomaly in the magnetization at 300 K (Figure 8.3(a)). Nhalil *et al.* report ordering at 286 K for a $x = 0.5$ single crystal [146]. A neutron powder diffraction experiment reported by Nair *et al.* indicates a non-zero magnetic contribution below 295 K [87]. It has also been found that the anomaly in the M(T) curves, which is associated with this magnetic phase transition, is not sharp, but takes place in the temperature range 280 to 303 K [87]. All these findings suggest that the triple point of the two different magnetic phases with the paramagnetic phase exists in the concentration range $0.5 < x < 0.55$. Consequently, since the triple point lies close to $x = 0.5$, the anomalies observed for $x = 0.6$ and 0.7 also lie on the same phase line, together with the anomaly observed by Kim *et al.* for $x = 0.75$ at 180 K [145].

At lower temperatures, the increase of the magnetization measured under FC conditions for $x = 0.5$, 0.6 and 0.7 at 27, 24, 19 and 11 K, respectively, is observed in Figures 8.3(a) to (c). These anomalies fit with change of the magnetic structure at 20, 42 and 33 K found for $x = 0.2$, 0.3 and 0.4. The phase transition taking place at 26 K in the composition with $x = 0.5$ has been studied by neutron diffraction and has been found to be associated with a change of the magnetic structure of the Mn/Fe sublattice [87]. Assuming that similar transition occurs, then these anomalies found in $x = 0.6$ and 0.7 also reflect the same change on the magnetic structure. This transition has been further investigated both by magnetization and heat capacity measurements under fixed applied magnetic field up to 3 T, whose results are shown in Figure 8.4. This particular transition on $TbMn_{0.5}Fe_{0.5}O_3$ seems to be highly dependent on the applied magnetic field. The heat-capacity measurements indicate that the peak associated with this phase transition is smeared out by the applied magnetic field, and eventually disappears for a magnetic field strength larger than 3T, emphasizing the magnetic character of this phase transition. When the sample is cooled down in FC conditions with a magnetic field below 140 Oe, a negative magnetization is developed (i.e. opposite do the field direction). This effect is no longer observed if the magnetic fields is of 140 Oe or higher, forcing the magnetization to be developed along its direction. The underlying mechanism of this effect is still a matter of discussion, though it might be associated with a antiparalel alignment of the Tb^{3+} spins, as found in $NdFeO_3$ and $SmFeO_3$.

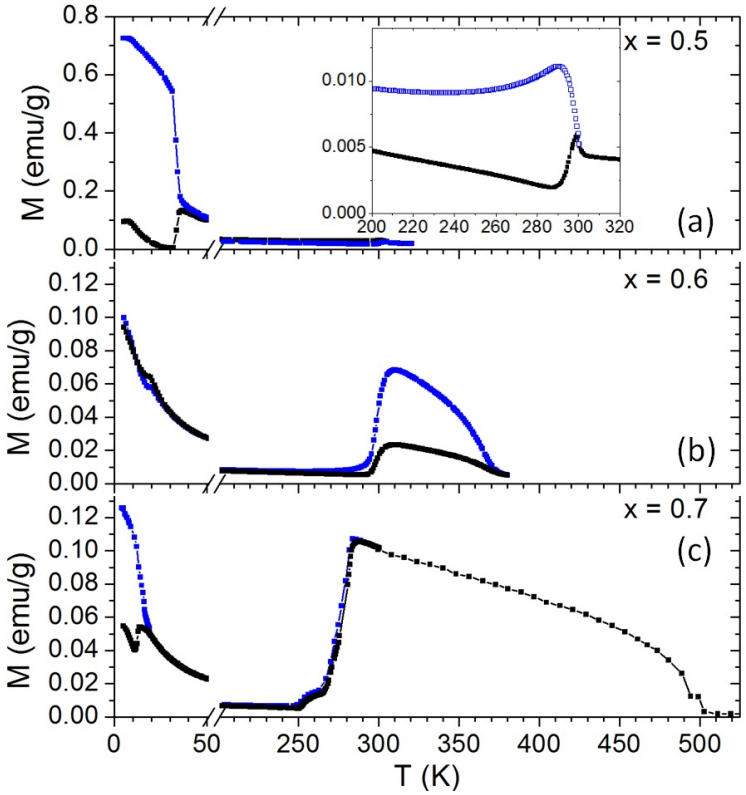

Figure 8.3: Temperature dependence of specific magnetization measured in ZFC (black) and FC (blue) conditions as a function of temperature at μ_0H = 0.014 T for $x = 0.5$ and at μ_0H = 0.004 T for $x = 0.6$ and 0.7. Inset of (a) shows the Néel temperature detail. The high magnetization temperature measurement for $x = 0.7$ was done by M. Mihalik group.

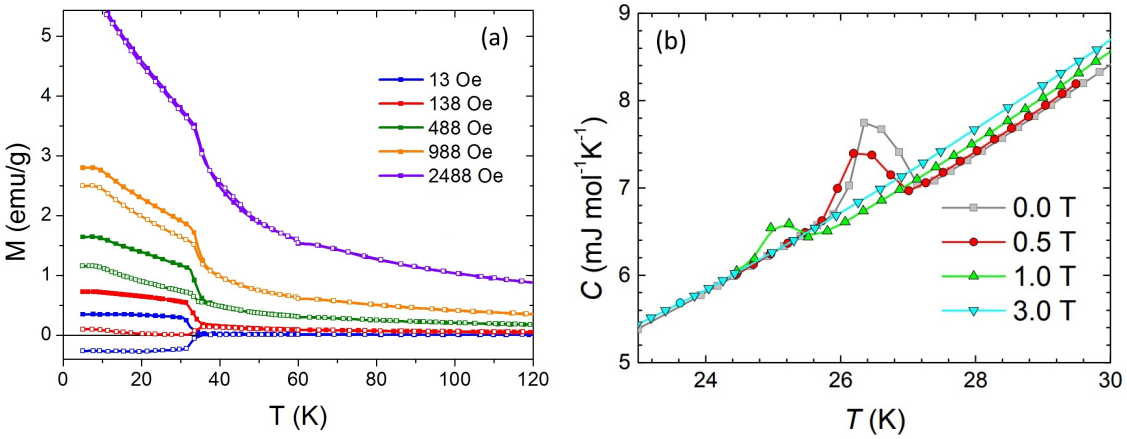

Figure 8.4: (a) Magnetization in ZFC (closed symbols) and FC (open symbols) conditions and (b) specific heat of $TbMn_{0.5}Fe_{0.5}O_3$ measured under different applied magnetic fields. The latter was measured by M. Mihalik group. Lines are guides for the eye.

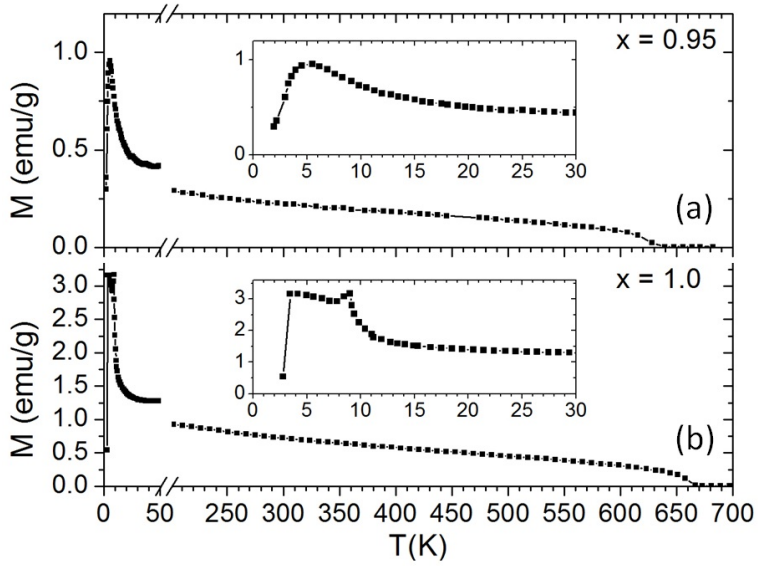

Figure 8.5: M(T) obtained in ZFC conditions as a function of temperature at μ_0H = 0.01 T, for $x = 0.95$ and 1.0 measured by M. Mihalik group. Insets show low temperature details.

8.4 Concentration range $0.95 \leq x \leq 1.0$

Figures 8.5 shows the magnetization data, of $x = 0.95$ and 1.0, measured in ZFC conditions by M. Mihalik group. For $x \geq 0.95$, only two transition temperatures are found, one above 600 K and another below 10 K. At high temperatures, the appearance of a magnetization marks $T_N = 626$ and 661 K for $x = 0.95$ and 1.0, respectively. However, for these concentrations, the anomalies associated with the changes of the magnetic structure found for lower Fe-concentrations, are not found in the magnetization curves of these compounds. Besides T_N, the only anomalies found in M(T) are below 10 K, as the insets of Figure 8.5 better evidence. For $x = 0.95$, the magnetization in the magnetically ordered state exhibits a bump around 5 K, quite different from the two distinct anomalies detected at 8 and 3 K for $x = 1.0$.

To further characterize this transition, the group of M. Mihalik has performed complex magnetic AC susceptibility measurements ($\chi = \chi' + i\chi''$) for these compounds, shown in Figures 8.6(a) and (b). A maximum in $\chi'(T)$ was found at 5 K for $x = 0.95$. For $x = 1.0$ ($TbFeO_3$), two anomalies in both $\chi'(T)$ and $\chi''(T)$ can be observed at 8 and 3 K. These anomalies are frequency independent up to driving frequencies of 1 kHz and coincide very well with the anomalies observed in the temperature dependence of the specific magnetization, associated with the Fe^{3+} spin-reorientation at 8 K and the ordering of the Tb^{3+} sublattice at 3 K [36]. Thus, for $x = 0.95$, we attribute the anomaly in $\chi'(T)$ at 5 K to a spin-reorientation of Fe/Mn sublattice [36]. However, a similar anomalous temperature dependence of $\chi'(T)$ and $\chi''(T)$ was reported for the case of $x < 0.95$. Moreover, Kim *et al.* did not report any phase transition in $TbMn_{0.75}Fe_{0.25}O_3$ at low temperatures [145]. This means that the change of the magnetic structure observed for concentrations $0.5 \leq x \leq 0.7$ are driven by different mechanisms from those responsible for the transition observed for $x = 0.95$ and 1.0.

For $x = 1.0$ an additional bump in both the real and the imaginary part of the complex magnetic susceptibility is observed around 4 K. The shifting to higher temperatures and smearing out of this bump with increasing frequency, evidences for the emergence of internal dynamics in this magnetic phase within the temperature range $3 < T < 8$ K.

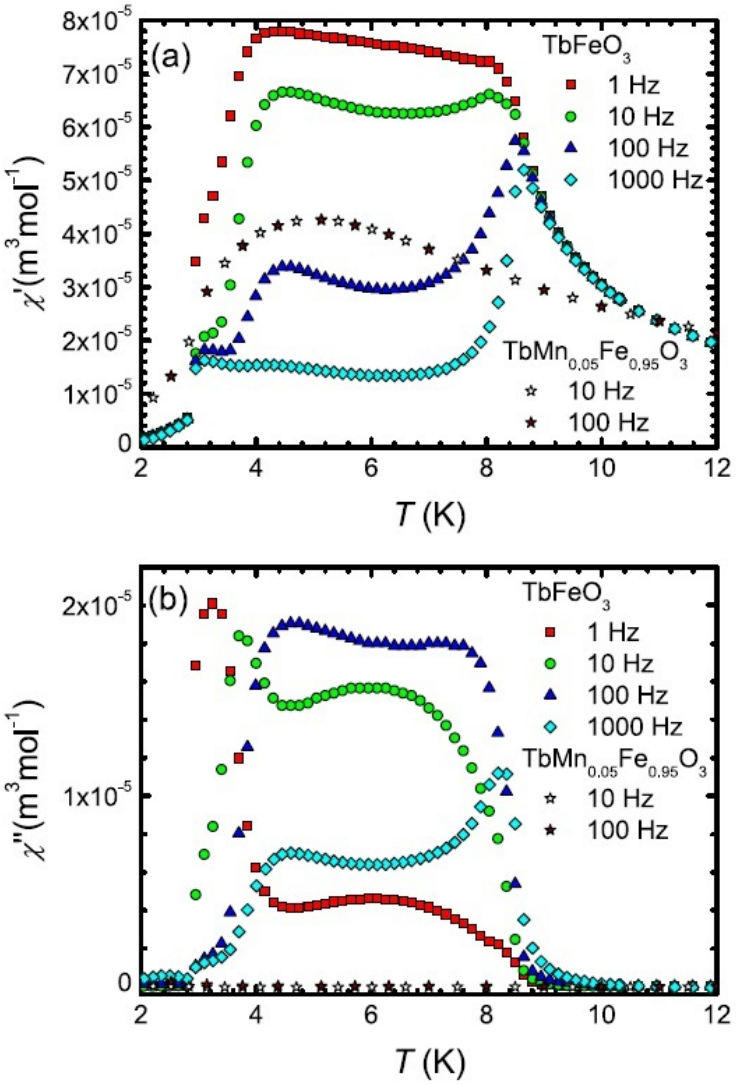

Figure 8.6: (a) The real part $\chi'(T)$ and (b) the imaginary part $\chi''(T)$ of the complex magnetic AC susceptibility (χ) for $TbMn_{0.05}Fe_{0.95}O_3$ and $TbFeO_3$ measured with different driving frequencies, by M. Mihalik group.

8.5 Magnetic phase diagram

Based on the aforementioned results, we propose a magnetic phase diagram for the $TbMn_{1-x}Fe_xO_3$ system, presented in Figure 8.7. For $0.05 \leq x \leq 0.1$ two different phase lines are traced wherein the critical temperatures decrease with increasing Fe concentration. The cycloidal modulated magnetic phase (Mn_{CYC}), associated with the emergence of ferroelectricity [50], vanishes below $x = 0.05$, while the spin-density wave phase (Mn_{SDW}) persists up to x close to 0.1. Around $x = 0.2$ an additional phase line between the paramagnetic and magnetically ordered state is found with the ordering temperature increasing with increasing of Fe-concentration. We assign this issue to the onset of the ordering of the Fe spins. For $0.2 \leq x \leq 0.7$, the temperature at which the change of magnetic structure was found decreases as the Fe-concentration increases. Yet, we must stress that between $x = 0.3$ and 0.4 there is a change of the magnetic character of the lower temperature phase, which is likely associated with an additional phase line between these concentrations. To confirm this, neutron diffraction studies are needed. While these results are not available, we assume that, in this concentration range, the magnetic phases are identical to the phases reported by Nair *et al.* for $TbMn_{0.5}Fe_{0.5}O_3$ [87]. The phase denoted as Fe_{AF3} is an antiferromagnetic phase with $G_xA_yF_z$ configuration of the Fe spins, or G_x (i.e. $A_y \approx 0$ and $F_z \approx 0$) which changes at higher temperatures and higher x values into a magnetic phase (Fe_{AF2} phase) [87]. It consists of two antiferromagnetic structures: the majority of Fe^{3+} ions is in the magnetic configuration $A_xG_yC_z$ and the minority of Fe^{3+} ions is in magnetic configuration $G_xA_yF_z$ [87]. Other group of authors report for this magnetic phase a pure G_y-type magnetic structure [86]. An additional phase line is found in the concentration range $0.5 < x \leq 0.75$. According to this phase line, the ordering temperature of Fe_{AF2} phase starts to decrease rapidly with increasing Fe-content, but an additional different antiferromagnetic phase (Fe_{AF1} phase) emerges at the paramagnetic magnetic-order phase transition. This phase is stable up to $x = 1.0$. Hence we assign the magnetic structure of this phase to be the same as for $TbFeO_3$, i.e. $G_xA_yF_z$ ordering of Fe spins [36], or G_xF_z (i.e. $A_y = 0$) as reported by Artyukhin *et al.* [36]. For the parent compound $TbFeO_3$, we observe two additional magnetic phase transitions at 8 and 3 K. These transitions were already reported in literature. The former is a spin-reorientation of the Fe spins to $F_xC_yG_z$ order, or F_xC_y (i.e. $G_z = 0$) order, as reported by [36] (Fe_{AF4} phase). At the latter temperature the high-temperature G_xF_z structure (Fe_{AF5} phase) is recovered [36]. The Fe_{AF5} phase is unstable, sufficing 5% of Mn substitution into $TbFeO_3$ to destabilize it. The Tb sublattice orders magnetically only below 7 and 8 K in $TbMnO_3$ and $TbFeO_3$, respectively. The substitution of Fe^{3+} ions into $TbMnO_3$ causes the decrease of the ordering temperature of the Tb sublattice, reaching its minimum in the concentration range $0.5 \leq x \leq 0.7$ at temperatures around 2 K. Further Fe-substitution slightly increases the ordering temperature.

8.6 Summary

A rich magnetic phase diagram of $TbMn_{1-x}Fe_xO_3$, from $x = 0.0$ to 1.0, is proposed, wherein seven magnetic phases have been considered for Mn/Fe spins. It has been shown that for x smaller than approximately 0.2, the Mn^{3+} ion is the dominant magnetic ion, which is responsible for the magnetic ordering. The only effect of the Fe ions is the weakening of the Mn–O–Mn superexchange interaction. This leads to a decreasing of the critical temperatures for both the Mn_{CYC} and the Mn_{SDW} phases. On the other hand, the magnetism in the concentration range $0.2 \leq x \leq 1$ is mainly driven by Fe^{3+} ions. In the concentration range $0.5 \leq x \leq 0.7$, the Fe-substitution reduces the ordering temperature of the Tb sublattice to temperatures close to 2 K. The pure $TbFeO_3$ undergoes a spin-reorientation transition at 3 K, but recovers the ground state magnetic structure above 8 K, leading to the conclusion that there exist two different magnetic structures in this compound with similar energies.

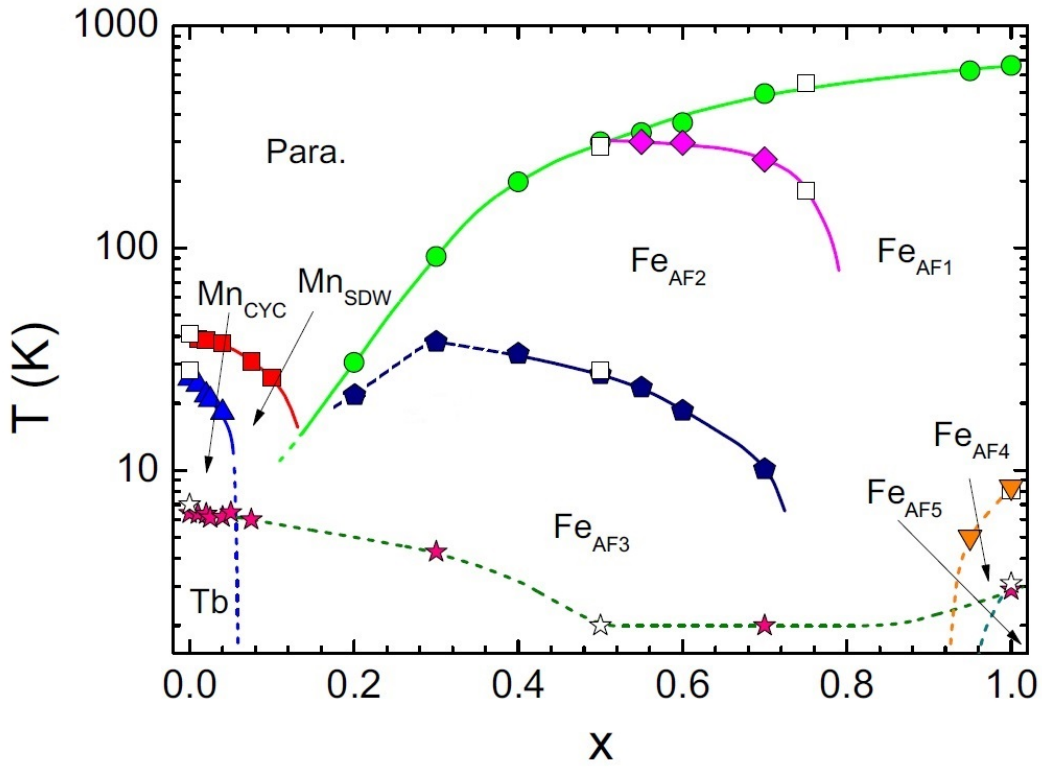

Figure 8.7: Magnetic phase diagram of the $TbMn_{1-x}Fe_xO_3$ system. The full symbols present the present results obtained from specific-heat, magnetization and magnetic AC susceptibility measurements. The open symbols are data taken from literature [36, 87, 145, 146]. The stars represent the magnetic ordering of the Tb sublattice.

Chapter 9

Magnetoelectricity of $TbMn_{1-x}Fe_xO_3$ with $x \leq 0.05$

The experimental studies on the effect of the substitution at the octahedral sites have been mainly focused on the effect on the magnetic behavior [84, 85]. Only few studies embrace its effect on the ferroelectric and magnetoelectric properties, and the range of compositions in which these properties are observed [147]. The partial substitution of Mn^{3+} by Fe^{3+}, exhibiting different electronic configurations of the d-orbitals in the high spin state, along with the available data concerning the effect of the substituent on the electric polarization, is a challenging matter, since it will achieve a deeper understanding of the role of the e_g-electrons in stabilizing different spin arrangements in $TbMn_{1-x}Fe_xO_3$, changing thoroughly its phase diagram. This Chapter aims at unraveling the effect of Fe^{3+} substitution in the magnetic, ferroelectric and magnetoelectric properties of $TbMn_{1-x}Fe_xO_3$ ceramics, with $x \leq 0.05$, both as a function of temperature and applied magnetic field, up to 9 T. Particular attention will be paid to the stability range of the magnetically induced ferroelectric phase and its sensitivity to an applied magnetic field. The results are discussed in the scope of available theoretical framework, with special focus on the role of the e_g-electrons and their non-degenerated ground-states.

9.1 Polar properties and phase diagram

In this Section we will present the experimental results that enable us to complete the phase diagram already presented in last Chapter. The upper panels of Figures 9.1(a) and (b) show the temperature dependence of the specific heat divided by temperature and the real and imaginary parts of the complex electric permittivity of a ceramic sample of $TbMnO_3$, measured at 85.7 kHz, with $x = 0.0$, 0.025 and 0.05. The three anomalies observed in both C/T and electric permittivity temperature curves of $TbMnO_3$ are associated with the following transitions to: (i) the collinear sinusoidal incommensurate modulated antiferromagnetic (IC-AFM) phase at $T_N = 41$ K; (ii) the cycloidal commensurate modulated antiferromagnetic (C-AFM) phase at $T_{lock} = 25$ K (marked by *), which is also ferroelectric; (iii) the modulated quasi-long range antiferromagnetic ordering of the Tb^{3+} ions at $T_1 = 7$ K. The experimental values obtained for the critical temperatures are in good agreement with those reported in the literature [52, 148]. Based on the phase sequence observed in $TbMnO_3$ and the existence of the three anomalies in the temperature dependence of C/T(T) and $\epsilon'(T)$, shown in the 2 bottom panels of Figures 9.1(a) and (b), we assign the same phase sequence as $TbMnO_3$ for the compositions with $x \leq 0.04$. The anomaly at T_1 barely shifts with Fe-substitution. This result is similar to that observed in $TbMn_{1-x}Cr_xO_3$ ($x \leq 0.06$) ceramics, and corroborates that the f-d exchange interaction between the Mn $3d$ spins and the Tb $4f$ moments in multiferroic $TbMnO_3$, which involves almost only the t_{2g} electrons [52].

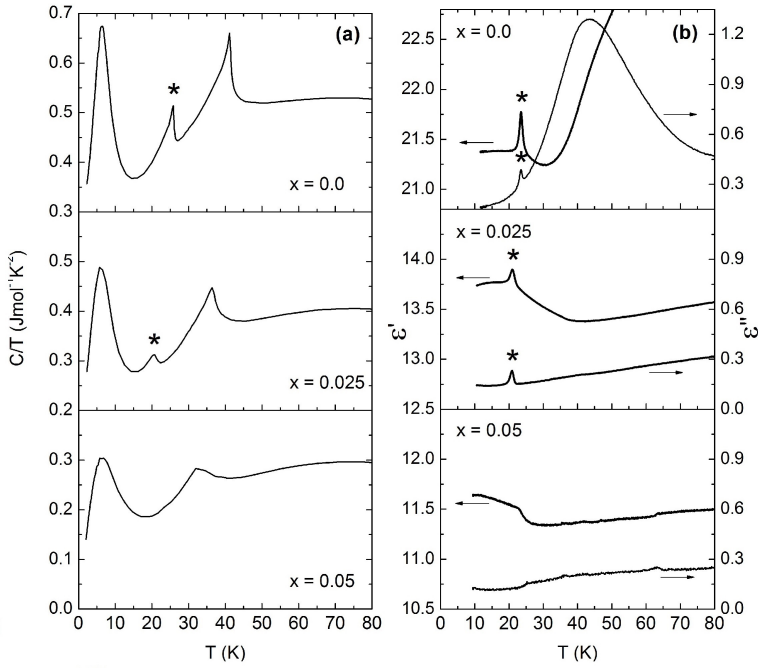

Figure 9.1: Temperature dependence of (a) specific heat divided by temperature and (b) real and imaginary parts of electric permittivity, measured in heating runs at 85.7 kHz, for $x = 0.0$, 0.025 and 0.05. Star (*) marks T_{lock}.

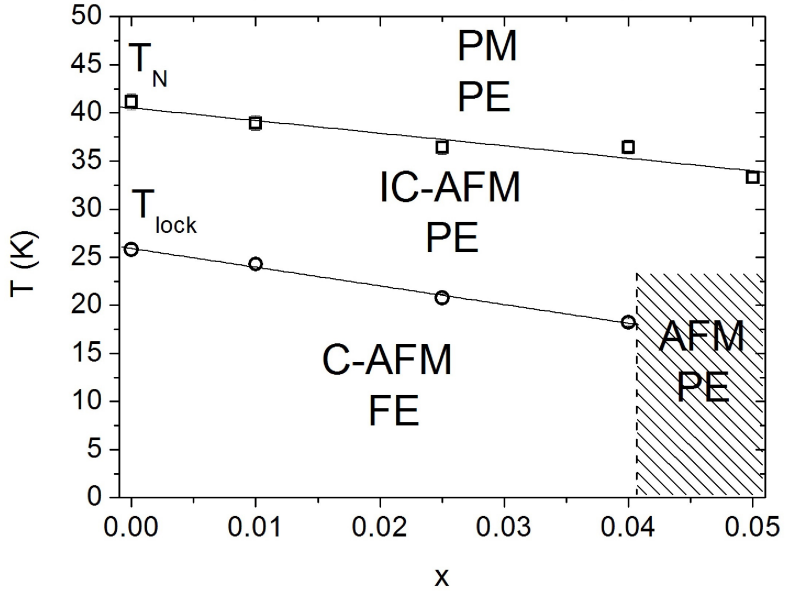

Figure 9.2: Magnetic (x, T) phase diagram of $TbMn_{1-x}Fe_xO_3$, where IC-AFM stands for sinusoidal incommensurate modulated antiferromagnetic and C-AFM for cycloidal commensurate antiferromagnetic. The gray area is a guess for the AFM-paraelectric phase.

For increasing x up to 0.025, both T_N and T_{lock} shift to lower temperatures whereas the corresponding anomalies in C/T(T) and ϵ'(T) become smaller in magnitude. For $x = 0.05$, we only observe two anomalies in the C/T(T) curve, detected at 35 and 6 K. The decrease of both T_N and T_{lock}, along with the decrease of the anomalies amplitudes, with increasing x up to 0.04 provide evidence for the weakening of the antiferromagnetic

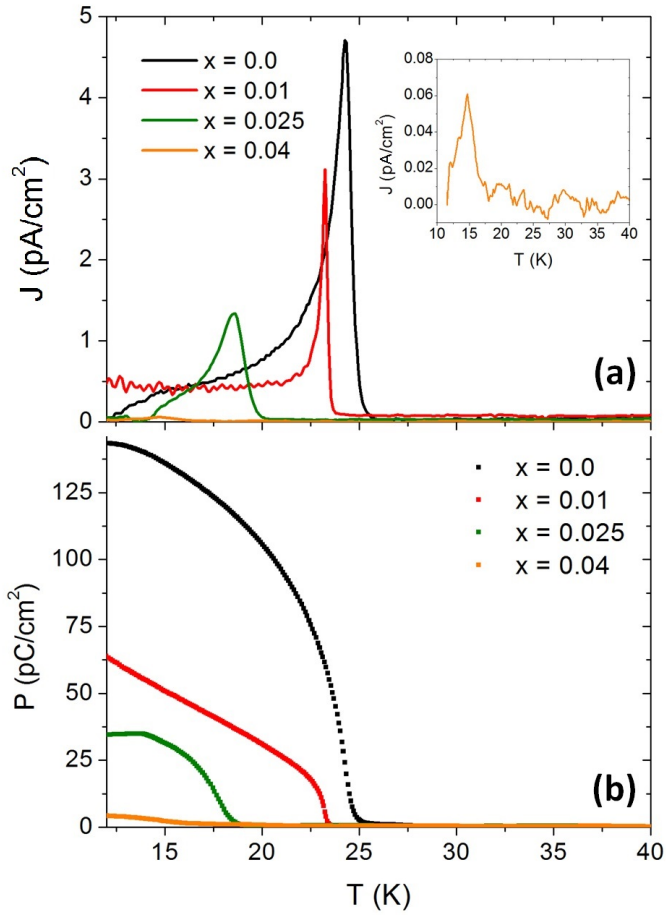

Figure 9.3: Temperature dependence of (a) pyroelectric current density and (b) respective electric polarization temperature curves as a function of x. The inset of figure (a) shows a detailed view of the temperature dependence of the pyroelectric current density measured from the sample with $x = 0.04$.

interactions, and thus yielding the proper energy balance that pushes T_N and T_{lock} towards lower temperatures. However, for Fe^{3+} concentrations above 4%, the anomaly associated with T_{lock} is no longer perceived in electric permittivity and specific heat curves. We interpret this result as the suppression of the cycloidal spin ordered phase for $x > 0.04$, which was already evidenced by powder neutron diffraction measurements for $x = 0.1$ [86]. The x dependence of the critical temperatures, along a proposal of identification of the magnetic phases, are summarized in the (x, T) phase diagram shown in Figure 9.2.

In order to unravel the effect of the Mn^{3+} substitution by Fe^{3+} on the polar nature of the magnetic phase observed below T_{lock}, the temperature dependence of the pyroelectric current was studied for different x-values. Figure 9.3(a) shows the temperature dependence of the pyroelectric current density of samples with different compositions, and Figure 9.3(b) refers to the temperature dependence of the electric polarization, calculated from time integration of pyroelectric current density. As Fe^{3+} concentration increases, it is observed that there is a decrease of both T_{lock} and the electric polarization at 10 K. The decrease of the electric polarization is associated with the gradual fading out of cycloidal spin ordering, whose disappearance prevents the occurrence of ferroelectricity in agreement with the Dzyaloshinskii-Moriya mechanism. This feature is similar to the $TbMn_{1-x}Cr_xO_3$ system and reveals the strong effect on the superexchange interactions due to the different e_g-electron configurations of the B-site cation on the stabilization of the cycloidal modulated structure, as it will be explain in the following [86].

The most suitable theoretical model to describe the phase diagram of the rare-earth manganites, proposed by M. Mochizuki and N. Furukawa, is based on the competition between nearest neighbor Mn^{3+} ferromagnetic exchanges (J_{ac}) and next nearest neighbor antiferromagnetic exchanges (J_2) [51, 81] (cf. Figure 1.19). The J_{ac} superexchange has a contribution arising from the ferromagnetic interactions of the staggered e_g-electrons in the ac-plane, while the J_2 has the contribution of the antiferromagnetic arrangement of the e_g-electrons [51]. The t_{2g}-electrons give always an antiferromagnetic contribution to both superexchange interactions, which we will take as x independent for low x values [51, 81]. In rare-earth manganites, the two J_{ac} and J_2 exchanges are comparable in strength, presenting values of 0.79 and 0.62 meV for $TbMnO_3$, respectively [51]. Thus, the next nearest neighbor J_2 exchange, which is usually negligibly weak in other compounds, actually plays important role in determining the magnetic structure [51]. The cycloidal spin ordering in $TbMnO_3$ is stabilized through the frustration of the competing ferromagnetic and antiferromagnetic interactions [51]. The main factor driving the magnetic modifications should be that the Fe^{3+} introduction locally alters both the number of the e_g-electrons and the Jahn–Teller distortion, in such a way that the local nearest neighbor ferromagnetic interaction of the e_g-electrons should increase as the next nearest neighbor antiferromagnetic one decreases, and thus, enhancing J_{ac} [50, 51, 86]. Similar ferromagnetic distortion of the spiral spin order was also reported arising from Mn-Cr interactions in the $TbMn_{1-x}Cr_xO_3$ system [149]. For $x > 0.04$, the ratio J_2/J_{ac} should become small enough that the cycloidal spin order is no longer stable.

9.2 Magnetoelectric properties

After addressing the polar properties, now we explore how the (x, T) phase diagram and the magnetoelectric coupling strength evolve under applied magnetic field. To reach these objectives, the temperature dependence of specific heat and pyroelectric current were studied under applied magnetic fields, for different x values. Figures 9.4(a) to (c) show representative examples of the temperature dependence of C/T for x = 0.0, 0.01 and 0.05, under different applied magnetic fields up to 9 T. It is worth mentioning that, for every studied composition, a large anomaly of C/T is observed at T_1 = 7 K for zero applied magnetic field, which signs the Tb^{3+} spin ordering occurring below to that temperature. For increasing magnetic field, this anomaly becomes a hump, and cannot be followed above 5 T, pointing to a field-induced magnetic transition. We will come back to this issue in the next Chapter. The anomalies identified as T_{lock} and T_N without applied magnetic field are much more stable with respect to the applied magnetic field. Yet, the nature of the phases may have field-induced changes, which for instance may suppress the spin-cycloidal and ferroelectricity. The x-, magnetic field- and temperature-dependencies of the temperatures where C/T(T) display anomalous behavior are plotted in Figure 9.4(d).

Figures 9.5(a) and (b) show, for x = 0.025, pyroelectric current density and corresponding electric polarization as a function of temperature, respectively, under magnetic fields up to 5.5 T. Moreover, Figure 9.5(c) shows the magnetic field dependence of the relative electric polarization (P_{rel}) for x = 0.0, 0.01, 0.025 and 0.04, defined as

$$P_{rel} = \frac{P(\mu_0 H)}{P(0)}\,, \tag{9.1}$$

where $P(0)$ is the polarization measured at 5 K without magnetic field, and $P(\mu_0 H)$ is the polarization measured at 5 K under magnetic field. In the case of $TbMnO_3$, no apparent change in the relative electric polarization curve is observed for applied magnetic fields below to 1 T. Furthermore, it decreases only to 85% of its initial value up to 5 T. The magnetic field dependence of the relative electric polarization is in good agreement with the magnetic dependence of the electric polarization in $TbMnO_3$ obtaining by "summing up" the c- and b-axis polarizations as a function of the magnetic field [13], wherein the former increases and the latter decreases with increasing applied magnetic field.

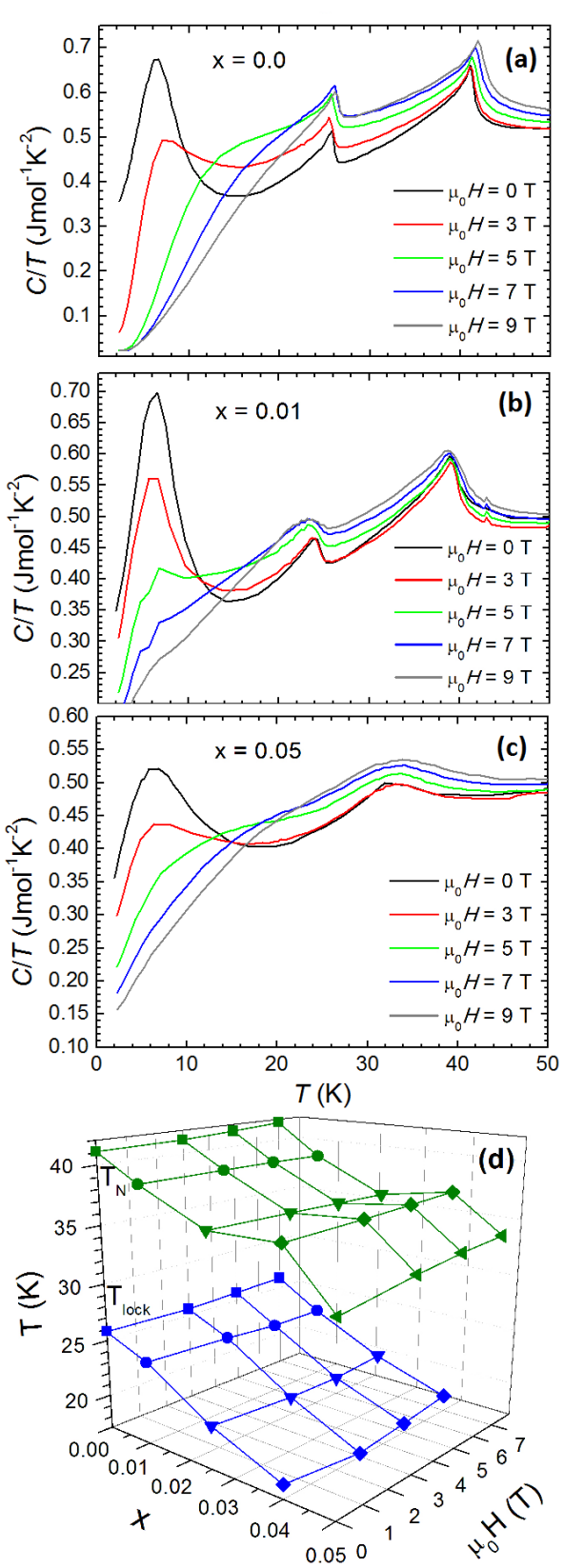

Figure 9.4: Temperature dependence of C/T for $TbMn_{1-x}Fe_xO_3$, with (a) x = 0.0, (b) 0.01, and (c) 0.05. (d) Dependency on temperature, Fe-concentration and applied magnetic field of the temperatures where C/T(T) display anomalous behavior.

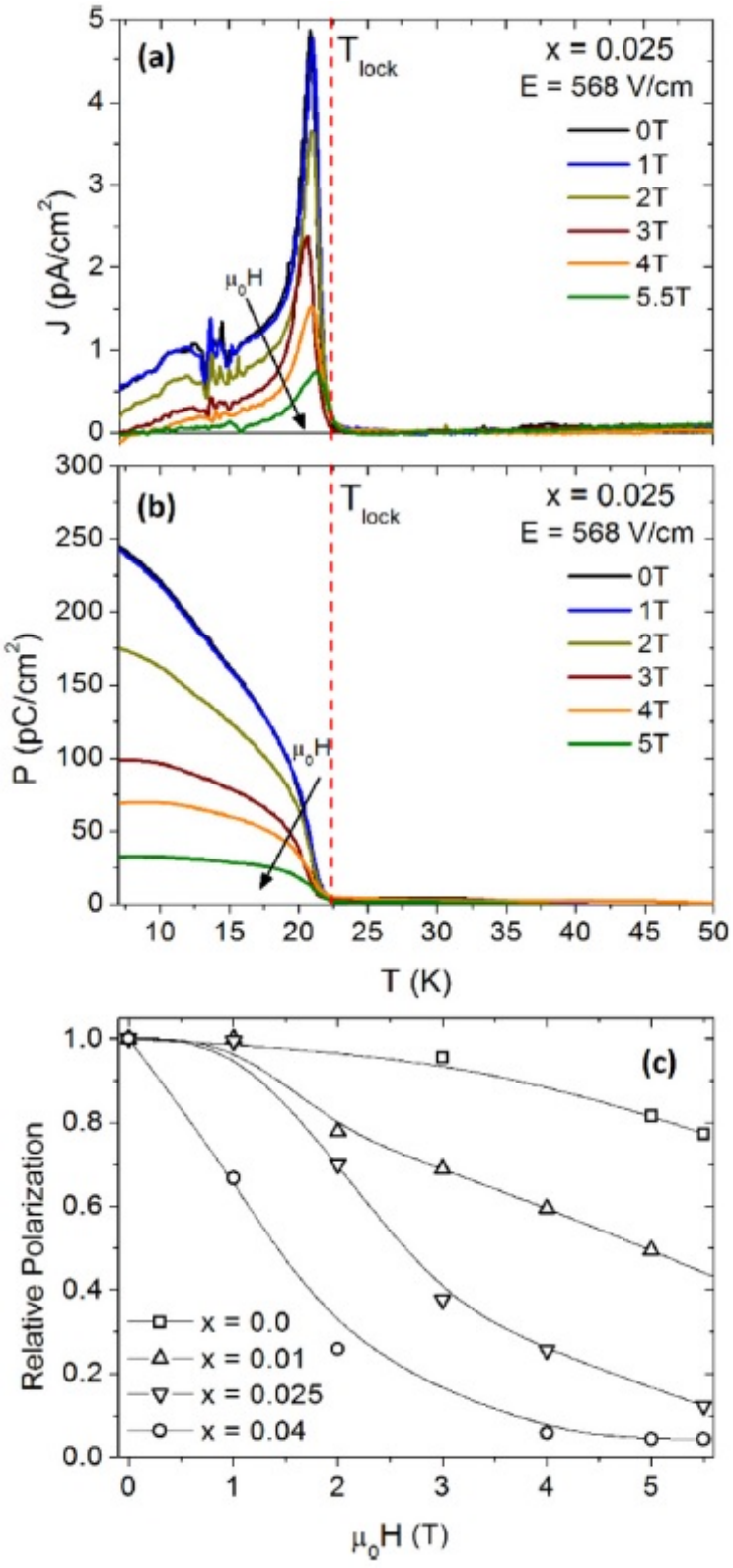

Figure 9.5: (a) Example of the pyroelectric current density and (b) corresponding electric polarization curves as a function of temperature under several magnetic fields for $x = 0.025$. Dashed lines mark T_{lock}. (c) Relative electric polarization, P_{rel}, at 5 K, with poling electric field of around 500 V/cm, as a function of applied magnetic field for $x = 0.0$ to 0.04. Lines are guides for the eyes.

As x increases, the sensitivity of the relative electric polarization to the applied magnetic field drastically increases, in the sense the sense that the fraction of the electric polarization reducing for a given applied magnetic field increases, as it can be observed in Figure 9.5(c). For the case of $x = 0.04$, a third of the relative electric polarization is already removed at a magnetic field of 1 T, and more than 95% of its value can be suppressed by applying a magnetic field above 4 T. Figure 9.5(c) clearly evidences that the inclusion of the Fe^{3+} ions has strong effect on sensibility of the electric polarization versus applied magnetic field. This means that the magnetoelectric coupling is strengthened by the Fe-substitution. It seems that for a strong enough applied magnetic field, the ferroelectricity would be completely suppressed, suggesting a field-induced magnetic transition, in agreement with the C/T(T) curves measured above 5 T. Furthermore, the necessary strength of the magnetic field to induced this magnetic transition should decrease as x-increases.

The increase of sensitivity of the electric polarization to an applied magnetic field with increasing x is understood by the magnetic field enhancement of the Fe-induced ferromagnetic contribution of the e_g-electrons to the J_{ac} exchange, which also explains the similar magnetic field dependence of the electric polarization found in $TbMn_{1-x}Cr_xO_3$ [147]. The lowest energy electronic states of these ions, under the influence of an octahedral crystal field and in the high spin configuration, are described by $t_{2g}^3e_g^0$, $t_{2g}^3e_g^2$ and $t_{2g}^4e_g^2$, respectively, while for the Mn^{3+} ion is $t_{2g}^3e_g^1$. In both systems, the e_g-electrons of the substituent magnetic ions increases the ferromagnetic J_{ac} exchange against the antiferromagnetic J_2 one, evidencing their important role underlying the magnetoelectric coupling in rare-earth manganites [149].

9.3 Summary

In this Chapter we have presented and discussed the effect of the e_g-electrons introduced by the substitution of Jahn–Teller active magnetic Mn^{3+} by the non-active Jahn–Teller active magnetic Fe^{3+} ions, on the magnetic, ferroelectric and magnetoelectric properties of $TbMn_{1-x}Fe_xO_3$, for x up to 0.05. The (x, μ_0H, T) phase diagram could be traced from the experimental results obtained by specific heat, dielectric permittivity and polar measurements. One of the most significant outcomes is the strong decrease of the electric polarization with increasing Fe^{3+} concentration, disappearing for $x > 0.04$. We propose that the transition to this phase can be understood on the basis of the increase of the nearest neighbor ferromagnetic J_{ac} exchanges with the concomitant decrease of the next nearest neighbor antiferromagnetic J_2 exchanges, which is induced by the local interaction of the e_g-electrons of the Fe^{3+} substituent with the Mn^{3+} ones. This interpretation is also in agreement with the decrease of T_N and T_{lock} with x, which indicates that the corresponding magnetic orderings are becoming less stable. Another important outcome is the large change of the low field magnetoelectric response through Fe^{3+} substitution, associated with the increase of the electric polarization sensitivity to the applied magnetic field. It is experimentally shown that for both Fe^{3+} and Cr^{3+} substituents, a monotonous decrease of the relative electric polarization, though the rate of decrease is apparently larger for Fe^{3+} substituted system. All these findings point to a specific role played by the e_g-electrons on the nearest neighbor ferromagnetic coupling. In this framework, Mn-Fe bonds are expected to show larger values of J_2 relatively to those of Mn-Cr.

A possible field-induced magnetic transition was found above 5 T, which deserved to be further investigated by other techniques, such as neutron diffraction.

Chapter 10

Magnetoelectricity and magnetic structure of $TbMn_{0.98}Fe_{0.02}O_3$

All the conclusions drawn up to this point, namely in the last Chapter, were obtained in polycrystalline samples, loosing the anisotropic properties of the electric polarization and magnetic properties. However, the physics of these materials, in particular of the multiferroic region of the $TbMn_{1-x}Fe_xO_3$ system, is highly anisotropic [13, 52]. In $TbMnO_3$, the direction of the electric polarization can be altered by changing the plane of the spin-cycloidal from which it emerges. The plane of the spin-cycloidal depends on the energy balance between the single ion anisotropy and the Dzyaloshinskii-Moriya interaction energies, which can be tuned by the octahedra distortions, the temperature, or even an applied magnetic field [51]. Furthermore, the direction of the applied magnetic field can have different effects on the physical properties [52]. In $TbMnO_3$, when the applied magnetic field is applied along the a-axis, a continuous change of the spin-cycloidal plane is observed at 10 K for 4 T up to 28 K at 10 T, when applied along the c-axis a sudden change of the spin-cycloidal plane is observed at 10 T; and when applied along the b-axis a suppression of the spin-cycloidal and its coupled ferroelectricity is found at 10 K for 8 T and at 28 K above 12 T [52].

To understand in more detail the physical properties of the multiferroic region of $TbMn_{1-x}Fe_xO_3$ ($x < 0.05$), this Chapter is devoted to the study of the electric polarization and magnetic structure of an oriented single crystal of $TbMn_{0.98}Fe_{0.02}O_3$, under an applied magnetic field along the a-axis. This will allow a much deeper understanding of the underlying microscopic effects. Though this is still an on-going work, it already provides some important outcomes that deserve further investigation, towards a fully comprehension of the open questions that still persist.

10.1 Magnetoelectric properties

Figure 10.1(a) and (b) show the temperature dependence of the pyroelectric current density of $TbMn_{0.98}Fe_{0.02}O_3$ measured along the b and c-axis, respectively, under different magnetic fields up to 5.5 T, applied along the a-axis. Sketches of the relative orientation of the fields to the crystallographic axes are also given in the same Figures. The pooling electric fields were of 20 and 100 V/mm, for the b- and c-axis, respectively, due to difference of crystal thickness.

For the case where no magnetic field is applied (i.e. 0 T), a sharp anomaly in the temperature dependence of the pyroelectric current density measured in the sample electrodes perpendicular to the b-axis is seen in Figure 10.1(a) at $T_{lock} = 22.5$ K. Figure 10.1(c) shows the temperature dependence of the b-component of the electric polarization (P_b), calculated from the time integration of the corresponding pyroelectric current

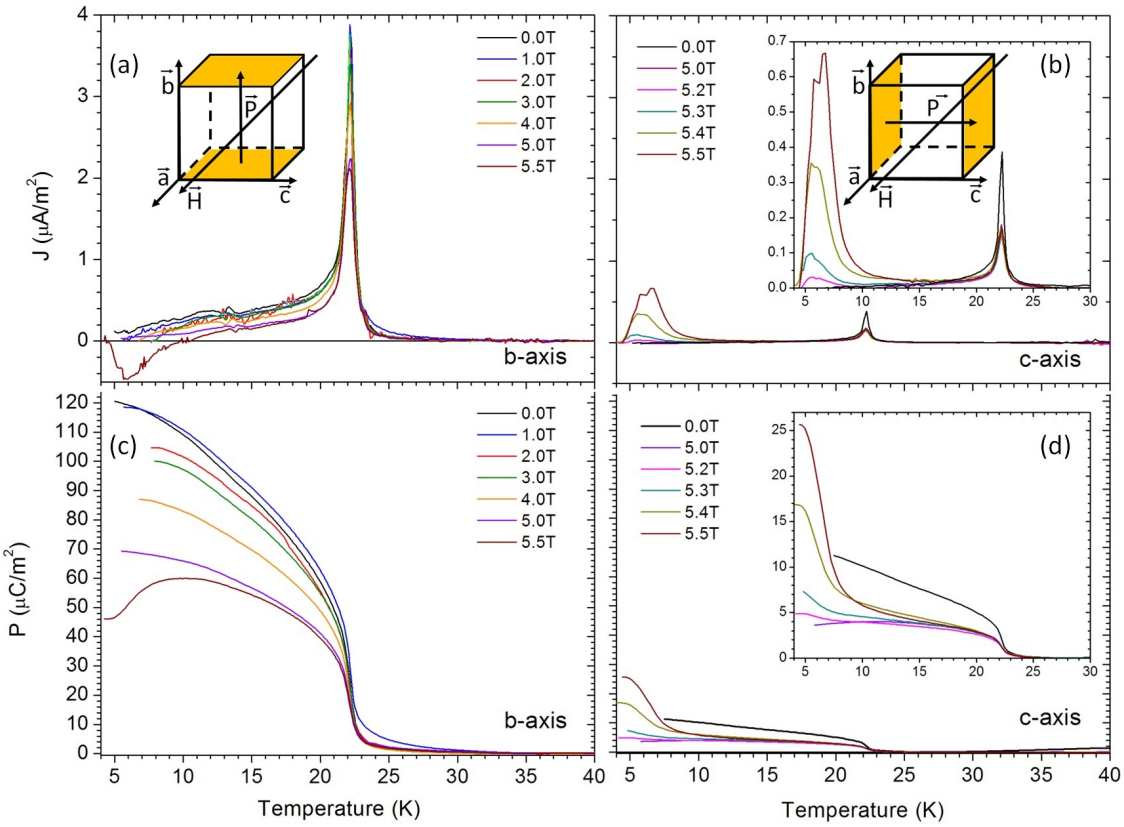

Figure 10.1: Pyroelectric current density as a function of temperature measured along the (a) b-axis and (b) c-axis, for different applied magnetic fields along the a-axis, along with schematic view of the crystal orientation. Pooling electric fields of 20 and 100 V/mm were applied along the b- and c-axis, respectively. Temperature dependence of electric polarization obtained from time integration of respective pyroelectric current density for (c) b-axis and (d) c-axis. Insets show detailed view of the c-axis data.

density presented in Figure 10.1(a). The value obtained at the lowest measured temperature is of 120 μC.m^{-2}, 5 times smaller than the 600 μC.m^{-2} obtained for pure $TbMnO_3$ by Kimura *et al.* along the same axis (note that they used pooling electric fields of 200V/mm) [52]. This relation is in agreement with the study in ceramics discussed in the previous section (cf. 9.3(b)). The step observed around T_{lock} in Figure 10.1(d), associated with P_c, is in fact only due to a misalignment, calculated from its magnitude to be of 6 degrees. This in fact is within our experimental error up to 10 degrees on the sample preparation.

The value of T_{lock} is maintained at 22.5 K for all the applied magnetic fields used in this work (5.5 T). As the applied magnetic field increases up to 5 T, P_b continuously decreases. At the lowest temperature, under 5 T, only about 50% of the initial polarization is found. The behavior of P_b with the applied magnetic field of $TbMnO_3$, seen by Kimura *et al.*, is strikingly different, where almost no change of P_b was found up to 4 T [52]. Up to 5 T, we detected nothing along the c-axis apart the projection from P_b.

Above 5 T and below 10 K, a negative peak of the pyroelectric current density curve measured along the b-axis is observed, while a positive peak emerges along the c-axis (see Figures 10.1(a) and (b), respectively). The time integration of these curves is plotted with the same scale in Figures 10.1(c) and (d), showing the decrease of P_b and the concomitant increase of P_c, respectively. This means that above 5 T, the magnetic field induces a gradual rotation of the electric polarization from the b-axis to the c-axis. As the electric polarization emerges from the spin-cycloidal structure, this means that this structure is changing from the ab- to the ac-plane. Moreover, as the magnetic field increases, the critical temperature, where this flop starts to occurs,

also increases. A similar changing of the spin-cycliodal plane induced by a applied magnetic field above 4 T was also reported for $TbMnO_3$ [52].

10.2 Mn^{3+} magnetic structure under applied magnetic field

Assuming that the electric polarization arises in $TbMn_{0.98}Fe_{0.02}O_3$ from the inverse Dzyaloshinskii-Moriya interaction of the Mn^{3+} spins, as in $TbMnO_3$, we suspect that the applied magnetic field induces changes on the magnetic structure. In order to unravel the magnetic structure, we performed single crystal neutron diffraction under magnetic field, applied along the a-axis. Unfortunately, the magnets surrounding the sample holder only enabled us to measure the scattered neutrons in a total angle of 15 degrees out of the bc-plane. Thus, the number of diffraction peaks is very limited, hindering any possibility to refine both atomic positions and magnetic structure. However, the available data are enough to get insight into the magnetic field induced changes of the spin structure in the different magnetic phases of $TbMn_{0.98}Fe_{0.02}O_3$. Figure 10.2 shows representative neutron diffraction patterns of $TbMn_{0.98}Fe_{0.02}O_3$ recorded at different fixed temperatures and different applied magnetic fields, along with the identification of the observed diffraction peaks. The vertical direction of the diffraction patterns corresponds to $(h, 0, 0)$ and the horizontal direction to $(0, k, l)$.

First we present and discuss the results obtained for the nuclear diffraction peaks. At 50 K, only nuclear diffraction peaks are observed. The peaks are indexed to $(0, 2, 0)$, $(0, 3, 1)$ and $(0, 5, 1)$ planes. These peaks are always observed for temperatures below 50 K and for different magnetic field strengths. From these peaks, we have determine the b- and c-lattice parameters as a function of temperature and applied magnetic field. Figure 10.3 shows the temperature dependence of the pseudocubic lattice parameters b_{pc} and c_{pc}, measured at 0 and 8 T, respectively. The pseudocubic lattice parameters decreases as the temperature decreases and no anomalous temperature behavior could be ascertained at the critical temperatures. Moreover, no effect of the applied magnetic field on the pseudocubic lattice parameters can be observed, and the variation of the lattice parameters measured at the same temperature and different applied magnetic field are within the experimental error. These results point out that the magnetic field has a negligible effect on the crystallographic structure, in good agreement with previous diffraction experiments in rare-earth manganites [144].

In the absence of an applied magnetic field, the paramagnetic to the incommensurate antiferromagnetic phase transition at T_N is revealed by the appearance of a satellite peak indexed to $(q_m, 1, 0)$, with $q_m = 0.28$ at 38 K. The appearance of this satellite is associated with the modulated ordering of the Mn^{3+} spins. Below 22 K, a second satellite peak appears, assigned to the stabilization of the cycloidal spin arrangement. Finally, the ordering of the Tb^{3+} spins gives rise to a diffuse scattering, observed at close to the satellite peak at $(q_m, 1, 0)$.

We start by analyzing the peaks associated with the modulation of the Mn^{3+} spins. Figures 10.4(a) and (b) show the temperature dependence of the modulation wave vector q_m and the peak intensity of the satellite peak assigned to the cycloidal ordering of the Mn^{3+} spin modulations, respectively. At 0 T, the modulation wave vector is temperature dependent in the incommensurate antiferromagnetic phase, exhibiting a minimum value at around 32 K. Below 20 K, the value of the modulation wave vector keeps a constant value of 0.27 down to 5 K, corroborating the stabilization of the commensurate modulated spin structure below T_{lock}. This value is very close that found in $TbMnO_3$ of $q_m = 0.27$ [50].

When a magnetic field is applied along the a-axis, the temperature dependence of the modulation wave vector changes. In the temperature range of stability of the incommensurate antiferromagnetic phase, the modulation wave vector exhibits large temperature variations. We can ascertain that at fixed temperatures, its value is a decreasing function of the magnetic field strength. The temperature where the minimum value of the wave vector is reached decreases from 32 K at 0 T down to 22 K at 8 T. Moreover, the temperature below which the wave vector becomes constant decreases as the applied magnetic field strength increases, from 20

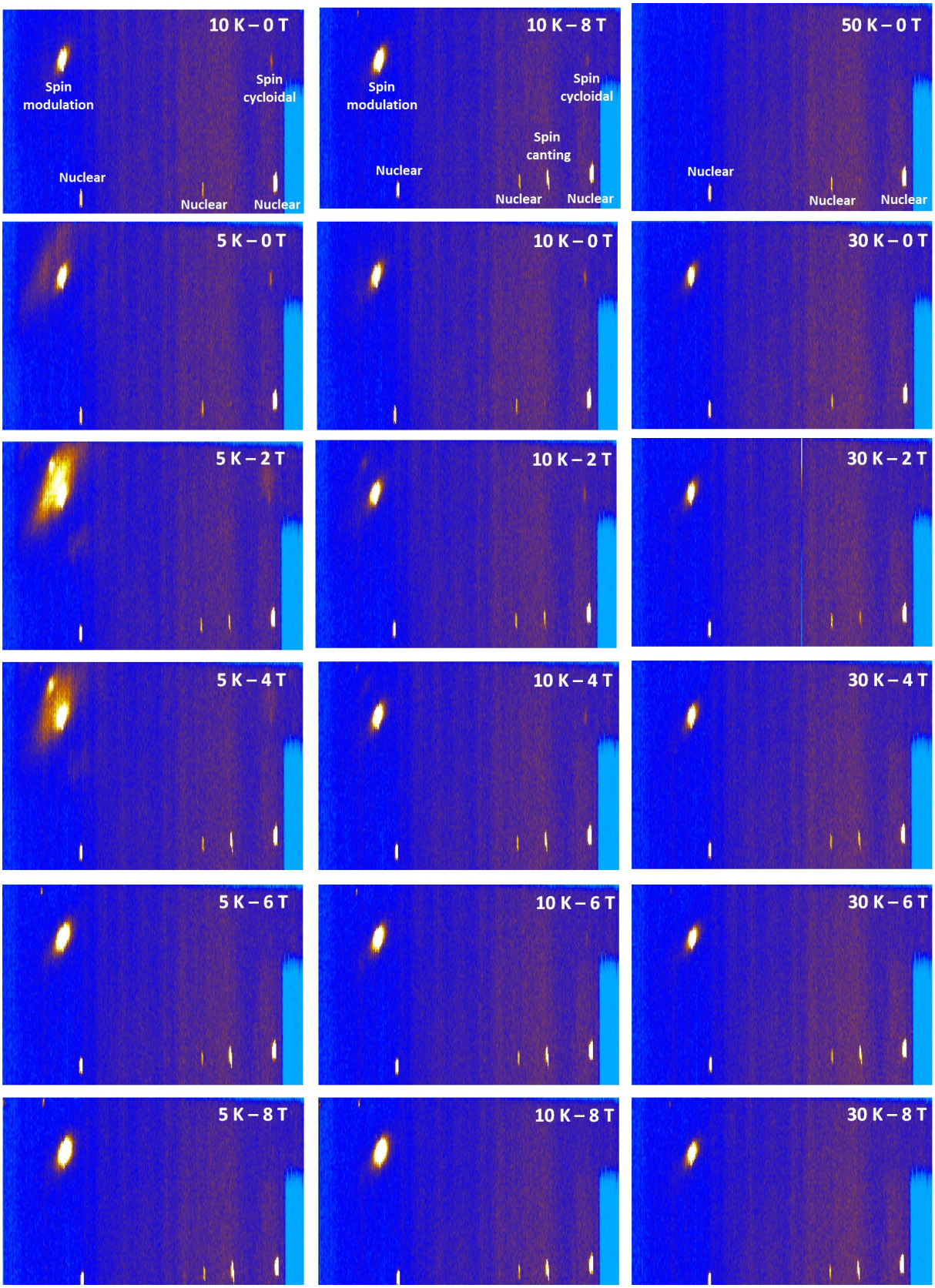

Figure 10.2: Neutron diffraction patterns of $TbMn_{0.98}Fe_{0.02}O_3$. Upper row (left to right): identification of the observed diffraction peaks measured at 10 K, with applied magnetic field along the a-axis of 0 T and 8 T, and at 50 K without applied magnetic field. Bottom 5 row (left to right): neutron diffraction patterns measured at 5, 10 and 30 K, with increasing applied magnetic field of 2 T each descending row. The vertical direction corresponds to $(h, 0, 0)$ and the horizontal direction to $(0, k, l)$.

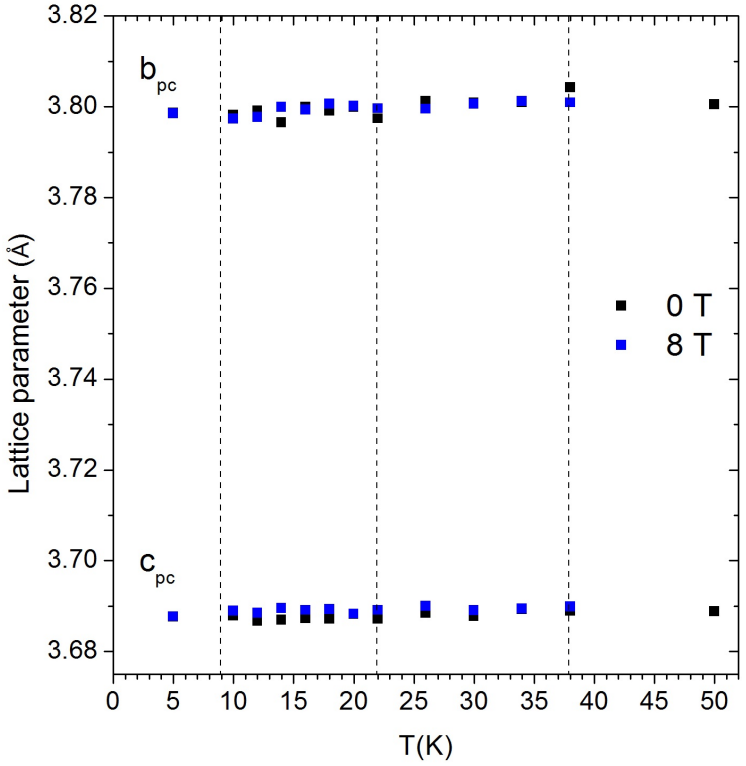

Figure 10.3: Temperature dependence of pseudocubic lattice parameters b_{pc} and c_{pc} under applied magnetic field of 0 and 8 T. Vertical dashed lines mark phase transition temperatures at 0 T.

K at 0 T down to 14 K at 5 T. Above to 6 T the wave vector never reaches a constant value in the measured temperature range. This result evidences for the destabilization of the commensurate spin modulation as the magnetic field increases, and its eventual suppression above 6 T.

The destabilization of the spin cycloidal ordering is also evidenced by the magnetic field dependence of the intensity of the satellite peak assigned to this modulation (see Figure 10.2(b)). The intensity of the satellite peak is always small. For a fixed magnetic field strength, the intensity of this peak increases as the temperature decreases from 22 K. However, the intensity measured at a fixed temperature, decreases as the magnetic field increases. At 10 K, the intensity reduction by the 8 T applied magnetic field is about 75% relatively to its value at 0 T. As the applied magnetic field destabilizes the cycloidal modulated spin structure, it induces the emergence of a diffraction peak assigned to a weak-ferromagnetic component, associated with a spin-canted structure. The magnetic field dependence of this peak is shown in Figure 10.4(c). It is worth to stress that, without an applied magnetic field, this diffraction peak is absent. When a magnetic field is applied, this peak starts to appear in the incommensurate antiferromagnetic phase. For a fixed magnetic field strength/temperature, the intensity of the ferromagnetic peak monotonously increases as the temperature decreases/magnetic field increases. The appearance of this peak is evidence of a spin-canting induced by the magnetic field.

The overall result here presented clearly chows that the magnetic field applied along the a-axis destabilizes both the incommensurate modulated phase and the commensurate modulated cycloidal phase, which allows for ferroeletricity. However, the applied magnetic field has another effects as we will see in the following.

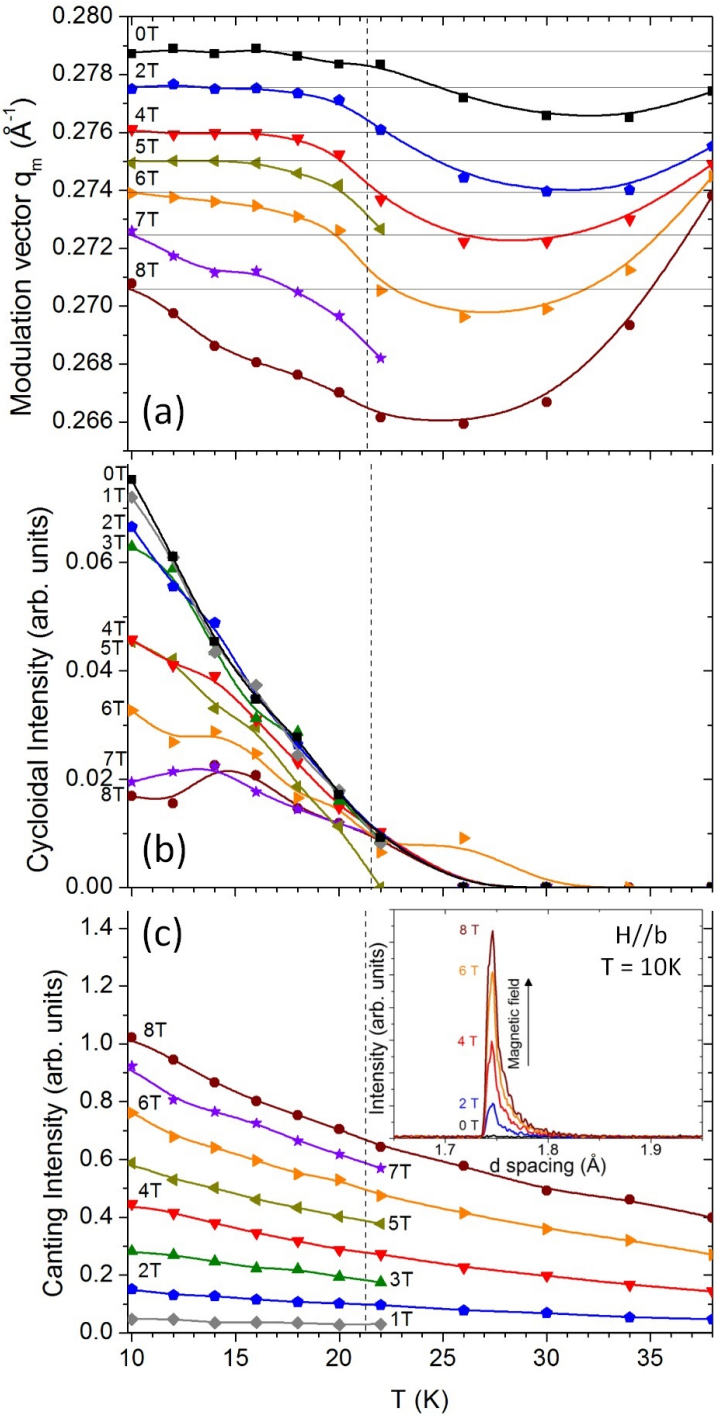

Figure 10.4: Temperature dependence, for different applied magnetic fields, of (a) modulation value (q_m) and (b) intensity of magnetic diffraction peaks associated (b) with spin cycloidal structure and (c) with spin canting structure. Dashed vertical line marks T_{lock}. Inset shows the intensity of the spin canting magnetic diffraction peak.

10.3 Tb^{3+} spins alignment and magnetic-field induced transition

As it was referred to above, the Tb^{3+} spins order in $TbMn_{0.98}Fe_{0.02}O_3$ below 8 K, and up to now, we have discussed the results obtained above 10 K. In the following, we shall focus our attention on the experimental results obtained below 10 K. In $TbMn_{0.98}Fe_{0.02}O_3$, the Tb^{3+}spin ordering reveals itself by the appearance of a diffuse scattering close to the $(q_m, 1, 0)$ satellite peak at 5 K. This region of the diffraction patterns at this temperature was isolated by zooming Figure 10.2, and it is shown in Figure 10.5(a) for the different applied magnetic field strengths. As the Tb^{3+} spins order under the influence of the local magnetic field arising from the Mn^{3+} spins, the appearance of a diffuse scattering associated with the Tb^{3+} ordering gives evidence of a magnetic field disorder in the compound. The intensity of the diffuse scattering behaves in a complex manner with the applied magnetic field. In order to clarify the discussion, we present in Figure 10.5(b) the integrated spectra as a function of d-spacing of this same region, for different fixed magnetic fields, along with the integrated spectrum obtained at 10 K and 0 T.

As the magnetic field increases towards 3 T, there is an intensity increase of the diffuse scattering around the (q_m,1,0) peak at 7.0 Å, associated with the Mn^{3+} spin ordering. Simultaneously, a new peak at 3.6 Å starts to appear at 1 T, and its intensity increases with increasing the magnetic field. Above 3 T, the diffuse scattering intensity decreases up to 5 T and it is no longer observed above 6 T. Moreover, the diffraction peak at 3.6 Å disappears at 6 T and a new small peak emerge at 4.7 Å, whose intensity increases as the magnetic field strength increases. The last result clearly points out for a magnetic field-induced phase transition at around 6 T.

In fact, it is at 6 T that the commensurability appears to be lost, as q_m no longer tends to a constant value in the measured temperature range. Moreover, it is around 6 T that the electric polarization is estimated to be completely suppressed by the applied magnetic field and that the C/T(T) anomalies associated with T_{lock} and T_1 smear out (cf. Figures 9.4(b) and 9.5(c) of the previous Chapter). It is thus possible that a magnetic field-induced phase transition that completely disrupts the cycloidal spin structure, eliminating the conditions for the emergence of ferroelectricity, occurs above 6 T for $TbMn_{0.98}Fe_{0.02}O_3$.

10.4 Summary

With oriented single-crystals of $TbMn_{0.98}Fe_{0.02}O_3$ we have seen that the polarization is very sensitive to an applied magnetic field below 5 T, along the *a*-axis, unlike the $TbMnO_3$, confirming the results obtained in the previous study with ceramic samples. We recently discovered that the spin-cycloidal flop, accompanied by the change in direction of the polarization, seen above 4 T in $TbMnO_3$, only happens above 5 T in $TbMn_{0.98}Fe_{0.02}O_3$. This flop occurs due to the change of the cycloidal spin structure from the *ab*- to the *ac*-plane, as a results of a delicate change between the ferro- and antiferromagnetic exchanges.

Using single-crystal neutron diffraction we unraveled the underlying mechanisms of this increase sensitivity. The introduced Fe^{3+} ions promote a canted alignment of the Mn^{3+} spins as a magnetic field is applied. This disrupts the cycloidal spin structure, necessary for the emergence of the ferroelectricity, and hinders its commensurable nature. At lower temperatures, a diffuse scattering of the Tb^{3+} spins was observed, similar to what occurs in $TbMnO_3$. With the applied magnetic field up to 4 T, the Tb^{3+} spins become better aligned, while for 6 T and above they change their spin structure associated with the emergence of a magnetic-field induced phase transition.

The work regarding the anisotropy of the magnetoelectric and multiferroic properties of $TbMn_{1-x}Fe_xO_3$ ($x < 0.05$) is still undergoing. At this moment, we are already studying single-crystals of $TbMn_{0.96}Fe_{0.04}O_3$, in the scope of the Master thesis of André Maia. An interesting result was already obtained, which reveals that even without an applied magnetic field the electric polarization of $TbMn_{0.96}Fe_{0.04}O_3$ is along the *c*-axis,

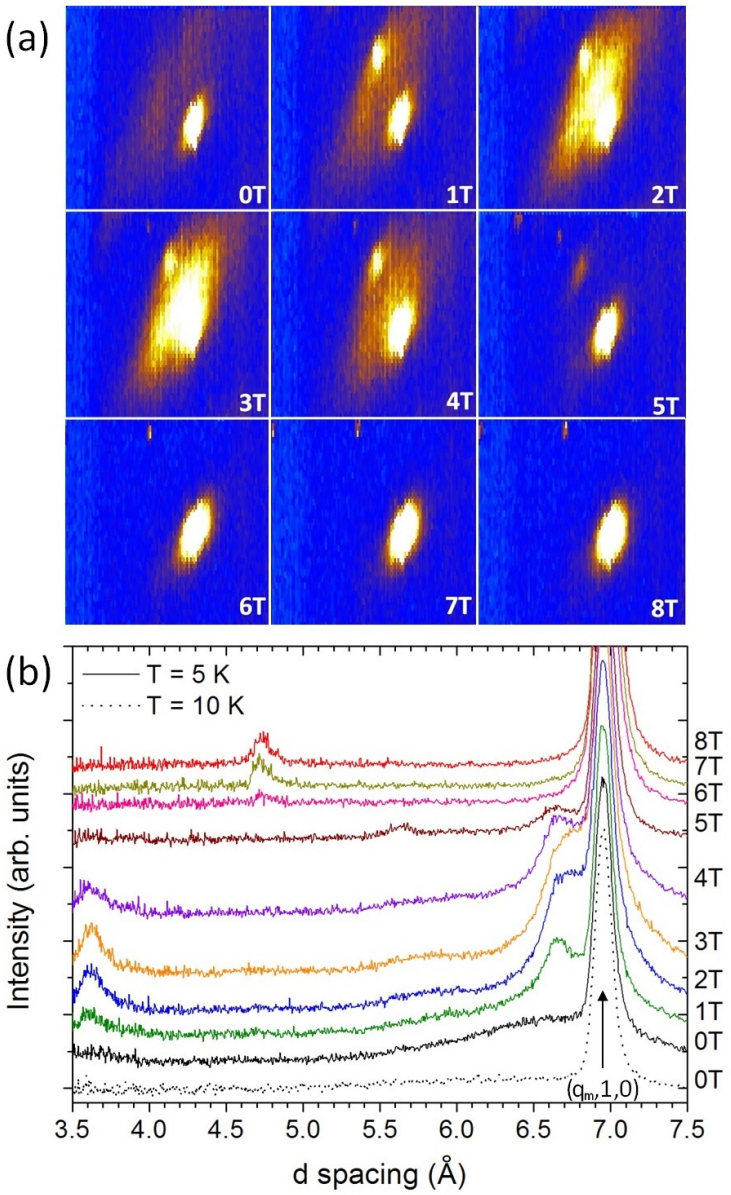

Figure 10.5: (a) Detail of the magnetic diffraction patterns around the (q_m,1,0) peak of the Mn/Fe sublattice, for different applied magnetic fields, at 5 K. (b) Integrated spectra of the regions presented in (a), compared to one taken at 0 T and 10 K (dotted line). The diffuse intensity seen at 0 T around the sharp (q_m,1,0) peak close to 7.0 Å is associated with the Tb spins alignment.

instead of along the b-axis, as observed in $TbMnO_3$ and $TbMn_{0.98}Fe_{0.02}O_3$. The 4% of Fe-concentration is enough to change the magnetic exchanges in a way that changes the plane of the spontaneous ordering of the spin-cycloidal flop from the ab- to the ac-plane. Moreover, we have found that when a magnetic field above 4 T is applied in $TbMn_{0.96}Fe_{0.04}O_3$ the electric polarization disappears beyond the measurement resolution. This gives further evidence for the magnetic-field induced phase transition ascertained by neutron diffraction in $TbMn_{0.98}Fe_{0.02}O_3$ above 6 T, which can be associated with the suppression of the electric polarization observed in $TbMn_{0.96}Fe_{0.04}O_3$ above 4 T.

Thus, we are now interested in obtaining low-temperature complete magnetic diffraction patterns for different concentrations (x = 0.02, 0.03 and 0.04) to better resolve and understand the role of the Fe-concentration on the stabilization of the spin-cycloidal structure. Then, to obtain complete magnetic diffraction patterns of single-crystals with applied magnetic field along the a-axis, to refine the observed magnetic structures, resolving both the possible cycloidal spin structure plane flop and the complex magnetic ordering of the Tb^{3+} spins, towards a complete (x, T, μ_0H) phase diagram.

Conclusions

This thesis is aimed at searching for a possible nexus between structural distortions and physical behavior of an outstanding class of compounds, the $R\mathrm{MnO_3}$ and $R\mathrm{FeO_3}$ series. The studied compounds belong to the GdFeO3-type perovskites. In this regard, the primary distortions yielding the symmetry reduction from the ideal $Pm\bar{3}m$ to the $Pnma$ space group are the octahedral tiltings. These distortions are thus potential components to be included in the microscopic mechanisms underlying the rich variety of physical properties exhibited by the rare-earth ferrites and manganites.

In order to highlight the major role that octahedral tiltings can play to describe the behavior of orthorhombic perovskites, we can refer to two representative studies carried out in this thesis. On one hand, we have shown in Chapter 4, for the case of the $R\mathrm{FeO_3}$ series, that there is a linear relation between the tilts and the tolerance factor. This relationship can be used to properly tune the octahedral tiltings by R-cation chemical substitution. On the second hand, we have provided in Chapter 5, a comprehensive description of how the tilt distortions evolve with pressure as a function of ionic radius. In particular, it is shown that a crossover behavior of the tilts is observed, denoting EuFeO3 as the borderline compound. Moreover, we were able to correlate the change of the critical pressure with the pressure dependence of the tilts, and show how they can trigger the high to low spin reconfiguration at P_{IM}.

Noteworthy, we have observed in other studies presented in this thesis that further microscopic mechanisms have to be incorporated in the discussion of the available experimental data. There are some examples in this thesis that clearly evidences this remark, like those presented in Chapters 9 and 10, which involve the $\mathrm{TbMn_{1-x}Fe_xO_3}$ solid solution. The striking changes observed in the polar, magnetic and magnetoelectric properties even at low concentration of iron (less than $x = 0.06$) cannot be explained by the octahedral tiltings nor the Jahn-Teller distortion as they do not change almost nothing across the whole solid solution. Contrarily, the driving mechanism involves the electronic configuration at the B-site, in particular, the local interaction of the e_g-electrons, which yield the suitable balance between the ferro- and antiferromagnetic exchanges.

Another structural distortion that was studied in this thesis was the cooperative, non-symmetry breaking Jahn-Teller distortion. From the outcomes of this thesis, we are led to assume that it should not be considered as a basic driving force of the physical behavior observed in the studied compounds at low temperatures. For example, we have ascertained that the cooperative Jahn-Teller is lost in $\mathrm{TbMn_{1-x}Fe_xO_3}$ for $x > 0.5$. Though for $x < 0.6$ significant changes in the magnetic, polar and magnetoelectric properties occur, the prevailing cooperative Jahn-Teller does not change apparently in this concentration range.

From the aforementioned examples, it is evident that an intrinsic entanglement of mechanisms of different nature should be considered to reach a deep understanding of the physical behavior in rare-earth ferrites and manganites.

This thesis is obviously integrated in the scope of the experimental physics. Thus, its main objectives were reached by using a whole set of experimental techniques, which involve at microscopic scale the study of the structural distortions and spin-reorientation phenomena and at macroscopic scale the characterization of

the magnetic, polar and magnetoelectric properties. Herewith, it is worth to focus on the benefit to study structural distortions through the combined usage of the x-ray diffraction and Raman scattering. The studies performed in Chapters 4 and 5 are best examples of this advantage, which is based on the linear scaling ascertained between the in-phase and anti-phase octahedral tiltings and respective Raman octahedra rotation modes. However, this scaling it not solely appropriate to explain the experimental data specially in studying the Jahn-Teller distortion, as we have shown in Chapter 7. It is worth to stress that even when Raman scattering is used alone, it is highly adequate to unravel spin-reorientation phenomena through the coupling between lattice and spins, as it is described in Chapter 6. During this work, we have used available experimental techniques, excepting the technique concerning the measurements of the magnetoelectric effect, wherein we have contributed to its implementation and development. The results obtained allowed a deeper insight on the way the driving mechanisms underlie the critical phenomena under study.

After the general remarks referred to above, we will now focus in highlighting the main outcomes of this thesis. In the case of rare-earth manganites, the Jahn-Teller distortion is an additional non-symmetry breaking structural distortion. One way to change it is by hydrostatic pressure. In this regard, the disappearance of the Jahn-Teller distortion in rare-earth manganites has been the subject of large discussion, as contradictory results have been published. In this thesis, using x-ray absorption, we have demonstrated that the Jahn-Teller distortion in both $GdMnO_3$ and $DyMnO_3$ is apparently weakened for applied pressure above 6 GPa, keeping then constant up to 30 GPa. Although we could not reach the critical pressure for the structural and insulating-to-metal phase transition (values around 50 GPa), we cannot rule out that other mechanisms are responsible for the high-pressure phase transition. Another way is by B-site chemical substitution of the Mn^{3+} ion. Though there are several options, Fe^{3+} ion provides a simplification of the altered parameters, since it presents the exact same ionic radius of Mn^{3+}, for the 6th coordination, in the high-spin configuration. From the x-dependencies of the distortion modes amplitudes and the Raman octahedra rotation modes, we observed that the Jahn-Teller distortion is reduced up to $x = 0.5$, being suppressed above this concentration. This result evidences the sensitivity of the Raman octahedra rotation modes to other distortions of the BO_6 octahedra other than their tilts, which we shall now discuss in more detail.

In the past, a rationale was found between the both BO_6 octahedra tilt and both the Raman octahedra rotation modes on RMnO$_3$, RCrO$_3$, and others. In this thesis we evidenced that, at least for the RFeO$_3$, actually two different rationales exist, being 21.1 cm^{-1}/deg for the in-phase tilt and 23.9 cm^{-1}/deg for the anti-phase tilt. This calls for a re-examination of the previous studies on other rare-earth families. Furthermore, using the $TbMn_{1-x}Fe_xO_3$ solid solution, where the changes on the tilt angles are negligible small, we determined how the Raman octahedra rotation modes are sensitive to the distortion of the BO_6 octahedra, namely to the magnitude of the Jahn-Teller distortion, adding to the previous knowledge that they were only sensitive to the average B-O bond length.

Structurally, the RMnO$_3$ and RFeO$_3$ series are quite similar. In fact, when hydrostatic pressure is applied, both series present a similar high-pressure insulator to metal phase transition. In the RFeO$_3$, we ascertained that the octahedra tilts have different pressure behaviors depending on the rare-earth ionic radius. For compounds with rare-earths smaller than Eu, the octahedra tilts increase with pressure, whereas for those with rare-earths larger than Eu, the octahedra tilts decrease with pressure. Yet, all the RFeO$_3$ present a similar isostructural high-pressure phase transition, opposed to the RMnO$_3$, where a myriad of high-pressure symmetries are obtained for the different rare-earths.

Interestingly, while in the RMnO$_3$ the structure has been enough to explain the physical properties and lattice dynamics, in the RFeO$_3$ this is not the case. In the RMnO$_3$, a continuous phase-diagram as a function of the rare-earth ionic radius can be drawn, yet, in the RFeO$_3$, this is not possible. This behavior can be interpreted if the strong interactions between R- and Fe-spins in the RFeO$_3$ are included, oppositely to the weaker and usually negligibly R- and Mn-spins interactions in the RMnO$_3$. Surprisingly, even in those

RFeO$_3$ with similar phase sequences, such as NdFeO$_3$, SmFeO$_3$ and TbFeO$_3$, the magnetic transitions reflect themselves in very different ways on the lattice dynamics. However, a strong coupling between magnetism and lattice dynamics is a common featured in these materials. Moreover, GdFeO$_3$ and EuFeO$_3$ present anomalous temperature behaviors of some Raman-active modes, even though no phase transitions are known in that temperature range. Thus, there are other important mechanisms underlying the physical properties of the RFeO$_3$ besides the structure that have to be taken into consideration. In this regard, it is thus understandable that, in the obtained (x, T) magnetic phase diagram for TbMn$_{1-x}$Fe$_x$O$_3$, the structural distortions actually play a secondary role in changing the magnetic interactions as iron is introduced.

A number of different magnetic phases and spin-reorientation phenomena were found, presenting complex behaviors with x. We have focused on the low iron concentrations, where the spin-cycloidal structure is expected, and thus the emergence of ferroelectricity.

In this regard, we noticed how delicate the stabilization of the spin-cycloidal structure is, sufficing less than 5% of Fe-concentration to completely disrupt it. Besides, even for $x < 0.05$, the electric polarization is continuously reduced by the Fe-substitution, when compared to the values obtained in TbMnO$_3$. This effect is even higher under an applied magnetic field. The Fe^{3+} spins tend to have a canted alignment, which competes with the cycloidal ordering. The applied magnetic field promotes this alignment, as seen by single-crystal neutron diffraction, thus increasing the sensitivity of the electric polarization to it via the magnetoelectric effect. In fact, if a strong enough magnetic field is applied along the a-axis (above 6 T for $x = 0.02$ and 4 T for $x = 0.04$), a field-induced phase transition occurs, where the spin-cycloidal structure and the associated ferroelectricity are lost.

Open questions and Future Work

To further answer some of the questions addressed on this thesis, there are already on-going experimental studies.

We have established two different proportionality constants between the tilt angles and the Raman octahedra rotation modes wavenumbers on the RFeO$_3$, while only one was considered up to now in these compounds. It it worth in the near future to check whether this result is also obtained for other systems, namely in the RMnO$_3$ series.

We presented a study of the spin-phonon of the RFeO$_3$, while a similar one was already done for the RMnO$_3$. Now, we are also working on a similar spin-phonon coupling study of the TbMn$_{1-x}$Fe$_x$O$_3$ system, which promises to be interesting as we found many different magnetic phases and spin-reorientations, as shown on the respective magnetic (x, T) phase diagram. Furthermore, the low energy magnetic excitations (magnons) will also be studied for both the RFeO$_3$ and TbMn$_{1-x}$Fe$_x$O$_3$, to further characterize the different magnetic structures.

To further probe the Jahn-Teller distortion on the TbMn$_{1-x}$Fe$_x$O$_3$ system, namely the different distortions present on the MnO$_6$ and on the FeO$_6$ octahedra, x-ray absorption spectroscopy was measured both on the K-edge of the Mn^{3+} and of the Fe^{3+} ions. With this, it is possible to obtain the Mn-O and Fe-O distances separately, unlike when x-ray diffraction is used, where an average value between both is obtained. These measurements were already done by Vera Cuartero at the BM23 and ID26 beam lines of the ESRF, though the analysis is still undergoing. So far, it appears that the FeO$_6$ octahedra remain always undistorted, independently of Fe-concentration, while the MnO$_6$ octahedra maintain their local distortion up to $x = 0.5$, reducing above.

Regarding the magnetoelectric properties, namely its anisotropy effects studied in the last Chapter, further single crystals of $x = 0.04$ and 0.06 were produced and oriented. They will be used to further understand the sensitivity of the ferroelectricity to the applied magnetic field, and to investigate the spin-cycloidal flop. Also,

THz spectroscopy will be used to study the elementary excitations coupling the polar and magnetic properties, designated electromagnons. These studies are part of the on-going Master thesis of André Maia both at our group and the group of Stanislav Kamba in Prague, Czech Republic.

Further proposals for magnetic neutron diffraction are under preparation for both the Isis-RAL and ILL neutron sources, to allow the refinement of the different magnetic phases of the $TbMn_{1-x}Fe_xO_3$ system ($x < 0.05$), finishing the study presented on the last Chapter.

To complement these neutron diffraction studies and to characterize the disorder and fluctuations of the local magnetic fields of $TbMn_{0.98}Fe_{0.02}O_3$, namely on the region of the Tb^{3+} spins quasi-long-range ordering, muon relaxation spectroscopy studies are already being done at both Isis-RAL and PSI muon sources. Muon relaxation spectroscopy is a local probing technique, consisting in the implantation of the muons into the sample, and measuring the precession of the decaying muon spins. Recently, three proposals were accepted for beam time (1720098 and 1810343 at Isis and 20180538 at PSI), though the data are still under analysis. These studies were performed in collaboration with Rui Vilão, João Gil and Helena Alberto from University of Coimbra, with the help of James Lord from Isis and Hubertus Luetkens from PSI.

Bibliography

[1] W. Eerenstein, N. D. Mathur and J. F. Scott, Multiferroic and magnetoelectric materials, *Nature*, **442**, 759, (2006).

[2] M. Bibes, Nanoferronics is a winning combination, *Nature Materials*, **11**, 354, (2012).

[3] M. Bibes and A. Barthélémy, Multiferroics: Towards a magnetoelectric memory, *Nature Materials*, **7**, 7–8, (2008).

[4] H Y Hwang, Y Iwasa, M Kawasaki, B Keimer, N Nagaosa and Y Tokura, Emergent phenomena at oxide interfaces, *Nature Materials*, **11**, 103–113, (2012).

[5] N. A. Spaldin, S.-W. Cheong and R. Ramesh, Multiferroics: Past, present, and future, *Physics Today*, **63**, 38, (2010).

[6] S-W Cheong and M. Mostovoy, Multiferroics: a magnetic twist for ferroelectricity, *Nature Materials*, **6**, 13–20, (2007).

[7] L. W. Martin, Y. H. Chu and R. Ramesh, Advances in the growth and characterization of magnetic, ferroelectric, and multiferroic oxide thin films, *Materials Science and Engineering R: Reports*, **68**, 89–133, (2010).

[8] N. A. Hill, Why Are There so Few Magnetic Ferroelectrics?, *The Journal of Physical Chemistry B*, **104**, 6694–6709, (2000).

[9] D. Talbayev, S. A. Trugman, Seongsu Lee, Hee Taek Yi, S.-W. Cheong and A. J. Taylor, Long-wavelength magnetic and magnetoelectric excitations in the ferroelectric antiferromagnet BiFeO3, *Physical Review B*, **83**, 094403, (2011).

[10] T. Lancaster, S. J. Blundell, D. Andreica, M. Janoschek, B. Roessli, S. N. Gvasaliya, K. Conder, E. Pomjakushina, M. L. Brooks, P. J. Baker, D. Prabhakaran, W. Hayes and F. L. Pratt, Magnetism in geometrically frustrated YMnO3 under hydrostatic pressure studied with muon spin relaxation, *Physical Review Letters*, **98**, 11–14, (2007).

[11] J. Neaton, C. Ederer, U. Waghmare, N. Spaldin and K. Rabe, First-principles study of spontaneous polarization in multiferroic BiFeO3, *Physical Review B*, **71**, 014113, (2005).

[12] J. Wang, J. B. Neaton and H. Zheng, Epitaxial BiFeO3 Multiferroic Thin Film Heterostructures, *Science*, **299**, 1719, (2003).

[13] T Kimura, T Goto, H Shintani, K Ishizaka, T Arima and Y Tokura, Magnetic control of ferroelectric polarization, *Nature*, **426**, 55–58, (2003).

[14] T. Goto, T. Kimura, G. Lawes, A. P. Ramirez and Y. Tokura, Ferroelectricity and Giant Magnetocapacitance in Perovskite Rare-Earth Manganites, *Physical Review Letters*, **92**, 257201, (2004).

[15] Victor M. Goldschmidt, Die Gesetze der Krystallochemie, *Die Naturwissenschaften*, **21**, 477, (1926).

[16] I. Loa, P. Adler, A. Grzechnik, K. Syassen, U. Schwarz, M. Hanfland, G. Rozenberg, P. Gorodetsky and M. Pasternak, Pressure-Induced Quenching of the Jahn-Teller Distortion and Insulator-to-Metal Transition in LaMnO3, *Physical Review Letters*, **87**, 125501, (2001).

[17] A. M. Glazer, The Classification of Tilted Octahedra in Perovskites, *Acta Crystallographica. Section B*, **28**, 3384, (1972).

[18] P. M. Woodward, Octahedral tilting in perovskites. I. Geometrical considerations, *Acta Crystallographica Section B*, **53**, 32, (1997).

[19] D. J. Passos. From manganites to ferrites: a study on the structural, magnetic and magnetoelectric properties, MSc Thesis. Technical report, University of Porto, (2015).

[20] H. D. Megaw. *Crystal Structures: A Working Approach.* W. B. Saunders Co., Philadelphia, PA, (1973).

[21] R. H. Mitchell. *Perovskites, Modern and Ancient.* Almaz Press, Ontario, Canada, (2002).

[22] J. M. Perez-Mato, D. Orobengoa and M. I. Aroyo, Mode crystallography of distorted structures, *Acta Crystallographica Section A*, **66**, 558–590, (2010).

[23] M. A. Carpenter and C. J. Howard, Symmetry rules and strain/order-parameter relationships for coupling between octahedral tilting and cooperative Jahn-Teller transitions in ABX3 perovskites. I. Theory, *Acta Crystallographica Section B*, **65**, 134, (2009).

[24] N. Miao, N. C. Bristowe, Bi. Xu, M. J. Verstraete and P. Ghosez, First-principles study of the lattice dynamical properties of strontium ruthenate, *Journal of Physics Condensed Matter*, **26**, 035401, (2014).

[25] P Chen, M N Grisolia, H Ji Zhao, O E González-vázquez, L Bellaiche, M Bibes, B-G Liu and J Iniguez, Energetics of oxygen-octahedra rotations in perovskite oxides from first principles, *Physical Review B*, **97**, 024113, (2018).

[26] R. Vilarinho, D. J. Passos, E.C. Queirós, P. B. Tavares, A. Almeida, M. C. Weber, M. Guennou, J. Kreisel and J. Agostinho Moreira, Suppression of the cooperative Jahn-Teller distortion and its effect on the Raman octahedra-rotation modes of TbMn1-xFexO3, *Physical Review B*, **97**, 144110, (2018).

[27] J. B. Goodenough, A. Wold, R. J. Arnott and N. Menyuk, Relationship Between Crystal Symmetry and Magnetic Properties of Ionic Compounds Containing Mn3+, *Physical Review*, **124**, 373, (1961).

[28] M. N. Iliev and M. V. Abrashev, Raman phonons and Raman Jahn Teller bands in perovskite like manganites, *Journal of Raman Spectroscopy*, **32**, 805, (2001).

[29] T. Arima, T. Goto, Y. Yamasaki, S. Miyasaka, K. Ishii, M. Tsubota, T. Inami, Y. Murakami and Y. Tokura, Magnetic-field-induced transition in the lattice modulation of colossal magnetoelectric GdMnO3 and TbMnO3 compounds, *Physical Review B*, **72**, 100102(R), (2005).

[30] N D Todorov, M V Abrashev and V G Ivanov, Frequency dependence of the quasi-soft Raman-active modes in rotationally distorted RBO3 perovskites (R=rare earth, B=Al, Sc, Ti, V, Cr, Mn, Fe, Co, Ni, Ga), *Journal of Physics: Condensed Matter*, **24**, 175404, (2012).

[31] M.C. Weber, M. Guennou, H. Ji. Zhao, J. Íñiguez, R. Vilarinho, A. Almeida, J. Agostinho Moreira and J. Kreisel, Raman spectroscopy of rare-earth orthoferrites RFeO3 (R = La, Sm, Eu, Gd, Tb, Dy), *Physical Review B*, **94**, 214103, (2016).

[32] M. Marezio, J P Remeika and P D Dernier, The crystal chemistry of the rare earth orthoferrites, *Acta Crystallographica Section B*, **26**, 2008–2022, (1970).

[33] M. W. Lufaso and P. M. Woodward, Jahn-Teller distortions, cation ordering and octahedral tilting in perovskites., *Acta crystallographica. Section B*, **60**, 10, (2004).

[34] D Treves, Studies on Orthoferrites at the Weizmann Institute of Science, *Journal of Applied Physics*, **36**, 1033, (1965).

[35] E. Bousquet and A. Cano, Non-collinear magnetism in multiferroic perovskites, *Journal of Physics: Condensed Matter*, **28**, 123001, (2016).

[36] S. Artyukhin, M. Mostovoy, N. P. Jensen, D. Le, K. Prokes, V. G. Paula, H. N Bordallo, A. Maljuk, S. Landsgesell, H. Ryll, B. Klemke, S. Paeckel, K. Kiefer, K. Lefmann, T. K. Luise and D. N. Argyriou, Solitonic lattice and Yukawa forces in the rare-earth orthoferrite TbFeO3, *Nature materials*, **11**, 694–699, (2012).

[37] C.-Y. Kuo, Y. Drees, M. T. Fernández-Díaz, L. Zhao, L. Vasylechko, D. Sheptyakov, A. M. T. Bell, T. W. Pi, H.-J. Lin, M.-K. Wu, E. Pellegrin, S. M. Valvidares, Z. W. Li, P. Adler, A. Todorova, R. Küchler, A. Steppke, L. H. Tjeng, Z. Hu and A. C. Komarek, k=0 Magnetic Structure and Absence of Ferroelectricity in SmFeO3, *Physical Review Letters*, **113**, 217203, (2014).

[38] S. J. Yuan, W. Ren, F. Hong, Y. B. Wang, J. C. Zhang, L. Bellaiche, S. X. Cao and G. Cao, Spin switching and magnetization reversal in single-crystal NdFeO3, *Physical Review B*, **87**, 184405, (2013).

[39] T Yamaguchi, Theory of spin reorientation in rare-earth orthochromites and orthoferrites, *Journal of Physics and Chemistry of Solids*, **35**, 479–500, (1974).

[40] J.-H. Lee, Y. K. Jeong, J. H. Park, Mi.-A. Oak, H.M. Jang, J. Y. Son and J. F. Scott, Spin-Canting-Induced Improper Ferroelectricity and Spontaneous Magnetization Reversal in SmFeO3, *Physical Review Letters*, **107**, 117201, (2011).

[41] H Shen, Z Cheng, F Hong, J Xu, S Yuan, S Cao and X Wang, Magnetic field induced discontinuous spin reorientation in ErFeO 3 single crystal, *Applied Physics Letters*, **103**, 192404, (2013).

[42] Y. Tokunaga, N. Furukawa, H. Sakai, Y. Taguchi, T. Arima and Y. Tokura, Composite domain walls in a multiferroic perovskite ferrite, *Nature materials*, **8**, 558–562, (2009).

[43] Y. Tokunaga, S. Iguchi, T. Arima and Y. Tokura, Magnetic-field-induced ferroelectric state in DyFeO3, *Physical Review Letters*, **101**, 3–6, (2008).

[44] H. C. Gupta, Manoj Kumar Singh and L. M. Tiwari, Lattice dynamic investigation of Raman and infrared wavenumbers at the zone center of orthorhombic RFeO3 (R = Tb, Dy, Ho, Er, Tm) perovskites, *Journal of Raman Spectroscopy*, **33**, 67–70, (2002).

[45] S Venugopalan, M Dutta, A K Ramdas and J P Remeika, Magnetic and vibrational excitations in rare-earth orthoferrites: A Raman scattering study, *Physical Review B*, **31**, 1490, (1985).

[46] R. M. White, R. J. Nemanich and C. Herring, Light scattering from magnetic excitations in orthoferrites, *Physical Review B*, **25**, 1822, (1982).

[47] G. Kh. Rozenberg, M. P. Pasternak and L. S. Dubrovinsky, Crystallographic transitions related to magnetic and electronic phenomena under high pressure in iron oxides and compounds, *Phase Transitions*, **80**, 1131, (2007).

[48] M P Pasternak, W M Xu, G. Kh Rozenberg and R D Taylor, Electronic , Magnetic and Structural Properties of the RFeO3 Antiferromagnetic-Perovskites at Very High Pressures, *Materials Research Society Symposium Proceedings*, **718**, D2.7.1, (2002).

[49] G. Kh Rozenberg, M. P Pasternak, W. M Xu, L. S Dubrovinsky, S Carlson and R. D Taylor, Consequences of pressure-instigated spin crossover in RFeO3 perovskites; a volume collapse with no symmetry modification, *Europhysics Letters (EPL)*, **71**, 228–234, (2005).

[50] T. Kimura, S. Ishihara, H. Shintani, T. Arima, K.T. Takahashi, K. Ishizaka and Y. Tokura, Distorted perovskite with eg1 configuration as a frustrated spin system, *Physical Review B*, **68**, 060403(R), (2003).

[51] M. Mochizuki and N. Furukawa, Microscopic model and phase diagrams of the multiferroic perovskite manganites, *Physical Review B*, **80**, 134416, (2009).

[52] T. Kimura, G. Lawes, T. Goto, Y. Tokura and A. Ramirez, Magnetoelectric phase diagrams of orthorhombic RMnO3 (R=Gd, Tb, and Dy), *Physical Review B*, **71**, 224425, (2005).

[53] M. Mostovoy, Ferroelectricity in Spiral Magnets, *Physical Review Letters*, **96**, 067601, (2006).

[54] I. A. Sergienko and E. Dagotto, Role of the Dzyaloshinskii-Moriya interaction in multiferroic perovskites, *Physical Review B*, **73**, 094434, (2006).

[55] H. Katsura, N. Nagaosa and A.V. Balatsky, Spin Current and Magnetoelectric Effect in Noncollinear Magnets, *Physical Review Letters*, **95**, 057205, (2005).

[56] M. Tokunaga, Y. Yamasaki, Y. Onose, M. Mochizuki, N. Furukawa and Y. Tokura, Novel Multiferroic State of Eu1-xYxMnO3 in High Magnetic Fields, *Physical Review Letters*, **103**, 187202, (2009).

[57] D. A. Mota, A. Almeida, V. H. Rodrigues, M. M. R. Costa, P. Tavares, P. Bouvier, M. Guennou, J. Kreisel and J. Agostinho Moreira, Dynamic and structural properties of orthorhombic rare-earth manganites under high pressure, *Physical Review B*, **90**, 054104, (2014).

[58] J. Oliveira, J. Agostinho Moreira, A. Almeida, V. Rodrigues, M. M. Costa, P. Tavares, P. Bouvier, M. Guennou and J. Kreisel, Structural and insulator-to-metal phase transition at 50 GPa in GdMnO3, *Physical Review B*, **85**, 052101, (2012).

[59] M. Baldini, V. V. Struzhkin, A. F. Goncharov, P. Postorino and W. L. Mao, Persistence of Jahn-Teller distortion up to the insulator to metal transition in LaMnO3, *Physical Review Letters*, **106**, 066402, (2011).

[60] H. J. Xiang, M. Guennou, J. Íñiguez, J. Kreisel and L. Bellaiche, Rules and mechanisms governing octahedral tilts in perovskites under pressure, *Physical Review B*, **96**, 054102, (2017).

[61] J. Zhao, N. L. Ross and R. J. Angel, New view of the high-pressure behaviour of GdFeO3-type perovskites, *Acta Crystallographica Section B: Structural Science*, **60**, 263–271, (2004).

[62] V. S. Bhadram, D. Swain, R. Dhanya, M. Polentarutti, A. Sundaresan and C. Narayana, Effect of pressure on octahedral distortions in RCrO3 (R= Lu, Tb, Gd, Eu, Sm): The role of R-ion size and its implications, *Materials Research Express*, **1**, 026111, (2014).

[63] H. J. Gerritsen and E. S. Sabisky, Paramagnetic resonance of trivalent manganese in rutile (TiO2), *Physical Review*, **132**, 1507–1512, (1963).

[64] T. Goto, Y. Yamasaki, H. Watanabe, T. Kimura and Y. Tokura, Anticorrelation between ferromagnetism and ferroelectricity in perovskite manganites, *Physical Review B*, **72**, 220403, (2005).

[65] J. Ribeiro, Symmetry and magnetically driven ferroelectricity in rare-earth manganites RMnO3 (R=Gd,Tb,Dy), *Physical Review B*, **76**, 144417, (2007).

[66] G. Lawes, A. B. Harris, T. Kimura, N. Rogado, R. J. Cava, A. Aharony, O. Entin-Wohlman, T. Yildirim, M. Kenzelmann, C. Broholm and A. P. Ramirez, Magnetically Driven Ferroelectric Order in Ni3V2O8, *Physical Review Letters*, **95**, 087205, (2005).

[67] J. Agostinho Moreira, A. Almeida, W. S. Ferreira, M. R. Chaves, B. Kundys, R. Ranjith, W. Prellier, S. M. F. Vilela and P. B. Tavares, Polar properties of Eu(0.6)Y(0.4)MnO(3) ceramics and their magnetic field dependence, *Journal of Physics: Condensed Matter*, **21**, 446002, (2009).

[68] J Agostinho Moreira, A Almeida, W S Ferreira, M R Chaves, J P Araújo, a M Pereira, S M F Vilela and P B Tavares, Polar properties and phase sequence in Eu(0.8)Y(0.2)MnO(3), *Journal of physics. Condensed matter: an Institute of Physics journal*, **22**, 125901, (2010).

[69] J. Agostinho Moreira, A. Almeida, W. S. Ferreira, J. P. Araújo, A. M. Pereira, M. R. Chaves, M. M. R. Costa, V. A. Khomchenko, J. Kreisel, D. Chernyshov, S. M. F. Vilela and P. B. Tavares, Strong magnetoelastic coupling in orthorhombic EuYMnO3 manganite, *Physical Review B*, **82**, 094418, (2010).

[70] J. Agostinho Moreira, A. Almeida, W. S. Ferreira, M. R. Chaves, J. B. Oliveira, J. M. Machado da Silva, M. A. Sá, S. M. F. Vilela and P. B. Tavares, Ferroelectricity in antiferromagnetic phases of Eu1-xYxMnO3, *Solid State Communications*, **151**, 368, (2011).

[71] H. Murakawa, Y. Onose and F. Kagawa, Rotation of an Electric Polarization Vector by Rotating Magnetic Field in Cycloidal Magnet EuYMnO3, *Physical Review Letters*, **101**, 197207, (2008).

[72] Y. Yamasaki, S. Miyasaka, T. Goto, H. Sagayama, T. Arima and Y. Tokura, Ferroelectric phase transitions of 3d-spin origin in Eu1-xYxMnO3, *Physical Review B*, **76**, 184418, (2007).

[73] V. Yu. Ivanov, A. A. Mukhin, V. D. Travkin, A. S. Prokhorov, Yu. F. Popov, A. M. Kadomtseva, G. P. Vorob'ev, K. I. Kamilov and A. M. Balbashov, New orthorhombic multiferroics R1-xYxMnO3 (R = Eu, Gd), *Physica Status Solidi B*, **243**, 107, (2006).

[74] J. Hemberger, F. Schrettle, A. Pimenov, P. Lunkenheimer, V. Ivanov, A. Mukhin, A. Balbashov and A. Loidl, Multiferroic phases of Eu1-xYxMnO3, *Physical Review B*, **75**, 035118, (2007).

[75] R. Vilarinho, A. Almeida, J.M. Machado da Silva, J.B. Oliveira, M.A. Sá, P.B. Tavares and J. Agostinho Moreira, Dzyaloshinskii Moriya nature of ferroelectric ordering in magnetoelectric GdYMnO3 system, *Solid State Communications*, **208**, 34–40, (2015).

[76] R. Vilarinho, E.C. Queirós, A. Almeida, P.B. Tavares, M. Guennou, J. Kreisel and J. Agostinho Moreira, Scaling spin phonon and spin spin interactions in magnetoelectric GdYMnO3, *Journal of Solid State Chemistry*, **228**, 76–81, (2015).

[77] J Oliveira, J Agostinho Moreira, A Almeida, M R Chaves, J M M da Silva, J B Oliveira, M A Sá, P B Tavares, R Ranjith and W Prellier, Phase diagram of the orthorhombic, lightly lutetium doped EuMnO3 magnetoelectric system, *Physical Review B*, **84**, 094414, (2011).

[78] D A Mota, Y Romaguera Barcelay, P B Tavares, M R Chaves, A Almeida, J Oliveira, W S Ferreira and J Agostinho Moreira, Competing exchanges and spin-phonon coupling in Eu(1-x)R(x)MnO3 (R=Y, Lu), *Journal of physics. Condensed matter : an Institute of Physics journal*, **25**, 235602, (2013).

[79] V Yu Ivanov, A A Mukhin, V V Glushkov and A M Balbashov, Spontaneous Reorientation of the Electric Polarization in Eu1-x HoxMnO3 Multiferroics, *Journal of Experimental and Theoretical Physics Letters*, **97**, 28–33, (2013).

[80] S Elsasser, J Geurts, A. A. Mukhin and A. M. Balbashov, Lattice dynamics and spin-phonon coupling in orthorhombic Eu1-xHoMnO3 (x$<$0.3) studied by Raman spectroscopy, *Physical Review B*, **93**, 1–054301, (2016).

[81] M. Mochizuki, N. Furukawa and N. Nagaosa, Theory of spin-phonon coupling in multiferroic manganese perovskites RMnO3, *Physical Review B*, **84**, 144409, (2011).

[82] R. D. Shannon, Revised effective ionic radii and systematic studies of interatomic distances in halides and chalcogenides, *Acta Crystallographica Section A*, **32**, 751–767, (1976).

[83] K. Bouziane, A. Yousif, I. A. Abdel-Latif, K. Hricovini and C. Richter, Electronic and magnetic properties of SmFe1-xMnxO3 orthoferrites (x=0.1, 0.2, and 0.3), *Journal of Applied Physics*, **97**, 10A504, (2005).

[84] F.-K. Chiang, M.-W. Chu, F. C. Chou, H. T. Jeng, H. S. Sheu, F. R. Chen and C. H. Chen, Effect of Jahn-Teller distortion on magnetic ordering in Dy(Fe,Mn)O3 perovskites, *Physical Review B*, **83**, 245105, (2011).

[85] F. Hong, Z. Cheng, H. Zhao, H. Kimura and X. Wang, Continuously tunable magnetic phase transitions in the DyMnFeO3 system, *Applied Physics Letters*, **99**, 092502, (2011).

[86] F. Hong, B. Yue, J. Wang, A. Studer, C. Fang, X. Wang and S. Dou, Collapse and reappearance of magnetic orderings in spin frustrated TbMnO3 induced by Fe substitution, *Applied Physics Letters*, **109**, 102401, (2016).

[87] H S Nair, T Chatterji, C M N Kumar, T Hansen, H Nhalil, S Elizabeth and A M Strydom, Magnetic structures and magnetic phase transitions in the Mn-doped orthoferrite TbFeO3 studied by neutron powder diffraction, *Journal of Applied Physics*, **119**, 053901, (2016).

[88] Y Fang, Y Yang, Xi Liu, Ji Kang, L Hao, X Chen, L Xie, G Sun, V Chandragiri, CW Wang, Y Cao, F Chen, Y Liu, D Chen, S Cao, C Lin, W Ren and J Zhang, Observation of re-entrant spin reorientation in TbFe1-xMnxO3, *Scientific Reports*, **6**, 33448, (2016).

[89] J. A. Moreira, A. Almeida and W. S. Ferreira, Structure and physical properties of Eu0. 8Y0. 2MnO3 ceramics, *Journal of Electroceramics*, **25**, 203, (2010).

[90] T. Carvalho. *Síntese e caracterização de materiais cerâmicos e filmes finos multiferróicos para aplicação em sensores e atuadores.* PhD thesis, Universidade de Trás-os-Montes e Alto Douro, (2013).

[91] M. Newville, Fundamentals of XAFS, *Reviews in Mineralogy and Geochemistry*, **78**, 33–74, (2014).

[92] N. Ishimatsu, N. Kawamura, M. Mizumaki, H. Maruyama, H. Sumiya and T. Irifune, Applications of nano-polycrystalline diamond anvils to X-ray absorption spectroscopy under high pressure, *High Pressure Research*, **36**, 381, (2016).

[93] B. Joseph, R. Torchio, C. Benndorf, T. Irifune, T. Shinmei, R. Pöttgen and A. Zerr, Experimental evidence of an electronic transition in CeP under pressure using Ce L3XAS, *Physical Chemistry Chemical Physics*, **19**, 17526, (2017).

[94] B. Ravel and M. Newville, Athena, Artemis, Hephaestus: data analysis for X-ray absorption spectroscopy using IFEFFIT, *Journal of Synchrotron Radiation*, **12**, 537–541, (2005).

[95] E. Kroumova, M.I. Aroyo, J.M. Perez-Mato, A. Kirov, C. Capillas, S. Ivantchev and H. Wondratschek, Bilbao Crystallographic Server : Useful Databases and Tools for Phase-Transition Studies, *Phase Transitions*, **76**, 155–170, (2003).

[96] T. C. Damen, S. P. S. Porto and B. Tell, Raman Effect in Zinc Oxide, *Physical Review*, **142**, 570, (1966).

[97] William Hayes and Rodney London. *Scattering of Light by Crystals*, volume 47. Wiley-Interscience, (1979).

[98] W. S. Ferreira. *Estudo do Efeito Magneto-Eléctrico e suas Aplicações*. PhD thesis, University of Porto, (2011).

[99] L. C. Chapon, P. Manuel, P. G. Radaelli, C. Benson, L. Perrott, S. Ansell, N. J. Rhodes, D. Raspino, D. Duxbury, E. Spill and J. Norris, Wish: The New Powder and Single Crystal Magnetic Diffractometer on the Second Target Station, *Neutron News*, **22**, 22–25, (2011).

[100] P. Blaha, K. Schwarz, G. K. H. Madsen, D. Kvasnicka, J. Luitz, R. Laskowski, F. Tran and L. D. Marks. *WIEN2K: An Augmented Plane Wave + Local Orbitals Program for Calculating Crystal Properties Title*. Karlheinz Schwarz, Techn. Universität Wien, Austria, (2018).

[101] David Koller, Fabien Tran and Peter Blaha, Improving the modified Becke-Johnson exchange potential, *Physical Review B*, **85**, 155109, (2012).

[102] John P. Perdew, Adrienn Ruzsinszky, Gábor I. Csonka, Oleg A. Vydrov, Gustavo E. Scuseria, Lucian A. Constantin, Xiaolan Zhou and Kieron Burke, Restoring the Density-Gradient Expansion for Exchange in Solids and Surfaces, *Physical Review Letters*, **100**, 136406, (2008).

[103] G. Kresse and J. Furthmüller, Efficient iterative schemes for ab initio total-energy calculations using a plane-wave basis set, *Physical Review B*, **54**, 11169–11186, (1996).

[104] G. Kresse and D. Joubert, From ultrasoft pseudopotentials to the projector augmented-wave method, *Physical Review B*, **59**, 1758–1775, (1999).

[105] S. L. Dudarev, G. A. Botton, S. Y. Savrasov, C. J. Humphreys and A. P. Sutton, Electron-energy-loss spectra and the structural stability of nickel oxide: An LSDA+U study, *Physical Review B*, **57**, 1505–1509, (1998).

[106] P. E. Blöchl, Projector augmented-wave method, *Physical Review B*, **50**, 17953–17979, (1994).

[107] M. C. Sánchez, G. Subías, J. Garcia and J. Blasco, XAS study of LaMn1-xGaxO3 series, *Physica Scripta*, **2005**, 641, (2003).

[108] V. Cuartero, S. Lafuerza, M. Rovezzi, J. García, J. Blasco, G. Subías and E. Jiménez, X-ray absorption and emission spectroscopy study of Mn and Co valence and spin states in TbMn1-xCoxO3, *Physical Review B*, **94**, 155117, (2016).

[109] J. M. Chen, T. L. Chou, J. M. Lee, S. A. Chen, T. S. Chan, T. H. Chen, K. T. Lu, W. T. Chuang, H.-S. Sheu, S. W. Chen, C. M. Lin, N. Hiraoka, H. Ishii, K. D. Tsuei and T. J. Yang, Pressure-induced structural distortion of TbMnO3: A combined x-ray diffraction and x-ray absorption spectroscopy study, *Physical Review B*, **79**, 165110, (2009).

[110] P. A. Fleury, J. F. Scott and J. M. Worlock, Soft phonon modes and the 110K phase transition in SrTiO3, *Physical Review Letters*, **21**, 16–19, (1968).

[111] J. F. Scott, R C C Leite and T C Damen, Resonant Raman Effect in Semiconductors, *Physical Review*, **188**, 1285, (1969).

[112] J F Scott, Soft-mode spectroscopy: Experimental studies of structural phase transitions, *Reviews of Modern Physics*, **46**, 83, (1974).

[113] M. N. Iliev, M. V. Abrashev, J. Laverdière, S. Jandl, M. M. Gospodinov, Y.Q. Wang and Y.Y. Sun, Distortion-dependent Raman spectra and mode mixing in RMnO3 perovskites (R = La , Pr , Nd , Sm , Eu , Gd , Tb , Dy , Ho , Y), *Physical Review B*, **73**, 064302, (2006).

[114] M C Weber, J Kreisel, P A Thomas, M Newton, K Sardar and R I Walton, Phonon Raman scattering of R CrO 3 perovskites (R = Y , La , Pr , Sm , Gd , Dy , Ho , Yb , Lu), *Physical Review B*, **85**, 054303, (2012).

[115] O Chaix-Pluchery and J Kreisel, Raman scattering of perovskite SmScO3 and NdScO3 single crystals, *Phase Transitions*, **84**, 542, (2011).

[116] J. Laverdière, S. Jandl, A. Mukhin, V.Y. Ivanov, V.G. Ivanov and M. Iliev, Spin-phonon coupling in orthorhombic RMnO3 (R=Pr,Nd,Sm,Eu,Gd,Tb,Dy,Ho,Y): A Raman study, *Physical Review B*, **73**, 214301, (2006).

[117] W. Ferreira, J. Agostinho Moreira, A. Almeida, M. Chaves, J. Araújo, J. Oliveira, J. Machado Da Silva, M. Sá, T. Mendonça, P. Simeão Carvalho, J. Kreisel, J. Ribeiro, L. Vieira, P. Tavares and S. Mendonça, Spin-phonon coupling and magnetoelectric properties: EuMnO3 versus GdMnO3, *Physical Review B*, **79**, 054303, (2009).

[118] J. Agostinho Moreira, A. Almeida, W. S. Ferreira, J. E. Araújo, A. M. Pereira, M. R. Chaves, J. Kreisel, S. M. F. Vilela and P. B. Tavares, Coupling between phonons and magnetic excitations in orthorhombic EuYMnO3, *Physical Review B*, **81**, 054447, (2010).

[119] M El Amrani, M Zaghrioui, V Ta Phuoc, F Gervais and Néstor E Massa, Local symmetry breaking and spin-phonon coupling in SmCrO3 orthochromite, *Journal of Magnetism and Magnetic Materials*, **361**, 1–6, (2014).

[120] V S Bhadram, B Rajeswaran, A Sundaresan and C Narayana, Spin-phonon coupling in multiferroic RCrO3 (R-Y, Lu, Gd, Eu, Sm): A Raman study, *Europhysics Letters (EPL)*, **101**, 17008, (2013).

[121] Y. Zhao, D. J. Weidner, J. B. Parise and D. E. Cox, Thermal expansion and structural distortion of perovskite - data for NaMgF3 perovskite. Part I, *Physics of the Earth and Planetary Interiors*, **76**, 1–16, (1993).

[122] M. Marezio and P D Dernier, The Bond Lengths in LaFeo3, *Materials Research Bulletin*, **6**, 23–30, (1971).

[123] D. Orobengoa, C. Capillas, M. I. Aroyo and J. M. Perez-Mato, AMPLIMODES: Symmetry-mode analysis on the Bilbao Crystallographic Server, *Journal of Applied Crystallography*, **42**, 820–833, (2009).

[124] M. N. Iliev, A. P. Litvinchuk, V. G. Hadjiev, Y. Q. Wang, J. Cmaidalka, R. L. Meng, Y. Y. Sun, N. Kolev and M. V. Abrashev, Raman spectroscopy of low-temperature (Pnma) and high-temperature (R3c) phases of LaCrO3, *Physical Review B*, **74**, 214301, (2006).

[125] MK Singh and HM Jang, Polarized Raman scattering and lattice eigenmodes of antiferromagnetic NdFeO3, *Journal of Raman Spectroscopy*, , 842–848, (2008).

[126] N Koshizuka and S. Ushioda, Inelastic-light-scattering study of magnon softening in ErFeO3, *Physical Review B*, **22**, 5394, (1980).

[127] S. Venugopalan and M. M. Becker, Raman scattering study of LuFeO3, *The Journal of Chemical Physics*, **93**, 3833, (1990).

[128] J. L. Birman, Proof of Worlock's conjecture on the Raman activity of soft modes, *Physics Letters A*, **45**, 196, (1973).

[129] T. Shigenari, On the Raman activity of soft modes in the lower symmetry phase of crystals, *Physics Letters A*, **46**, 243–244, (1973).

[130] M.C. Weber. *Electronic and Structural Properties of Bismuth- and Rare-Earth-Ferrites.* PhD thesis, (2016).

[131] L. M. Daniels, M. C. Weber, M.R. Lees, M. Guennou, R.J. Kashtiban, J. Sloan, J. Kreisel and R. I. Walton, Structures and magnetism of the rare-earth orthochromite perovskite solid solution LaxSm1-xCrO3, *Inorganic Chemistry*, **52**, 12161, (2013).

[132] J. S. Zhou and J. B. Goodenough, Universal octahedral-site distortion in orthorhombic perovskite oxides, *Physical Review Letters*, **94**, 065501, (2005).

[133] T Aoyama, K Yamauchi, A Iyama, S Picozzi, K Shimizu and T Kimura, Giant spin-driven ferroelectric polarization in TbMnO3 under high pressure., *Nature communications*, **5**, 4927, (2014).

[134] A. G. Gavriliuk, G. N. Stepanov, I. S. Lyubutin, A. S. Stepin, I. A. Trojan and V. A. Sidorov, High pressure studies of magnetic, electronic, and local structure properties in the rare-earth orthoferrites RFeO3 (R = Nd, Lu), *Hyperfine Interactions*, **126**, 305–311, (2000).

[135] F. Birch, Finite elastic strain of cubic crystals, *Physical Review*, **71**, 809–824, (1947).

[136] M. Etter, M. Müller, M. Hanfland and R. E. Dinnebier, High-pressure phase transitions in the rare-earth orthoferrite LaFeO3, *Acta Crystallographica Section B: Structural Science, Crystal Engineering and Materials*, **70**, 452–458, (2014).

[137] A. G. Gavriliuk, I. A. Troyan, R. Boehler, M. I. Eremets, I. S. Lyubutin and N. R. Serebryanaya, Electronic and structural transitions in NdFeO3 orthoferrite under high pressures, *Journal of Experimental and Theoretical Physics Letters*, **77**, 619–624, (2003).

[138] S. M. Selbach, J. R. Tolchard, A. Fossdal and T. Grande, Non-linear thermal evolution of the crystal structure and phase transitions of LaFeO3 investigated by high temperature X-ray diffraction, *Journal of Solid State Chemistry*, **196**, 249–254, (2012).

[139] I. Fita, A. Wisniewski, R. Puzniak, E. E. Zubov, V. Markovich and G. Gorodetsky, Common exchange-biased spin switching mechanism in orthoferrites, *Physical Review B*, **98**, 1–7, (2018).

[140] J.D. Gordon, G. Gorodetsky and R.M. Hornreich. Magnetization studies of TbFeO3, (1976).

[141] M. Balkanski, R. F. Wallis and E. Haro, Anharmonic effects in light scattering due to optical phonons in silicon, *Physical Review B*, **28**, 1928, (1983).

[142] R. L. White, Review of Recent Work on the Magnetic and Spectroscopic Properties of the Rare-Earth Orthoferrites, *Journal of Applied Physics*, **40**, 1061, (1969).

[143] J Kreisel, S Pignard, H Vincent and J P Sénateurg Lucazeau, Raman study of thin films Raman study of BaFe12O19 thin films, *Applied Physics Letters*, **73**, 1194, (1998).

[144] N Aliouane, O Prokhnenko, R Feyerherm, M Mostovoy, J Strempfer, K Habicht, K C Rule, E Dudzik, A U B Wolter, A Maljuk and D N Argyriou, Magnetic order and ferroelectricity in RMnO 3 multiferroic manganites : coupling between R- and Mn-spins, *Journal of physics: Condensed matter*, **20**, 434215, (2008).

[145] W. Kim, B.Y. Kum and C. S. Kim, Spin-Reorientation and Mossbauer Study of Orthoferrite TbFe0.75Mn0.25O3, *Journal of Superconductivity and Novel Magnetism*, **24**, 867–870, (2011).

[146] H. Nhalil, H. S. Nair, S. R., A. M. Strydom and S. Elizabeth, Spin-reorientation and weak ferromagnetism in antiferromagnetic TbMn0.5Fe0.5O3, *Journal of Applied Physics*, **117**, 173904, (2015).

[147] Y. Y. Guo, Y. L. Wang, J.-M. Liu and T. Wei, Role of t2g electrons in Mn-Tb coupling of multiferroic TbMnO3, *Journal of Applied Physics*, **116**, 063905, (2014).

[148] R. Kajimoto, H. Yoshizawa, H. Shintani, T. Kimura and Y. Tokura, Magnetic structure of TbMnO3 by neutron diffraction, *Physical Review B*, **70**, 012401, (2004).

[149] M Staruch and M Jain, Evidence of antiferromagnetic and ferromagnetic superexchange interactions in bulk TbMnCrO3, *Journal of Physics: Condensed Matter*, **26**, 046005, (2014).